



Università degli Studi di Pavia

ROSE School

**EUROPEAN SCHOOL FOR ADVANCED STUDIES IN
REDUCTION OF SEISMIC RISK**

**Advanced Computational Techniques
for the Study of
Traditional and Innovative Seismic Devices**

**A Thesis Submitted in Partial Fulfilment of the Requirements
for the Degree of Philosophiæ Doctor in
EARTHQUAKE ENGINEERING**

by

ALESSANDRO REALI

Supervisor: Prof. Ferdinando Auricchio (Università degli Studi di Pavia)

Coadvisors: Prof. Thomas J.R. Hughes (University of Texas at Austin)

Dr. Lorenza Petrini (Politecnico di Milano)

Pavia, August 2005

ABSTRACT

With the new developments of structural engineering and the continuously increasing need for more and more complete and complex analysis tools, the study of advanced computational techniques is becoming a very important issue also in the field of earthquake engineering.

The employment in structural design of seismic devices as isolators and of smart materials as shape memory alloys, together with the use of new nonlinear analysis strategies, requires the capability of dealing with difficult topics as geometric and material nonlinearity, incompressibility constraints, 3D inelasticity, modeling and meshing complexity, which in many situations still need to be deeply understood and studied.

It is in this framework that the present work has its basis, focusing on the development of advanced computational tools able to treat some of the delicate issues cited above.

Keywords: finite element method, isogeometric analysis, NURBS, structural vibrations, frame, truss, plate, membrane, 3D inelastic models, shape memory alloys, permanent plasticity, large strains, incompressibility, enhanced strain technique, seismic devices, nonlinear analysis

ACKNOWLEDGEMENTS

I want to thank Professor Ferdinando Auricchio for the support that he has always given me and for all the years that I have spent (and, hopefully, I will spend) working with him. I really have learnt more than a lot from him and I am sure to be just at the beginning.

I thank Professor Tom Hughes for giving me the great opportunity to be part of his team. I started to know Finite Elements and Computational Mechanics through his books and working with him has been a dream as well as a fantastic and fruitful experience, that I hope to repeat in the future.

Thanks to Doctor Lorenza Petrini for her help in assembling and reviewing this thesis, but even more for her friendship in these years.

I also wish to thank Professor Gian Michele Calvi and his collaborators for starting and supporting the stimulating environment which ROSE School indeed is.

Thanks a lot to my friends: all of them have played an important role in my life. In particular I want to thank here my Italian “ROSE friends” Andrea, Chiara, Claudio, Fugo, Giorgio, Iunio, Maria, Paola, Paolo, Sandrina, SandraJ, Simone and all those who have shared with me this period, because they have made studying together an exciting experience.

Many thanks to my “ICES friends”, too, because without them I would be lost in Texas. In particular, I wish to thank Austin (the NURBS-man), Giancarlo, Gugo and Yuri. Thanks also to the “mathematicians”, Carlo, Lourenço and Ulisse, for their precious collaboration as well as for their friendship.

I want to thank with all my heart my mom, my dad, Federica, Eli & Baldo, as well as all the members of my family (meaning of course also Carlo, Rita and Fra). Without their love and constant support it would have been impossible every step up to now.

Finally (“last but not least”, I daresay), I thank the most important person in my life, my wife Paola, because she is the real sense of what I do, every day. I feel that today an era of my life is closing, but I do not fear the future as I know that she will always be by my side and we will face together everything.

Pavia, 31 August 2005

“All we have to decide is what to do with the time that is given us.”

J. R. R. Tolkien

TABLE OF CONTENTS

ABSTRACT	i
ACKNOWLEDGEMENTS	iii
TABLE OF CONTENTS	vii
LIST OF TABLES	xiii
LIST OF FIGURES	xv
1. INTRODUCTION	1
1.1. Organization of the Work	2
2. THE NEED FOR ADVANCED COMPUTATIONAL TOOLS IN EARTHQUAKE ENGINEERING	3
2.1. Seismic isolation: high-damping rubber bearings	3
2.2. Smart materials for seismic devices: shape memory alloys	6
2.3. Innovative design guidelines: nonlinear analysis strategies	7
3. ISOGEOMETRIC ANALYSIS FOR STRUCTURAL DYNAMICS	9
3.1. NURBS and Isogeometric Analysis	13
3.1.1. B-Splines	13
3.1.2. Non-Uniform Rational B-Splines	16
3.1.3. Isogeometric Analysis	18

3.1.4. k -refinement	19
3.2. Structural vibrations	21
3.3. Longitudinal vibrations of an elastic rod	22
3.3.1. Numerical experiments	23
3.3.2. Analytical determination of the discrete spectrum	24
3.4. Transverse vibrations of a Bernoulli-Euler beam	29
3.4.1. Numerical experiments	30
3.4.2. Boundary conditions on rotations	33
3.5. Transverse vibrations of an elastic membrane	36
3.6. Transverse vibrations of a Poisson-Kirchhoff plate	37
3.7. Vibrations of a clamped thin circular plate using three-dimensional solid elements	38
3.8. NASA Aluminum Testbed Cylinder	43
3.9. Conclusive considerations	58
4. SHAPE MEMORY ALLOYS FOR EARTHQUAKE ENGINEERING: APPLICATIONS AND MODELING	61
4.1. Shape memory alloys	61
4.1.1. General aspects	62
4.1.2. Commercial SMAs	63
4.1.3. SMA applications	65
4.2. SMAs in earthquake engineering	70

4.2.1. Studies on the mechanical behaviour of SMA elements	70
4.2.2. The MANSIDE project	74
4.2.3. Numerical studies on SMA-based devices	78
4.2.4. Experimental studies on SMA-based devices	80
4.2.5. Applications of SMA devices for seismic retrofit of existing structures .	81
4.3. A new three-dimensional model describing stress-induced solid phase trans- formation with permanent inelasticity	85
4.3.1. 3D phenomenological model for stress-induced solid phase transforma- tion with permanent inelasticity	86
4.3.2. Time-discrete frame	94
4.3.3. Numerical results	96
4.3.4. Conclusive considerations for Section 4.3	100
5. MIXED-ENHANCED STRAIN TECHNIQUES FOR THE STUDY OF INCOMPRESSIBILITY AND GEOMETRIC NONLINEARITIES	105
5.1. An analysis of some mixed-enhanced finite elements for plane linear elasticity	106
5.1.1. The linear elasticity problem	107
5.1.2. Error analysis	110
5.1.3. Examples of triangular elements	113
5.1.4. Numerical tests	115
5.1.5. Conclusive considerations for Section 5.1	121
5.2. A stability study of some mixed finite elements for large deformation elas- ticity problems	129

5.2.1. The finite strain incompressible elasticity problem	130
5.2.2. A model problem for finite strain incompressible elasticity	132
5.2.3. The stability range	135
5.2.4. Discrete stability range: some theoretical results	137
5.2.5. Numerical tests	141
5.2.6. Conclusive considerations for Section 5.2	143
6. CONCLUSIONS	145
REFERENCES	148
A. COMPUTATION OF THE ISOGEOMETRIC ANALYSIS ORDER OF ACCURACY FOR THE ROD PROBLEM	161
A.1. Order of accuracy employing quadratic NURBS and consistent mass	161
A.2. Order of accuracy employing cubic NURBS and consistent mass	163
A.3. Order of accuracy employing lumped mass	163
B. PROOFS FOR PROPOSITIONS AND THEOREMS OF CHAPTER 5	167
B.1. Proof for Proposition 5.1.3	167
B.2. Proof for Theorem 5.1.4	168
B.3. Proof for Proposition 5.1.7	169
B.4. Proof for Proposition 5.1.7	170
B.5. Proof for Proposition 5.2.5	172
B.6. Proof for Proposition 5.2.7	175

B.7.Proof for Proposition 5.2.8	176
B.8.Proof for Proposition 5.2.9	179

LIST OF TABLES

3.1	Clamped circular plate. Geometric and material parameters.	39
3.2	Clamped circular plate. Numerical results compared with the exact solution.	40
4.1	Material parameters.	97
5.1	Bending test. Quadrilateral elements with $\lambda/\mu = 1$. Undistorted ($a = 0$) and distorted ($a = .5$) 1×1 meshes, distorted ($a = .5$) 4×4 , 16×16 and 64×64 meshes.	122
5.2	Bending test. Triangular elements with $\lambda/\mu = 1$. Undistorted ($a = 0$) and distorted ($a = .5$) 1×1 meshes, distorted ($a = .5$) 4×4 , 16×16 and 64×64 meshes.	122
5.3	Bending test. Quadrilateral and triangular elements with $\lambda/\mu = 10^7$. Undistorted ($a = 0$) 1×1 mesh and distorted ($a = .5$) 4×4 , 16×16 and 64×64 meshes.	123
5.4	Bending test. Quadrilateral and triangular elements with $\lambda/\mu = +\infty$. Undistorted ($a = 0$) 1×1 mesh and distorted ($a = .5$) 4×4 , 16×16 and 64×64 meshes.	123
5.5	Cook's membrane. Quadrilateral and triangular elements with $\lambda/\mu = 2$. Meshes: 4×4 , 16×16 and 64×64	124
5.6	Cook's membrane. Quadrilateral and triangular elements with $\lambda/\mu = 2 \times 10^7$. Meshes: 4×4 , 16×16 and 64×64	124
5.7	Cook's membrane. Quadrilateral and triangular elements with $\lambda/\mu = +\infty$. Meshes: 4×4 , 16×16 and 64×64	125
5.8	Load increments $\Delta\gamma$ (depending on the load level γ) for the Newton-Raphson scheme.	143
5.9	MINI element: numerical stability limits for the model problem.	144

5.10 QME element: numerical stability limits for the model problem. 144

5.11 Q2P1 element: numerical stability limits for the model problem. 144

LIST OF FIGURES

2.1	University of California at San Diego: SRMD dynamic testing of a lead-rubber bearing at 208% shear strain.	4
2.2	Bridgestone KL301 high-damping rubber bearing (cf. Grant <i>et al.</i> [2005]).	5
2.3	SMA seismic devices produced by FIP Industriale SpA [2005].	6
3.1	Schematic illustration comparing finite element analysis and isogeometric analysis meshes for a bracket.	10
3.2	“What is a circle?” In finite element analysis it is an idealization attained in the limit of mesh refinement but never for any finite mesh. In isogeometric analysis, the same exact geometry and parameterization are maintained for all meshes.	11
3.3	Cubic basis functions formed from the open knot vector $\Xi = \{0, 0, 0, 0, 1/6, 1/3, 1/2, 2/3, 5/6, 1, 1, 1, 1\}$	14
3.4	Piece-wise cubic B-Spline curve (solid line) and its control polygon (dotted).	15
3.5	Comparison of control variable growth in one dimension.	20
3.6	Comparison of control variable growth in two dimensions.	20
3.7	Comparison of control variable growth in three dimensions.	20
3.8	Fixed-fixed-rod. Normalized discrete spectra using quadratic finite elements and NURBS.	23
3.9	Fixed-fixed rod. Normalized discrete spectra using different order NURBS basis functions.	24
3.10	Fixed-fixed rod. Last normalized frequencies for $p = 2, \dots, 10$	25

3.11 Fixed-fixed rod. Order of convergence for the first three frequencies using quadratic NURBS.	25
3.12 Fixed-fixed rod. Order of convergence for the first three frequencies using cubic NURBS.	26
3.13 Fixed-fixed rod. Order of convergence for the first three frequencies using quartic NURBS.	26
3.14 Fixed-fixed rod. Comparison of analytical and numerical discrete spectra computed for quadratic and cubic NURBS.	28
3.15 Control points for linear parameterization (dots) compared with uniformly-spaced control points (asterisks) for cubic NURBS.	29
3.16 Plot of the parameterization for the cases of uniformly-spaced control points and linear parameterization (cubic NURBS, 21 control points).	29
3.17 Plot of the Jacobian of the parameterization for the cases of uniformly-spaced control points and linear parameterization (cubic NURBS, 21 control points).	30
3.18 Fixed-fixed rod. Normalized discrete spectra using uniformly-spaced control points. (These results are identical to those presented in Figure 3.9 except the outliers have been eliminated.)	30
3.19 Fixed-fixed rod. Normalized discrete spectra using different order NURBS basis functions with “row sum” lumped mass matrices.	31
3.20 Simply-supported beam. Normalized discrete spectra using cubic finite elements and NURBS.	31
3.21 Simply-supported beam. Normalized discrete spectra using different order NURBS basis functions.	32
3.22 Simply-supported beam. Last normalized frequencies for $p = 2, \dots, 10$	32
3.23 Simply-supported beam. Order of convergence for the first three frequencies using quadratic NURBS.	33

3.24 Simply-supported beam. Order of convergence for the first three frequencies using cubic NURBS.	33
3.25 Simply-supported beam. Order of convergence for the first three frequencies using quartic NURBS.	34
3.26 Simply-supported beam. Analytical and numerical discrete spectra computed using cubic and quartic NURBS.	34
3.27 Simply-supported beam. Normalized discrete spectra using equally spaced control points. (These results are identical to those presented in Figure 3.21 except the outliers are eliminated.)	35
3.28 Cantilever beam with weakly enforced rotation boundary condition. Normalized discrete spectra using different order NURBS basis functions.	35
3.29 Cantilever beam with Lagrange multiplier. Normalized discrete spectra using different order NURBS basis functions.	36
3.30 Square membrane. Normalized discrete spectra using different order NURBS basis functions (90×90 control points). Note the presence of optical branches.	37
3.31 Square membrane. Detail of the low-frequency part of the normalized discrete spectra.	38
3.32 Square membrane. Normalized discrete spectra using a uniformly-spaced control net. Note, the optical branches of Figure 3.30 are eliminated.	39
3.33 Poisson-Kirchhoff plate. Normalized discrete spectra using different order NURBS basis functions (90×90 control points). Note the presence of optical branches.	40
3.34 Poisson-Kirchhoff plate. Detail of the low-frequency part of the normalized discrete spectra.	41
3.35 Poisson-Kirchhoff plate. Normalized discrete spectra using a uniformly-spaced control net. Note, the optical branches of Figure 3.33 are eliminated.	41

3.36	Clamped circular plate. Eight element mesh.	41
3.37	Clamped circular plate. Eigenmode corresponding to ω_{01}	42
3.38	Clamped circular plate. Eigenmode corresponding to ω_{11}	42
3.39	Clamped circular plate. Eigenmode corresponding to ω_{02}	42
3.40	NASA Aluminum Testbed Cylinder (ATC). Frame and skin.	44
3.41	NASA ATC. Frame only.	44
3.42	NASA ATC frame and skin: Isogeometric model.	44
3.43	NASA ATC frame: Isogeometric model.	45
3.44	NASA ATC. Isogeometric model of the main rib.	45
3.45	NASA ATC. Typical 15° segment of the main rib. Mesh 1, the coarsest mesh, encapsulates the exact geometry.	45
3.46	NASA ATC. Typical 15° segment of the main rib. Mesh 2. Knot insertion has been used selectively to help even out the aspect ratios of elements making Mesh 2 more uniform and suitable for analysis.	46
3.47	NASA ATC. Typical 15° segment of the main rib. Mesh 3. Further refinement may be necessary to resolve the solution, as is the case with standard finite element analysis, but the geometry is never altered as the mesh is refined.	46
3.48	NASA ATC. Detail of the “notch” region in the main rib. The control net is on the left and the exact geometry is on the right.	46
3.49	NASA ATC. Isogeometric model of the longitudinal stringer. Sample meshes.	47
3.50	NASA ATC. Typical 15° segment of an end rib. Mesh 1 (coarsest mesh). .	47
3.51	NASA ATC. Typical 15° segment of an end rib. Mesh 2.	47

3.52 NASA ATC. Typical 15° segment of and end rib. Mesh 3.	47
3.53 NASA ATC. Detail of the “notch” region in an end rib. The control net is on the left and the exact geometry is on the right.	48
3.54 NASA ATC. Stringer–main rib junction.	48
3.55 NASA ATC. Stringer–end rib junction.	48
3.56 NASA ATC. Comparison of numerical and experimental frequency results for the longitudinal stringer.	50
3.57 NASA ATC. Selected calculated mode shapes for the stringer. Three lowest x - z modes.	50
3.58 NASA ATC. Comparison of numerical and experimental frequency results for the main rib.	50
3.59 NASA ATC. Computed mode shapes for the main rib. First three out-of- plane modes.	51
3.60 NASA ATC. Computed mode shapes for the main rib. First three in-plane modes.	52
3.61 NASA ATC. Comparison of numerical and experimental frequency results for the frame assembly.	53
3.62 NASA ATC. Relative frequency error for the frame assembly.	53
3.63 NASA ATC. Calculated first torsional mode for the frame assembly; side view. The color contours represent the vertical displacement.	54
3.64 NASA ATC. Detail of first torsional mode for the frame assembly; stringer–main rib junction.	54
3.65 NASA ATC. Calculated first torsional mode for the frame assembly; end view. The color contours represent the vertical displacement.	55

3.66 NASA ATC. Calculated first bending mode for the frame assembly. The color contours represent the vertical displacement.	55
3.67 NASA ATC. Comparison of numerical and experimental frequency results for the frame and skin assembly.....	56
3.68 NASA ATC. Relative frequency error for the frame skin assembly.	56
3.69 NASA ATC. Calculated first Rayleigh mode of the frame and skin assembly. The color contours represent the ovalization of the assembly.	57
3.70 NASA ATC. Calculated first Love mode of the frame and skin assembly. The color contours represent the ovalization of the assembly.	57
3.71 NASA ATC. Calculated first Love mode of the frame and skin assembly. The color contours represent the axial displacement of the assembly.	58
4.1 Shape-memory effect.....	69
4.2 Superelastic effect	69
4.3 Dissipated and potential energy: superelastic effect in tension (continuous line) and in compression (dashed line). (a) ΔW and W are respectively the dissipated energy and the maximum strain energy in a tensile loading-unloading test while (b) U is the maximum potential energy in a tension-compression test (cf. Piedboeuf and Gauvin [1998]).	82
4.4 Seismic retrofit of a multi-span bridge using SMA restrainers	82
4.5 Particular of a SMA restrainer for bridge retrofit	83
4.6 Beam-to-column connection equipped with martensitic bars.....	83
4.7 Particular of a brace system equipped with SMA wires	83
4.8 SMA devices for seismic rehabilitation	84
4.9 SMA devices for seismic rehabilitation	84

4.10 Experimental results on a SMA NiTi wire. Cyclic tension test: stress versus strain up to 6% strain.	86
4.11 Plots of $s = s(e^{tr})$ in the cases of unloading from compression (left) and from tension (right).	91
4.12 Translated plots of $s = s(e^{tr})$ in the cases of unloading from compression (left) and from tension (right).	92
4.13 Uniaxial tests: tension cycles with permanent inelasticity ($H = 0$ MPa, $A = 0$ MPa, $\kappa = 2\%$, $T=298K$). Axial stress–axial strain output for single (left) and multiple (right) tension loops.	100
4.14 Uniaxial tests: single tension cycle with permanent inelasticity ($H = 0$ MPa, $A = 0$ MPa, $\kappa = 2\%$, $T=298K$). Output histories for e_{11}^{tr} and q_{11} (left) and $\ \mathbf{X}\ $ and $\ \mathbf{Q}\ $ (right).	101
4.15 Uniaxial tests: ten tension cycles with permanent inelasticity ($H = 0$ MPa, $A = 0$ MPa, $\kappa = 2\%$, $T=298K$). Output histories for e_{11}^{tr} and q_{11} (left) and $\ \mathbf{X}\ $ and $\ \mathbf{Q}\ $ (right).	101
4.16 Uniaxial tests: ten tension cycles (left) and ten tension followed by fifteen compression cycles (right) with saturating permanent inelasticity ($H = 1.5 \cdot 10^4$ MPa, $A = 0$ MPa, $\kappa = 2\%$, $T=298K$). Axial stress–axial strain output.	101
4.17 Uniaxial tests: ten tension cycles with saturating permanent inelasticity, including degradation effect ($H = 1.5 \cdot 10^4$ MPa, $A = 10^3$ MPa, $\kappa = 2\%$, $T = 298$ K). Axial stress–axial strain output.	102
4.18 Uniaxial tests: multiple (ten) tension cycles at $T = M_f$, each one followed by heating strain recovery, with $H = 0$ MPa, $A = 0$ MPa (left) and $H = 1.5 \cdot 10^4$ MPa, $A = 10^3$ MPa (right) and $\kappa = 2\%$. Axial stress–axial strain output.	102
4.19 Biaxial tests: non-proportional hourglass-shaped test ($H = 1.5 \cdot 10^4$ MPa, $A = 10^3$ MPa, $\kappa = 10\%$, $T = 298$ K). $\sigma_{11} - \sigma_{12}$ input (left) and 1 st and 10 th cycle $\varepsilon_{11} - \gamma_{12}$ output (right).	102

4.20	Biaxial tests: non-proportional square-shaped test ($H = 1.5 \cdot 10^4$ MPa, $A = 10^3$ MPa, $\kappa = 10\%$, $T = 298$ K). $\sigma_{11} - \sigma_{22}$ input (left) and 1^{st} and 10^{th} cycle $\varepsilon_{11} - \varepsilon_{22}$ output (right).	103
4.21	Combined uniaxial tests: ten tension cycles in direction 1 followed by twenty in direction 2 ($H = 1.5 \cdot 10^4$ MPa, $A = 0$ MPa, $\kappa = 2\%$, $T = 298$ K). Stress input histories (left) and q_{11} and q_{22} output histories (right). . .	103
4.22	Combined uniaxial tests: ten tension cycles in direction 1 followed by twenty in direction 2 ($H = 1.5 \cdot 10^4$ MPa, $A = 0$ MPa, $\kappa = 2\%$, $T = 298$ K). $\sigma_{11} - \varepsilon_{11}$ output (left) and $\sigma_{22} - \varepsilon_{22}$ output (right).	103
5.1	Fully constrained block. Problem geometry and boundary conditions. Undistorted quadrilateral, distorted quadrilateral and triangular meshes. .	125
5.2	Fully constrained block. Polynomial load test. L^2 -norm convergence rate for \mathbf{u}	126
5.3	Fully constrained block. Polynomial load test. L^2 -norm convergence rate for p	126
5.4	Fully constrained block. Polynomial load test. Energy-norm convergence rate for \mathbf{u}	126
5.5	Fully constrained block. Trigonometric load test. L^2 -norm convergence rate for \mathbf{u}	127
5.6	Fully constrained block. Trigonometric load test. L^2 -norm convergence rate for p	127
5.7	Fully constrained block. Trigonometric load test. Energy-norm convergence rate for \mathbf{u}	127
5.8	Bending test. Problem geometry, boundary and loading conditions. Distorted 4×4 meshes.	128
5.9	Cook's membrane. Problem geometry, boundary and loading conditions. 8×8 meshes.	128

5.10 Problem domain Ω .	133
5.11 Triangular mesh for the MINI element.	139
A.1 Rod problem: normalized discrete spectrum using quadratic NURBS versus $1 + (\omega h)^4/1440$ for low frequencies.	162
A.2 Rod problem: normalized discrete spectrum using cubic NURBS versus $1 + (\omega h)^6/60480$ for low frequencies.	163
A.3 Rod problem: analytical versus numerical discrete spectrum computed using quadratic and cubic NURBS; lumped mass formulation.	164
A.4 Rod problem: normalized discrete spectrum using cubic NURBS versus $1 - (\omega h)^2/8$ for low frequencies; lumped mass formulation.	165
A.5 Rod problem: normalized discrete spectrum using cubic NURBS versus $1 - (\omega h)^2/6$ for low frequencies; lumped mass formulation.	165
B.1 Oriented paths γ_X^1 and γ_X^2 on Ω .	173

1. INTRODUCTION

As the development of the field of earthquake engineering is growing rapidly in many directions, it can be stated that there really exists the need of giving an adequate computational support to this growth.

In this framework, it is possible to identify a number of computational issues, needing new formulations and deeper investigations, which can turn out useful for a correct and complete modeling of structures, in particular when subjected to strong ground motions.

When studying isolators, it is not unfrequent to deal with both material and geometric nonlinearities, as well as with the incompressibility constraint when rubbers are employed. Moreover, when 3D finite element simulations of seismic devices are required, also mesh complexity (and related geometric approximations) may become a problem. Other examples of fields where material or geometric nonlinearities play an important role are the study of the behaviour of smart materials (as shape memory alloys) that can be employed in earthquake engineering and the introduction of innovative design guidelines based on nonlinear analysis strategies.

It is from these considerations that the idea behind this thesis arises. Its goal is giving a collection of numerical tools able to overcome some numerical difficulties that can be faced in earthquake engineering. In particular, the themes treated within this work are:

- isogeometric analysis for structural dynamics;
- shape memory alloys for earthquake engineering: applications and modeling;
- mixed-enhanced strain techniques for the study of incompressibility and geometric nonlinearities.

In the following Chapters, contributions to all of these issues are given, as detailed in Section 1.1 which describes the organization of the work.

1.1 Organization of the Work

The present work is organized in four main Chapters.

The first one consists of the presentation of some important earthquake engineering problems implying the need for a deep study of advanced computational issues.

In the second one, the concept of Isogeometric Analysis applied to structural dynamics is presented (cf. Reali [2004, 2005]; Cottrell *et al.* [2005a,b]). Case studies are the modal analysis of truss, frame and two-dimensional elements, as well as some three-dimensional structural members and the whole resulting structure for which modal experimental results are available from NASA.

The third main Chapter refers to shape memory alloys: some seismic applications for these smart materials are presented, together with the introduction and the assessment of a new constitutive model able to reproduce their three-dimensional macroscopic behaviour, including permanent inelastic effects (cf. Auricchio and Reali [2005a,b]; Auricchio *et al.* [2005d]).

The last Chapter, then, deals with finite element approximation of incompressibility in both the small and the large strain regimes: a solution to some of the related problems is found in the framework of mixed-enhanced strain elements (cf. Auricchio *et al.* [2004, 2005a,b]).

Afterwards, conclusions about the numerical tools developed within this work are discussed together with possible future ways of investigation.

Finally, the two Appendices report, respectively, some analytical computations of isogeometric analysis orders of accuracy and the mathematical proofs for Chapter 5 Propositions and Theorems.

2. THE NEED FOR ADVANCED COMPUTATIONAL TOOLS IN EARTHQUAKE ENGINEERING

Earthquake engineering is a research field in continuous expansion and the development of numerical methods able to support its new frontiers constitutes an important field of investigation as well.

In this context, the aim of the present Chapter is to briefly analyze some earthquake engineering problems from which computational difficulties may arise, justifying the research project described in this thesis.

The seismic applications considered in the following are:

- seismic isolation: high-damping rubber bearings;
- smart materials for seismic devices: shape memory alloys;
- innovative design guidelines: nonlinear analysis strategies.

As shown in next Sections, these research directions call for deeper studies on some delicate topics such as *geometric nonlinearity*, *inelasticity*, *incompressibility*, *mesh and geometry complexity*. Subsequent Chapters will then focus on some numerical techniques for dealing with these issues.

2.1 Seismic isolation: high-damping rubber bearings

Seismic isolation is a widespread method for seismic protection of bridges and buildings. The main idea is to place flexible bearings between the primary mass of the structure and the source motion, typically isolating bridge superstructures from piers or buildings from foundations. Such a procedure can be used for both new and existing structures and its main advantages will be briefly discussed in the following.

As a first effect, adding a flexible bearing lengthens the fundamental period of the whole structure, decreasing design forces for short period structures.

Then, a higher flexibility may increase structure displacements, but, on the other side,

inelastic deformation is confined to the isolation device so that an elastic design for the remainder of the structure is possible.

Moreover, isolators are able to dissipate seismic energy by means of hysteretic damping or through supplemental damper insertion.

Finally, it is to be considered also that in some cases the isolator can act as a “fuse” for the structure, when the forces transferred to the structure are limited by the maximum amount of force that can be transmitted across the bearing.

Rubber-based isolators, as lead-rubber and high-damping rubber bearings, are a particularly significative example within this study, because their characteristics constitute a reason for the study of incompressibility (always to be taken into account when modeling rubber materials) as well as of material and geometric nonlinearities (for instance, Figure 2.1 shows the response of a lead-rubber bearing subjected to 208% shear strain). In the following, we focus on a particular type of seismic isolation device, the so-called *high-damping rubber bearing* (HDRB), about which the interested reader can find a detailed discussion in Grant *et al.* [2005] and references therein.



Figure 2.1. University of California at San Diego: SRMD dynamic testing of a lead-rubber bearing at 208% shear strain.

HDRBs are seismic isolators commonly used in both construction and retrofit of bridges and buildings. As usual with elastomeric seismic devices, HDRBs are composed of elastomeric compound layers reinforced by steel layers in order to increase vertical stiffness (see Figure 2.2 for a sketch of a typical HDRB). The elastomer usually consists of a filled natural or synthetic rubber in order to provide seismic energy dissipation under cyclic loading without needing supplemental damping.

The nonlinear constitutive law of the employed rubbers (both in the cases of filled natural or synthetic) implies high horizontal stiffness for low shear strains, low stiffness for medium strains and increasing shear modulus for higher strains. In this way, at service conditions a high bearing stiffness makes forces and deformations in the structure to be

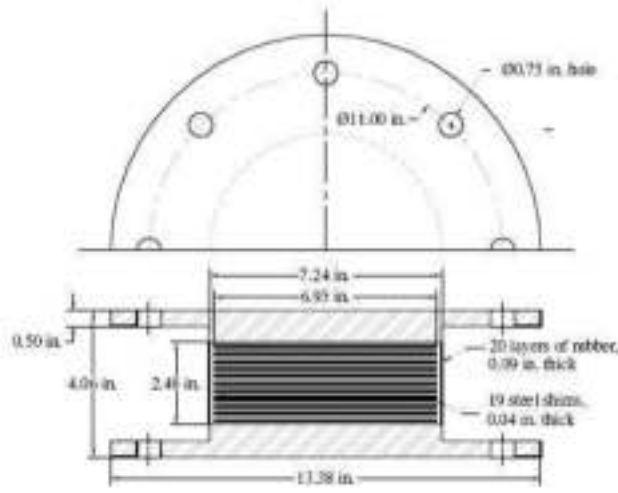


Figure 2.2. Bridgestone KL301 high-damping rubber bearing (cf. Grant *et al.* [2005]).

expected in the elastic range; at a moderate earthquake, instead, the bearing deformation isolates the structure and provides energy dissipation; at an extreme seismic event, finally, the elastomer strain-stiffening limits the isolator deformation, thus reducing the risk of instabilities of the bearing itself.

We remark that this brief (and not satisfactory at all) presentation of such a device aims only at introducing to the reader's attention the presence of problems like *large deformation*, *inelasticity* and *incompressibility* in earthquake engineering state-of-the-practice, so highlighting the necessity of computational tools able to simulate these important behaviours. In Chapter 5, we will deal with mixed-enhanced finite element methods for treating incompressibility, and, in particular, in the second part of the Chapter, we will focus on incompressible large strain (i.e. geometrically nonlinear) problems.

Moreover, Figure 2.2 shows that the geometry of an isolator of this type, though simple in each of its parts, can be rather complex in its entirety. Accordingly, if an analysis of the device is required, also *geometry approximation* and *mesh complexity* problems play an important role for a successful simulation procedure. In fact, the introduction of a faceted mesh approximating a smooth surface may for instance give rise to non-physical stress concentrations at mesh corners. So, in Chapter 3, we will show, with particular reference to structural dynamics, a new method (referred to as Isogeometric Analysis) able to deal with geometric problems like this by means of an *exact geometry* approach.

2.2 Smart materials for seismic devices: shape memory alloys

Earthquake engineering, and in particular its branch devoted to the design of seismic protection devices, is a field strongly influenced by material science progresses, as the availability of new materials often opens roads previously considered difficult to be followed. A first example could be the development of rubbers with high damping properties, whose use has made possible the design of the HDRB isolators described in the previous Section.

Among the many smart materials that have been successfully employed in seismic devices in last years, we find particularly interesting the so-called *shape memory alloys* (SMAs), whose name comes from their capability of recovering the original shape after being subjected to large deformations. Though developed in the 1960s, it is only in the last decade that SMA use in earthquake engineering has been really considered and studied, opening new possibilities and applications due to their unique characteristics (Figure 2.3 reports an example of commercial SMA seismic devices). As a consequence, the development of constitutive models able to reproduce the three-dimensional inelastic behaviour of SMAs is a subject to be tackled, as it is basilar in order to construct reliable numerical tools for simulating the response of any SMA-based devices.

So, we entirely devote Chapter 4 to SMAs and, after a general introduction to their main features and a review of the state-of-the-art on the employment of such materials in earthquake engineering, we present in detail a new 3D constitutive model capable of reproducing their main macroscopic behaviours.



Figure 2.3. SMA seismic devices produced by FIP Industriale SpA [2005].

2.3 Innovative design guidelines: nonlinear analysis strategies

The field of earthquake engineering is increasingly influenced by the significant development of the performance-based seismic engineering concepts and methodologies that is taking place in the last two decades (cf. Penelis and Kappos [1997] and references therein). Accordingly, innovative design guidelines and analysis procedures, as nonlinear time-history or pushover (nonlinear static) analysis, are becoming more and more popular (see, e.g., FEMA 440 [2005]; NZS 1170.5 [2004]; OPCM 3274 [2003]).

An essential requisite in performance-based seismic design is the estimation of inelastic deformation demands in structural members; in fact, the main idea consists in accounting for the structural ductility developed by a structure when entering its nonlinear response range to reach a predetermined performance limit state (cf., e.g., Paulay and Priestley [1992]). In this context, the study of analysis strategies able to model in a reliable way the nonlinear behaviour of the structures under investigation becomes of primary importance.

The matter of nonlinear analysis techniques within performance-based seismic engineering would indeed deserve a detailed and complete discussion, as proved by the wide literature devoted to this topic. The aim of this Section, instead, just consists in pointing out that also the diffusion of these research directions, which are becoming more and more an important part in design guidelines, highlights the necessity of deeper studies on issues like *material and geometric nonlinearities*, basilar to correctly implement the numerical tools needed for these kinds of analysis.

3. ISOGEOMETRIC ANALYSIS FOR STRUCTURAL DYNAMICS

As seen in the previous Chapter, mesh and geometry problems may constitute important issues in the field of earthquake engineering and, more in general, of structural dynamics. Here a new method, referred to as Isogeometric Analysis, showing a number of advantages with respect to standard finite element methods is presented and discussed.

The concept of Isogeometric Analysis, introduced by Hughes *et al.* [2005], may be viewed as a logical extension of finite element analysis. The objectives of the isogeometric approach are to develop an analysis framework based on functions employed in Computer Aided Design (CAD) systems, capable of representing many engineering geometries exactly; to employ one, and only one, geometric description for all meshes and all orders of approximation; and to vastly simplify mesh refinement procedures. As a primary tool in the establishment of this new framework for analysis, Hughes *et al.* [2005] selected NURBS (Non-Uniform Rational B-Splines; see, e.g., Rogers [2001] and Piegł and Tiller [1997]), obtaining excellent results for problems of linear solid and structural mechanics and linear shells modeled as three-dimensional solids (as well as for advection-diffusion problems).

A fundamental tenet of isogeometric analysis is to represent geometry as accurately as possible, because the faceted nature of finite element geometries could lead to significant errors and difficulties. This is schematically conveyed in Figure 3.1. In order to generate meshes, geometrical simplifications are introduced in finite element analysis. For example, features such as small holes and fillets are often removed. Stress concentrations produced by holes are then missing, and artificial, non-physical, stress concentrations are induced by the removal of fillets. The stresses at sharp, reentrant corners will be infinite, which makes adaptive mesh refinement strategies meaningless. If the refinement is performed to capture geometrical features in the limit, then tight, automated communication with the geometry definition, typically a CAD file, must exist for the mesh generator and solver. It is rarely the case that this ideal situation is attained in industrial settings, which seems to be the reason that automatic, adaptive, refinement procedures

have had little industrial penetration despite enormous academic research activity. In isogeometric analysis, the first mesh is designed to represent the exact geometry, and subsequent refinements are obtained without further communication with the CAD representation. This idea is dramatized in Figure 3.2 in which the question “What is a circle?” is asked rhetorically. In finite element analysis, a circle is an ideal achieved in the limit of mesh refinement (i.e., h -refinement) but never achieved in reality, whereas a circle is achieved exactly for the coarsest mesh in isogeometric analysis, and this exact geometry, and its parameterization, are maintained for all mesh refinements. It is interesting to note that, in the limit, the isogeometric model converges to a polynomial representation on each element, but not for any finite mesh. This is the obverse of finite element analysis in which polynomial approximations exist on all meshes, and the circle is the idealized limit.

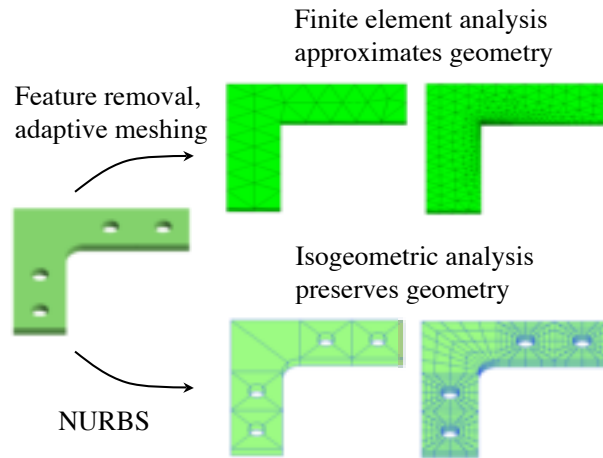


Figure 3.1. Schematic illustration comparing finite element analysis and isogeometric analysis meshes for a bracket.

In this Chapter we discuss the isogeometric analysis methodology in structural vibration analysis. In Section 3.1 we briefly review the basic concepts of isogeometric analysis (the interested reader may consult Hughes *et al.* [2005] for a more comprehensive introduction). We emphasize the concept of k -refinement, a higher-order procedure employing smooth basis functions, which is used repeatedly in the vibration calculations later on. After a brief recall on the equations governing structural vibrations (Section 3.2), in Sections 3.3-3.7 we investigate isogeometric approaches to some simple model problems

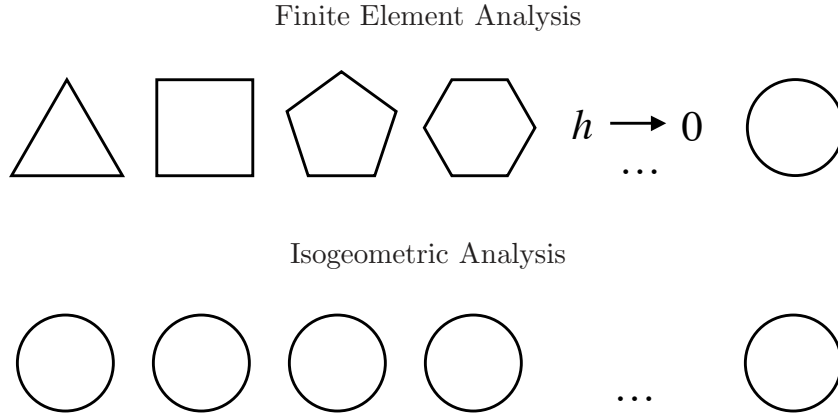


Figure 3.2. “What is a circle?” In finite element analysis it is an idealization attained in the limit of mesh refinement but never for any finite mesh. In isogeometric analysis, the same exact geometry and parameterization are maintained for all meshes.

of structural vibration, including the longitudinal vibration of a rod (and, equivalently, the transverse vibration of a string, or shear beam), the transverse vibration of a thin beam governed by Bernoulli-Euler theory, the transverse vibration of membranes, the transverse vibration of thin plates governed by Poisson-Kirchhoff theory, and the transverse vibration of a thin plate modeled as a three-dimensional elastic solid. In the cases of Bernoulli-Euler beam theory and Poisson-Kirchhoff plate theory, we have employed *rotationless* formulations, an important theme of contemporary research in structural mechanics (see, e.g., Oñate and Cervera [1993]; Oñate and Zarate [2000]; Cirak *et al.* [2000]; Cirak and Ortiz [2001]; Cirak *et al.* [2002]; Engel *et al.* [2002]; Phaal and Calladine [1992a,b]).

In the one-dimensional cases we perform numerical analyses of discrete frequency spectra. We are also able to theoretically derive the continuous, limiting spectra and we determine that these spectra are invariant if normalized by the total number of degrees-of-freedom in the model. In other words, one is able to determine *a priori* the error in frequency for a particular mode from a single function, no matter how many degrees-of-freedom are present in the model. These elementary results are very useful in determining the vibration characteristics of isogeometric models and provide a basis for comparison with standard finite element discretizations. It is well known that, in the case of higher-order finite elements, “optical” branches are present in the spectra (see Brillouin [1953]) and

that these are responsible for the large errors in the high-frequency part of the spectrum (see Hughes [2000]) and contribute to the oscillations (i.e., “Gibbs phenomena”) that appear about discontinuities in wave propagation problems. The accurate branch, the so-called “acoustic” branch (see Brillouin [1953]), corresponds to the low-frequency part of the spectrum. In finite element analysis, both acoustic and optical branches are continuous, and the optical branches vitiate a significant portion of the spectrum. In isogeometric analysis, when a linear parameterization of the geometrical mapping from the patch to its image in physical space is employed, only a finite number of frequencies constitute the optical branch. The number of modes comprising the optical branch is constant once the order of approximation is set, independent of the number of elements, but increases with order. In this case, almost the entire spectrum corresponds to the acoustic branch. A linear parameterization of the mapping requires a non-uniform distribution of control points. Hughes *et al.* [2005] describe the algorithm which locates control points to attain a linear parameterization. Spacing control points uniformly produces a nonlinear parameterization of the mapping and in this case, remarkably, the optical branch is entirely eliminated. The convergence rates of higher-order finite elements and isogeometric elements constructed by k -refinement are the same for the same order basis, but the overall accuracy of the spectrum is *much* greater for isogeometric elements. These observations corroborate the speculation that the k -method would be a more accurate and economical procedure than p -method finite elements in vibration analysis of structural members. Studies of membranes and thin plates provide additional corroboration. We also present some initial studies of mass lumping within the isogeometric approach. The “row sum” technique is employed (see Hughes [2000]). Due to the pointwise non-negativity of B-Spline and NURBS bases, the row sum technique is guaranteed to produce positive lumped masses but only second-order accurate frequencies are obtained, independently of the order of basis functions employed. This is unsatisfactory but we conjecture that, by appropriately locating knots and control points, higher-order-accurate lumping procedures may exist. This is a topic requiring further research.

In Section 3.8, we apply the isogeometric approach to the NASA Aluminum Testbed Cylinder (ATC) which has been extensively studied experimentally to determine its vibration characteristics. Our isogeometric model is an *exact* three-dimensional version of the “as drawn” geometry. All fine-scale features of the geometry, such as fillets, are precisely accounted for. Comparisons are made between the experimental data and the numerical results.

In Section 3.9 we draw conclusions. Appendix A presents analytical and numerical results

concerning the order of accuracy of consistent and lumped mass schemes.

Finally, we remark that details on isogeometric analysis for structural vibrations can be found in Reali [2004, 2005] and Cottrell *et al.* [2005a,b].

3.1 NURBS and Isogeometric Analysis

Non-Uniform Rational B-Splines (NURBS) are the standard way of describing and constructing curves and surfaces in the field of CAD and computer graphics, so these functions are widely described in the corresponding literature (refer for instance to Piegl and Tiller [1997] and to Rogers [2001]). The aim of this Section is to introduce them briefly and to present the guidelines of isogeometric analysis. The interested reader may refer to Hughes *et al.* [2005] for a detailed presentation of isogeometric analysis.

3.1.1 B-Splines

B-Splines are piece-wise polynomial curves whose components are defined as the linear combination of B-Spline basis functions and the components of some points in the space, referred to as *control points*. Fixed the *order* of the B-Spline (i.e. the degree of polynomials), to construct the basis functions the so-called *knot vector* needs to be introduced, as it is a fundamental ingredient for this operation.

3.1.1.1 Knot vectors.

A *knot vector*, Ξ , is a set of non-decreasing real numbers representing coordinates in the parametric space of the curve:

$$\Xi = \{\xi_1, \dots, \xi_{n+p+1}\}, \quad (3.1)$$

where p is the order of the B-Spline and n is the number of basis functions (and control points) necessary to describe it. The interval $[\xi_1, \xi_{n+p+1}]$ is called a *patch*. A knot vector is said to be *uniform* if its knots are uniformly-spaced and *non-uniform* otherwise. Moreover, a knot vector is said to be *open* if its first and last knots are repeated $p + 1$ times. In what follows, we always employ open knot vectors. Basis functions formed from open knot vectors are interpolatory at the ends of the parametric interval $[\xi_1, \xi_{n+p+1}]$ but are not, in general, interpolatory at interior knots.

3.1.1.2 Basis functions.

Given a knot vector, Ξ , B-Spline basis functions are defined recursively starting with

$p = 0$ (piecewise constants):

$$N_{i,0}(\xi) = \begin{cases} 1 & \text{if } \xi_i \leq \xi < \xi_{i+1} \\ 0 & \text{otherwise.} \end{cases} \quad (3.2)$$

For $p > 1$:

$$N_{i,p}(\xi) = \frac{\xi - \xi_i}{\xi_{i+p} - \xi_i} N_{i,p-1}(\xi) + \frac{\xi_{i+p+1} - \xi}{\xi_{i+p+1} - \xi_{i+1}} N_{i+1,p-1}(\xi). \quad (3.3)$$

In Figure 3.3 we present an example consisting of $n = 9$ cubic basis functions generated from the open knot vector $\Xi = \{0, 0, 0, 0, 1/6, 1/3, 1/2, 2/3, 5/6, 1, 1, 1, 1\}$.

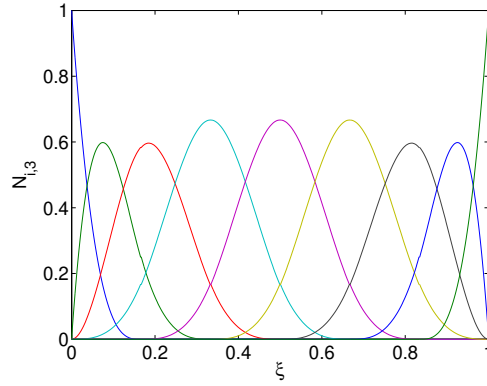


Figure 3.3. Cubic basis functions formed from the open knot vector $\Xi = \{0, 0, 0, 0, 1/6, 1/3, 1/2, 2/3, 5/6, 1, 1, 1, 1\}$.

An important property of B-Spline basis functions is that they are C^{p-1} -continuous, if internal knots are not repeated. If a knot has multiplicity k , the basis is C^{p-k} -continuous at that knot. In particular, when a knot has multiplicity p , the basis is C^0 and interpolatory at that location.

Other remarkable properties are that:

- B-Spline basis functions from an open knot vector constitute a partition of unity, i.e. $\sum_{i=1}^n N_{i,p}(\xi) = 1 \ \forall \xi$.
- The support of each $N_{i,p}$ is compact and contained in the interval $[\xi_i, \xi_{i+p+1}]$.
- B-Spline basis functions are non-negative, i.e. $N_{i,p} \geq 0 \ \forall \xi$.

3.1.1.3 B-Spline curves.

As a consequence of what seen above, given the order of a B-Spline and a knot vector, n basis functions are defined. Now, given n points in \mathbb{R}^d , referred to as *control points*, by taking the linear combination of the basis functions weighted by the components of control points, the components of the piece-wise polynomial B-Spline curve $\mathbf{C}(\xi)$ of order p can be obtained:

$$\mathbf{C}(\xi) = \sum_{i=1}^n N_{i,p}(\xi) \mathbf{B}_i, \quad (3.4)$$

being \mathbf{B}_i the i^{th} control point.

The piece-wise linear interpolation of the control points is called *control polygon*.

In Figure 3.4, a cubic 2D B-Spline curve, generated with the basis functions shown in Figure 3.3, is reported together with its control polygon.

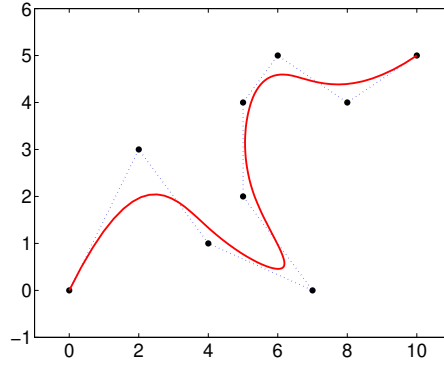


Figure 3.4. Piece-wise cubic B-Spline curve (solid line) and its control polygon (dotted).

It is important to stress that a B-Spline curve has continuous derivatives of order $p - 1$, which can be decreased by k if a knot or a control point has multiplicity $k + 1$.

Moreover, an important property of these curves is the so-called *affine covariance*, i.e. an affine transformation of the curve is obtained by applying the transformation to its control points.

3.1.1.4 B-Spline surfaces.

By means of tensor products, B-Spline surfaces can be constructed starting from a net

of $n \times m$ control points $\mathbf{B}_{i,j}$ (*control net*) and knot vectors:

$$\Xi = [\xi_1, \dots, \xi_{n+p+1}] \text{ and } H = [\eta_1, \dots, \eta_{m+q+1}].$$

Defined from the two knot vectors the 1D basis functions $N_{i,p}$ and $M_{j,q}$ (with $i = 1, \dots, n$ and $j = 1, \dots, m$) of order p and q respectively, the B-Spline surface is then constructed as:

$$\mathbf{S}(\xi, \eta) = \sum_{i=1}^n \sum_{j=1}^m N_{i,p}(\xi) M_{j,q}(\eta) \mathbf{B}_{i,j}. \quad (3.5)$$

3.1.1.5 B-Spline solids.

By means of tensor products, also B-Spline solids can be constructed. Given an $n \times m \times l$ control net and three knot vectors:

$$\Xi = [\xi_1, \dots, \xi_{n+p+1}], H = [\eta_1, \dots, \eta_{m+q+1}] \text{ and } Z = [\zeta_1, \dots, \zeta_{l+r+1}],$$

from which the 1D basis functions $N_{i,p}$, $M_{j,q}$ and $L_{k,r}$ (with $i = 1, \dots, n$, $j = 1, \dots, m$ and $k = 1, \dots, l$) of order p , q and r respectively are defined, the B-Spline solid is then:

$$\mathbf{S}(\xi, \eta, \zeta) = \sum_{i=1}^n \sum_{j=1}^m \sum_{k=1}^l N_{i,p}(\xi) M_{j,q}(\eta) L_{k,r}(\zeta) \mathbf{B}_{i,j,k}. \quad (3.6)$$

3.1.2 Non-Uniform Rational B-Splines

A rational B-Spline in \mathbb{R}^d is the projection onto d -dimensional physical space of a polynomial B-Spline defined in $(d+1)$ -dimensional homogeneous coordinate space. For a complete discussion of these space projections, see Farin [1995] and references therein. In this way, a great variety of geometrical entities can be constructed and, in particular, all conic sections can be obtained exactly. The projective transformation of a B-Spline curve yields a rational polynomial curve. Note that when we refer to the “order” of a NURBS curve, we mean the order of the polynomial curve from which the rational curve was generated.

To obtain a NURBS curve in \mathbb{R}^d , we start from a set \mathbf{B}_i^w ($i = 1, \dots, n$) of control points (“projective points”) for a B-Spline curve in \mathbb{R}^{d+1} with knot vector Ξ . Then the control points for the NURBS curve are:

$$(\mathbf{B}_i)_j = \frac{(\mathbf{B}_i^w)_j}{w_i}, \quad j = 1, \dots, d \quad (3.7)$$

where $(\mathbf{B}_i)_j$ is the j^{th} component of the vector \mathbf{B}_i and $w_i = (\mathbf{B}_i^w)_{d+1}$ is referred to as the i^{th} weight. The NURBS basis functions of order p are then defined as:

$$R_i^p(\xi) = \frac{N_{i,p}(\xi)w_i}{\sum_{\hat{i}=1}^n N_{\hat{i},p}(\xi)w_{\hat{i}}} \quad (3.8)$$

and their first and second derivatives are given by:

$$(R_i^p)'(\xi) = \frac{N_{i,p}'(\xi)w_i}{\sum_{\hat{i}=1}^n N_{\hat{i},p}(\xi)w_{\hat{i}}} - \frac{N_{i,p}(\xi)w_i \sum_{\hat{i}=1}^n N_{\hat{i},p}'(\xi)w_{\hat{i}}}{(\sum_{\hat{i}=1}^n N_{\hat{i},p}(\xi)w_{\hat{i}})^2} \quad (3.9)$$

and

$$\begin{aligned} (R_i^p)''(\xi) = & \frac{N_{i,p}''(\xi)w_i}{\sum_{\hat{i}=1}^n N_{\hat{i},p}(\xi)w_{\hat{i}}} + \frac{2N_{i,p}(\xi)w_i (\sum_{\hat{i}=1}^n N_{\hat{i},p}'(\xi)w_{\hat{i}})^2}{(\sum_{\hat{i}=1}^n N_{\hat{i},p}(\xi)w_{\hat{i}})^3} \\ & - \frac{2N_{i,p}'(\xi)w_i \sum_{\hat{i}=1}^n N_{\hat{i},p}'(\xi)w_{\hat{i}} + N_{i,p}(\xi)w_i \sum_{\hat{i}=1}^n N_{\hat{i},p}''(\xi)w_{\hat{i}}}{(\sum_{\hat{i}=1}^n N_{\hat{i},p}(\xi)w_{\hat{i}})^2}. \end{aligned} \quad (3.10)$$

The NURBS curve is defined by:

$$\mathbf{C}(\xi) = \sum_{i=1}^n R_i^p(\xi)\mathbf{B}_i. \quad (3.11)$$

Rational surfaces and solids are defined in an analogous way in terms of the basis functions (respectively)

$$R_{i,j}^{p,q}(\xi, \eta) = \frac{N_{i,p}(\xi)M_{j,q}(\eta)w_{i,j}}{\sum_{\hat{i}=1}^n \sum_{\hat{j}=1}^m N_{\hat{i},p}(\xi)M_{\hat{j},q}(\eta)w_{\hat{i},\hat{j}}} \quad (3.12)$$

and

$$R_{i,j,k}^{p,q,r}(\xi, \eta, \zeta) = \frac{N_{i,p}(\xi)M_{j,q}(\eta)L_{k,r}(\zeta)w_{i,j,k}}{\sum_{\hat{i}=1}^n \sum_{\hat{j}=1}^m \sum_{\hat{k}=1}^l N_{\hat{i},p}(\xi)M_{\hat{j},q}(\eta)L_{\hat{k},r}(\zeta)w_{\hat{i},\hat{j},\hat{k}}}. \quad (3.13)$$

In the following, we summarize remarkable properties of NURBS:

- NURBS basis functions from an open knot vector constitute a partition of unity, i.e. $\sum_{i=1}^n R_i^p(\xi) = 1 \forall \xi$.
- The continuity and supports of NURBS basis functions are the same as for B-Splines.
- NURBS possess the property of affine covariance.

- If all weights are equal, NURBS become B-Splines.
- NURBS surfaces and solids are the projective transformations of tensor product piece-wise polynomial entities.

3.1.3 Isogeometric Analysis

Hughes *et al.* [2005] propose the concept of *Isogeometric Analysis* as an *exact geometry* alternative to standard finite element analysis. In the following the guidelines for such a technique are reported:

- A mesh for a NURBS patch is defined by the product of knot vectors. For example, in three-dimensions, a mesh is given by $\Xi \times H \times Z$.
- Knot spans subdivide the domain into “elements.”
- The support of each basis function consists of a small number of elements.
- The control points associated with the basis functions define the geometry.
- The isoparametric concept is invoked, that is, the unknown variables are represented in terms of the basis functions which define the geometry. The coefficients of the basis functions are the degrees-of-freedom, or *control variables*.
- Three different mesh refinement strategies are possible: analogues of classical *h*-refinement (by knot insertions) and *p*-refinement (by order elevation of the basis functions), and a new possibility referred to as *k*-refinement, which increases smoothness in addition to order.
- The element arrays constructed from isoparametric NURBS can be assembled into global arrays in the same way as finite elements (see Hughes [2000], Chapter 2). Compatibility of NURBS patches is attained by employing the same NURBS edge and surface representations on both sides of patch interfaces. This gives rise to a standard continuous Galerkin method and mesh refinement necessarily propagates from patch to patch. There is also the possibility of employing discontinuous Galerkin methods along patch boundaries.
- Dirichlet boundary conditions are applied to the control variables. If the Dirichlet conditions are homogeneous, this results in exact pointwise satisfaction. If they are inhomogeneous, the boundary values must be approximated by functions lying within the NURBS space, and this results in “strong” but approximate satisfaction of the boundary conditions, as in finite elements. Another option is to impose Dirichlet conditions “weakly” (we will discuss this later on). Neumann boundary

conditions are satisfied naturally as in standard finite element formulations (see Hughes [2000], Chapters 1 and 2).

When applied to structural analysis, which is the field of interest for the present work, it is possible to verify (as highlighted in Hughes *et al.* [2005]) that isoparametric NURBS patches represent all rigid body motion and constant strain states exactly. So structures assembled from compatible NURBS patches pass standard “patch tests” (see Hughes [2000], Chapters 3 and 4, for a description of patch tests).

3.1.4 *k*-refinement

Isogeometric analysis is fundamentally a higher-order approach. While it is true that the first two NURBS bases consist of constants and linears, identical in every way to standard finite elements, it takes at least quadratic-level NURBS to exactly represent conic sections. Refinement procedures are also fundamental components of NURBS technology. There are analogues of finite element *h*- and *p*-refinement procedures, and a new, potentially more efficient, higher-order procedure, *k*-refinement (see Hughes *et al.* [2005]). In *p*-refinement, C^0 -continuity is maintained across knots (i.e., “element” boundaries). In *k*-refinement, continuity of order C^{p-1} is attained across knots, at least within patches. The additional smoothness in *k*-refinement seems intuitively appealing for situations in which exact solutions are dominantly very smooth, such as free vibrations of structures and bifurcation buckling of thin beams, plates and shells. *k*-refinement also offers a very concise parameterization of smooth functions. The potential efficiency gains of *k*-refinement are suggested by the following calculations comparing *p*- and *k*-refinement. First, consider a one-dimensional mesh with n basis functions of order p . Note that the number of basis functions is equal to the number of control variables, and is also equal to the number of control points. After r refinements (i.e., order elevations), the number of basis functions, each of order $p + r$, is $(r + 1)n - rp$ for *p*-refinement and $n + r$ for *k*-refinement. The growth in the number of control variables is depicted graphically in Figure 3.5. Next, consider a d -dimensional mesh with n^d basis functions. After r refinements, assuming r to be large, the number of basis functions asymptotically approaches $n^d(r^d + dr^{d-1})$ for *p*-refinement and $n^d(1 + drn^{-1})$ for *k*-refinement. The difference is seen to be very significant. Graphical comparisons for two and three dimensions are presented in Figures 3.6 and 3.7, respectively. Keep in mind that the mesh, defined by the knot locations, is fixed and is the same for *p*- and *k*-refinement. See Hughes *et al.* [2005] for further details.

n initial control points

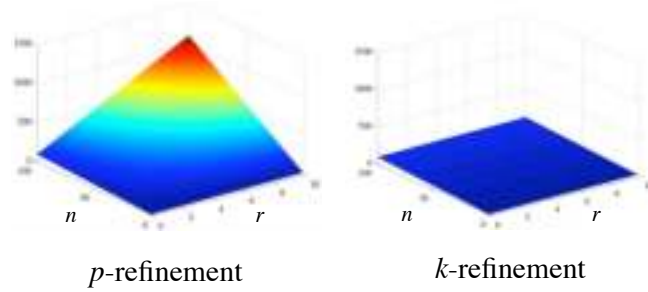


Figure 3.5. Comparison of control variable growth in one dimension.

n^2 initial control points

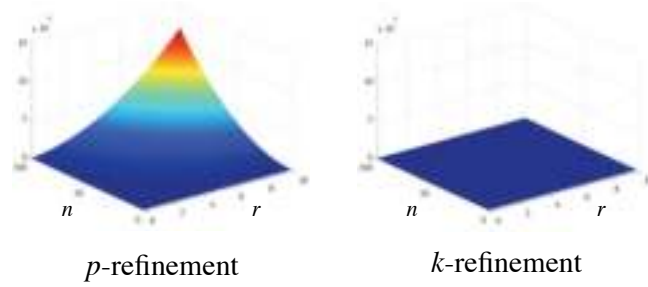


Figure 3.6. Comparison of control variable growth in two dimensions.

n^3 initial control points

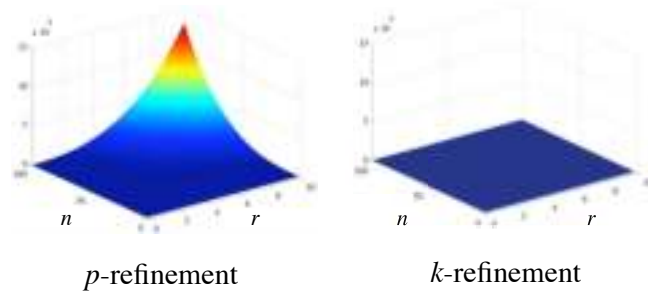


Figure 3.7. Comparison of control variable growth in three dimensions.

3.2 Structural vibrations

The goal of this Section is to briefly recall the main equations governing structural vibrations; for a complete discussion on the subject refer to Hughes [2000] and to classical books of structural dynamics such as Clough and Penzien [1993] and Chopra [2001].

Given a multi-degree-of-freedom structural linear system, the undamped, unforced equations of motion which govern the free vibrations of the system are:

$$\mathbf{M}\ddot{\mathbf{u}} + \mathbf{K}\mathbf{u} = \mathbf{0} \quad (3.14)$$

where \mathbf{M} and \mathbf{K} are, respectively, the consistent mass and the stiffness matrices of the system, $\mathbf{u} = \mathbf{u}(\mathbf{x}, t)$ is the displacement vector and $\ddot{\mathbf{u}} = \frac{d^2\mathbf{u}}{dt^2}$ is the acceleration vector. The free vibrations of the system in its n^{th} natural mode can be described (by variable separation) by:

$$\mathbf{u}(\mathbf{x}, t) = \boldsymbol{\varphi}_n(\mathbf{x})q_n(t), \quad (3.15)$$

where $\boldsymbol{\varphi}_n$ is the n^{th} natural mode vector and $q_n(t)$ is a harmonic function, depending on the n^{th} natural frequency ω_n , of the form:

$$q_n(t) = A_n \cos(\omega_n t) + B_n \sin(\omega_n t). \quad (3.16)$$

Combining equations (3.15) and (3.16) gives:

$$\mathbf{u}(\mathbf{x}, t) = \boldsymbol{\varphi}_n(\mathbf{x})(A_n \cos(\omega_n t) + B_n \sin(\omega_n t)) \quad (3.17)$$

which yields:

$$\ddot{\mathbf{u}} = -\omega_n^2 \mathbf{u}. \quad (3.18)$$

Substituting equation (3.18) into the equations of motion (3.14) gives the following linear system:

$$(\mathbf{K} - \omega_n^2 \mathbf{M})\boldsymbol{\varphi}_n q_n = \mathbf{0}. \quad (3.19)$$

Asking for nontrivial solutions of this linear system gives rise to the generalized eigenvalue problem:

$$\det(\mathbf{K} - \omega_n^2 \mathbf{M}) = 0, \quad (3.20)$$

whose solutions are the natural frequencies ω_n (with $n = 1, \dots, N$, where N is the number of degrees-of-freedom of the system) associated to the natural modes $\boldsymbol{\varphi}_n$. Once a natural frequency ω_n is found, it is possible to compute the corresponding natural mode by solving the following linear system for $\boldsymbol{\varphi}_n$:

$$(\mathbf{K} - \omega_n^2 \mathbf{M})\boldsymbol{\varphi}_n = \mathbf{0}. \quad (3.21)$$

We remark that the natural modes resulting from (3.21) are defined up to a multiplicative normalization constant. Different standard ways of normalization have been proposed, the most used probably being:

$$\boldsymbol{\varphi}_n^T \mathbf{M} \boldsymbol{\varphi}_n = 1. \quad (3.22)$$

In conclusion, to employ the concepts of Isogeometric Analysis to study structural vibrations, the steps to be performed are:

1. assemble the stiffness matrix \mathbf{K} as proposed in Hughes *et al.* [2005];
2. assemble the mass matrix \mathbf{M} in an analogous way;
3. solve the eigenvalue problem (3.20).

Then, if there exists also an interest in computing the natural modes, it is necessary to solve as many linear systems like (3.21) as the desired modes are.

3.3 Longitudinal vibrations of an elastic rod

In this and in the following Section, we study 1D problems such as of rod and beam element vibrations. We stress that for these cases, due to the simplicity of the geometry, all of the weights are equal to 1 (i.e., NURBS basis functions become B-Splines).

To begin with, we study the problem of the structural vibrations of an elastic fixed-fixed rod of unit length, whose natural frequencies and modes, assuming unit material parameters, are governed by:

$$\begin{aligned} u_{,xx} + \omega^2 u &= 0 \text{ for } x \in]0, 1[\\ u(0) &= u(1) = 0, \end{aligned} \quad (3.23)$$

and for which the exact solution in terms of natural frequencies is:

$$\omega_n = n\pi, \text{ with } n = 1, 2, 3... \quad (3.24)$$

After writing the weak formulation and performing the discretization, a problem of the form of (3.19) is obtained.

3.3.1 Numerical experiments

As a first numerical experiment, the generalized eigenproblem (3.19) is solved with both finite elements and isogeometric analysis using quadratic basis functions. The resulting natural frequencies, ω_n^h , are presented in Figure 3.8, normalized with respect to the exact solution (3.24), and plotted versus the mode number, n , normalized by the total number of degrees-of-freedom, N . To produce the spectra of Figure 3.8, we use $N = 999$ but the results are in fact independent of N .

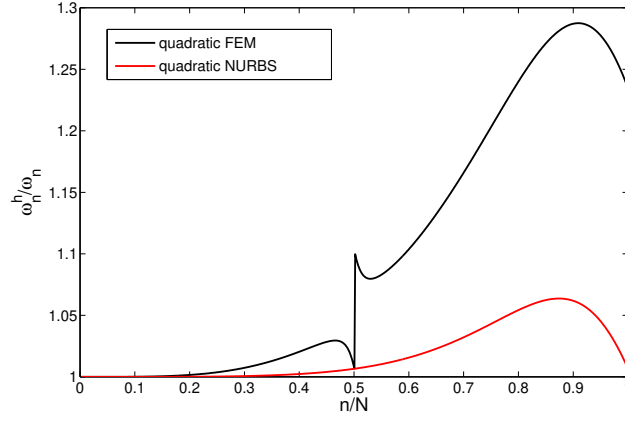


Figure 3.8. Fixed-fixed-rod. Normalized discrete spectra using quadratic finite elements and NURBS.

Figure 3.8 illustrates the superior behaviour of NURBS basis functions compared with finite elements. In this case, the finite element results depict an acoustical branch for $n/N < 0.5$ and an optical branch for $n/N > 0.5$ (see Brillouin [1953]).

We then perform the same eigenvalue analysis using higher-order NURBS basis functions. The resulting spectra are presented in Figure 3.9; the analyses were carried out using $N = 1000$ degrees-of-freedom.

Increasing the order, p , of the basis functions, the results show higher accuracy, namely, $2p$ (see Appendix A for the computation of the order of accuracy using quadratic and cubic NURBS). Figures 3.11-3.13 confirm that the order of convergence for frequencies computed using NURBS is $O(h^{2p})$, as with polynomial-based finite elements. Increasing p also results in the appearance of strange frequencies at the very end of the spectrum, referred to in the following as “outlier frequencies” (in analogy with outlier values in statistics, see, e.g., Montgomery *et al.* [2003]), whose number and magnitude increase with

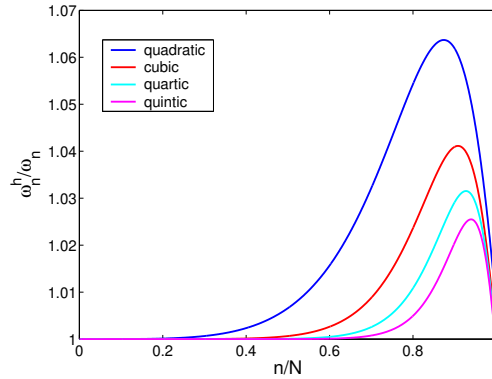


Figure 3.9. Fixed-fixed rod. Normalized discrete spectra using different order NURBS basis functions.

p . In Figure 3.10, this behaviour is highlighted by plotting the last computed frequencies for $p = 2, \dots, 10$. To understand the outliers, we first remark that the finite element spectrum for quadratic elements consists of acoustic (low-mode) and optical (high-mode) branches, in the sense of Brillouin [1953]. Both these branches are continuous as may be seen from Figure 3.8. There are only two distinct equations in the discrete system, corresponding to element middle and end nodes, and this gives rise to the two branches. In the case of NURBS, all but a *finite* number of equations are the same. The ones associated with the open knot vectors are different, and are responsible for the outliers. The outliers constitute a discrete optical branch. The typical equation of the interior knots gives rise to the continuous acoustic branch, as will be analytically verified in the next Section. In finite element analysis, the frequencies associated with the optical branch are regarded as inaccurate and, obviously, the same is true for NURBS. In many applications, these frequencies are harmless. They can be ignored in vibration analysis and their participation in transient response can be suppressed through the use of dissipative, implicit time integration algorithms (see, e.g., Chung and Hulbert [1993], Miranda *et al.* [1989], Hilber and Hughes [1978], Hughes *et al.* [1976], and Hughes [2000]). However, they would be detrimental in explicit transient analysis because the frequencies of the highest modes are grossly overestimated and stability would necessitate an unacceptably small time step, but it will be shown in the next Section how to completely eliminate the outliers by a reparameterization of the isogeometric mapping.

3.3.2 Analytical determination of the discrete spectrum

Following the derivations of Hughes [2000], Chapter 9, it is possible to analytically compute the discrete spectra previously determined numerically. The starting point is the

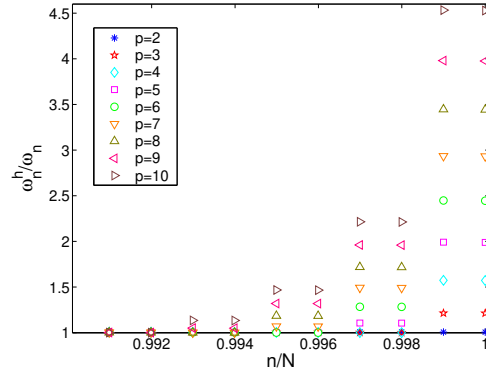


Figure 3.10. Fixed-fixed rod. Last normalized frequencies for $p = 2, \dots, 10$.

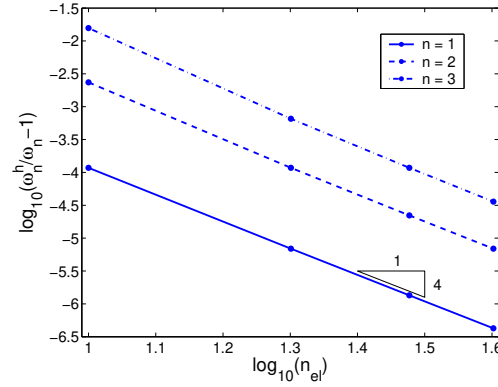


Figure 3.11. Fixed-fixed rod. Order of convergence for the first three frequencies using quadratic NURBS.

mass and stiffness matrices for a typical interior element (note that, for interior elements, the basis functions are all identical). For quadratic NURBS, the mass and stiffness of a typical interior element are:

$$\mathbf{M}^e = \frac{h}{120} \begin{bmatrix} 6 & 13 & 1 \\ 13 & 54 & 13 \\ 1 & 13 & 6 \end{bmatrix}, \quad \mathbf{K}^e = \frac{1}{6h} \begin{bmatrix} 2 & -1 & -1 \\ -1 & 2 & -1 \\ -1 & -1 & 2 \end{bmatrix}, \quad (3.25)$$

where $h = 1/n_{el} = 1/(N - p)$, n_{el} is the number of elements, N is the number of control points, and $p = 2$ is the order of the basis functions. The equation of motion for the

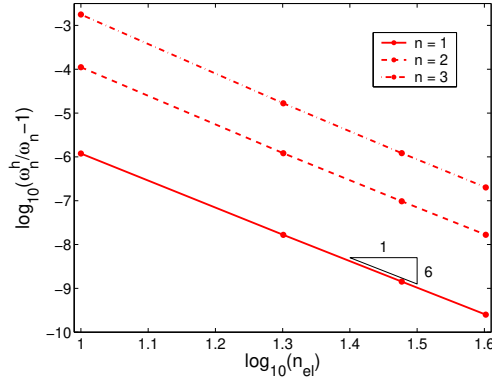


Figure 3.12. Fixed-fixed rod. Order of convergence for the first three frequencies using cubic NURBS.

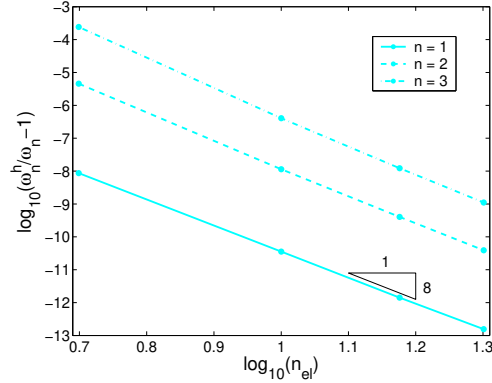


Figure 3.13. Fixed-fixed rod. Order of convergence for the first three frequencies using quartic NURBS.

typical interior control point, A , is:

$$\begin{aligned} & \frac{h}{120}(\ddot{u}_{A-2} + 26\ddot{u}_{A-1} + 66\ddot{u}_A + 26\ddot{u}_{A+1} + \ddot{u}_{A+2}) \\ & - \frac{1}{6h}(u_{A-2} + 2u_{A-1} - 6u_A + 2u_{A+1} + u_{A+2}) = 0, \end{aligned} \quad (3.26)$$

which can be compactly written as:

$$\frac{h^2}{20}\alpha\ddot{u}_A - \beta u_A = 0, \quad (3.27)$$

where α and β are operators defined as follows:

$$\begin{aligned} \alpha x_A &= x_{A-2} + 26x_{A-1} + 66x_A + 26x_{A+1} + x_{A+2}, \\ \beta x_A &= x_{A-2} + 2x_{A-1} - 6x_A + 2x_{A+1} + x_{A+2}. \end{aligned} \quad (3.28)$$

Separating variables,

$$u_A(t) = \varphi_A q(t), \quad (3.29)$$

and substituting this expression into (3.27), after adding and subtracting $\frac{(\omega^h h)^2}{20} \alpha u_A$, we obtain:

$$(\ddot{q} + (\omega^h)^2 q) \frac{h^2}{20} \alpha \varphi_A - \left(\frac{(\omega^h h)^2}{20} \alpha \varphi_A + \beta \varphi_A \right) q = 0. \quad (3.30)$$

The satisfaction of (3.30) is achieved by selecting φ_A and q such that:

$$\left(\frac{(\omega^h h)^2}{20} \alpha + \beta \right) \varphi_A = 0 \quad (3.31)$$

and

$$\ddot{q} + (\omega^h)^2 q = 0. \quad (3.32)$$

Assuming a solution for (3.31) of the form (for fixed-fixed boundary conditions):

$$\varphi_A = C \sin(A\omega h), \quad \omega = n\pi, \quad (3.33)$$

(3.31) can be rewritten as:

$$\left(\frac{(\omega^h h)^2}{20} \alpha + \beta \right) \sin(A\omega h) = 0. \quad (3.34)$$

Substituting expressions (3.28) for α and β , and using the trigonometric identity $\sin(a \pm b) = \sin(a) \cos(b) \pm \sin(b) \cos(a)$, yields:

$$\frac{(\omega^h h)^2}{20} (16 + 13 \cos(\omega h) + \cos^2(\omega h)) - (2 - \cos(\omega h) - \cos^2(\omega h)) = 0, \quad (3.35)$$

which can be solved for $\frac{\omega^h}{\omega}$, giving:

$$\frac{\omega^h}{\omega} = \frac{1}{\omega h} \sqrt{\frac{20(2 - \cos(\omega h) - \cos^2(\omega h))}{16 + 13 \cos(\omega h) + \cos^2(\omega h)}}. \quad (3.36)$$

Equation (3.36) is the analytical expression for the normalized discrete spectrum for our problem, using quadratic NURBS basis functions. Analogous calculations can be performed for higher-order approximations. The expression for cubic NURBS is:

$$\frac{\omega^h}{\omega} = \frac{1}{\omega h} \sqrt{\frac{42(16 - 3 \cos(\omega h) - 12 \cos^2(\omega h) - \cos^3(\omega h))}{272 + 297 \cos(\omega h) + 60 \cos^2(\omega h) + \cos^3(\omega h)}}. \quad (3.37)$$

In Figure 3.14 we present the analytical and numerical spectra for quadratic and cubic NURBS. For the computation of the numerical spectra, 2000 control points were

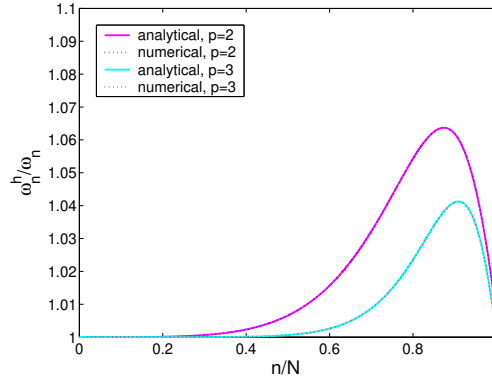


Figure 3.14. Fixed-fixed rod. Comparison of analytical and numerical discrete spectra computed for quadratic and cubic NURBS.

employed. The only differences are the outlier frequencies at the end of the numerical spectrum obtained for cubic NURBS.

Remark 3.4.1. Equations (3.36) and (3.37), and Figure 3.14, confirm that the continuous part of the NURBS frequency spectra are invariant, that is, are independent of the number of degrees-of-freedom.

Remark 3.4.2. All the numerical results described up to now have been obtained using control points computed with the procedure proposed by Hughes *et al.* [2005], which leads to linear parameterization (i.e., constant Jacobian determinant). The results obtained are seen to be very good, except for the outliers, which get progressively worse for higher-order approximations. A way to avoid this behaviour is to employ uniformly-spaced control points. The difference between a distribution of 21 control points in the case of linear parameterization and of uniformly-spaced points, using cubic NURBS, is presented in Figure 3.15. This choice corresponds to a nonlinear parameterization (see Figure 3.16 and 3.17 for plots of the parameterization $x(\xi)$ and its Jacobian $J(\xi) = \frac{dx(\xi)}{d\xi}$ for the cases in Figure 3.15). Figure 3.18 presents spectra computed using uniformly-spaced control points. The outlier frequencies are eliminated and the continuous spectra coincide with the ones computed analytically and presented previously in Figure 3.14 for quadratic and cubic NURBS.

Remark 3.4.3. In this work, consistent mass is emphasized because it seems more suitable than lumped mass when higher-order approximations are involved. However, some preliminary tests were performed with a “row sum” lumped mass (see Hughes

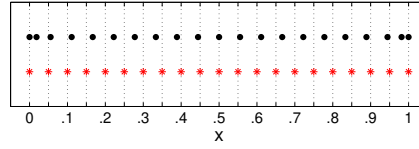


Figure 3.15. Control points for linear parameterization (dots) compared with uniformly-spaced control points (asterisks) for cubic NURBS.

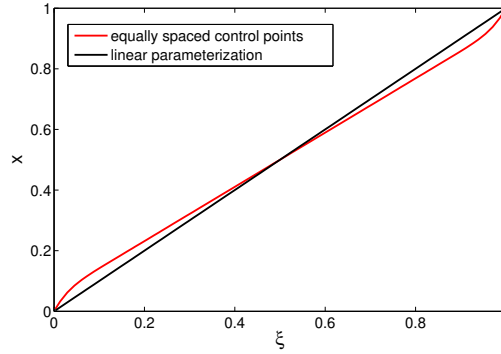


Figure 3.16. Plot of the parameterization for the cases of uniformly-spaced control points and linear parameterization (cubic NURBS, 21 control points).

[2000], Chapter 7). This approach proves satisfactory for some low-order finite elements but it is incapable of maintaining full accuracy in the present context (see Figure 3.19). In all cases, accuracy is limited to second-order. Analytical and numerical lumped mass results for quadratic and cubic NURBS are presented in Appendix A. Despite these negative results, we do not think the issue of lumped mass and NURBS is closed. There may be ways to develop higher-order accurate lumped mass matrices. Inspiration may be taken from the work of Fried and Malkus [1976]. Perhaps nonlinear parameterizations and nonuniform knot distributions, in conjunction with a lumping scheme, are worthwhile directions to explore. This seems to be an interesting problem of applied mathematics with practical significance.

3.4 Transverse vibrations of a Bernoulli-Euler beam

The transverse vibrations of a simply-supported, unit length Bernoulli-Euler beam are considered (see Hughes [2000], Chapter 7). For this case, the natural frequencies and modes, assuming unit material and cross-sectional parameters, are governed by:

$$\begin{aligned} u_{,xxxx} - \omega^2 u &= 0 \text{ for } x \in]0, 1[\\ u(0) = u(1) = u_{,xx}(0) = u_{,xx}(1) &= 0, \end{aligned} \quad (3.38)$$

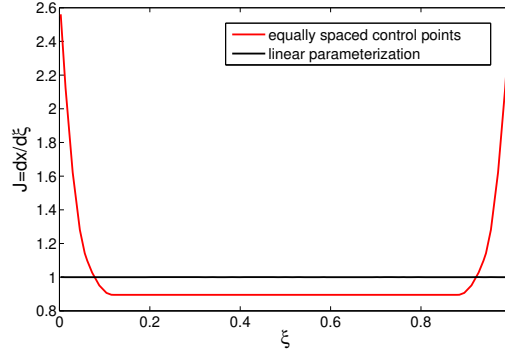


Figure 3.17. Plot of the Jacobian of the parameterization for the cases of uniformly-spaced control points and linear parameterization (cubic NURBS, 21 control points).

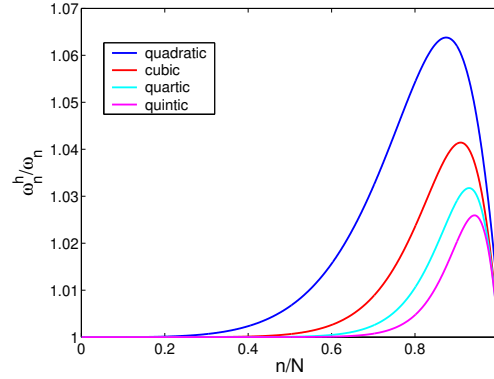


Figure 3.18. Fixed-fixed rod. Normalized discrete spectra using uniformly-spaced control points. (These results are identical to those presented in Figure 3.9 except the outliers have been eliminated.)

where

$$\omega_n = (n\pi)^2, \text{ with } n = 1, 2, 3, \dots \quad (3.39)$$

3.4.1 Numerical experiments

The numerical experiments and results for the Bernoulli-Euler beam problem are analogous to the ones reported for the rod. A remark about the formulation is in order before presenting the results. The classical beam finite element employed to solve problem (3.38) is a two-node Hermite cubic element with two degrees-of-freedom per node (transverse displacement and rotation), whereas our isogeometric analysis formulation is rotation-free (see, for example, Engel *et al.* [2002]). Later in this Section we will discuss

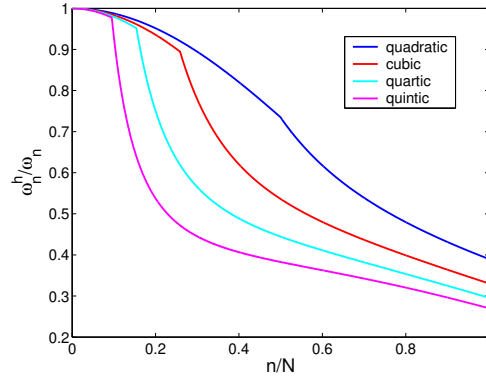


Figure 3.19. Fixed-fixed rod. Normalized discrete spectra using different order NURBS basis functions with “row sum” lumped mass matrices.

the problem of the imposition of rotation boundary conditions.

Discrete spectra obtained using classical cubic finite element and NURBS basis functions are presented in Figure 3.20. The NURBS solution is significantly more accurate but two outlier frequencies are present at the end of the spectrum.

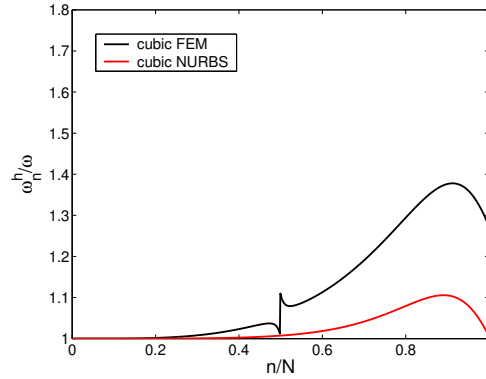


Figure 3.20. Simply-supported beam. Normalized discrete spectra using cubic finite elements and NURBS.

Figure 3.21 presents the discrete spectra obtained using different order NURBS basis functions. The behaviour is similar to the case of the rod, including the outlier frequencies (see Figure 3.22). Note that quadratic NURBS are admissible in the present context because they are C^1 -continuous on patches. Slope continuity may be weakly enforced across patch boundaries by way of the technique described in Engel *et al.* [2002]. There

are no outliers for quadratic NURBS but the accuracy level is rather poor compared with cubics.

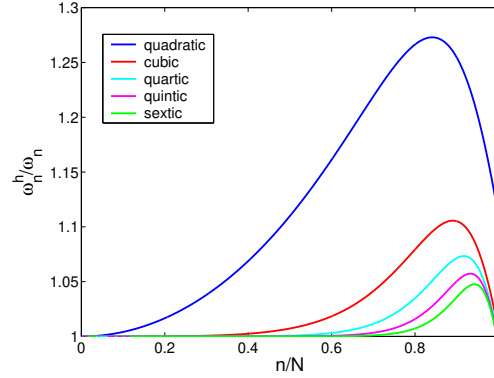


Figure 3.21. Simply-supported beam. Normalized discrete spectra using different order NURBS basis functions.

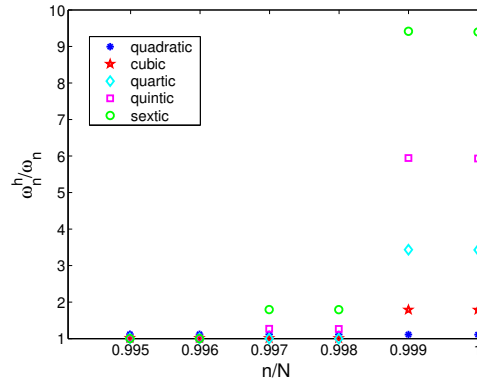


Figure 3.22. Simply-supported beam. Last normalized frequencies for $p = 2, \dots, 10$.

Figures 3.23-3.25 show that the order of convergence of frequencies using NURBS is optimal, that is $O(h^{2(p-1)})$.

The analytical computation of the discrete spectrum, performed previously for the rod problem, can also be done in the present case. Employing cubic NURBS shape functions, for example, gives rise to the following expression:

$$\frac{\omega^h}{\omega} = \frac{1}{\omega h^2} \sqrt{\frac{210(2 - 3 \cos(\omega h) + \cos^3(\omega h))}{272 + 297 \cos(\omega h) + 60 \cos^2(\omega h) + \cos^3(\omega h)}}. \quad (3.40)$$

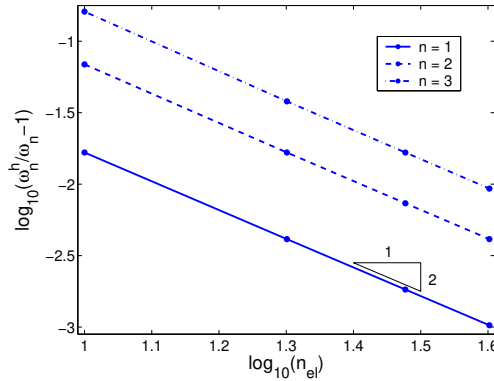


Figure 3.23. Simply-supported beam. Order of convergence for the first three frequencies using quadratic NURBS.

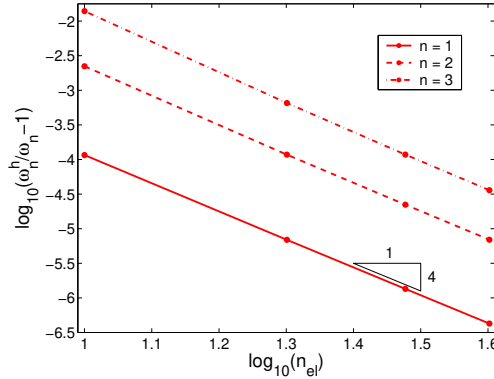


Figure 3.24. Simply-supported beam. Order of convergence for the first three frequencies using cubic NURBS.

The analytical and numerical discrete spectra for cubic and quartic approximations are compared in Figure 3.26. For the computation of the numerical discrete spectra, 2000 control points were used. The only differences are in the outlier frequencies at the end of the numerical discrete spectra. As previously shown for the rod problem, the outliers can be removed by nonlinear parameterization derived from a uniformly-spaced distribution of control points. In this way, the discrete spectra of Figure 3.27 are obtained, which coincide with the analytically computed ones.

3.4.2 Boundary conditions on rotations

The Bernoulli-Euler beam formulation employed is “rotation-free,” that is, only displacements are degrees-of-freedom. Rotations (i.e., slopes) can be computed as derivatives of

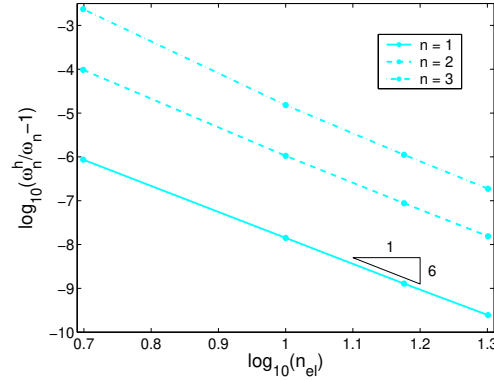


Figure 3.25. Simply-supported beam. Order of convergence for the first three frequencies using quartic NURBS.

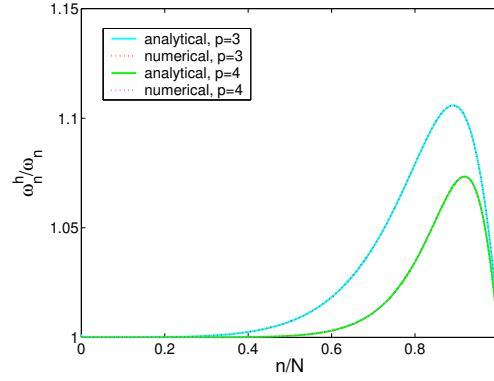


Figure 3.26. Simply-supported beam. Analytical and numerical discrete spectra computed using cubic and quartic NURBS.

displacement but are not degrees-of-freedom. To illustrate the method utilized to enforce rotation boundary conditions, we consider the following problem of a cantilever beam:

$$\begin{aligned} u_{,xxxx} - \omega^2 u &= 0 \text{ for } x \in]0, 1[\\ u(0) &= u_{,x}(0) = u_{,xx}(1) = u_{,xxx}(1) = 0, \end{aligned} \quad (3.41)$$

The natural frequencies are (see Chopra [2001]) $\omega_n = \beta_n^2$, with $\beta_1 = 1.8751$, $\beta_2 = 4.6941$, $\beta_3 = 7.8548$, $\beta_4 = 10.996$, and $\beta_n = (n - 1/2)\pi$ for $n > 4$. Two strategies were employed to solve this problem. One is based on weak boundary condition imposition and the other on Lagrange multipliers. The former is the approach used in Engel *et al.* [2002]. In this case, the bilinear form, from which the stiffness matrix derives, is given by:

$$A(v^h, u^h) = \int_0^1 v_{,xx}^h u_{,xx}^h dx + v_{,x}^h u_{,xx}^h|_{x=0} + v_{,xx}^h u_{,x}^h|_{x=0} + \tau v_{,x}^h u_{,x}^h|_{x=0}, \quad (3.42)$$

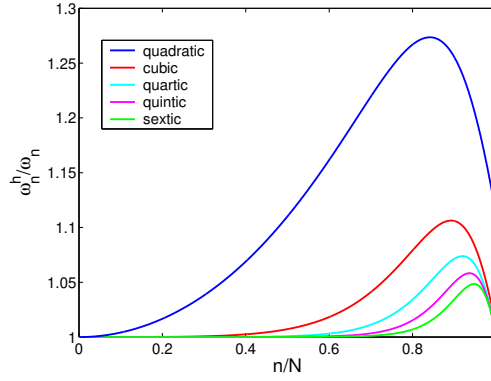


Figure 3.27. Simply-supported beam. Normalized discrete spectra using equally spaced control points. (These results are identical to those presented in Figure 3.21 except the outliers are eliminated.)

where v^h and u^h are the discrete weighting and trial solution, respectively, and τ is a stabilization parameter. Analogous to what is done in Prudhomme *et al.* [2001] for the Poisson problem, it can be shown that the choice of τ needs to be proportional to p^2/h , where p is the order of the NURBS basis and h is the mesh parameter. With this formulation, the cantilever beam problem (3.41) is solved, and corresponding discrete spectra for different order NURBS are shown in Figure 3.28 (1000 control points and $\tau = p^2/h$ are used). Figure 3.28 shows the same behaviour seen in Figure 3.21 for the simply-supported case.

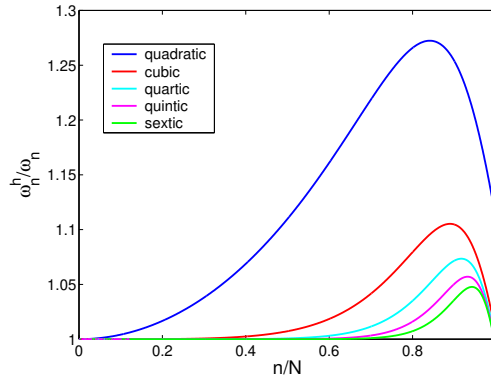


Figure 3.28. Cantilever beam with weakly enforced rotation boundary condition. Normalized discrete spectra using different order NURBS basis functions.

The other way to enforce rotation boundary conditions is through Lagrange multipliers.

In this case the bilinear form is:

$$A(v^h, \mu, u^h, \lambda) = \int_0^1 v_{,xx}^h u_{,xx}^h dx + \lambda v_{,x}^h|_{x=0} + \mu u_{,x}^h|_{x=0}, \quad (3.43)$$

where λ is the Lagrange multiplier and μ is its weighting counterpart. The advantage of the Lagrange multiplier approach is that the rotation boundary condition is exactly enforced. Results for the Lagrange multiplier approach are presented in Figure 3.29. For all practical purposes, the results of the two approaches are the same (cf., Figures 3.28 and 3.29).

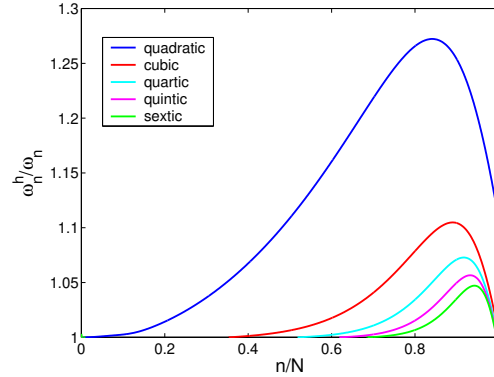


Figure 3.29. Cantilever beam with Lagrange multiplier. Normalized discrete spectra using different order NURBS basis functions.

3.5 Transverse vibrations of an elastic membrane

In this Section and in the next one, we present some numerical experiments for two-dimensional counterparts of the rod and Bernoulli-Euler beam problems considered previously, namely, the transverse vibrations of an elastic membrane and transverse vibrations of a Poisson-Kirchhoff plate, respectively.

The first problem we consider consists of the study of the transverse vibrations of a square, elastic membrane, whose natural frequencies and modes, assuming unit tension, density and edge length, are governed by:

$$\begin{aligned} \nabla^2 u(x, y) + \omega^2 u(x, y) &= 0, \quad (x, y) \in \Omega =]0, 1[\times]0, 1[\\ u(x, y)|_{\partial\Omega} &= 0, \end{aligned} \quad (3.44)$$

where ∇^2 is the Laplace operator. The exact natural frequencies are (see, e.g., Meirovitch [1967]):

$$\omega_{mn} = \pi \sqrt{m^2 + n^2}, \quad m, n = 1, 2, 3, \dots \quad (3.45)$$

The numerical results are qualitatively similar to the ones obtained in the study of the one-dimensional problems. The normalized discrete spectra obtained employing different order NURBS basis functions and using a linear parameterization over a 90×90 control net are presented in Figure 3.30. Note that l is the number of modes sorted from the lowest to the highest in frequency, while N is the total number of degrees-of-freedom. Figure 3.31 shows the lower half of the frequency spectra to highlight the accuracy of the different approximations. The optical branches seen in Figure 3.30 can again be eliminated by a uniformly-spaced control net, as shown in Figure 3.32.

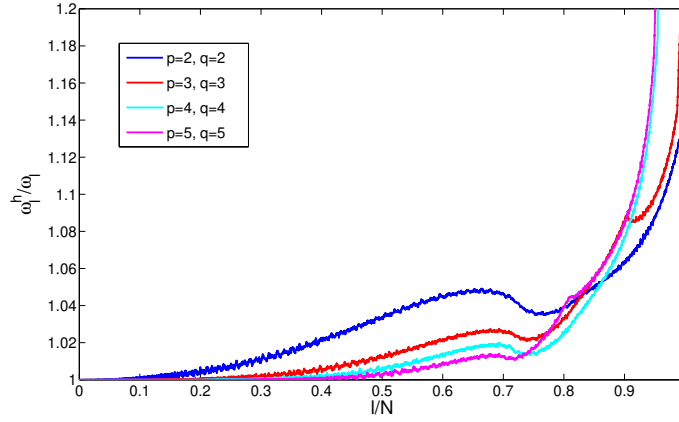


Figure 3.30. Square membrane. Normalized discrete spectra using different order NURBS basis functions (90×90 control points). Note the presence of optical branches.

3.6 Transverse vibrations of a Poisson-Kirchhoff plate

We now consider the transverse vibrations of a simply-supported, square plate governed by Poisson-Kirchhoff plate theory. The natural frequencies and modes, assuming unit flexural stiffness, density and edge length, are governed by the biharmonic problem:

$$\begin{aligned} \nabla^4 u(x, y) - \omega^2 u(x, y) &= 0 \text{ for } (x, y) \in \Omega =]0, 1[\times]0, 1[\\ u(x, y)|_{\partial\Omega} &= 0, \end{aligned} \quad (3.46)$$

for which the exact solution natural frequencies (see, e.g., Meirovitch [1967]) are:

$$\omega_{mn} = \pi^2(m^2 + n^2), \quad m, n = 1, 2, 3... \quad (3.47)$$

For this case, as for the Bernoulli-Euler beam, the NURBS formulation results in a

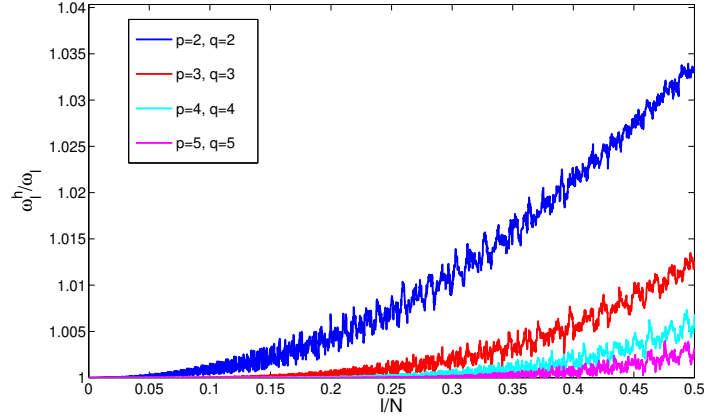


Figure 3.31. Square membrane. Detail of the low-frequency part of the normalized discrete spectra.

rotation-free approach. The boundary conditions on rotations can be imposed in similar fashion to the way described for the beam (see Engel *et al.* [2002] for further details).

The numerical results are similar to the ones obtained for the elastic membrane. In Figure 3.33, the normalized discrete spectra using a linear parameterization and a 90×90 control net are presented. Figure 3.34 shows a detail of the lower-frequency part. The y -axis of Figure 3.33 is cut off at a value of 1.4 because the outlier frequencies for the highest-order approximations would make the remaining part of the plot completely unreadable. Figure 3.35 shows the spectra obtained employing a uniformly-spaced control net.

3.7 Vibrations of a clamped thin circular plate using three-dimensional solid elements

Hughes *et al.* [2005] have shown that higher-order three-dimensional NURBS elements could be effectively utilized in the analysis of thin structures. In this Section we consider the vibrations of a clamped, thin circular plate modeled as a three-dimensional solid. A coarse mesh, but one capable of exactly representing the geometry, is utilized and the order of the basis functions is increased by way of the k -refinement strategy (see Hughes *et al.* [2005]). The exact Poisson-Kirchhoff solution for this problem, given, for example, in Meirovitch [1967], is

$$\omega_{mn} = C_{mn}^2 \frac{\pi^2}{R^2} \sqrt{\frac{D}{\rho t}} [\text{rad/s}], \quad (3.48)$$

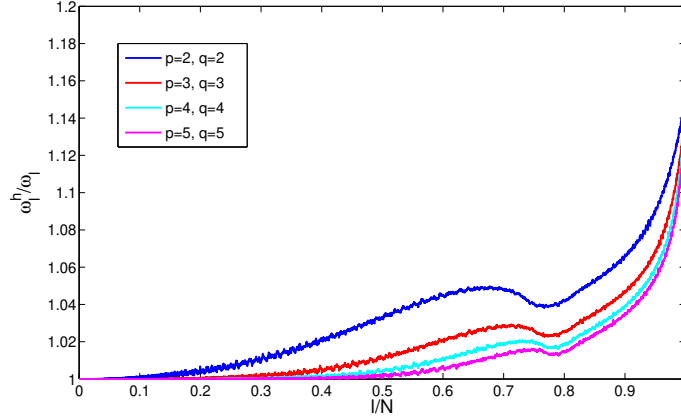


Figure 3.32. Square membrane. Normalized discrete spectra using a uniformly-spaced control net. Note, the optical branches of Figure 3.30 are eliminated.

where R is the radius of the plate, t is the thickness, $D = \frac{Et^3}{12(1-\nu^2)}$ is the flexural stiffness (E and ν are Young's modulus and Poisson's ratio, resp.) and ρ is the density (mass per unit volume). For the first three frequencies, the values of the coefficients C_{mn} are $C_{01} = 1.015$, $C_{11} = 1.468$ and $C_{02} = 2.007$. The data for the problem are presented in Table 3.1. Note that, because the radius to thickness ratio is 100, the plate may be considered thin, and the results of Poisson-Kirchhoff theory may be considered valid.

Table 3.1. Clamped circular plate. Geometric and material parameters.

R	2.000	[m]
t	0.020	[m]
E	$30 \cdot 10^6$	[KN/m ²]
ν	0.200	[-]
ρ	2.320	[KN s/m ⁴]

The initial control net consists of $9 \times 4 \times 3$ control points in the θ , r , and z directions, respectively, and quadratic approximations in all the parametric directions are employed. Figure 3.36 shows the mesh, consisting of eight elements within a single patch. The numerical results are compared with the exact solution in Table 3.2, where p , q and r are the orders of the basis functions in the circumferential, radial and vertical directions, respectively. Figures 3.37-3.39 show the first three eigenmodes (computed using $p = 4$, $q = 5$,

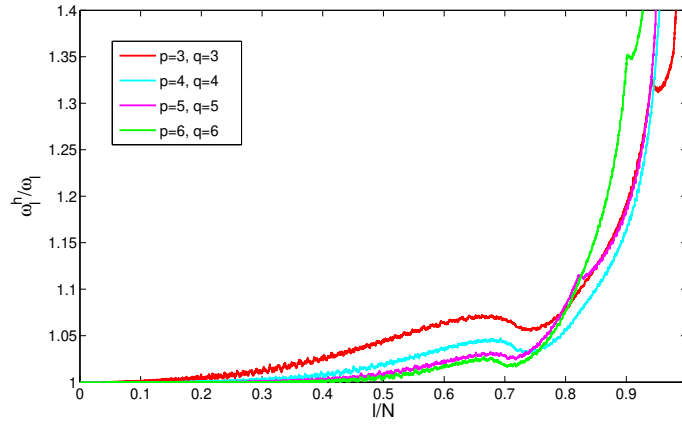


Figure 3.33. Poisson-Kirchhoff plate. Normalized discrete spectra using different order NURBS basis functions (90×90 control points). Note the presence of optical branches.

$r = 2$), which are in qualitative agreement with the ones depicted in Meirovitch [1967]. The relative errors (i.e., $(\omega^h - \omega)/\omega$) for these cases are, respectively, 0.0054, 0.00027, and 0.0012.

Table 3.2. Clamped circular plate. Numerical results compared with the exact solution.

p	q	r	ω_{01} [rad/s]	ω_{11} [rad/s]	ω_{02} [rad/s]
2	2	2	138.133	1648.800	2052.440
2	3	2	56.702	267.765	276.684
3	3	2	56.051	126.684	232.788
3	4	2	54.284	124.417	212.451
4	4	2	54.284	113.209	212.451
4	5	2	54.153	112.700	210.840
exact			53.863	112.670	210.597

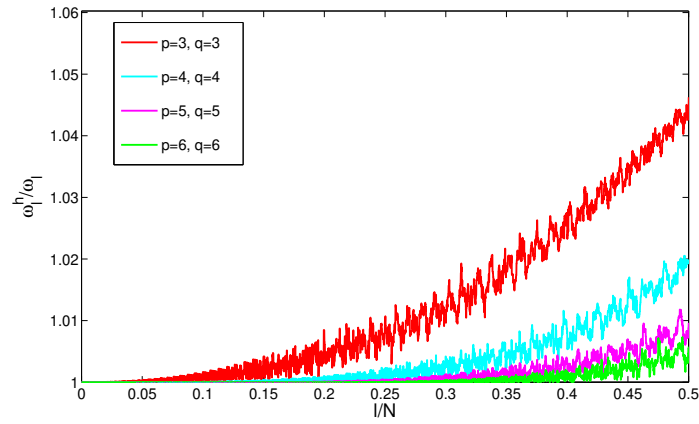


Figure 3.34. Poisson-Kirchhoff plate. Detail of the low-frequency part of the normalized discrete spectra.

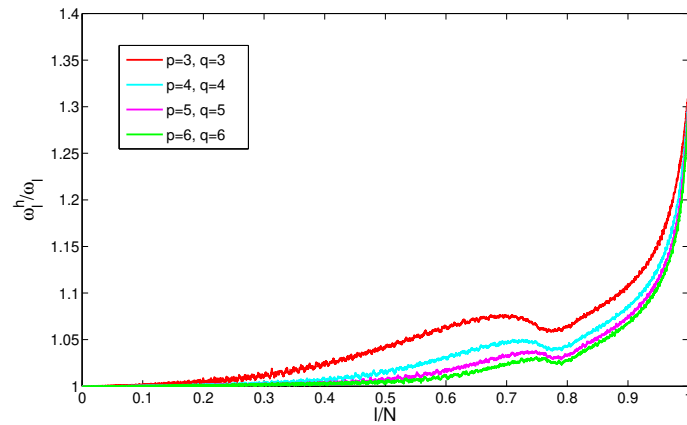


Figure 3.35. Poisson-Kirchhoff plate. Normalized discrete spectra using a uniformly-spaced control net. Note, the optical branches of Figure 3.33 are eliminated.

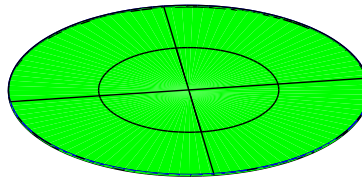


Figure 3.36. Clamped circular plate. Eight element mesh.

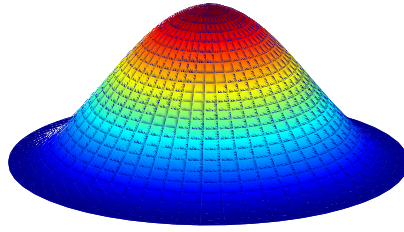


Figure 3.37. Clamped circular plate. Eigenmode corresponding to ω_{01} .

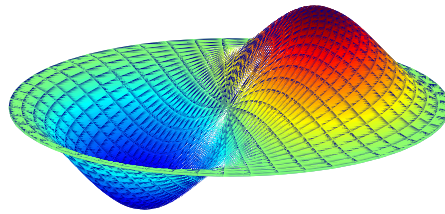


Figure 3.38. Clamped circular plate. Eigenmode corresponding to ω_{11} .

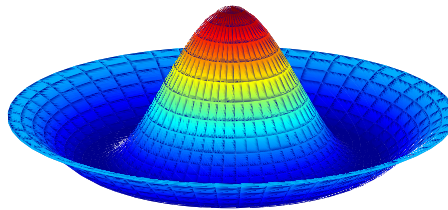


Figure 3.39. Clamped circular plate. Eigenmode corresponding to ω_{02} .

3.8 NASA Aluminum Testbed Cylinder

Comparison studies between computational and experimental results are often humbling to analysts and experimentalists alike. Occasionally, large discrepancies occur. Sometimes, through careful reanalysis and/or careful re-experimentation, the root cause of the discrepancies can be identified but this is not always the case. Differences in “as-built” and “as-drawn” geometries, and ambiguities concerning material properties and boundary conditions, often make precise correlation impossible. In addition, errors can obviously be made in analysis. The same is true in experimentation. Nevertheless, comparison between calculations and experimental tests is fundamentally important in engineering. Here we compare frequencies calculated for exact, “as-drawn” models of structures for which considerable experimental data are available.

The NASA Aluminum Testbed Cylinder (ATC) is shown in Figures 3.40 and 3.41. An isogeometric model (see Figure 3.42) was constructed from design drawings. There are three distinct members composing the framework (see Figure 3.43): nine identical main ribs (see Figures 3.44-3.48); twenty-four identical, prismatic stringers (see Figure 3.49); and two end ribs, which are mirror images of each other (see Figures 3.50-3.53). Note that every geometrical feature is *exactly* represented in the model. It is also interesting to note that control nets amount to a typical trilinear hexahedral mesh (see Figures 3.48 and 3.53). This suggests the possibility that hexahedral finite element mesh generators (see, e.g., CUBIT Blacker [1994]) may be useful in building isogeometric NURBS models. The stringer–main rib and stringer–end rib junctions are shown in Figures 3.54 and 3.55, respectively. Note that there are gaps between the stringer and the ribs in the notch regions. Experimental vibration data has been obtained for a typical isolated stringer, a typical isolated main rib, the frame assembly, and the frame and skin assembly (see Grosveld *et al.* [2002]; Buehrle *et al.* [2000]; Couchman *et al.* [2003] for details and reference computational results). Calculations were performed of each of the corresponding isogeometric models. The Arnoldi Package (see ARPACK [1999]) eigensolver was used in the calculations of the individual components of the ATC, while the Automated Multi-Level Substructuring (AMLS) eigensolver (see Benninghof and Lehoucq [2004]) was used in the calculations of the framework and the full ATC structure.



Figure 3.40. NASA Aluminum Testbed Cylinder (ATC). Frame and skin.



Figure 3.41. NASA ATC. Frame only.

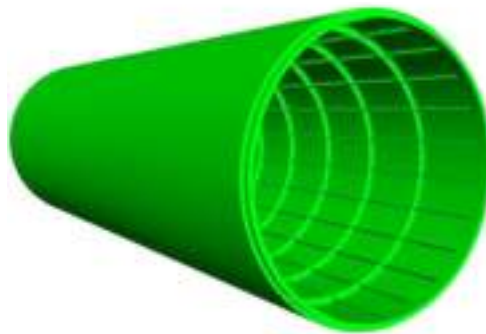


Figure 3.42. NASA ATC frame and skin: Isogeometric model.

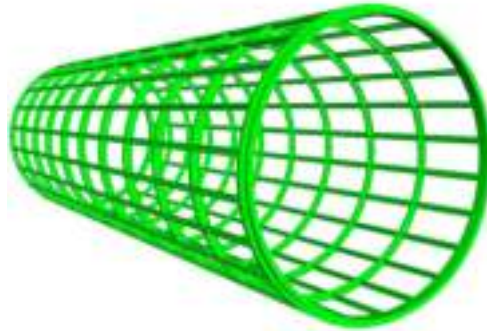


Figure 3.43. NASA ATC frame: Isogeometric model.

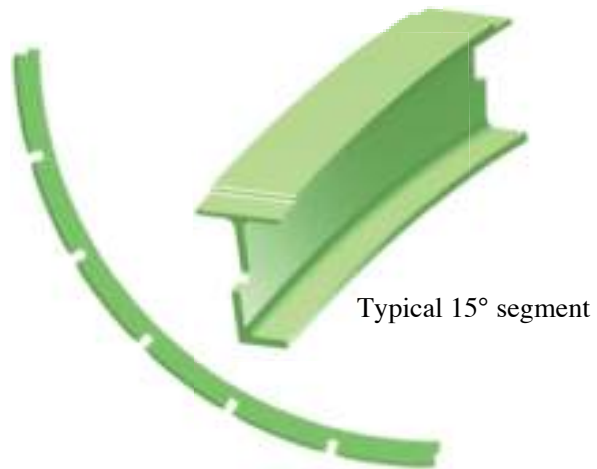


Figure 3.44. NASA ATC. Isogeometric model of the main rib.



Figure 3.45. NASA ATC. Typical 15° segment of the main rib. Mesh 1, the coarsest mesh, encapsulates the exact geometry.



Figure 3.46. NASA ATC. Typical 15° segment of the main rib. Mesh 2. Knot insertion has been used selectively to help even out the aspect ratios of elements making Mesh 2 more uniform and suitable for analysis.



Figure 3.47. NASA ATC. Typical 15° segment of the main rib. Mesh 3. Further refinement may be necessary to resolve the solution, as is the case with standard finite element analysis, but the geometry is never altered as the mesh is refined.

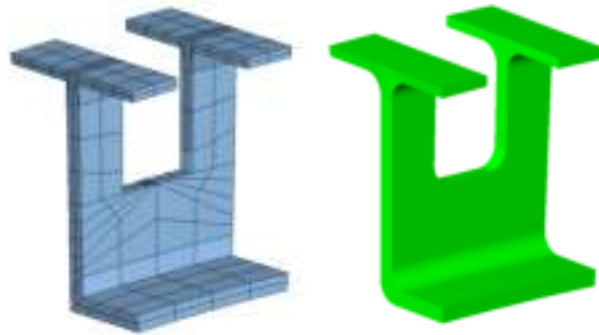


Figure 3.48. NASA ATC. Detail of the “notch” region in the main rib. The control net is on the left and the exact geometry is on the right.

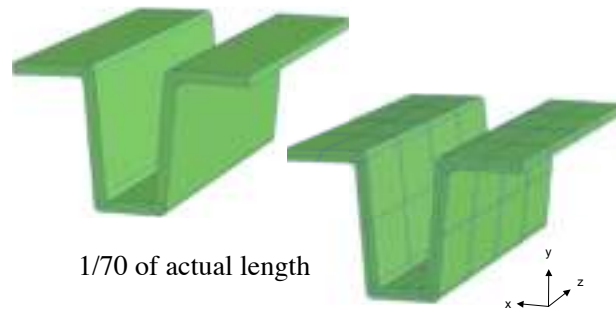


Figure 3.49. NASA ATC. Isogeometric model of the longitudinal stringer. Sample meshes.



Figure 3.50. NASA ATC. Typical 15° segment of an end rib. Mesh 1 (coarsest mesh).

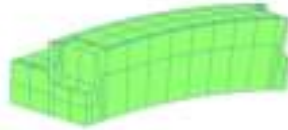


Figure 3.51. NASA ATC. Typical 15° segment of an end rib. Mesh 2.

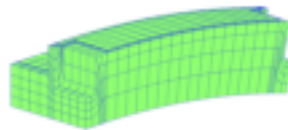


Figure 3.52. NASA ATC. Typical 15° segment of and end rib. Mesh 3.

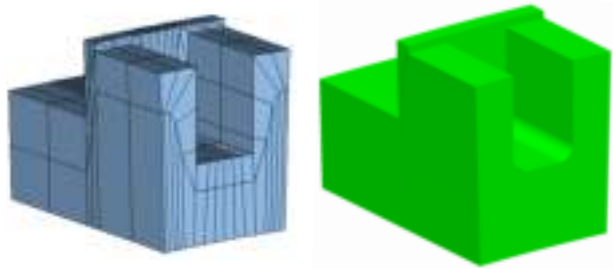


Figure 3.53. NASA ATC. Detail of the “notch” region in an end rib. The control net is on the left and the exact geometry is on the right.

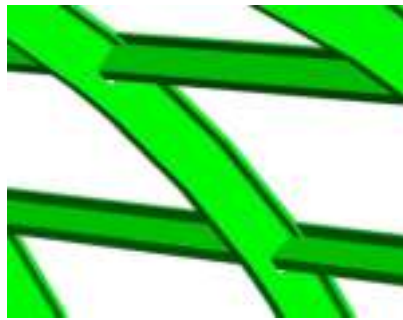


Figure 3.54. NASA ATC. Stringer–main rib junction.

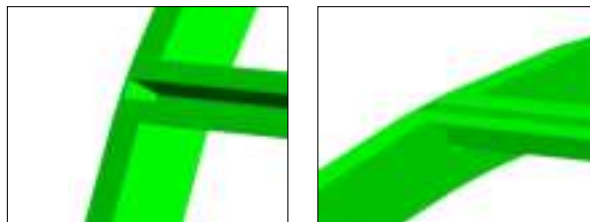


Figure 3.55. NASA ATC. Stringer–end rib junction.

Frequency results for the stringer are presented in Figure 3.56 and the first three bending modes are depicted in Figure 3.57. The results shown are from analysis of a single patch with one rational quadratic element in the thickness, nine rational quadratic elements through the cross-section (the smallest number capable of exactly representing the geometry), and sixteen C^5 rational sextic ($p = 6$) elements in the longitudinal direction. The resulting 144 element module has a total of 11,286 degrees of freedom. Other combinations of polynomial order, continuity and mesh size in the longitudinal direction are investigated. Higher-order, smooth meshes provide the most accuracy per degree-of-freedom but the overall run-time inevitably suffers if the polynomial order is raised indefinitely.

The main rib frequency results are presented in Figure 3.58. The “coarse mesh” (not shown) is comprised of twenty-four identical but rotated 15° sections, each comprised of six NURBS patches. Rational quadratic elements are used throughout. The full mesh for an individual rib has 34,704 degrees-of-freedom. Both h - and p -refinement are investigated for the reasons described below. In all cases, the results converge to the fine mesh results in Figure 3.58.

The isolated main rib is the only case in which some of the numerically calculated frequencies are smaller than the experimental results. The fine mesh results fall below the coarse mesh results which for theoretical reasons must occur (see, e.g., Strang and Fix [1973]). The average error for the first eight modes is larger for the fine mesh than the coarse mesh, a somewhat surprising result. Due to the upper bound property of frequencies in our formulation, and the fact that our model is geometrically exact in the sense of the design drawings, we surmise there is some discrepancy between the drawings and the as-built configuration, or some other discrepancy between the experimental configuration and our model. Nevertheless, the correlation is still reasonable. Further study is needed to determine the cause of the differences. Selected modes shapes for the fine mesh are shown in Figures 3.59 and 3.60.

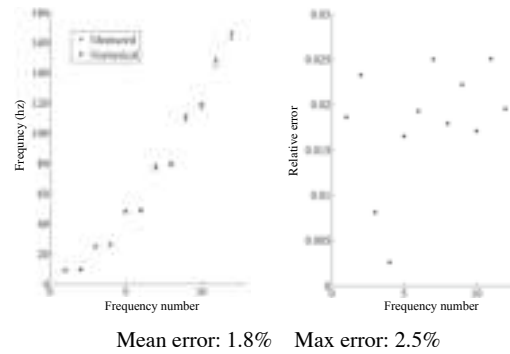


Figure 3.56. NASA ATC. Comparison of numerical and experimental frequency results for the longitudinal stringer.

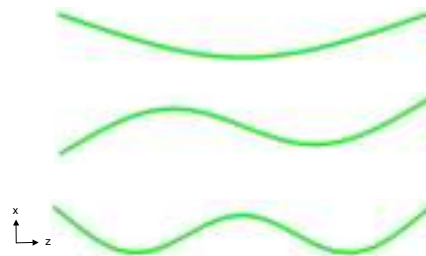


Figure 3.57. NASA ATC. Selected calculated mode shapes for the stringer. Three lowest x - z modes.

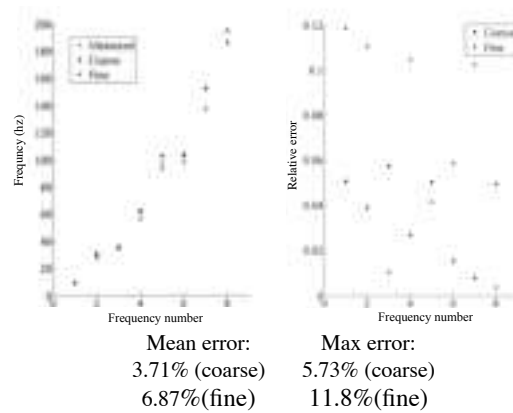


Figure 3.58. NASA ATC. Comparison of numerical and experimental frequency results for the main rib.

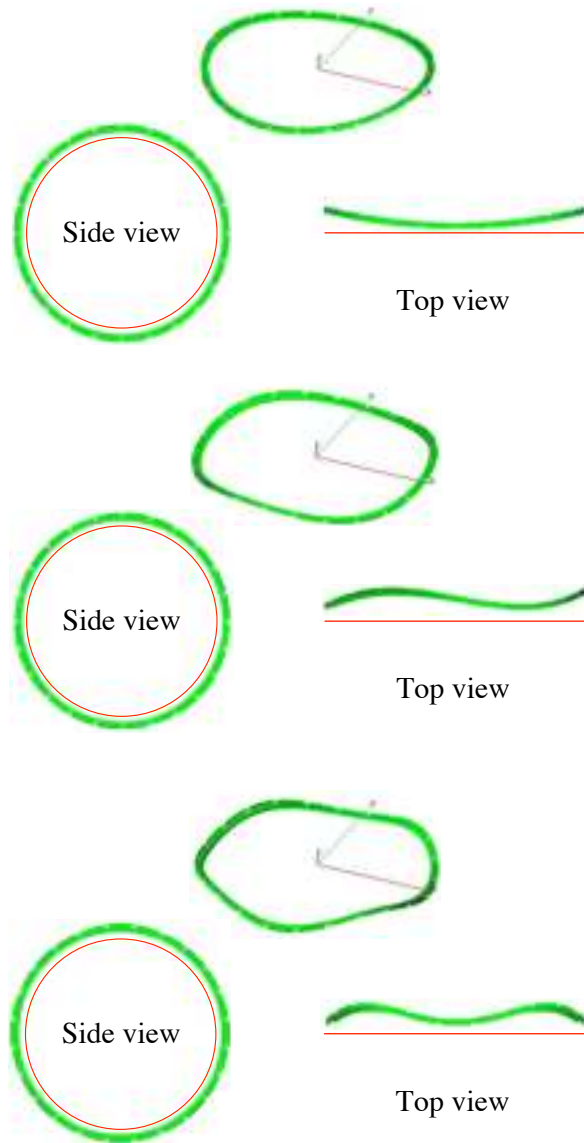


Figure 3.59. NASA ATC. Computed mode shapes for the main rib. First three out-of-plane modes.

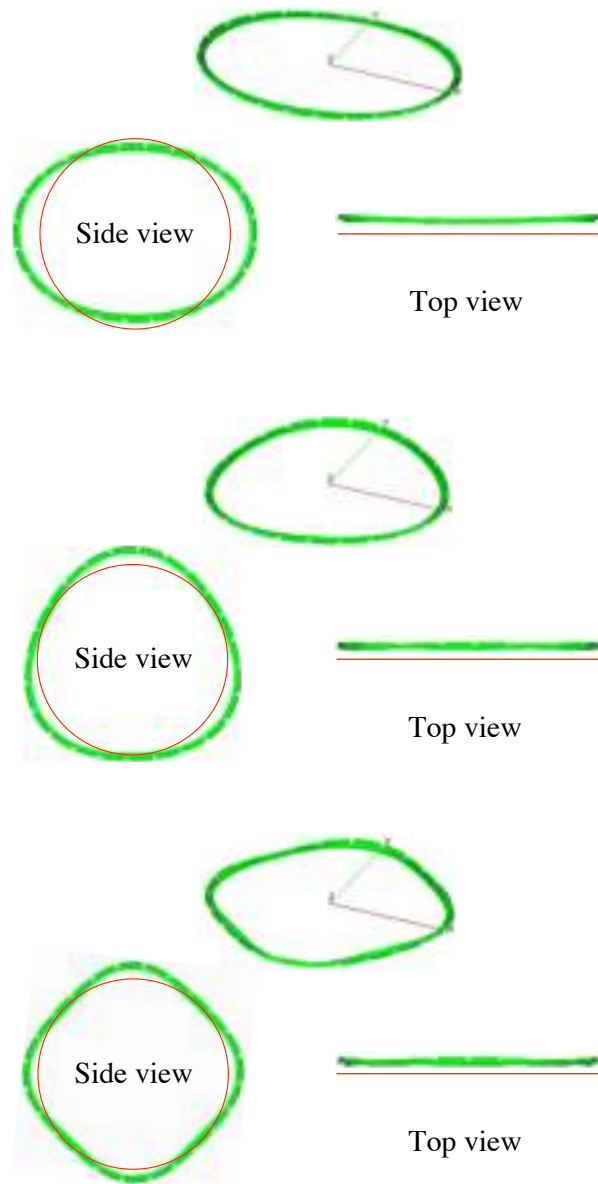


Figure 3.60. NASA ATC. Computed mode shapes for the main rib. First three in-plane modes.

Frequency results for the frame assembly are presented in Figures 3.61 and 3.62. As for the case of the isolated stringer, the numerical results lie above the experimental results. The first bending and torsional modes of the frame assembly are shown in Figures 3.63-3.66. A detail of the deformation pattern in the vicinity of a main rib-stringer junction for the first torsional mode of the frame assembly is shown in Figure 3.64. A mesh of 112,200 rational quadratic elements and 1,281,528 degrees-of-freedom is used for the analysis shown. One could reduce the number of degrees-of-freedom significantly by exploiting rotational symmetry and modeling only 1/24 of the frame assembly (as others have done, see Couchman *et al.* [2003]), but part of the goal of this work is to demonstrate the feasibility of modeling an entire real structure of engineering interest using isoparametric NURBS elements, and so no such simplifications are employed.

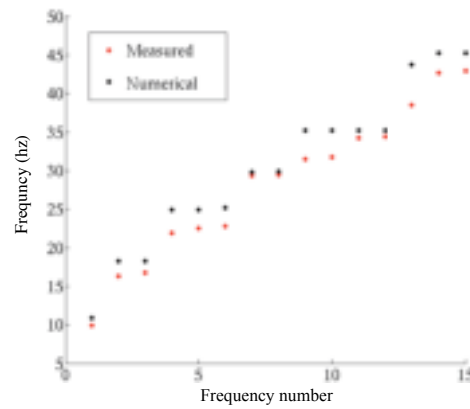
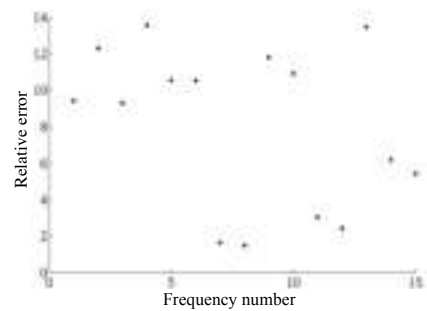


Figure 3.61. NASA ATC. Comparison of numerical and experimental frequency results for the frame assembly.



Mean error 8.1% Max error 13.5%

Figure 3.62. NASA ATC. Relative frequency error for the frame assembly.

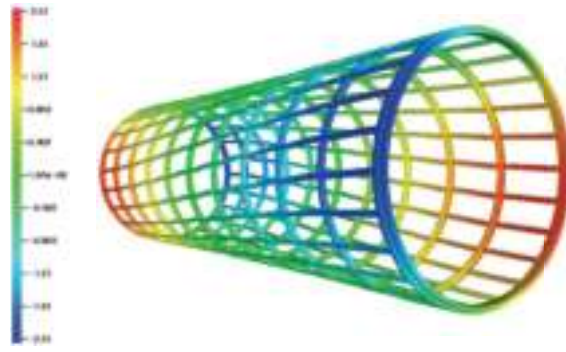


Figure 3.63. NASA ATC. Calculated first torsional mode for the frame assembly; side view. The color contours represent the vertical displacement.



Figure 3.64. NASA ATC. Detail of first torsional mode for the frame assembly; stringer-main rib junction.

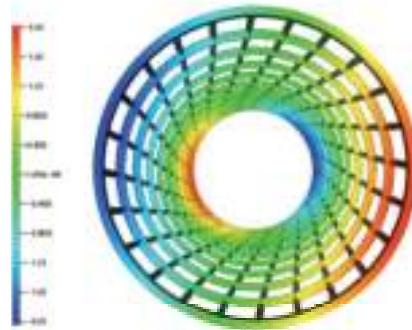


Figure 3.65. NASA ATC. Calculated first torsional mode for the frame assembly; end view. The color contours represent the vertical displacement.

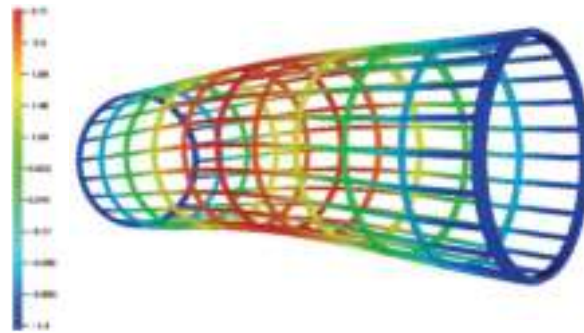


Figure 3.66. NASA ATC. Calculated first bending mode for the frame assembly. The color contours represent the vertical displacement.

Results for the frame and skin assembly are presented in Figures 3.67 and 3.68. Once again, the numerical results lie above the experimental results. The first two modes are shown in Figures 3.69-3.71. The mesh consists of 228,936 rational quadratic elements and 2,219,184 degrees-of freedom.

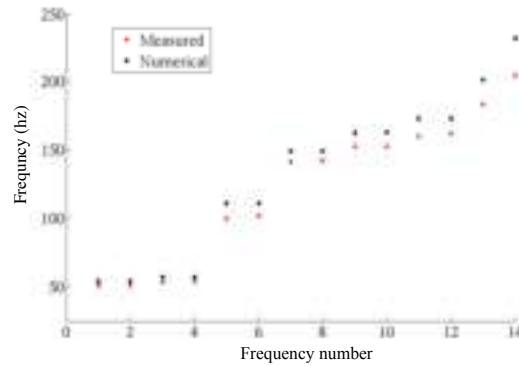
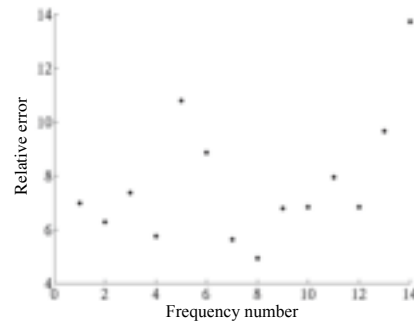


Figure 3.67. NASA ATC. Comparison of numerical and experimental frequency results for the frame and skin assembly.



Mean error 7.7% Max error 13.7%

Figure 3.68. NASA ATC. Relative frequency error for the frame skin assembly.

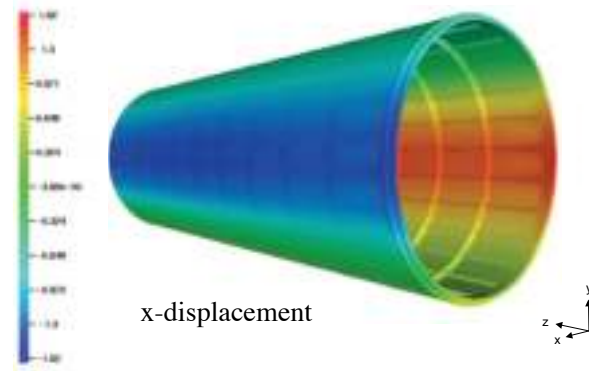


Figure 3.69. NASA ATC. Calculated first Rayleigh mode of the frame and skin assembly. The color contours represent the ovalization of the assembly.

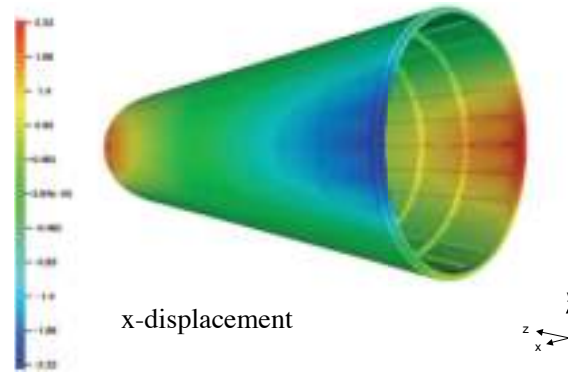


Figure 3.70. NASA ATC. Calculated first Love mode of the frame and skin assembly. The color contours represent the ovalization of the assembly.

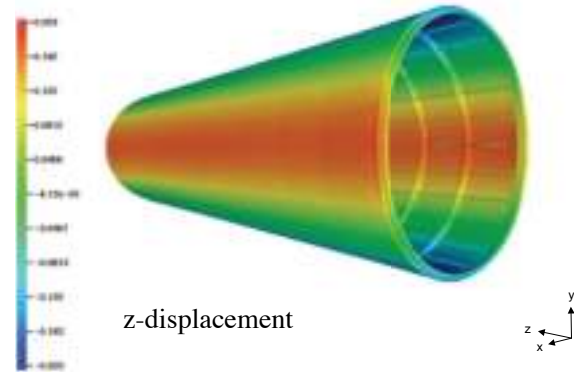


Figure 3.71. NASA ATC. Calculated first Love mode of the frame and skin assembly. The color contours represent the axial displacement of the assembly.

3.9 Conclusive considerations

In this Chapter the recently introduced concept of Isogeometric Analysis has been applied to the study of structural vibrations.

After a review of some basics of Non-Uniform Rational B-Splines and of the main ideas of Isogeometric Analysis, the determination of the structural frequencies for different problems has been performed.

In particular one-dimensional problems, like rods and beams, and two-dimensional ones, like membranes and plates, have been studied.

The method has shown very good results in all these cases and a superior behaviour when compared with analogous classical finite element results.

Another investigated issue has been the possibility of developing, in a natural way, one- and two-dimensional rotation-free thin bending elements. The problem of the imposition of boundary conditions on rotations both weakly and with Lagrange multipliers has been discussed for one-dimensional rotation-free elements.

Then, the exact geometry property of the method has been tested on a three-dimensional circular problem. In this example, the capability of the method of studying thin bending structures (a plate in this case) by means of 3D solid elements has also been tested, obtaining again good results. Finally, Isogeometric Analysis has been employed to study a geometrically complicated real problem, the NASA Aluminium Testbed Cylinder, for which experimental modal results were available for single members as well as for the whole structure. The good agreement between numerical and experimental results has highlighted the great potential of the method.

As a conclusion, we remark that, since all of these preliminary results have shown that this technique could be an important tool in the framework of structural vibration study, more research in this context is needed for the future. Some interesting issues could be deeper studies on different parametrizations (in particular to avoid the appearance of what have been called “outlier frequencies”, i.e. spectrum “optical” branches) and on lumped mass formulations.

4. SHAPE MEMORY ALLOYS FOR EARTHQUAKE ENGINEERING: APPLICATIONS AND MODELING

In this Chapter we deal with *shape memory alloys* (SMAs) and their applications and modeling in the field of earthquake engineering.

The Chapter is divided into two main parts. In the first one we introduce SMAs and report a review of the state-of-the-art of studies and applications of these smart alloys in earthquake engineering (the interested reader may refer to Auricchio [1995] for more details on SMAs and, in particular, to Fugazza [2003] and to Wilson and Wesolowsky [2005] for a complete review of the state-of-the-art of SMAs for seismic applications). In the second part of the Chapter a new contribution to the research field of SMA constitutive modeling is proposed: a phenomenological 3D model describing stress-induced solid phase transformation with permanent plasticity is presented and validated through a number of numerical experiments.

4.1 Shape memory alloys

Buehler and Wiley developed in the 1960s a series of nickel-titanium alloys, with a nickel weight composition of 53-57%, exhibiting a very interesting effect: severely deformed specimens of that alloy, with residual strain of 8-15%, recovered their original shape after a thermal cycle. Such an effect was referred to as the *shape-memory effect* and the alloys able to produce it were called *shape memory alloys*. It was later found that at sufficiently high temperatures such materials also possess the property of *superelasticity* (or *pseudoelasticity*), i.e. the property of recovering large deformations during loading-unloading cycles at constant temperature. Due to these distinctive macroscopic behaviours, not typical of traditional materials, SMAs have become the basis for a number of innovative applications, in many fields of engineering as biomechanics and aeronautics, as well as in earthquake engineering, where they can be successfully employed in devices for protecting buildings from structural vibrations.

4.1.1 General aspects

The peculiar properties of SMAs are related to reversible martensitic phase transformations, i.e. solid-to-solid diffusionless processes between a crystallographically more-ordered phase (referred to as *austenite*) and a crystallographically less-ordered one (referred to as *martensite*). Austenite is typically stable at lower stresses and higher temperatures, while martensite is stable at higher stresses and lower temperatures. These transformations can be thermal- or stress-induced (cf. Duerig *et al.* [1990]; Van Humbeeck [1999a]).

At relatively high temperatures a SMA is in its austenitic state and, when cooled, undergoes a transformation to its martensitic state. The austenite phase is characterized by a cubic crystal structure, while the martensite phase has a monoclinic (orthorhombic) crystal structure. The transformation from austenite to martensite occurs through a displacive distortion process, which does not imply, however, macroscopic changes in the shape of the specimen. This is because several differently oriented plates of martensite (generally called *variants*) form within a single grain of austenite. The martensite variants are arranged in self-accomodating groups at the end of the thermal-induced transformation, thus keeping unchanged the specimen shape.

In a stress-free state, there are four transformation temperatures defining a SMA: M_s and M_f ($M_s > M_f$) on cooling and A_s and A_f ($A_s < A_f$) on heating. M_s and M_f are the temperatures defining, respectively, the beginning and the end of the transformation from austenite into martensite, while A_s and A_f are the temperatures defining, respectively, the beginning and the end of the inverse transformation.

4.1.1.1 Shape-memory effect and superelasticity.

When an unidirectional stress is applied to a martensitic specimen (see Figure 4.1), there exists a critical value whereupon the *detwinning* process of the martensitic variants takes place (cf. Duerig *et al.* [1990]). This process consists in the spatial re-orientation of the original martensitic variants, i.e. if there is a preferred direction for the occurrence of the transformation, often associated with a state of stress, only the most favorable variant is formed. The product phase is then termed *single-variant martensite* and it is characterized by a detwinned structure. During such a process, the stress remains practically constant until the martensite is fully detwinned (theoretically having a single variant aligned with the strain direction). Further straining causes the elastic loading of the detwinned martensite. Upon unloading, a large residual strain remains. However, by heating above A_f , martensite transforms into austenite and the specimen recovers

its initial undeformed shape, which is then kept during cooling below M_f , when the material re-transforms into twinned martensite. This phenomenon is generally referred to as *shape-memory effect*.

When an unidirectional stress is applied to an austenitic specimen (see Figure 4.2) at a temperature greater than A_f , there exists a critical value whereupon a transformation from austenite to detwinned martensite occurs. As deformation proceeds in isothermal conditions, the stress remains almost constant until the material is fully transformed. Further straining causes the elastic loading of the detwinned martensite. Upon unloading, since martensite is unstable, without stress, at a temperature greater than A_f , a reverse transformation takes place, but at a lower stress level than during loading so that a hysteretic effect is produced. If the material temperature is greater than A_f , the strain attained during loading is completely and spontaneously recovered at the end of unloading. This remarkable process gives rise to an energy-absorption capacity with zero residual strain, which is referred to as *superelasticity* (or *pseudoelasticity*). If the material temperature is lower than A_f , only a part of stress-induced martensite re-transforms into austenite. A residual strain is then found at the end of unloading, which can be recovered by heating above A_f . This phenomenon is generally referred to as *partial superelasticity*.

4.1.2 Commercial SMAs

Despite the fact that many alloy systems show the shape-memory effect, only few of them have been developed on a commercial scale for engineering applications. Accordingly, in this Section, we discuss some of the characteristics exhibited by those SMAs that, so far, have had the strongest market impact, i.e., nickel-titanium and copper-based alloys.

4.1.2.1 Nickel-titanium SMAs.

Nickel-titanium (NiTi, often referred to as Nitinol) systems are based on equiatomic compounds of nickel and titanium (cf. Johnson Matthey [2005]; Memry Corporation [2005]; Memory-Metalle GmbH [2005]; Nitinol Devices & Components [NDC]; Shape Memory Applications Inc. [2005]; Special Metals Corporation [2005]; The A to Z of Materials (AZoM) [2005]).

Besides the ability of tolerating quite large amounts of shape-memory strain, NiTi alloys show high stability in cyclic applications, possess an elevated electrical resistivity and are corrosion resistant. They also have a moderate solubility range, enabling changes in composition and alloying with other elements to modify both their shape-memory and mechanical characteristics. A third metal is usually added to the binary system to improve its properties. The most common modification is an extra nickel quantity up to

1%, which results in increasing the yield strength of the austenitic phase while depressing transformation temperatures.

Manufacture of NiTi alloys is not easy, as machining techniques are difficult to be used; this fact explains the reason for their elevated cost. However, the excellent mechanical properties of Nitinol make it the most widespread SMA material for commercial applications.

4.1.2.2 Copper-based SMAs.

Copper-zinc-aluminum (CuZnAl) alloys have been the first copper-based SMAs to be commercially exploited (cf. Barns [2003]; Shape Memory Applications Inc. [2005]; The A to Z of Materials (AZoM) [2005]). Such alloys take their origin from copper-aluminium binary systems, which, despite their shape-memory characteristics, have transformation temperatures considered too high for practical use.

CuZnAl alloys have the advantage to be constituted by relatively cheap metals using conventional metallurgical processes. These reasons make them among the cheapest of the available commercial SMAs, especially as compared to Nitinol.

Their major drawback is that the martensitic phase is stabilized by long term ageing at room temperatures, which causes an increase in transformation temperature over time and a decomposition of their structure when exposed to temperatures above 100° C. Moreover, as compared to other SMAs, CuZnAl alloys have modest shape-memory properties with a maximum recoverable strain of about 5% and, without the addition of grain growth control additives, their grain size can be quite large leading to brittleness problems.

Copper-aluminum-nickel (CuAlNi) alloys have undergone extensive development and are now preferred to CuZnAl alloys (cf. Barns [2003]; Shape Memory Applications Inc. [2005]; The A to Z of Materials (AZoM) [2005]); they are popular for their wide range of useful transformation temperatures and because they can be used above 100° C.

The aluminium percentage strongly influences alloy transformation temperatures and the reduction of its content to below 12% can also improve mechanical properties.

Also CuAlNi alloys are made from relatively inexpensive elements, but their processing is particularly difficult to machine. In fact, they can only be hot worked, and the final heat treatment has to be tightly controlled to produce alloys with the desired transformation temperatures. These difficulties have made such systems more expensive than CuZnAl, even if cheaper than Nitinol.

4.1.3 SMA applications

As described above, SMAs have unique properties which are not present in materials traditionally employed in engineering applications. Accordingly, their use gives new possibilities of designing and producing innovative commercial products.

The present Section briefly reviews, through practical examples, the most important applications exploiting both the superelastic and the shape-memory effects (cf. Auricchio [1995]; Barns [2003]; Van Humbeeck [1999a,b]).

Note that earthquake engineering applications are discussed in detail in the next Section.

4.1.3.1 Superelastic applications.

Superelasticity-based applications take advantage of one of the following features:

- The possibility of recovering large deformations (up to strain of 8-15%).
- The existence of a transformation stress plateau, which guarantees constant stress over non-negligible strain intervals.

In the following we report some interesting examples, such as medical guidewires, stents, orthodontic wires and eyeglass frame components.

A *medical guidewire* is a long, thin, metallic wire passing into the human body through a natural opening or a small incision. It serves as a guide for the safe introduction of various therapeutic and diagnostic devices. The use of superelastic alloys may reduce the complications that can derive from guidewire permanent kinks.

Stent is the technical word indicating self-expanding micro-structures, employed for the treatment of hollow-organ or duct-system occlusions. The stent is initially stretched out to reach a small profile, which facilitates a safe, atraumatic insertion of the device. After being released from the delivery system, the stent self-expands to over twice its compressed diameter and exerts a nearly constant, gentle, radial force on the vessel wall.

Other considered biomedical applications are *orthodontic wires*. During orthodontic therapy, tooth movement is obtained through a bone remodeling process, due to forces applied to the dentition which can be created by elastically deforming an orthodontic wire and allowing its stored energy to be released over a certain period of time. Excellent results are produced because of the constant stress that SMAs are able to exert during a substantial part of the transformation.

The last superelastic-based application we mention consists of *eyeglass frame components* which, by using the SMA superelastic property, withstand extreme deformations springing back completely.

4.1.3.2 Shape-memory applications.

The applications described in what follows take advantage of the SMA ability to recover the configuration associated with the austenitic phase. In some devices the shape recovery is performed only once, while, in some others, it is possible to switch cyclically between two different configurations, through the use of a *bias* system.

A widely exploited use of the shape-memory effect is one in which an external constraint prevents the material from returning to its original shape on heating (*constrained recovery*), resulting in the generation of large recovery forces. Consider for example a ring, initially in a multiple-variant martensitic state. The ring is first mechanically expanded in the single-variant martensitic state and, then, a shaft is inserted in the ring. Upon heating, the ring freely recovers until contact with the shaft is made.

The main application of constrained recovery is in coupling devices and fasteners. In fact, the use of SMAs provides substantial advantages over other joining techniques because of a number of reasons:

- The installation procedure is simple and fast, very little operator training is needed, and light, easy-to-use tools are required for assembly and disassembly. The final quality of SMA joints is relatively insensitive to the assembly procedure; hence, only minimum post-installation inspection is needed. These are all important aspects when the coupling must be performed in unfriendly environments (e.g., tight places, deep sea, space).
- The contact stress is fairly constant beyond a certain level of contact strain, hence the stress level attainable in the joints is well defined.
- The joints operate over a wide range of temperatures and loading conditions.
- Once applied, as structural elements, the joints usually have excellent response in terms of corrosion, strength, fatigue resistance. Accordingly, they seldom weaken the overall structural behaviour.

Examples of SMA coupling devices currently used are:

- *Airplane-pipe coupling*: it gives the possibility of obtaining closely packed

hydraulic-tubing assemblies and the freedom of designing the hydraulic system without the joining method providing constraints because of tool access.

- *Electrical connectors*: SMAs are used to drive the opening and the closure of connectors such as those on computer boards. In such cases, almost no insertion force is needed and very little (if any) of the mating force is transmitted to the supporting structure (the connector mounting structure does not need to be stiffened). Moreover, once the connector is closed, it exerts high retention forces, inhibiting any relative movement between connector members and preventing fretting corrosion from occurring.

SMA coupling devices are also successfully used in marine deep-sea applications, in braid termination, missile retain rings and hermetic seals. An interesting application for the joining of optical fibers has also been proposed.

SMAs can be easily used to perform work (i.e., as *actuators*). Think of a weight hung from a SMA spring; assume that the spring is in a single-variant martensitic state under the stress induced by the weight, which means that it is in an extended configuration due to the alignment of all the variants. On heating, the martensite is converted to austenite and the weight is lifted; on cooling, the reverse transformation occurs (due to the presence of the weight) and the spring stretches again, causing a *two-way effect*. Accordingly, upon multiple heating-cooling cycles a progressively increasing amount of work is performed. The *biasing* stress for the conversion of austenite into single-variant martensite upon cooling is often obtained by coupling the SMA spring with a regular spring. In general, a distinction is made between thermal and electrical actuators. Both of them work upon heating and the difference is that thermal actuators are heated by changes in the surrounding environment, while electrical actuators are heated by passing electricity directly through the SMA:

- *Thermal actuators* are usually designed to behave as sensors (detecting a temperature change) and as actuators. Both nickel-titanium and copper-based alloys are used depending upon the exact requirements; NiTi alloys are better in fatigue and work output, while the Cu-based alloys have a higher transformation temperature and are cheaper. Compared to other actuation methods, SMAs are generally simpler, less expensive, more compact and provide very large, sudden motions. However, the presence of the hysteresis makes it difficult to perform an accurate temperature control. Recently, devices based on the memory effect associated with phase transitions characterized by a much smaller hysteresis (the so-called R-phase transition) have been used.

- *Electrical actuators* are used to replace solenoids, servomotors, hydraulic and pneumatic devices. They are typically simpler in design, quieter, more compact and less expensive. Nickel-titanium alloys are often preferred because of their high resistivity, work output and long fatigue lifetime. The major limitation is in the possibility of actuating (heating) quite quickly, while cooling is in general much slower.

SMA actuators have also been used in conjunction with active vibration control for linkage mechanisms, active buckling of stiffened panels, control surfaces for adjustable chambers, bending and shape control of beams, composites with embedded SMA actuators. Other applications are shutters for air-conditioners, fans for automobile radiators, switches for automatic kettles, thermal valves for fire protection, liquid-gas switches.

SMA's are having a substantial impact also in *robotics*, where all the mechanical elements usually used (motors, gears, cams) have limitations in the minimum dimension in which they can be produced. On the other hand, SMA wires can be produced in almost any thickness and can be used as actuators driven by electric current. The absence of rotating or sliding parts helps even further the super-miniaturization and the integration. The major limitation is again due to the difficulty of quickly cooling the actuators; various methods are being investigated, such as forced-air cooling, cooling in water, cooling by thermoelectric devices or by heat pipes. Finally, SMA micro-actuators show an intrinsic capacity of controlling the applied forces, a property similar to the human touch and fundamental for advanced robotic applications. For example, SMA robots can grip a soft ball loosely and a hard ball tightly.

Shape-memory effects have also been exploited for *medical applications*, such as blood-clot filters, intracranial aneurysm clips, artificial hearts, ropes for the treatment of scoliosis, micropumps. For example, a micropump consists of a bellows, a SMA wire and two one-way valves: when the wire is heated by current, it shrinks and a liquid medication is forced out. The mechanism is light and a small amount of energy is needed for the activation (as an example, an artificial kidney pump weights only 4.4 g and consumes only 0.2 W of power, making it portable). Another area for interesting and commercially viable applications is *orthopedics*. The healing of fractured bones proceeds more rapidly if the fractured faces are under steady compressive stress. During surgery to reset fractures, SMA plates can be attached on both sides of the fracture, producing the necessary compressive stress in the fracture gap by exploiting the memory effect. In general, for medical applications only NiTi alloys are used, due to their good corrosion resistance and biocompatibility.

Moreover, the use of SMAs has opened new frontiers also in terms of *space applications*. SMA-based devices have very simple design and activation procedures and this makes them extremely reliable, hence ideal for space applications, where every action to be performed presents an enormous degree of difficulty.

Finally, in the design of eyeglass frames, also the shape-memory effect can be exploited, as it allows a frame, which is accidentally bent, to be restored to a like-new shape merely by heating. Other reasons for using Nitinol in eyeglass frame production are that it has about 70% of the density of most common frame materials and that it is extremely corrosion-resistant and needs no coating or electroplating to protect it from perspiration or skin oils. Moreover, no allergic reactions have been noted.

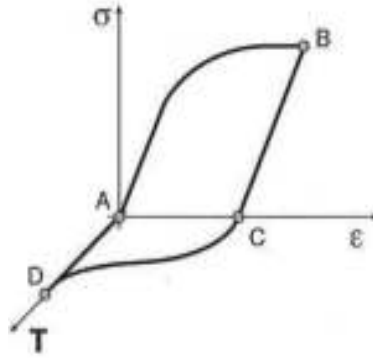


Figure 4.1. Shape-memory effect. At the end of a mechanical loading-unloading cycle (ABC) at a constant low temperature, the material shows a residual strain (AC), which can be recovered by means of a thermal cycle (CDA).

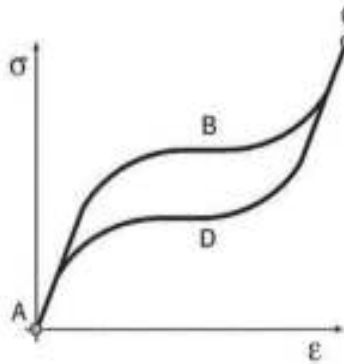


Figure 4.2. Superelastic effect. During a mechanical loading-unloading cycle at a constant high temperature, the material is able to undergo large deformations without showing any residual strain. A hysteretic effect is produced as well.

4.2 SMAs in earthquake engineering

In this Section, the use of SMAs in earthquake engineering is discussed in detail. We start proposing an overview on the mechanical behaviour of SMA elements (as wires and bars) under static and dynamic loading conditions and then we present a state-of-the-art of the most promising investigations on SMA-based devices presented in the last years. We finally conclude this Section with two examples of existing structures retrofitted by means of SMAs.

4.2.1 Studies on the mechanical behaviour of SMA elements

SMA elements as wires and bars have been studied by many authors (Lim and McDowell [1995]; Strnadel *et al.* [1995]; Piedboeuf and Gauvin [1998]; Tobushi *et al.* [1998]; Wolons *et al.* [1998]; Moroni *et al.* [2002]; Tamai and Kitagawa [2002]; DesRoches *et al.* [2004]) to understand their response under different loading conditions. We now present a review of some recent experimental investigations dealing with the mechanical behaviour of SMA elements.

Lim and McDowell [1995] analyze SMA path dependence during cycling loadings through experimental tests performed on 2.54 mm diameter wires. They focus on cyclic uniaxial tension and tension-compression behaviours. The most interesting results are that:

1. during cyclic loading with an imposed maximum strain, the critical stress starting the stress-induced martensite transformation decreases, the strain-hardening rate increases, residual strain accumulates and the hysteresis energy progressively decreases over many cycles of loading;
2. the stress at which forward or reverse transformations occur depends on the strain level before the last unloading event, due to distribution and configuration of austenite-martensite interfaces which evolve during transformation.

Strnadel *et al.* [1995] investigate the behaviour of NiTi and NiTiCu thin plates in super-elastic phase. Their goal mainly consists in evaluating cyclic stress-strain behaviour; in particular, they focus on the effect of the nickel content in specimen response. Significant aspects are that:

1. ternary NiTiCu alloys show lower transformation strains and stresses than binary NiTi alloys;

2. in both NiTi and NiTiCu alloys, as the number of cycles increases, a higher nickel content corresponds to a lower residual deformation increasing rate.

Piedboeuf and Gauvin [1998] examine SMA wire damping behaviour. They perform many experiments on 100 μm diameter NiTi wires at three amplitude levels (2, 3 and 4% strain), over four frequency values (0.01, 0.1, 1, 5 and 10 Hz) and at two temperatures (25 and 35 °C). The main findings carried out are that:

1. an increase in temperature causes a linear increase in transformation stresses and an upward shift of the stress-strain curves;
2. up to a frequency of 0.1 Hz and for a fixed value of deformation of 4%, the stress difference between the two plateaux increases, producing an increase in the stress hysteresis as well as in the dissipated energy; for higher frequencies the lower plateau deforms and rises, causing a reduction of the hysteresis loop;
3. frequency interacts with deformation amplitude; in particular, at a strain of 2%, there is only a small variation in the dissipated energy varying frequency, while, at 4%, the variation is significative, with a maximum about at 0.1 Hz; for higher values of frequency the dissipated energy decreases;
4. the loss factor $\eta = \Delta W/(\pi U)$ (see Figure 4.3) decreases with an increase in temperature which, anyway, has no significant effect on the dissipated energy.

Tobushi *et al.* [1998] study the influence of the strain rate $\dot{\epsilon}$ on the superelastic properties of 0.75 mm diameter superelastic wires through tensile tests with strain rates between $1.67 \cdot 10^{-3} \% \text{ s}^{-1}$ and $1.67 \% \text{ s}^{-1}$. They moreover consider temperature variation effects on the wire mechanical response. The main considerations pointed out are that:

1. for $\dot{\epsilon} \geq 1.67 \cdot 10^{-1} \% \text{ s}^{-1}$, a larger value of $\dot{\epsilon}$ corresponds to a higher starting stress for the forward transformation and to a lower starting stress for the reverse transformation;
2. for each considered temperature level, a larger value of $\dot{\epsilon}$ corresponds to a larger residual strain after unloading; moreover, also a higher temperature corresponds to a larger residual strain;
3. when the number of cyclic deformation increases, the stress at which forward and reverse transformations start decreases with different variations; also the residual strain after unloading increases;

4. for each considered temperature level, the transformation stress is almost constant for $\dot{\epsilon} \leq 3.33 \cdot 10^{-2} \% \text{ s}^{-1}$; for $\dot{\epsilon} \geq 1.67 \cdot 10^{-1} \% \text{ s}^{-1}$, instead, the upper plateau stress level at which the forward transformation starts increases, while the one correlated to the lower plateau decreases with a lower variation; the same trend is also observed when the wire has been subjected to mechanical training;
5. the strain energy increases with temperature, while the dissipated work depends on it only slightly; moreover, at each temperature level, it is observed that both quantities do not depend on the strain rate for values of $\dot{\epsilon} \leq 3.33 \cdot 10^{-2} \% \text{ s}^{-1}$, while, for values of $\dot{\epsilon} \geq 1.67 \cdot 10^{-1} \% \text{ s}^{-1}$, the dissipated work increases and the strain energy decreases linearly.

Wolons *et al.* [1998] focus on 0.5 mm diameter superelastic NiTi wires to study their damping properties and the effects of cycling, frequency oscillation (from 0 to 10 Hz), temperature level (from about 40 °C to about 90 °C) and static strain offset (i.e. the strain level from which cycling deformation starts). Their main findings are that:

1. a SMA wire requires a significant amount of mechanical cycling to have a stable hysteresis loop shape; the amount of residual strain depends on both temperature and strain amplitude, but not on cycling frequency;
2. the shape of hysteresis loops is significantly affected by frequency, in particular, during the reverse transformation from detwinned martensite to austenite;
3. energy dissipation is dependent on frequency, temperature, strain amplitude and static strain offset (chosen in the range 2.9 to 4.7 %); the dissipated energy per unit volume initially decreases up to 1-2 Hz, then approaching a stable level at 10 Hz; the dissipation capacity at 6-10 Hz is about 50% lower than the corresponding one at low frequencies and decreases when temperature increases above 50 °C;
4. reducing the static strain offset, the dissipated energy per unit volume increases;
5. energy dissipation per unit volume of SMA wires undergoing cyclic strains at moderate strain amplitudes (about 1.5 %) is twenty times larger than the one of typical elastomers undergoing cyclic shear strain.

Moroni *et al.* [2002] propose to use copper-based SMAs to dissipate energy in civil engineering structures. Their idea is to design a new efficient beam-column connection incorporating SMAs. Cyclic tension-compression tests are performed on martensitic 5 and 7 mm diameter bars, characterized by different processing histories (hot rolled or

extrusion) and grain size composition. Experimental investigations are performed in both strain and stress control at different loading frequencies (from 0.1 to 2 Hz). The conclusions carried out are that:

1. martensitic CuZnAlNi alloy is able to dissipate substantial energy through repeated cycling, hence highlighting a possible use as material for seismic devices;
2. damping depends on strain amplitude and tends to become stable for large strains; moreover, frequency is observed to have small influence on damping values;
3. the considered mechanical treatments (rolling and extrusion) do not influence bar behaviour;
4. fractures due to tensile actions are observed and present brittle intergranular morphology.

Tamai and Kitagawa [2002] test 1.7 mm diameter superelastic NiTi wires for employment in brace and exposed-type column base for building structures. The experimental investigations consist of both monotonic and pulsating tension loading tests performed with constant, increasing and decreasing strain amplitudes, at a stroke speed of the test machine maintained equal to $0.074\% \text{ s}^{-1}$ throughout all the experiments. The observations arising from this work are that:

1. a spindle shaped hysteresis loop showing a great deal of absorbed energy is observed;
2. the starting stress of the phase transformation is sensitive to ambient temperature; moreover, wire temperature varies during cyclic loading due to its latent heat;
3. residual strain increment and dissipated energy decrement per cycle decrease with the number of loading cycles;
4. the increase and decrease in the wire temperature during forward and reverse transformations have almost the same intensity; in particular, forward and reverse transformations are respectively exothermal and endothermal.

Finally, DesRoches *et al.* [2004] perform several experimental tests on NiTi superelastic wires and bars to assess their potential for applications in seismic resistant design and retrofit. In particular, they study the effects of the cyclic loading on residual strain, forward and reverse transformation stresses and energy dissipation capability. Specimens of different diameters (1.8, 7.1, 12.7 and 25.4 mm respectively) and with nearly identical

composition are considered. The loading protocol is made of increasing strain cycles of 0.5%, 1% to 5% by 1% increments, and by four 6% cycles. Two series of tests are performed: the first one, in quasi-static condition, is conducted at a frequency of 0.025 Hz, while the second at frequencies of 0.5 and 1 Hz, to simulate dynamic loads. The following findings are pointed out:

1. nearly ideal superelastic properties are obtained in both wires and bars; the residual strain generally increases from an average of 0.15% at 3% strain to an average of 0.65% strain after four 6% strain cycles and seems independent on both the section size and the loading rate;
2. the values of equivalent damping range from 2% for the 12.7 mm bars to a maximum of 7.6% for the 1.8 mm wires and are in agreement with the values found by other authors (Dolce *et al.* [2000]; Dolce and Cardone [2001a]); the bars show a lower dissipation capability than wires;
3. the value of stress at which forward transformation starts when testing bars is lower by about 30% than the corresponding value in wires.

4.2.2 The MANSIDE project

In the period 1995-1999, the European Commission co-funded a project, referred to as MANSIDE (Memory Alloys for New Seismic Isolation and energy dissipation DEvices), aimed at the development and experimental validation of new seismic protection devices based on the properties of SMAs (cf. Bernardini and Brancaloni [1999]; Cardone *et al.* [1999]; Pence [1999]; Van Humbeeck [1999a]; Valente *et al.* [1999]; Dolce *et al.* [2000]; Dolce and Cardone [2001a,b]; Dolce *et al.* [2001]; Bruno and Valente [2002]). The main goals of the research program were:

1. the study of SMA components for new devices exploiting superelasticity and SMA high damping properties;
2. the design and testing of prototypes (seismic isolators and dissipating braces);
3. the proposal of guidelines for the design and use of new SMA-based devices, including reliability requirements.

In the following, we present a summary of experimental investigations carried out within this project.

4.2.2.1 Tests on Martensite and Austenite NiTi bars.

Dolce and Cardone [2001a] investigate the mechanical behaviour of NiTi SMA bars through a large experimental test program. SMA elements are different in size, shape (circular and hexagonal) and physical characteristics (composition, thermomechanical treatment and material phase). Experimental results are carried out by applying repeated cyclic deformations: strain rate, strain amplitude, temperature and number of cycles are considered as test parameters, and their values are selected taking into account the typical range of interest for seismic applications. SMA bars have a diameter of 7-8 mm (small size bars) and 30 mm (big size bars), but special attention is devoted to big size bars, being the most likely candidates for full scale seismic devices.

- **Torsional tests on martensite specimens**

All tests are carried out at room temperature (about 25 °C) on only one big size martensite specimen. Frequencies of loading range from 0.01 to 1 Hz. Up to 24% maximum nominal tangential strain (γ) is attained.

- *Tests in normal working conditions:* four groups of cycles at 0.01, 0.1, 0.5 and 1 Hz, respectively constituted by 4 times 10 consecutive cycles, with γ equal to 3%, 6%, 9% and 11%. The aim is to evaluate the cyclic behaviour of the specimen as a function of strain rate and amplitude.
- *Fatigue tests:* groups of up to 1650 cycles, at 0.5 Hz and γ equal to 11%. The aim is to verify the fatigue behaviour in terms of decay and resistance of the specimen.
- *Tests in normal working conditions:* two groups of cycles at 0.1 and 0.5 Hz, respectively constituted by 4 times 10 consecutive cycles, with γ equal to 3%, 6%, 9% and 11%. The aim is to check the mechanical behaviour after the large number of cycles undergone by the specimen during the fatigue tests.
- *Test at very large strain amplitudes:* one test at 0.1 Hz, constituted by 4 times 10 cycles with γ equal to 15%, 18%, 21%, 24%. The aim is to evaluate the cyclic behaviour of the specimen under extreme strain amplitude conditions.
- *Fatigue tests:* groups of 100 cycles, at 0.5 Hz and γ equal to 15% or 18%. The aim is to verify the fatigue resistance of the specimen under extreme strain amplitude conditions.

- **Torsional tests on austenite specimens**

The tests are carried out on one big size austenite specimen at room temperature (about 25 °C). Frequencies of loading range from 0.01 to 1 Hz. Up to 11%

maximum nominal tangential strain is attained.

- *Tests in normal working conditions*: four group of cycles at 0.01, 0.1, 0.5 and 1 Hz, respectively constituted by 4 times 10 consecutive cycles, with γ equal to 3%, 6%, 9% and 11%. The aim is to evaluate the cyclic behaviour of the specimen as a function of the strain rate and amplitude.
- *Fatigue tests*: two groups of several cycles (100 the first group, up to failure the second), at 0.5 Hz and γ equal to 11%. The aim is to verify the fatigue behaviour in terms of decay and resistance of the specimen.
- *Tests in normal working conditions*: two groups of cycles at 0.1 and 0.5 Hz respectively constituted by 4 times 10 consecutive cycles, with γ equal to 3%, 6%, 9% and 11%. The aim is to check the mechanical behaviour after the large number of cycles undergone by the specimen during the fatigue test.

The most interesting findings of the experimental investigation are that:

1. the mechanical behaviour of SMA bars subjected to torsion is independent on the frequency of loading in the case of martensite elements and slightly dependent in the case of austenite elements;
2. the energy loss per unit weight increases more than linearly with strain amplitude, reaching, at relatively large strain amplitudes, values of the order of 0.5 J/g for martensite bars and of the order of 0.25 J/g for austenite bars;
3. damping properties are good for martensite (up to 17% in terms of equivalent damping), but rather low for austenite (of the order of 5-6%);
4. austenite bars show small residual strains at the end of the tests (i.e. of the order of 10% of the maximum attained deformation);
5. the fatigue resistance at large strains is good for austenite bars (hundreds of cycles) and very good for martensitic bars (thousands of cycles). In both cases, the cyclic behaviour (after an initial stabilization) is stable and repeatable.

In conclusion, experimental tests prove that SMA bars subjected to torsion have a good potential for employment as kernel components in seismic devices. Martensite bars can provide large energy dissipation and very good fatigue resistance capabilities. Austenite bars, even having less energy dissipation capability, can undergo very large strains without showing significative residual strain, after a correct calibration of the transformation temperatures with respect to the operating temperature. These two types of behaviour can be used for obtaining devices satisfying different needs in seismic protection problems.

4.2.2.2 Tests on Austenite NiTi wires.

Within the same research program, Dolce and Cardone [2001b] study the mechanical behaviour of NiTi superelastic wires in tension. Tests are performed on austenite wire samples of 1-2 mm diameter and 200 mm length. Many wire types are considered, with different alloy compositions and thermomechanical treatments.

Cyclic tests on pre-tensioned wires, with loading frequencies ranging from 0.01 to 4 Hz and strain amplitude up to 10%, are carried out at room temperature (about 20 °C). Subsequently, loading-unloading tests are performed under temperature control, between 40 °C and 10 °C (with a step of 10 °C), at about 7% strain amplitude and 0.02-0.2 Hz loading frequencies.

The superelastic behaviour is deeply investigated and in particular the dependence of the mechanical properties on temperature, loading frequency and number of cycles is studied. The mechanical behaviour is described in terms of secant stiffness, energy loss per cycle, equivalent damping and residual strain.

The most important results of the experimental investigations can be summarized as follows:

1. the dependence on temperature of the wires is compatible with normal ambient temperature variations (of the order of 50 °C);
2. loading frequency influences the SMA behaviour, in particular when going from low frequency (0.01 Hz or less) to the frequency range of interest for seismic applications (0.2-4 Hz); moreover, a decrease in energy loss and equivalent damping is observed as temperature increases, due to the latent heat of transformation (that cannot be dissipated in case of high strain rates);
3. the number of cycles influences austenite SMA superelastic behaviour, decreasing energy dissipation while increasing cyclic strain hardening;
4. the typical loading-unloading cycle of an austenite wire shows a low equivalent damping; this results in a better performance of SMAs when used in a re-centering mechanism.

In conclusion, experimental results show how the characteristics of the superelastic wires are well suited for seismic applications and both re-centering and energy dissipation features of devices can be obtained.

The cyclic behaviour of superelastic wires is found to be stable after few cycles, whose number is of the same order of the number of cycles that would be experienced during

an earthquake: to get a stable response, then, a device should be subjected to a pre-established initial training, which could be a part of the testing program for the device qualification of acceptance. An alternative strategy could rely on the better energy dissipation properties of the virgin material, avoiding or limiting any preliminary training of the device before its use in a structural system.

4.2.3 Numerical studies on SMA-based devices

Among the huge literature dealing with SMA materials, some authors (Bruno and Valente [2002]; Baratta and Corbi [2002]; Wilde *et al.* [2000]; DesRoches and Delemont [2002]; DesRoches and Smith [2004]) study the seismic behaviour of civil engineering structures, such as frames and bridges, endowed with SMA-based devices.

In the following we present a review of numerical applications where such new materials are used as vibration control devices (Bruno and Valente [2002]; Baratta and Corbi [2002]; Corbi [2003a,b]) and isolation systems (Wilde *et al.* [2000]; DesRoches and Delemont [2002]; DesRoches and Smith [2004]).

Bruno and Valente [2002] present a comparison of different passive seismic protection devices, in order to quantify the improvements from SMA-based devices with respect to traditional steel braces and rubber base isolation systems.

A large number of nonlinear seismic analyses with an increasing seismic intensity level are performed. The structural typology studied is characterized by an appropriate structural scheme to be effectively protected with base isolators or braces. New and existing buildings, either protected or not, depending on whether seismic provisions are complied with in the building design or not, are examined. Base isolation and energy dissipation are equally addressed for both conventional and innovative SMA-based design.

SMA-based devices result to be more effective than rubber isolators in reducing seismic vibrations, but the same conclusions cannot be extended to SMA braces as compared to steel ones, being the reduction of the structural response almost identical from a practical point of view. SMA braces seem, however, to be preferable because of their re-centering capabilities. Furthermore, the use of such new smart systems guarantees better performance in consideration of reduced functional and maintenance requirements.

Baratta and Corbi [2002] and Corbi [2003a,b] study the behaviour of SMA tendon elements which collaborate to the strength of a portal frame model subjected to horizontal ground motion. The investigated structure is assumed to be elastic-perfectly plastic, while tendons are supposed superelastic.

Such a system is compared in terms of performance with a similar one with fully elastoplastic or unilaterally plastic (i.e. unable to resist compression) tendons.

Numerical results prove that the structure equipped with superelastic tendons shows a better dynamic response as compared to the case of elasto-plastic tendons. In fact, SMA tendons produce smaller response amplitudes and much smaller residual drifts. Moreover, such a device yields an excellent attenuation of the P- Δ effect.

Wilde *et al.* [2000] consider a smart isolation system combining a laminated rubber bearing (LRB) with a device based on SMA bars.

The simplest configuration of the SMA device is considered: it consists of a set of two bars working in tension and compression attached to the pier and the superstructure. The design of the SMA device is performed on the Kobe earthquake record scaled to different amplitudes.

The SMA bars combined with a laminated rubber bearing can provide a damper with the desired variable characteristics based just on the material properties of the alloy. Furthermore, the proposed device has an inherent centering ability due to superelastic behaviour of SMAs.

This isolation system provides stiff connection between the pier and the deck for small external loading, while, for a medium size earthquake, the SMA bars increase the damping capacity of the isolation due to stress-induced martensitic transformation of the alloy. Moreover, for the largest considered earthquake, the SMA bars provide hysteretic damping and, in addition, act as a displacement controlling device due to the hardening of the alloy after completion of the phase transformation.

The performances of the proposed smart isolation system are also compared with the ones of a conventional isolation system consisting of a lead LRB with an additional stopper device. Numerical tests show that the damage energy of the bridge equipped with the SMA isolation system is small even if the structure input energy is large as compared to the case of the bridge isolated by LRB. It is to be also considered the possible need for additional devices to prevent long SMA bar buckling.

DesRoches and Delemont [2002] and DesRoches and Smith [2004] consider the application of SMA restrainers to a multi-span bridge. The structure studied consists of three spans supported by multi-column bents. Each bent has four columns and each span has 11 girders. The concrete slabs are supported by steel girders resisting on elastomeric bearings. The SMA restrainers (see Figure 4.4 and 4.5) are connected from the pier cap to the bottom flange of the beam in a way similar to typical cable restrainers. They are used in tension only, but they can be employed to act in both tension and compression if an adequate lateral bracing device is provided.

Obtained results show that SMA restrainers reduce relative hinge displacements at the abutment more than conventional steel cable restrainers. SMA devices are observed to

undergo large deformations while remaining elastic. Moreover, SMA superelastic properties provide energy dissipation at hinges. Finally, for particularly strong earthquakes, SMA increased stiffness at large strains gives additional restraint to limit relative openings in the bridge.

4.2.4 Experimental studies on SMA-based devices

In the following we present and discuss some interesting experimental tests carried out on structures equipped with SMA-based devices. Basically we focus our attention on smart connections (Ocel *et al.* [2004]) and brace systems for framed structures (Valente *et al.* [1999]; Dolce *et al.* [2000, 2001]; Bruno and Valente [2002]; Han *et al.* [2003]), which seem to be the most promising applications of SMAs in the field of earthquake engineering.

Ocel *et al.* [2004] study different types of partially-restrained connections, as an alternative to fully restrained welded connections, exploring the use of SMAs. The behaviour of a beam-column joint equipped with SMA tendons exhibiting the shape-memory effect is studied (see Figure 4.6). The connection consists of a W24x94 beam connected to a W14x159 column; four 381 mm long SMA tendons are threaded into anchorages designed to allow the tendons to resist load in both tension and compression. The tendons (circular 34.9 mm diameter rods) are connected to the column from the top and bottom flanges of the beam, whose anchorage includes two rectangular tubes welded on three sides with a fillet to the beam flange. The connection is tested on a specially designed shear tab at increasing cycles up to 4% drift, showing a stable and repeatable behaviour with significant energy dissipation. The SMA tendons are then reheated beyond their transformation temperature and retested, showing to be able to recover 80% of their original shape; moreover the connection presents a behaviour nearly identical to the first series of tests.

Valente *et al.* [1999], Dolce *et al.* [2000, 2001] and Bruno and Valente [2002] examine in detail the possibility of SMA-based braces for framed structures (see Figure 4.7). Because of SMA great versatility, it is possible to get different cyclic behaviours simply varying the number and the characteristics of the employed SMAs. In particular, the following three categories of devices which are designed, constructed and tested are proposed:

- *supplemental re-centering devices*: typically based only on a re-centering group, they show no residual displacements at the end of the action and the capability of providing an auxiliary re-centering force compensating possible reacting forces external to the device, such as friction of bearings (isolation systems) or plastic

forces of structural elements (bracing systems);

- *non re-centering devices*: based only on a dissipating group, they show great dissipation capabilities but large residual displacements at the end of the action;
- *re-centering devices*: based on both re-centering and dissipating groups, they show negligible residual displacements, but they cannot recover the initial configuration in the presence of reacting forces external to the device.

Also Han *et al.* [2003] study the possibility of employing SMA bracing systems.

An experimental test is performed on a two-storey steel frame equipped with eight SMA dampers. The dimensions of the structure are 2 m high, 1 m long and 0.25 m wide, and it is loaded vertically with four blocks of 20 Kg each (two per floor). Each damper consists of a SMA wire (0.75 mm diameter) connected between two steel wires (7 mm diameter). The steel wire is 582 mm long and the SMA wire is 250 mm long. The tests is mainly focused on the vibration decay history of the frame with or without SMA dampers: it turns out that the frame without dampers takes about 45 seconds to reduce its initial displacement of 50%, while it takes about 1 second when dampers are present. Finally, finite element analyses are performed to simulate both the frames with or without SMA dampers subjected to the El Centro ground motion, in order to show the capability of SMA dampers of reducing the dynamic response of the structure.

4.2.5 Applications of SMA devices for seismic retrofit of existing structures

SMA's have also been employed for the rehabilitation of monuments and historical buildings. We now discuss two of the first applications of SMA-based devices in existing structures: the retrofit of the Basilica of San Francesco in Assisi and of the bell tower of the church of San Giorgio in Trignano, two ancient constructions in Italy.

The Basilica of San Francesco in Assisi (Mazzolani and Mandara [2002]) was severely damaged during the 1997 Umbria-Marche earthquake. The main goal of the restoration consisted in pursuing a good safety level without changing too much the original structure. Hence, to reduce seismic forces in the tympanum, a connection with the roof was created by means of superelastic SMA devices (see Figure 4.8), showing different structural properties depending on horizontal force levels. In fact, for low horizontal forces they are stiff and no significant displacements are allowed, for high forces their stiffness reduces for controlled wall displacements, while for very high forces their stiffness increases preventing collapse.

As a last example, we mention the bell tower of the church of San Giorgio in Trignano (DesRoches and Smith [2004]). The ancient structure (XIV century), made of masonry, was severely damaged by the 1996 Modena and Reggio Emilia earthquake. The tower is 18.5 m high and has a square base with an edge of 3 m. It is surrounded on three edges by others buildings up to the height of 11 m. The masonry walls are 0.42 m thick close to the corners and 0.3 m in the central part. Four large windows closed using thin brick walls are present at 13 m level. Hence, the corresponding section results quite weak and in fact it broke during the seismic event. After the earthquake, the tower was rehabilitated using SMAs. Four vertical prestressing steel bars in series with SMA devices (see Figure 4.9) were placed in the internal corners of the bell tower to increase its flexural strength. The smart devices were made up of 60 wires, 1 mm in diameter and 300 mm in length, anchored at the top and bottom of the tower, with the aim of limiting the forces applied to the masonry.

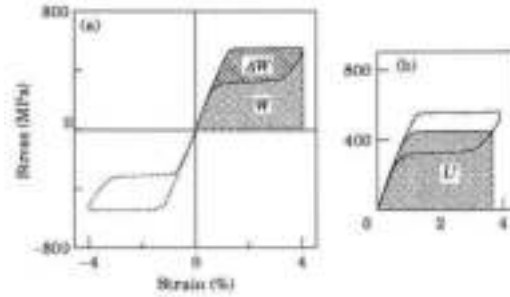


Figure 4.3. Dissipated and potential energy: superelastic effect in tension (continuous line) and in compression (dashed line). (a) ΔW and W are respectively the dissipated energy and the maximum strain energy in a tensile loading-unloading test while (b) U is the maximum potential energy in a tension-compression test (cf. Piedboeuf and Gauvin [1998]).

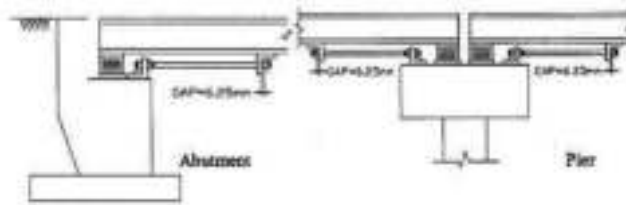


Figure 4.4. Seismic retrofit of the bridge studied by DesRoches and Delemont [2002] using superelastic restrainer cables: particular of the connection between deck and abutment and between deck and pier.

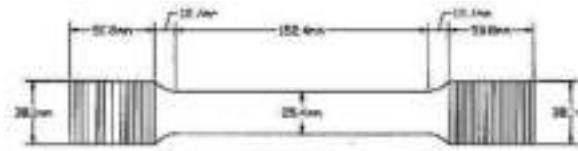


Figure 4.5. Particular of the superelastic restrainer used by DesRoches and Delemont [2002] for the seismic retrofit of bridges.



Figure 4.6. The smart beam-to-column connection studied by Ocel *et al.* [2004].

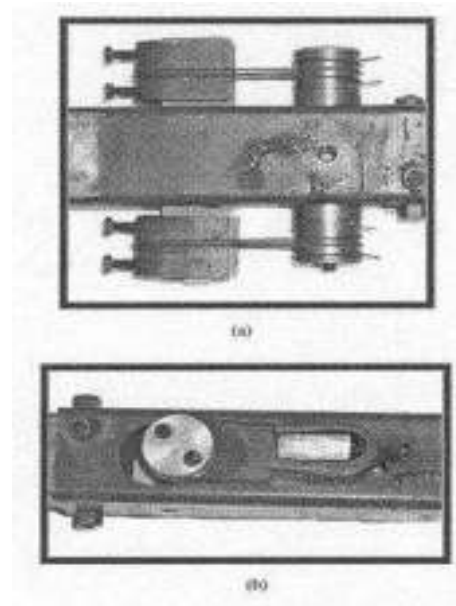
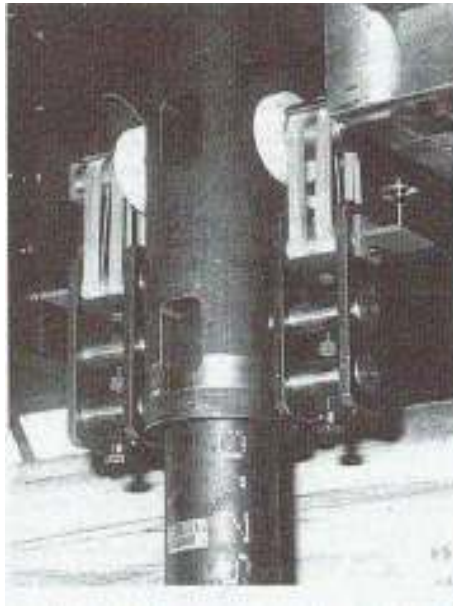


Figure 4.7. Particular of the brace systems studied by Dolce *et al.* [2000, 2001].

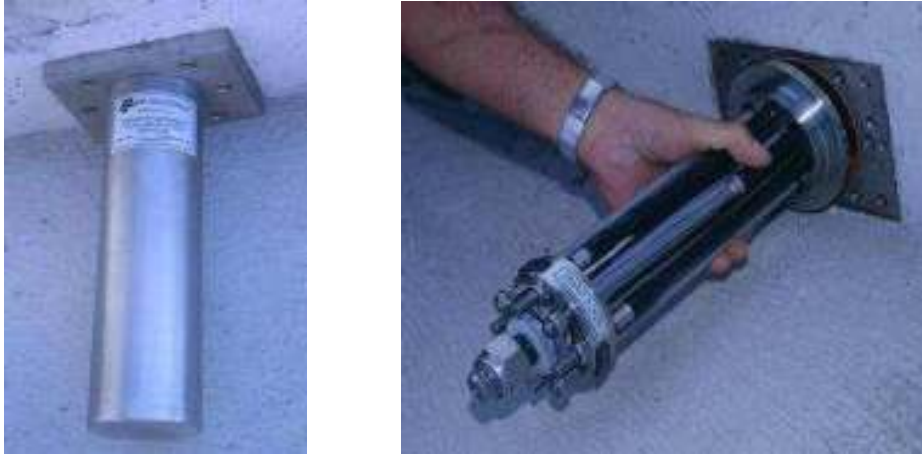


Figure 4.8. Seismic retrofit of the Basilica of San Francesco in Assisi: particular of the SMA devices.

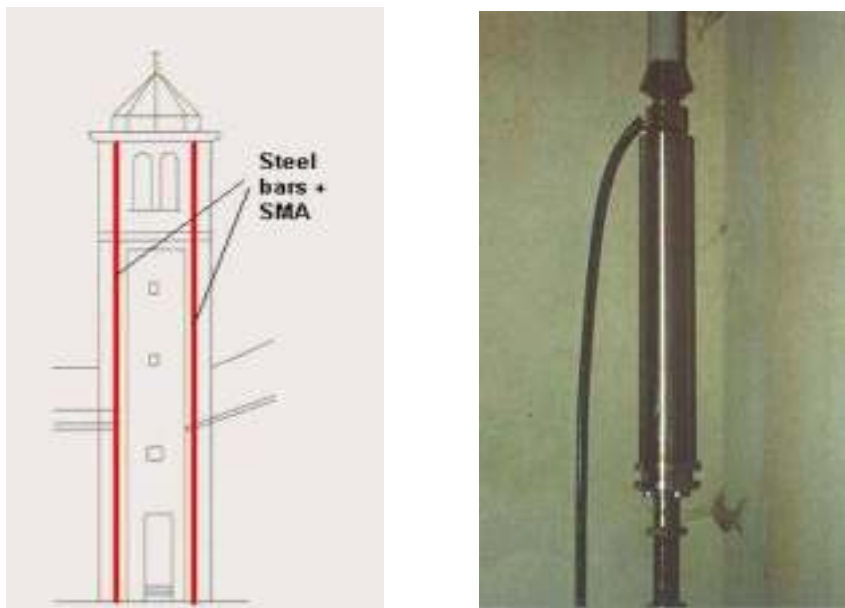


Figure 4.9. Seismic retrofit of the bell tower of the church of San Giorgio in Trignano: (left) elevation of the structure and (right) particular of the SMA rod used.

4.3 A new three-dimensional model describing stress-induced solid phase transformation with permanent inelasticity

As discussed in previous Sections, there exists a great and always increasing interest in SMA materials and their industrial applications in many branches of engineering (cf. Duerig and Pelton [2003]) which is deeply stimulating the research on constitutive laws. As a consequence, many models able to reproduce one or both of the well-known SMA macroscopic behaviours, referred to as *pseudo-elasticity* and *shape-memory effect*, have been proposed in the literature in the last years (refer for instance to Bouvet *et al.* [2004]; Govindjee and Miehe [2001]; Helm and Haupt [2003]; Lagoudas and Entchev [2004]; Leclercq and Lexcellent [1996]; Levitas [1998]; Paiva *et al.* [2005]; Peultier *et al.* [2004]; Raniecki and Lexcellent [1994]). In particular, the constitutive law proposed by Souza *et al.* [1998] and improved by Auricchio and Petrini [2004a] seems to be attractive for its features as well as for the clarity and the relative simplicity of its equations and corresponding solution algorithm. Anyway, as in many other classical models, permanent inelastic effects are not included, while experimental results show that they are not negligible. As an example, Figure 4.10 (originally reported in Arrigoni *et al.* [2001]) shows a typical experimental stress-strain response for a SMA NiTi wire subjected to an uniaxial cyclic tension test. It is remarkable that the pseudo-elastic loops show an increasing level of permanent inelasticity that saturates on a stable value after a certain number of cycles. Moreover, the same Figure highlights that also degradation effects should be taken into account.

Moving from these experimental evidences, this Section addresses a new three-dimensional phenomenological constitutive model able to reproduce pseudo-elastic and shape-memory behaviours as well as to include permanent inelasticity and degradation effects. The model consists of an extension of the model discussed in Souza *et al.* [1998] and Auricchio and Petrini [2004a], by means of the introduction of a new internal variable describing permanent inelastic strains. In this work, an analytic description of the constitutive equations is presented together with numerical experiments which show main features and performance of the model.

We remark that this model has been presented in Auricchio and Reali [2005a,b] in its one-dimensional version and in Auricchio *et al.* [2005d] in three dimensions.

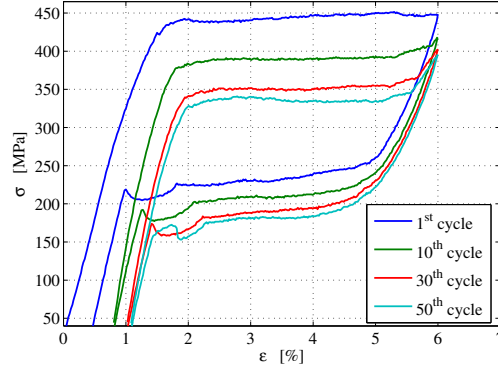


Figure 4.10. Experimental results on a SMA NiTi wire. Cyclic tension test: stress versus strain up to 6% strain.

4.3.1 3D phenomenological model for stress-induced solid phase transformation with permanent inelasticity

Starting from the SMA constitutive model addressed in Auricchio and Petrini [2004a], in this Section we describe an extended set of constitutive equations, including as a new internal variable a second-order tensor able to activate and take into account the effects of permanent inelastic strains.

4.3.1.1 Time-continuous frame.

The model assumes the total strain $\boldsymbol{\varepsilon}$ and the absolute temperature T as control variables, the transformation strain \boldsymbol{e}^{tr} and the permanent inelastic strain \boldsymbol{q} as internal ones. As in Auricchio and Petrini [2004a], the second-order tensor \boldsymbol{e}^{tr} describes the strain associated to the transformation between the two solid phases referred to as martensite and austenite. Here, this quantity has no fully reversible evolution and the permanent inelastic strain \boldsymbol{q} gives a measure of the part of \boldsymbol{e}^{tr} that cannot be recovered when unloading to a zero stress state. Moreover, we require that

$$\|\boldsymbol{e}^{tr}\| \leq \varepsilon_L, \quad (4.1)$$

where $\|\cdot\|$ is the usual Euclidean norm and ε_L is a material parameter corresponding to the maximum transformation strain reached at the end of the transformation during an uniaxial test.

Assuming a small strain regime and the standard decomposition

$$\boldsymbol{\varepsilon} = \frac{\theta}{3} \mathbf{1} + \boldsymbol{e},$$

where $\theta = \text{tr}(\boldsymbol{\varepsilon})$ and \mathbf{e} are respectively the volumetric and the deviatoric part of the total strain $\boldsymbol{\varepsilon}$, while $\mathbf{1}$ is the second-order identity tensor, the free energy density function Ψ for a polycrystalline SMA material is expressed as the convex potential

$$\begin{aligned} \Psi(\theta, \mathbf{e}, T, \mathbf{e}^{tr}, \mathbf{q}) = & \frac{1}{2}K\theta^2 + G\|\mathbf{e} - \mathbf{e}^{tr}\|^2 + \beta\langle T - M_f \rangle \|\mathbf{e}^{tr} - \mathbf{q}\| + \\ & + \frac{1}{2}h\|\mathbf{e}^{tr}\|^2 + \frac{1}{2}H\|\mathbf{q}\|^2 - A\mathbf{e}^{tr} : \mathbf{q} + \mathcal{J}_{\varepsilon_L}(\mathbf{e}^{tr}), \end{aligned} \quad (4.2)$$

where K and G are respectively the bulk and the shear modulus, β is a material parameter related to the dependence of the critical stress on the temperature, M_f is the temperature below which only martensite phase is stable, h defines the hardening of the phase transformation, H controls the saturation of the permanent inelastic strain evolution, and A is the bilinear coupling modulus between \mathbf{e}^{tr} and \mathbf{q} . Moreover, we make use of the indicator function

$$\mathcal{J}_{\varepsilon_L}(\mathbf{e}^{tr}) = \begin{cases} 0 & \text{if } \|\mathbf{e}^{tr}\| < \varepsilon_L \\ +\infty & \text{otherwise,} \end{cases}$$

in order to satisfy the transformation strain constraint (4.1); we also introduce the positive part function $\langle \cdot \rangle$, defined as

$$\langle a \rangle = \begin{cases} a & \text{if } a > 0 \\ 0 & \text{otherwise.} \end{cases}$$

We remark that in the expression of the free energy we neglect the contributions due to thermal expansion and change in temperature with respect to the reference state, since we are not interested here in a complete description of the thermomechanical coupled problem. However, the interested reader may refer to Auricchio and Petrini [2004a,b] to see how it is possible to take into account these aspects in the formulation.

Moreover, since we use only a single internal variable second-order tensor to describe phase transformations, at most it is possible to distinguish between a generic parent phase (not associated to any macroscopic strain) and a generic product phase (associated to a macroscopic strain), as in Auricchio and Petrini [2004a]. Accordingly, the model does not distinguish between the austenite and the twinned martensite, as both these phases do not produce macroscopic strain.

Starting from the free energy function Ψ and following standard arguments, we can derive

the constitutive equations

$$\left\{ \begin{array}{lll} p & = & \frac{\partial \Psi}{\partial \theta} = K\theta, \\ \mathbf{s} & = & \frac{\partial \Psi}{\partial \mathbf{e}} = 2G(\mathbf{e} - \mathbf{e}^{tr}), \\ \eta & = & -\frac{\partial \Psi}{\partial T} = -\beta \|\mathbf{e}^{tr} - \mathbf{q}\| \frac{\langle T - M_f \rangle}{|T - M_f|}, \\ \mathbf{X} & = & -\frac{\partial \Psi}{\partial \mathbf{e}^{tr}} = \mathbf{s} - \beta \langle T - M_f \rangle \frac{\mathbf{e}^{tr} - \mathbf{q}}{\|\mathbf{e}^{tr} - \mathbf{q}\|} - h\mathbf{e}^{tr} + A\mathbf{q} - \gamma \frac{\mathbf{e}^{tr}}{\|\mathbf{e}^{tr}\|}, \\ \mathbf{Q} & = & -\frac{\partial \Psi}{\partial \mathbf{q}} = \beta \langle T - M_f \rangle \frac{\mathbf{e}^{tr} - \mathbf{q}}{\|\mathbf{e}^{tr} - \mathbf{q}\|} - H\mathbf{q} + A\mathbf{e}^{tr}, \end{array} \right. \quad (4.3)$$

where $p = \text{tr}(\boldsymbol{\sigma})/3$ and \mathbf{s} are respectively the volumetric and the deviatoric part of the stress $\boldsymbol{\sigma}$, \mathbf{X} is a thermodynamic stress-like quantity associated to the transformation strain \mathbf{e}^{tr} , \mathbf{Q} is a thermodynamic stress-like quantity associated to the permanent inelastic strain \mathbf{q} , and η is the entropy. The variable γ results from the indicator function subdifferential $\partial \mathcal{I}_{\varepsilon_L}(\mathbf{e}^{tr})$ and it is defined as

$$\left\{ \begin{array}{ll} \gamma = 0 & \text{if } \|\mathbf{e}^{tr}\| < \varepsilon_L, \\ \gamma \geq 0 & \text{if } \|\mathbf{e}^{tr}\| = \varepsilon_L, \end{array} \right.$$

so that $\partial \mathcal{I}_{\varepsilon_L}(\mathbf{e}^{tr}) = \gamma \frac{\mathbf{e}^{tr}}{\|\mathbf{e}^{tr}\|}$.

To describe phase transformation and inelasticity evolution, we choose a limit function F defined as

$$F(\mathbf{X}, \mathbf{Q}) = \|\mathbf{X}\| + \kappa \|\mathbf{Q}\| - R, \quad (4.4)$$

where κ is a material parameter defining a scaling modulus between the inelastic effect and the phase transformation, while R is the radius of the elastic domain. Considering an associative framework, the flow rules for the internal variables take the form

$$\left\{ \begin{array}{lll} \dot{\mathbf{e}}^{tr} & = & \dot{\zeta} \frac{\partial F}{\partial \mathbf{X}} = \dot{\zeta} \frac{\mathbf{X}}{\|\mathbf{X}\|}, \\ \dot{\mathbf{q}} & = & \dot{\zeta} \frac{\partial F}{\partial \mathbf{Q}} = \dot{\zeta} \kappa \frac{\mathbf{Q}}{\|\mathbf{Q}\|}. \end{array} \right. \quad (4.5)$$

The model is finally completed by the classical Kuhn-Tucker conditions

$$\left\{ \begin{array}{l} \dot{\zeta} \geq 0, \\ F \leq 0, \\ \dot{\zeta} F = 0. \end{array} \right. \quad (4.6)$$

Observation 1. By exploiting basic Convex Analysis tools (see, e.g., Clarke [1990]) we can rewrite our constitutive model (4.3)-(4.6) in the equivalent form

$$\begin{pmatrix} -p \\ -\mathbf{s} \\ \eta \\ \partial D \begin{pmatrix} \mathbf{e}^{tr} \\ \dot{\mathbf{q}} \end{pmatrix} \end{pmatrix} + \partial \Psi \begin{pmatrix} \theta \\ \mathbf{e} \\ T \\ \mathbf{e}^{tr} \\ \mathbf{q} \end{pmatrix} \ni \mathbf{0}. \quad (4.7)$$

Here ∂D stands for the subdifferential of

$$\begin{aligned} D(\mathbf{e}^{tr}, \mathbf{q}) &= \sup_{F(\mathbf{a}, \mathbf{b}) \leq 0} \{ \mathbf{a} : \mathbf{e}^{tr} + \mathbf{b} : \mathbf{q} \} = \\ &= \begin{cases} \max \left\{ \frac{R\|\mathbf{q}\|}{\kappa}, R\|\mathbf{e}^{tr}\| \right\} & \text{if } \kappa \neq 0, \\ R\|\mathbf{e}^{tr}\| & \text{if } \kappa = 0 \text{ and } \|\mathbf{q}\| = 0, \\ +\infty & \text{if } \kappa = 0 \text{ and } \|\mathbf{q}\| \neq 0, \end{cases} \end{aligned} \quad (4.8)$$

which is the dissipation function associated to the phase transformation mechanism. In particular, D is the Fenchel-Legendre conjugate of the indicator function of the non-empty, convex, and closed elastic domain

$$\mathcal{E} = \{(\mathbf{e}^{tr}, \mathbf{q}) : F(\mathbf{e}^{tr}, \mathbf{q}) \leq 0\}.$$

Hence, it is easy to check that D is positively 1-homogeneous, that is

$$D(\lambda(\mathbf{e}^{tr}, \mathbf{q})) = \lambda D(\mathbf{e}^{tr}, \mathbf{q}) \quad \forall \lambda > 0.$$

Namely, the time-evolution of $(\mathbf{e}^{tr}, \mathbf{q})$ is of rate-independent type since we readily have that

$$\partial D(\lambda(\mathbf{e}^{tr}, \mathbf{q})) = \partial D(\mathbf{e}^{tr}, \mathbf{q}) \quad \forall \lambda > 0.$$

The formulation of rate-independent evolution problems in terms of a doubly-nonlinear differential inclusion as in (4.7) has recently attracted a good deal of attention. In particular, the mathematical treatment of relations as (4.7) is nowadays fairly settled and existence, uniqueness, and time-discretization results are available. The interested reader is referred to the recent survey Mielke [2005] where a comprehensive collection of mathematical results on doubly-nonlinear rate-independent problems is provided.

Observation 2. We highlight that the choice $\kappa = 0$ leads to recover the model without permanent inelasticity discussed in Auricchio and Petrini [2004a]. In fact, setting $\kappa = 0$

in (4.5)₂, we get $\dot{\mathbf{q}} = \mathbf{0}$, which means that \mathbf{q} does not evolve and is always equal to its initial value, i.e. $\mathbf{q} \equiv \mathbf{0}$.

Observation 3. We start by introducing here some considerations on the model presented in Auricchio and Petrini [2004a], which aim to explain its capability to undergo fully reversible phase transformations. Such considerations are basilar in order to understand the key idea we follow to construct the new model introduced in this Section.

We focus on the case $\beta\langle T - M_f \rangle > R$, which is indeed the most interesting, and for simplicity we start considering scalar quantities instead of second-order tensors. This is equivalent to study a proportional loading process (i.e. developed along a fixed direction) so that the scalars X , s , and e^{tr} assume the physical meaning of norm for the corresponding tensor-valued quantities. Then, we suppose to be in the condition $F = 0$, that is (recall that $\kappa = 0$)

$$|X| = \left| s - \beta\langle T - M_f \rangle \frac{e^{tr}}{|e^{tr}|} - h e^{tr} \right| = R, \quad (4.9)$$

which implies

$$s = \beta\langle T - M_f \rangle \frac{e^{tr}}{|e^{tr}|} + h e^{tr} \pm R. \quad (4.10)$$

Figure 4.11 reports the graphical representations of the relation $s = s(e^{tr})$ obtained from expressions (4.10) for the two cases of unloading from compression and unloading from tension, respectively. The Figure shows that for each case there exists an interval for s inside which $e^{tr} = 0$. Considering the intersection of the intervals for the two cases, it is possible to conclude that

$$s \in [-\beta\langle T - M_f \rangle + R, \beta\langle T - M_f \rangle - R] \Rightarrow e^{tr} = 0, \quad (4.11)$$

i.e., if s belongs to the interval $[-\beta\langle T - M_f \rangle + R, \beta\langle T - M_f \rangle - R]$, e^{tr} is necessarily equal to zero. Accordingly, this implies that, due to the continuity of the considered functions, if we are coming from a state with s outside the indicated interval and we are unloading, e^{tr} necessarily approaches zero as s approaches the extreme of such an interval.

Indeed, the very same conclusion holds also in a 3D framework. Still referring to the unloading situation, one can prove that, whenever $\|\mathbf{s}\|$ approaches $\beta\langle T - M_f \rangle - R$ and \mathbf{e}^{tr} is such that

$$\|\mathbf{X}\| = \left\| \mathbf{s} - \beta\langle T - M_f \rangle \frac{\mathbf{e}^{tr}}{\|\mathbf{e}^{tr}\|} - h \mathbf{e}^{tr} \right\| = R,$$

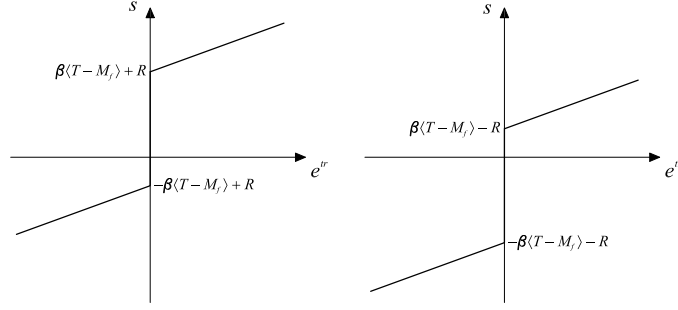


Figure 4.11. Plots of $s = s(e^{tr})$ in the cases of unloading from compression (left) and from tension (right).

then $\|e^{tr}\|$ tends to zero. A proof follows.

Assume that this is not the case. Hence, there exists $\varepsilon > 0$ such that, for all $\delta > 0$, there exist s_δ, e_δ^{tr} such that

$$\|s_\delta\| - \beta\langle T - M_f \rangle + R < \delta,$$

$$\left\| s_\delta - \beta\langle T - M_f \rangle \frac{e_\delta^{tr}}{\|e_\delta^{tr}\|} - h e_\delta^{tr} \right\| = R,$$

but

$$\|e_\delta^{tr}\| > \varepsilon.$$

Then, it suffices to choose $\delta \leq h\varepsilon$ and check that

$$\begin{aligned} -\|s_\delta\| &> -\beta\langle T - M_f \rangle + R - \delta, \\ \left\| \beta\langle T - M_f \rangle \frac{e_\delta^{tr}}{\|e_\delta^{tr}\|} + h e_\delta^{tr} \right\| &> \beta\langle T - M_f \rangle + h\varepsilon. \end{aligned}$$

Now, we take the sum of the latter relations and exploit the Lipschitz continuity of the norm in order to obtain that

$$\begin{aligned} R &< \left\| \beta\langle T - M_f \rangle \frac{e_\delta^{tr}}{\|e_\delta^{tr}\|} + h e_\delta^{tr} \right\| - \|s_\delta\| \\ &\leq \left\| s_\delta - \beta\langle T - M_f \rangle \frac{e_\delta^{tr}}{\|e_\delta^{tr}\|} - h e_\delta^{tr} \right\| = R, \end{aligned}$$

which is clearly a contradiction and proves the correctness of our thesis.

Observation 4. We now show the basic idea behind the new model proposed herein, arising from the above considerations.

Still referring to the 1D case, if we want to avoid a complete shape recovery (i.e. a fully reversible phase transformation), a simple and effective option consists in substituting the term $\beta\langle T - M_f \rangle e^{tr}/|e^{tr}|$ with the new one $\beta\langle T - M_f \rangle (e^{tr} - q)/|e^{tr} - q|$. This operation results in translating the graphs in Figure 4.11 by a quantity q , as depicted in Figure 4.12, leading to the following implication

$$s \in [-\beta\langle T - M_f \rangle + R, \beta\langle T - M_f \rangle - R] \Rightarrow e^{tr} = q. \quad (4.12)$$

Relation (4.12) means that, whenever s is approaching the extreme of the interval $[-\beta\langle T - M_f \rangle + R, \beta\langle T - M_f \rangle - R]$, e^{tr} tends to q , i.e., a permanent inelastic effect is introduced.

Analogously, in a 3D setting, substituting the term $\beta\langle T - M_f \rangle \mathbf{e}^{tr}/\|\mathbf{e}^{tr}\|$ in equation (4.9) with $\beta\langle T - M_f \rangle (\mathbf{e}^{tr} - \mathbf{q})/\|\mathbf{e}^{tr} - \mathbf{q}\|$, we obtain that, when unloading, the tensor \mathbf{e}^{tr} tends to the permanent inelastic strain tensor \mathbf{q} .

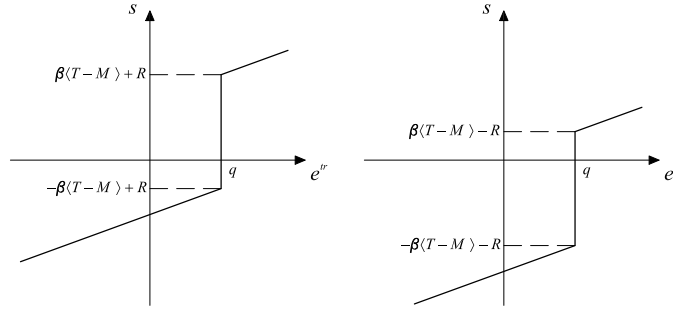


Figure 4.12. Translated plots of $s = s(e^{tr})$ in the cases of unloading from compression (left) and from tension (right).

Observation 5. The parameter κ controls the entity of the inelastic effect and its choice is not completely free. For simplicity, we show how to compute an upper bound for this parameter when $h = H = A = 0$ MPa and $\|\mathbf{e}^{tr}\| < \varepsilon_L$. Introducing these positions in equations (4.3)₄ and (4.3)₅, the constitutive equations for \mathbf{X} and \mathbf{Q} take the form

$$\begin{cases} \mathbf{X} &= s - \beta\langle T - M_f \rangle \frac{\mathbf{e}^{tr} - \mathbf{q}}{\|\mathbf{e}^{tr} - \mathbf{q}\|}, \\ \mathbf{Q} &= \beta\langle T - M_f \rangle \frac{\mathbf{e}^{tr} - \mathbf{q}}{\|\mathbf{e}^{tr} - \mathbf{q}\|}. \end{cases} \quad (4.13)$$

Now, substituting (4.13) in the limit function (4.4) and taking into account the second Kuhn-Tucker condition (4.6)₂, we get

$$F = \|\mathbf{X}\| + \kappa\beta\langle T - M_f \rangle - R \leq 0.$$

In order to satisfy this inequality, since $\|\mathbf{X}\| \geq 0$, it is necessary to have

$$\kappa\beta\langle T - M_f \rangle - R \leq 0,$$

that leads to the following upper bound for the parameter κ

$$\kappa \leq \frac{R}{\beta\langle T - M_f \rangle}.$$

Observation 6. Many experimental studies highlight that SMA materials show a permanent inelasticity which is not indefinitely evolving but saturates (see for instance Figure 4.10). In our model, in the case $T > M_f$, we can introduce such an effect by taking the parameter H different from zero. Considering for computation simplicity the case with $A = 0$ MPa, the constitutive equation for \mathbf{Q} simplifies as follows

$$\mathbf{Q} = \beta\langle T - M_f \rangle \frac{\mathbf{e}^{tr} - \mathbf{q}}{\|\mathbf{e}^{tr} - \mathbf{q}\|} - H\mathbf{q}.$$

Moreover, recalling position (4.5)₂, the evolution of \mathbf{q} necessarily stops when $\mathbf{Q} = \mathbf{0}$, that is when \mathbf{e}^{tr} and \mathbf{q} are collinear and

$$\|\mathbf{q}\| = \frac{\beta\langle T - M_f \rangle}{H}.$$

Hence, whenever the quantities β and M_f and the absolute temperature T are given, we can control the saturated value of $\|\mathbf{q}\|$ acting on the material parameter H .

In this way, if we are performing an uniaxial test, we can compute the positive and negative limit values of the scalar q as

$$q_{max}^{\pm} = \pm \sqrt{\frac{2}{3}} \frac{\beta\langle T - M_f \rangle}{H}.$$

We finally highlight that, as proved by the above equations, in the case of stable martensite phase (i.e. $T < M_f$) we cannot obtain an evolution for \mathbf{q} unless we take a value of A different from zero.

4.3.2 Time-discrete frame

Let us now focus on the crucial issue of computing the stress and internal variable evolution of a SMA sample in a strain-driven situation. We shall directly concentrate ourselves on the solution of the time-incremental problem. Namely, we discretize the time-interval of interest $[0, t_f]$ by means of the partition $I = \{0 = t_0 < t_1 < \dots < t_{N-1} < t_n = t_f\}$, assume to be given the state of the system $(p_n, s_n, \eta_n, \mathbf{e}_n^{tr}, \mathbf{q}_n)$ at time t_n , the actual total strain (θ, \mathbf{e}) and temperature T at time t_{n+1} (note that for the sake of notation simplicity here and in the following we drop the subindex $n+1$ for all the variables computed at time t_{n+1}), and solve for $(p, s, \eta, \mathbf{e}^{tr}, \mathbf{q})$. For the sake of numerical convenience, instead of solving (4.3) we prefer to perform some regularization. Indeed, we let $\overline{\|\cdot\|}$ be defined as

$$\overline{\|\mathbf{a}\|} = \sqrt{\|\mathbf{a}\|^2 + \delta} - \sqrt{\delta},$$

(δ is a user-defined parameter controlling the smoothness of the norm regularization) and introduce the regularized free energy density $\overline{\Psi}$ and limit function \overline{F} as

$$\begin{aligned} \overline{\Psi}(\theta, \mathbf{e}, T, \mathbf{e}^{tr}, \mathbf{q}) &= \frac{1}{2}K\theta^2 + G\|\mathbf{e} - \mathbf{e}^{tr}\|^2 + \beta\langle T - M_f \rangle \overline{\|\mathbf{e}^{tr} - \mathbf{q}\|} + \\ &+ \frac{1}{2}h\|\mathbf{e}^{tr}\|^2 + \frac{1}{2}H\|\mathbf{q}\|^2 - A\mathbf{e}^{tr} : \mathbf{q} + \mathcal{J}_{\varepsilon_L}(\mathbf{e}^{tr}), \end{aligned} \quad (4.14)$$

$$\overline{F}(\mathbf{X}, \mathbf{Q}) = \|\mathbf{X}\| + \kappa\overline{\|\mathbf{Q}\|} - R, \quad (4.15)$$

Finally, the updated values $(p, s, \eta, \mathbf{e}^{tr}, \mathbf{q})$ for regularized constitutive model can be computed from the following relations

$$\left\{ \begin{array}{l} p = K\theta, \\ s = 2G(\mathbf{e} - \mathbf{e}^{tr}), \\ \eta = -\beta\overline{\|\mathbf{e}^{tr} - \mathbf{q}\|} \frac{\langle T - M_f \rangle}{|T - M_f|}, \\ \mathbf{X} = \mathbf{s} - \beta\langle T - M_f \rangle \frac{\mathbf{e}^{tr} - \mathbf{q}}{\sqrt{\|\mathbf{e}^{tr} - \mathbf{q}\|^2 + \delta}} - h\mathbf{e}^{tr} + A\mathbf{q} - \gamma \frac{\mathbf{e}^{tr}}{\|\mathbf{e}^{tr}\|}, \\ \mathbf{Q} = \beta\langle T - M_f \rangle \frac{\mathbf{e}^{tr} - \mathbf{q}}{\sqrt{\|\mathbf{e}^{tr} - \mathbf{q}\|^2 + \delta}} - H\mathbf{q} + A\mathbf{e}^{tr}, \\ \mathbf{e}^{tr} = \mathbf{e}_n^{tr} + \Delta\zeta \frac{\mathbf{X}}{\|\mathbf{X}\|}, \\ \mathbf{q} = \mathbf{q}_n + \Delta\zeta \kappa \frac{\mathbf{Q}}{\sqrt{\|\mathbf{Q}\|^2 + \delta}}, \\ \overline{F} = \|\mathbf{X}\| + \kappa\overline{\|\mathbf{Q}\|} - R, \end{array} \right. \quad (4.16)$$

along with the requirements

$$\begin{cases} \gamma \geq 0, \\ \|e^{tr}\| \leq \varepsilon_L, \\ \Delta\zeta \geq 0, \quad \bar{F} \leq 0, \quad \Delta\zeta\bar{F} = 0, \end{cases} \quad (4.17)$$

where $\Delta\zeta = \zeta - \zeta_n = \int_{t_n}^{t_{n+1}} \dot{\zeta} dt$ is the time-integrated consistency parameter.

4.3.2.1 Solution algorithm.

The solution of the discrete model is performed by means of an elastic-predictor inelastic-corrector return map procedure as in classical plasticity problems (cf. Simo and Hughes [1998]). An elastic trial state is evaluated keeping frozen the internal variables, then a trial value of the limit function is computed to verify the admissibility of the trial state. If this is not verified, the step is inelastic and the evolution equations have to be integrated.

We remark that, as in Auricchio and Petrini [2004a], we distinguish two inelastic phases in our model: a non-saturated phase ($\|e^{tr}\| < \varepsilon_L$, $\gamma = 0$) and a saturated one ($\|e^{tr}\| = \varepsilon_L$, $\gamma \geq 0$). In our solution procedure we start assuming to be in a non-saturated phase, and when convergence is attained we check if our assumption is violated. If the non-saturated solution is not admissible, we search for a new solution considering saturated conditions.

For each inelastic step, we have to solve the nonlinear system constituted by equations (4.16). As our aim is to show the model behaviour without focusing on algorithmic problems, we find a solution to the nonlinear system by means of the function *fsolve* implemented in the optimization toolbox of the program MATLAB®.

Observation 7. In the same spirit of Observation 1, we shall now recast the aforementioned algorithm (4.16)-(4.17) in terms of dissipation. Exactly as above, we assume to be given the current state of the system $(p_n, s_n, \eta_n, e_n^{tr}, q_n)$ at time t_n and the actual total strain (θ, e) and temperature T at time t_{n+1} . Then, relations (4.16)-(4.17) are nothing but the Euler-Lagrange relations for the following minimum problem

$$\min_{e_*^{tr}, q_*} \{ \bar{D}(e_*^{tr} - e_n^{tr}, q_* - q_n) + \bar{\Psi}(\theta, e, \eta, e_*^{tr}, q_*) \} \quad (4.18)$$

along with positions (4.16)₁-(4.16)₃. In the latter, the regularized dissipation

$$\bar{D}(e^{tr}, q) = \sup_{\bar{F}(a,b) \leq 0} \{ a : e^{tr} + b : q \}$$

is defined as the Fenchel-Legendre conjugate of the indicator function of the regularized non-empty, convex, and closed elastic domain

$$\overline{\mathcal{E}} = \{(\mathbf{e}^{tr}, \mathbf{q}) : \overline{F}(\mathbf{e}^{tr}, \mathbf{q}) \leq 0\}.$$

The minimum problem (4.18) corresponds in this setting to the Euler method where, nevertheless, the usual incremental quotients are replaced by the weaker distance $\overline{D}(\mathbf{e}_*^{tr} - \mathbf{e}_n^{tr}, \mathbf{q}_* - \mathbf{q}_n)$.

It is beyond the purposes of this work to provide mathematical results on the above introduced minimum problem (4.18). Following reference Mielke [2005] and the upcoming contribution Auricchio *et al.* [2005c], we however stress that problem (4.18) is uniquely solvable and that the incremental solutions arising from the step-by-step solution of the minimization problem converge to a time-continuous solution of the constitutive relation as the diameter of the time partition I goes to zero. Moreover, the model is stable with respect to the regularization parameter $\delta > 0$. In particular, solutions to the incremental problem (4.18) converge to the unique minimizer of problem

$$\min_{\mathbf{e}_*^{tr}, \mathbf{q}_*} \{D(\mathbf{e}_*^{tr} - \mathbf{e}_n^{tr}, \mathbf{q}_* - \mathbf{q}_n) + \Psi(\theta, \mathbf{e}, \eta, \mathbf{e}_*^{tr}, \mathbf{q}_*)\}, \quad (4.19)$$

as δ goes to zero.

4.3.3 Numerical results

To show the model capability of reproducing the macroscopic behaviour of SMA materials, we perform a number of stress-driven numerical experiments. In all tests we consider the material properties specified in Table 4.1 and describing a NiTi alloy, where E and ν are respectively the Young's modulus and the Poisson's ratio, while all the other material constants have already been introduced in Section 2.

The investigated problems are of the following types:

- uniaxial tests,
- biaxial tests,
- combined uniaxial tests.

Uniaxial tests represent the simplest setting on which it is possible to show the main features of the model as well as to appreciate the role played by the single material parameters, while biaxial tests allow to assess the model behaviour under complex non-proportional multi-axial loading conditions. Finally, combined uniaxial tests consist of

Table 4.1. Material parameters.

parameter	value	unit
E	$5 \cdot 10^4$	MPa
ν	0.35	-
β	2	MPa K ⁻¹
M_f	223	K
h	1000	MPa
R	50	MPa
ε_L	4	%
δ	10^{-8}	-

uniaxial loops in one direction followed by uniaxial loops in an orthogonal direction and they are suited for studying the model response under a sudden loading direction change. All the numerical experiments have been performed in both the pseudo-elastic and the shape-memory regimes, but for brevity we report here only the most significative examples.

4.3.3.1 Uniaxial tests.

To begin with, we consider the following uniaxial tests in the pseudo-elastic regime

- single and multiple tension cycles with permanent inelasticity,
- multiple tension cycles followed by multiple compression cycles with saturating permanent inelasticity,
- multiple tension cycles with saturating permanent inelasticity, including degradation effect.

On the other hand, in the shape-memory regime we consider

- multiple tension cycles at $T = M_f$, each one followed by heating strain recovery.

For each experiment, we plot the output axial stress–axial strain curve. Moreover, for the tests consisting of single and multiple tension cycles with permanent inelasticity, we report also the output histories for the axial components of the internal variables (e_{11}^{tr} and q_{11}) and for the associated stress norms ($\|\mathbf{X}\|$ and $\|\mathbf{Q}\|$).

- Single and multiple tension cycles with permanent inelasticity.

The first considered uniaxial test consists in studying the response of the model under tension cycles reaching a maximum axial stress of $\sigma_{max} = 300$ MPa. The numerical experiments are performed at a temperature $T = 298$ K and using the following model parameters: $H = 0$ MPa, $A = 0$ MPa and $\kappa = 2\%$. The choice of a non-zero parameter κ gives rise to a permanent inelasticity phenomenon. The left part of Figure 4.13 and Figure 4.14 refer to a single tension cycle, while the right part of Figure 4.13 and Figure 4.15 refer to ten tension cycles. It is possible to observe the significant evolution of q_{11} , which represents the level of transformation strain that is not recovered during the unloading phase to $\sigma_{11} = 0$.

- Multiple tension cycles followed by multiple compression cycles with saturating permanent inelasticity.

The goal of this test is to show the saturation of the permanent inelasticity (see Observation 6). The experiment is performed at a temperature $T = 298$ K and using the following model parameters: $H = 1.5 \cdot 10^4$ MPa, $A = 0$ MPa and $\kappa = 2\%$. The left part of Figure 4.16 shows the response to ten tension cycles. We note that, since H is different from zero, the permanent strain saturates and does not exceed the threshold

$$\sqrt{2/3}\beta\langle T - M_f \rangle / H = \sqrt{2/3} \cdot 150 / (1.5 \cdot 10^4) = 0.816\%.$$

The right part of Figure 4.16 reports the results when fifteen compression cycles follow the tension ones. Again, we can observe that permanent inelasticity is accumulated and saturates when reaching the same threshold as in the case of tension.

- Multiple tension cycles with saturating permanent inelasticity, including degradation effect.

We now want to investigate the effect induced on the model by the parameter A coupling the two internal variables. The experiment consists in ten tension loops performed at a temperature $T = 298$ K and using the following model parameters: $H = 1.5 \cdot 10^4$ MPa, $A = 10^3$ MPa and $\kappa = 2\%$. As shown in Figure 4.17, the choice of a non-zero value for A results in shifting down the loops. This sort of degradation effect is an important feature of the model as an analogous phenomenon is observed in experimental tests (see Figure 4.10).

- Multiple tension cycles at $T = M_f$, each one followed by heating strain recovery.

The aim of this last uniaxial experiment is to study the behaviour of the model when reproducing the shape-memory effect. The input consists in ten cycles, each

one constructed as a tension loop with a maximum stress $\sigma_{max} = 150$ MPa at a temperature $T = M_f$ followed by a heating process at a constant zero stress up to a temperature of 298 K. The left part of Figure 4.18 refers to a test with $H = 0$ MPa, $A = 0$ MPa and $\kappa = 2\%$, while the right part refers to a test with $H = 1.5 \cdot 10^4$ MPa, $A = 10^3$ MPa and $\kappa = 2\%$. Both of them show that an inelastic effect is activated, so that we observe only a partial shape recovery. We finally stress that in the first case, since $A = 0$ MPa, inelasticity is activated only during the heating process.

4.3.3.2 Biaxial tests.

The goal of biaxial tests is to verify the behaviour of the model and its capability of reproducing permanent inelasticity when subjected to non-proportional multi-axial loading. Accordingly, we study the model response under the two following loading conditions

- non-proportional hourglass-shaped test,
- non-proportional square-shaped test.

For both of these numerical experiments, we report the stress input and the corresponding strain output plots.

- Non-proportional hourglass-shaped test.

The first considered biaxial test consists in a non-proportional test where σ_{11} and σ_{12} are led to $\sigma_{max} = 300$ MPa in the hourglass-shaped loading history of Figure 4.19 (left), which is repeated ten times. The experiment is performed at a temperature $T = 298$ K and using the following model parameters: $H = 1.5 \cdot 10^4$ MPa, $A = 10^3$ MPa and $\kappa = 10\%$. The numerical results, reported in terms of first and tenth cycle in Figure 4.19 (right), show that the new formulation proposed is capable of introducing and controlling permanent inelasticity effects even in non-proportional multi-axial tests.

- Non-proportional square-shaped test.

The second biaxial test consists in a square-shaped loading history, repeated ten times, where σ_{11} and σ_{22} are led to $\sigma_{max} = 300$ MPa as reported in Figure 4.20 (left). The experiment is performed at a temperature $T = 298$ K and using the following model parameters: $H = 1.5 \cdot 10^4$ MPa, $A = 10^3$ MPa and $\kappa = 10\%$. The numerical results, shown in Figure 4.20 (right), confirm the considerations from the previous test.

4.3.3.3 Combined uniaxial tests.

The last numerical experiment shows the model response under loading conditions changing in their direction of application. It consists of uniaxial tension cycles whose direction is suddenly rotated of $\pi/2$.

- Ten tension cycles in direction 1 followed by twenty tension cycles in direction 2.

This experiment is performed at a temperature $T = 298$ K and using the following model parameters: $H = 1.5 \cdot 10^4$ MPa, $A = 0$ MPa and $\kappa = 2\%$. Figure 4.21 reports the stress input and the q_{11} and q_{22} output histories, while Figure 4.22 shows the axial stress–axial strain curves for the two loading directions. The numerical results prove the capability of the model of reproducing the features shown in uniaxial tests even under multi-axial loading conditions.

4.3.4 Conclusive considerations for Section 4.3

In this Section, a new 3D constitutive model for describing the macroscopic behaviour of SMA has been proposed. With respect to the existing model considered as a starting point (cf. Souza *et al.* [1998]; Auricchio and Petrini [2004a]), this new one is able to describe SMA macroscopic behaviours taking into account also permanent inelasticity effects. Such effects can be introduced both with a saturating or a non-saturating evolution. Moreover, also degradation can be included. Many numerical experiments have been presented in order to show and assess the model performances both in uniaxial and non-proportional multi-axial problems.

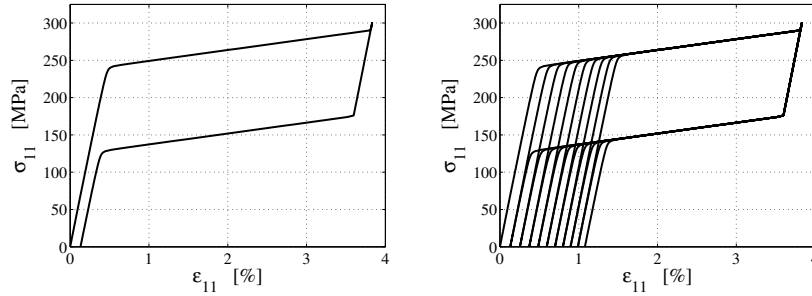


Figure 4.13. Uniaxial tests: tension cycles with permanent inelasticity ($H = 0$ MPa, $A = 0$ MPa, $\kappa = 2\%$, $T = 298$ K). Axial stress–axial strain output for single (left) and multiple (right) tension loops.

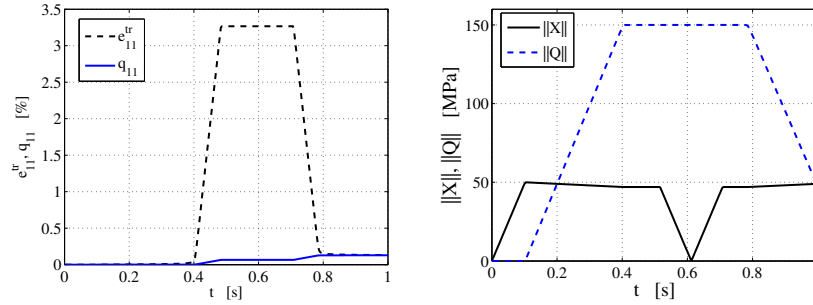


Figure 4.14. Uniaxial tests: single tension cycle with permanent inelasticity ($H = 0$ MPa, $A = 0$ MPa, $\kappa = 2\%$, $T=298K$). Output histories for e_{11}^{tr} and q_{11} (left) and $\|X\|$ and $\|Q\|$ (right).

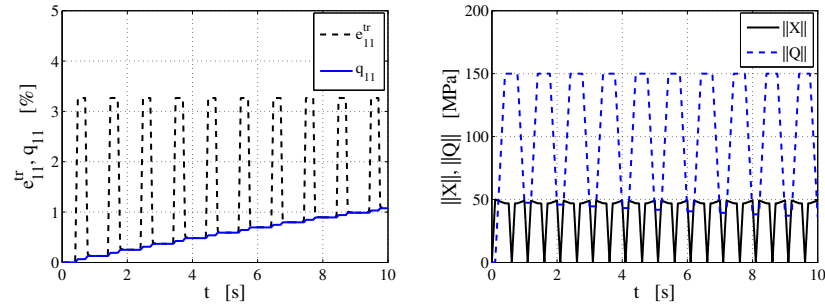


Figure 4.15. Uniaxial tests: ten tension cycles with permanent inelasticity ($H = 0$ MPa, $A = 0$ MPa, $\kappa = 2\%$, $T=298K$). Output histories for e_{11}^{tr} and q_{11} (left) and $\|X\|$ and $\|Q\|$ (right).

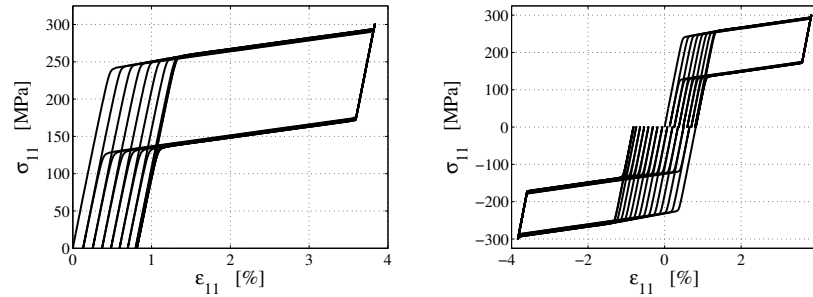


Figure 4.16. Uniaxial tests: ten tension cycles (left) and ten tension followed by fifteen compression cycles (right) with saturating permanent inelasticity ($H = 1.5 \cdot 10^4$ MPa, $A = 0$ MPa, $\kappa = 2\%$, $T=298K$). Axial stress–axial strain output.

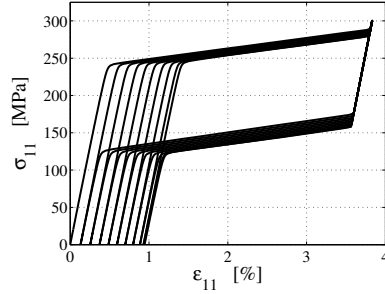


Figure 4.17. Uniaxial tests: ten tension cycles with saturating permanent inelasticity, including degradation effect ($H = 1.5 \cdot 10^4$ MPa, $A = 10^3$ MPa, $\kappa = 2\%$, $T = 298$ K). Axial stress–axial strain output.

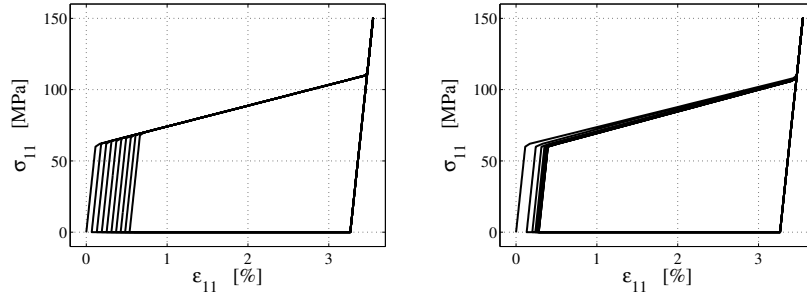


Figure 4.18. Uniaxial tests: multiple (ten) tension cycles at $T = M_f$, each one followed by heating strain recovery, with $H = 0$ MPa, $A = 0$ MPa (left) and $H = 1.5 \cdot 10^4$ MPa, $A = 10^3$ MPa (right) and $\kappa = 2\%$. Axial stress–axial strain output.

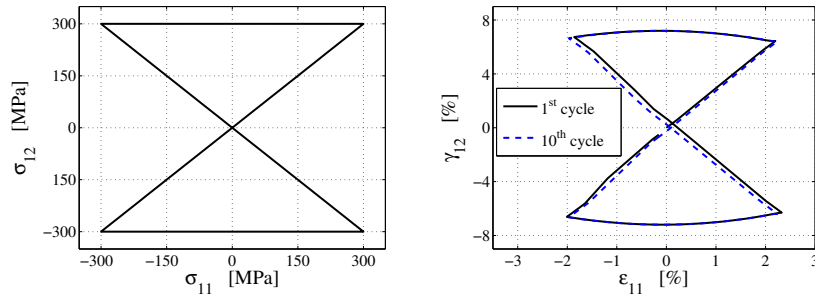


Figure 4.19. Biaxial tests: non-proportional hourglass-shaped test ($H = 1.5 \cdot 10^4$ MPa, $A = 10^3$ MPa, $\kappa = 10\%$, $T = 298$ K). $\sigma_{11} - \sigma_{12}$ input (left) and 1^{st} and 10^{th} cycle $\varepsilon_{11} - \gamma_{12}$ output (right).

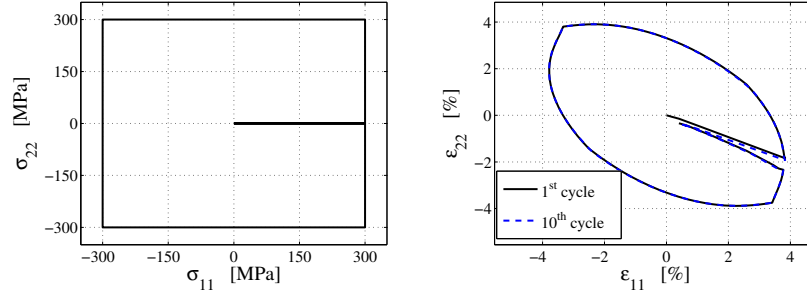


Figure 4.20. Biaxial tests: non-proportional square-shaped test ($H = 1.5 \cdot 10^4$ MPa, $A = 10^3$ MPa, $\kappa = 10\%$, $T = 298$ K). $\sigma_{11} - \sigma_{22}$ input (left) and 1st and 10th cycle $\varepsilon_{11} - \varepsilon_{22}$ output (right).

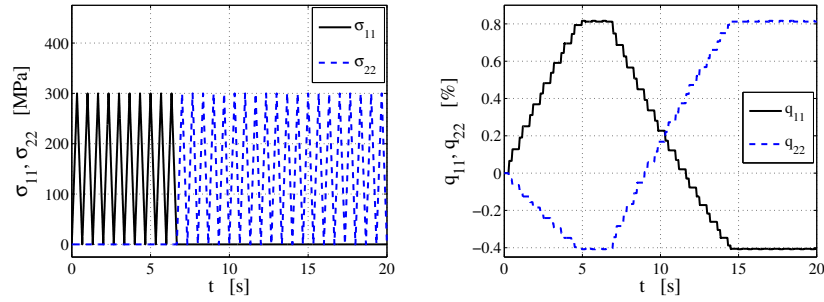


Figure 4.21. Combined uniaxial tests: ten tension cycles in direction 1 followed by twenty in direction 2 ($H = 1.5 \cdot 10^4$ MPa, $A = 0$ MPa, $\kappa = 2\%$, $T = 298$ K). Stress input histories (left) and q_{11} and q_{22} output histories (right).

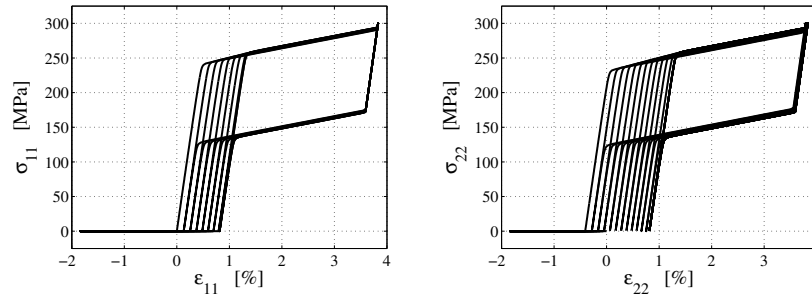


Figure 4.22. Combined uniaxial tests: ten tension cycles in direction 1 followed by twenty in direction 2 ($H = 1.5 \cdot 10^4$ MPa, $A = 0$ MPa, $\kappa = 2\%$, $T = 298$ K). $\sigma_{11} - \varepsilon_{11}$ output (left) and $\sigma_{22} - \varepsilon_{22}$ output (right).

5. MIXED-ENHANCED STRAIN TECHNIQUES FOR THE STUDY OF INCOMPRESSIBILITY AND GEOMETRIC NONLINEARITIES

As previously seen in Chapter 2, the study of incompressible and nearly incompressible materials as well as of geometrically nonlinear structural problems is an important issue for some earthquake engineering applications. In this Chapter, we explore the possibility of exploiting *mixed-enhanced* finite element methods in order to study both linear and nonlinear incompressible problems.

The present Chapter is divided into two Sections.

The first one consists of a brief state-of-the-art of the Enhanced Strain method, followed by an analysis of some mixed-enhanced elements for plane linear elasticity problems in the cases of compressible, nearly incompressible and incompressible materials. Both theoretical and numerical results are presented (while mathematical proofs are reported in Appendix B), showing the approximation and convergence properties of the investigated formulations. We remark that the results herein have been presented in Auricchio *et al.* [2004, 2005a].

The second Section deals with the applications of mixed (and in particular mixed-enhanced) finite elements to the study of plane geometrically nonlinear elasticity problems for incompressible materials. We consider a two-dimensional model problem for which it is possible to compute the solution in closed form as well as to provide some indications on the stability of both the continuum and the discrete problems. Mixed and mixed-enhanced formulations are then studied and theoretical considerations are validated through numerical experiments (again, mathematical proofs are reported in Appendix B). This piece of research has been presented in Auricchio *et al.* [2004, 2005b]. We finally remark that the theory reported in this Chapter has been developed, for simplicity, with reference to two dimensional problems; however, from a conceptual point of view, extension to three-dimensions should not introduce more efforts than mere notation difficulties.

5.1 An analysis of some mixed-enhanced finite elements for plane linear elasticity

In this Section we study some *Enhanced Strain* finite element methods for compressible, nearly incompressible and incompressible linear elasticity problems. Introduced by Simo and Rifai [1990], the enhanced strain technique, essentially consists in augmenting the space of discrete strains with local functions, which may not derive from admissible displacements. A suitable choice of these additional modes can improve the numerical performance of low-order elements and, more importantly, it can greatly alleviate the well-known *volumetric locking* phenomenon in the nearly incompressible regime.

Several theoretical contributions about the enhanced strain technique are nowadays available in the literature. The first one is probably the work by Reddy and Simo [1995], where *a priori* error estimates have been developed starting from the Hu-Washizu variational principle. Braess [1998] provided an extensive study concerning the effect of the strain enhancement on the resulting stiffness matrix. This analysis has been improved in Braess *et al.* [2004], where λ -uniform error estimates for the displacement field have been established. However, uniform error estimates for the volumetric part of the stress field could not be obtained, since the corresponding *mixed* method does not satisfy the *inf-sup* condition (cf. Brezzi and Fortin [1991]). Pantuso and Bathe [1995] applied the enhanced strain philosophy in the framework of the displacement/pressure formulation for elasticity problems (cf. e.g. Brezzi and Fortin [1991]; Bathe [1996]; Hughes [2000]). They proposed a four-noded quadrilateral element which indeed satisfies the *inf-sup* condition, thus leading to an optimally convergent method, as theoretically proved by Lovadina [1997].

It is interesting to notice that most of the schemes taking advantage of the enhanced strain technique have been designed in connection with *quadrilateral* elements. This because, when *displacement-based* (low-order) triangular elements are considered, the additional strain degrees of freedom do not provide any improvement, as highlighted by Reddy and Simo [1995]. On the other hand (cf. Lovadina and Auricchio [2003]), the mixed *displacement/pressure* formulation opens the possibility to select effective *triangular* enhanced strain modes. We also wish to remark that triangular enhanced strains have already been used by Piltner and Taylor [2000] for a low-order element with rotational degrees of freedom.

The main aim of this Section is to investigate on the numerical performance of the triangular mixed-enhanced methods briefly presented by Lovadina and Auricchio [2003]. We also develop a general theoretical analysis which can be considered as an extension of

the results presented by Lovadina [1997]; in particular, we provide optimal uniform error bounds both for the natural norms (H^1 for the displacements and L^2 for the pressure), and for the L^2 -norm of the displacements.

The structure of the discussion is as follows. In Section 5.1.1 we recall the mixed displacement/pressure formulation for the deformation problem of a linearly elastic body, together with its discretization by means of the enhanced strain technique. In Section 5.1.2 we develop our stability and convergence analysis, while in Section 5.1.3 we show that two examples of triangular elements, briefly presented by Lovadina and Auricchio [2003], actually fall into the framework of our theory. Finally, in Section 5.1.4 we develop extensive and significant numerical tests, showing the computational performance of our elements. In particular, we show the accordance of the numerical results with the theoretical predictions by means of two incompressible elasticity problems for which the analytical solution is known.

We remark that we use here standard notations, especially for Sobolev norms and seminorms (cf. e.g. Ciarlet [1978]; Brezzi and Fortin [1991]).

5.1.1 The linear elasticity problem

We consider the plane linear elasticity problem in the framework of the infinitesimal theory (cf. Bathe [1996]) for a homogeneous isotropic material. Within the several possible formulations of the problem we adopt the *mixed* displacement/pressure formulation (cf. Brezzi and Fortin [1991]; Bathe [1996]; Hughes [2000], for instance). If the elastic body occupies a regular region Ω in \mathbf{R}^2 with boundary $\partial\Omega$, we are therefore led to solve the following boundary-value problem:

Find (\mathbf{u}, p) such that

$$\left\{ \begin{array}{ll} -\mathbf{div} (2\mu \boldsymbol{\varepsilon}(\mathbf{u}) + p \boldsymbol{\delta}) = \mathbf{f} & \text{in } \Omega \\ \mathbf{div} \mathbf{u} - \lambda^{-1} p = 0 & \text{in } \Omega \\ \mathbf{u} = \mathbf{0} & \text{on } \partial\Omega . \end{array} \right. \quad (5.1)$$

where $\mathbf{u} = (u_1, u_2) : \Omega \rightarrow \mathbf{R}^2$ is the displacement field, $p : \Omega \rightarrow \mathbf{R}$ is the pressure field and $\mathbf{f} = (f_1, f_2) : \Omega \rightarrow \mathbf{R}^2$ is the loading term. Moreover, $\boldsymbol{\varepsilon}(\cdot)$ is the usual symmetric gradient operator acting on vector fields, while $\boldsymbol{\delta}$ is the second-order identity tensor. Finally, μ and λ are the Lamé coefficients, for which we suppose that $0 < \mu_0 \leq \mu \leq \mu_1 < +\infty$ and $0 < \lambda_0 \leq \lambda \leq +\infty$. We notice that $\lambda = +\infty$ (and therefore $\lambda^{-1} = 0$ in (5.1))

refers to the case of an incompressible material.

Remark 5.1.1. For simplicity, we consider only homogeneous boundary conditions for the displacement field along the whole $\partial\Omega$, but most of the subsequent results can be extended to other more realistic situations.

A standard variational formulation of problem (5.1) consists in finding $(\mathbf{u}, p) \in V \times P = (H_0^1(\Omega))^2 \times L^2(\Omega)/\mathbf{R}$ which solves the system

$$\begin{cases} 2\mu \int_{\Omega} \varepsilon(\mathbf{u}) : \varepsilon(\mathbf{v}) + \int_{\Omega} p \operatorname{div} \mathbf{v} = \int_{\Omega} \mathbf{f} \cdot \mathbf{v} & \forall \mathbf{v} \in V \\ \int_{\Omega} q \operatorname{div} \mathbf{u} - \lambda^{-1} \int_{\Omega} pq = 0 & \forall q \in P . \end{cases} \quad (5.2)$$

Remark 5.1.2. In the case of homogeneous Dirichlet boundary conditions for \mathbf{u} on the whole $\partial\Omega$, we work with the space $P = L^2(\Omega)/\mathbf{R} = \left\{ q \in L^2(\Omega) : \int_{\Omega} q = 0 \right\}$ because, from (5.1) we get

$$\int_{\Omega} p = \lambda \int_{\Omega} \operatorname{div} \mathbf{u} = \lambda \int_{\partial\Omega} \mathbf{u} \cdot \mathbf{n} = 0 .$$

Therefore, for every choice of \mathbf{f} and λ , the pressure solution p is always in P .

It is well-known that problem (5.2) is well-posed and it fits into the theory extensively studied in Brezzi and Fortin [1991], for instance. We recall that the nearly incompressible case, we mainly focus on, corresponds to λ “very large” compared to μ . We also notice that in the incompressible *limit* $\lambda \rightarrow \infty$, formulation (5.2) does not degenerate, leading to the following Stokes-like problem:

Find $(\mathbf{u}_0, p_0) \in V \times P$ such that

$$\begin{cases} 2\mu \int_{\Omega} \varepsilon(\mathbf{u}_0) : \varepsilon(\mathbf{v}) + \int_{\Omega} p_0 \operatorname{div} \mathbf{v} = \int_{\Omega} \mathbf{f} \cdot \mathbf{v} & \forall \mathbf{v} \in V \\ \int_{\Omega} q \operatorname{div} \mathbf{u}_0 = 0 & \forall q \in P . \end{cases} \quad (5.3)$$

5.1.1.1 Enhanced strain discretization.

It is now well-established (cf. Brezzi and Fortin [1991]; Bathe [1996]) that the finite element analysis of problem (5.2) requires some care in the case of nearly incompressible materials. This fact is highlighted by the *limit* situation (5.3), where the divergence-free

constraint imposes a suitable choice of the discretization spaces, in order to overcome the so-called *volume locking phenomenon*. Several methods have been proposed, analyzed and proved to be efficient in actual computations (cf. Brezzi and Fortin [1991]; Bathe [1996]; Hughes [2000] and the references therein). Among them, there are the ones based on the *Enhanced Strain Technique*, whose basic idea is briefly recalled below.

As usual, given a regular (triangular or quadrilateral) mesh \mathcal{T}_h of Ω , h being the mesh-size, we choose a finite element space $V_h \subset V$ for the approximation of the displacements, and a finite element space $P_h \subset P$ for the pressure field. A *conforming* mixed method is thus given by the discrete problem

find $(\mathbf{u}_h, p_h) \in V_h \times P_h$ such that

$$\begin{cases} 2\mu \int_{\Omega} \boldsymbol{\varepsilon}(\mathbf{u}_h) : \boldsymbol{\varepsilon}(\mathbf{v}_h) + \int_{\Omega} p_h \operatorname{div} \mathbf{v}_h = \int_{\Omega} \mathbf{f} \cdot \mathbf{v}_h & \forall \mathbf{v}_h \in V_h \\ \int_{\Omega} q_h \operatorname{div} \mathbf{u}_h - \lambda^{-1} \int_{\Omega} p_h q_h = 0 & \forall q_h \in P_h . \end{cases} \quad (5.4)$$

An *Enhanced Strain Method* in this mixed context can be seen as a *nonconforming and inconsistent* scheme (cf. Lovadina [1997]), for which the strains arising from the displacements are “enriched” by means of some additional modes. Therefore, we are led to introduce a further finite element space E_h of symmetric tensors, and we solve the problem

find $(\mathbf{u}_h, \tilde{\boldsymbol{\varepsilon}}_h, p_h) \in V_h \times E_h \times P_h$ such that

$$\begin{cases} 2\mu \int_{\Omega} (\boldsymbol{\varepsilon}(\mathbf{u}_h) + \tilde{\boldsymbol{\varepsilon}}_h) : (\boldsymbol{\varepsilon}(\mathbf{v}_h) + \tilde{\boldsymbol{\tau}}_h) + \int_{\Omega} p_h (\operatorname{div} \mathbf{v}_h + \operatorname{tr} \tilde{\boldsymbol{\tau}}_h) = \int_{\Omega} \mathbf{f} \cdot \mathbf{v}_h \\ \int_{\Omega} q_h (\operatorname{div} \mathbf{u}_h + \operatorname{tr} \tilde{\boldsymbol{\varepsilon}}_h) - \lambda^{-1} \int_{\Omega} p_h q_h = 0 \end{cases} \quad (5.5)$$

for every $(\mathbf{v}_h, \tilde{\boldsymbol{\tau}}_h) \in V_h \times E_h$ and for every $q_h \in P_h$. Above and in the sequel, we denote with “tr” the trace operator acting on tensors. The space E_h of strain enhancement typically consists of functions for which *no continuity* is required across the mesh elements. As a consequence, a static condensation procedure can be performed at the element level, so that the introduction of these additional degrees of freedom does not severely increase the computational costs. More importantly, the enhanced strains can improve the stability of the method at hand, leading to a *robust scheme* with respect to the choice of the material parameter λ . Therefore, the resulting element can be successfully applied to both compressible and incompressible case.

The inconsistency of the scheme is clearly seen by inserting the *analytical* solution (\mathbf{u}, p) of problem (5.2) into (5.5). As the *analytical* strain enhancement is obviously $\mathbf{0}$, we have that $(\mathbf{u}, \mathbf{0}, p)$ fails to satisfy the first equation of (5.5), because

$$2\mu \int_{\Omega} \varepsilon(\mathbf{u}) : \tilde{\boldsymbol{\tau}}_h + \int_{\Omega} p \operatorname{tr} \tilde{\boldsymbol{\tau}}_h = 0 \quad \forall \tilde{\boldsymbol{\tau}}_h \in E_h \quad (5.6)$$

does not generally hold true. This drawback can be overcome by suitably choosing the space E_h , as detailed in the next Section.

5.1.2 Error analysis

In this Section we present an analysis for the methods based on the enhanced strain technique. Since the stability estimate of Proposition 5.1.3 and the error bound of Theorem 5.1.4 have been already established by Lovadina [1997] for the incompressible limit case, we only sketch the proofs (see Appendix B), for the sake of completeness. However, in subsection 5.1.2.1 we develop L^2 -norm displacement error estimates, which, to our best knowledge, have not explicitly appeared in the existing literature for the enhanced strain technique.

Before proceeding, we introduce in $V_h \times E_h$ the following norm

$$\|(\mathbf{v}_h, \tilde{\boldsymbol{\tau}}_h)\| = \left(|\varepsilon(\mathbf{v}_h)|_0^2 + |\tilde{\boldsymbol{\tau}}_h|_0^2 \right)^{1/2}. \quad (5.7)$$

Moreover, we endow $V_h \times E_h \times P_h$ with the norm

$$\|(\mathbf{v}_h, \tilde{\boldsymbol{\tau}}_h, q_h)\| := \left(\|(\mathbf{v}_h, \tilde{\boldsymbol{\tau}}_h)\|^2 + |q_h|_0^2 \right)^{1/2}. \quad (5.8)$$

We finally introduce the notation

$$b_h(\mathbf{v}_h, \tilde{\boldsymbol{\tau}}_h; q_h) := \int_{\Omega} q_h (\operatorname{div} \mathbf{v}_h + \operatorname{tr} \tilde{\boldsymbol{\tau}}_h), \quad (5.9)$$

for every $(\mathbf{v}_h, \tilde{\boldsymbol{\tau}}_h) \in V_h \times E_h$ and $q_h \in P_h$.

The basic assumptions we make on the choice of the discretization spaces V_h , E_h and P_h are the following (cf. Lovadina [1997] and also Reddy and Simo [1995]).

- *The discrete inf-sup condition:* there exists a positive constant β , independent of h , such that

$$\inf_{q_h \in P_h} \sup_{(\mathbf{v}_h, \tilde{\boldsymbol{\tau}}_h) \in V_h \times E_h} \frac{b_h(\mathbf{v}_h, \tilde{\boldsymbol{\tau}}_h; q_h)}{\|(\mathbf{v}_h, \tilde{\boldsymbol{\tau}}_h)\| |q_h|_0} \geq \beta. \quad (5.10)$$

- *The minimum angle condition:* there exists a constant $\theta < 1$, independent of h , such that

$$\sup_{(\mathbf{v}_h, \tilde{\boldsymbol{\tau}}_h) \in V_h \times E_h} \frac{\int_{\Omega} \boldsymbol{\varepsilon}(\mathbf{v}_h) : \tilde{\boldsymbol{\tau}}_h}{|\boldsymbol{\varepsilon}(\mathbf{v}_h)|_0 |\tilde{\boldsymbol{\tau}}_h|_0} \leq \theta . \quad (5.11)$$

This condition implies, in particular, that $\boldsymbol{\varepsilon}(V_h) \cap E_h = (0)$. Moreover, the spaces $\boldsymbol{\varepsilon}(V_h)$ and E_h “stays far from being parallel” uniformly in h . We remark that condition (5.11) has been recognized to be crucial for the analysis of enhanced strain methods also by Braess [1998].

- *The approximation property:* there exists an integer $k \geq 1$ such that for $\mathbf{v} \in H^{k+1}(\Omega)^2$ and $q \in H^k(\Omega)$, it holds

$$\inf_{\mathbf{v}_h \in V_h} \|\mathbf{v} - \mathbf{v}_h\|_1 + \inf_{q_h \in P_h} |q - q_h|_0 \leq Ch^k (|\mathbf{v}|_{k+1} + |q|_k) . \quad (5.12)$$

Obviously, this condition is fulfilled by the standard (triangular or quadrilateral) finite element space of order k (see Ciarlet [1978]).

- *The consistency condition:* in each element the enhanced strain modes should be L^2 -orthogonal to the polynomials of order up to $k-1$, i.e. for every $K \in \mathcal{T}_h$

$$\int_K \tilde{\boldsymbol{\tau}}_h : \mathbf{p}_{k-1} = 0 \quad \forall \tilde{\boldsymbol{\tau}}_h \in E_h , \quad \forall \mathbf{p}_{k-1} \in \mathcal{P}_{k-1}(K)_s^4 . \quad (5.13)$$

This condition allows to control the consistency error arising from the introduction of the space E_h (cf. (5.6)).

For the sake of notational simplicity, in the sequel we will denote with (\cdot, \cdot) the usual inner product in L^2 . Moreover, we introduce the bilinear form $\mathcal{A}_h(\cdot, \cdot, \cdot; \cdot, \cdot, \cdot)$ on $V_h \times E_h \times P_h$ by setting

$$\begin{aligned} \mathcal{A}_h(\mathbf{v}_h, \tilde{\boldsymbol{\tau}}_h, q_h; \mathbf{w}_h, \tilde{\boldsymbol{\sigma}}_h, r_h) &:= 2\mu \left(\boldsymbol{\varepsilon}(\mathbf{v}_h) + \tilde{\boldsymbol{\tau}}_h, \boldsymbol{\varepsilon}(\mathbf{w}_h) + \tilde{\boldsymbol{\sigma}}_h \right) \\ &+ b_h(\mathbf{w}_h, \tilde{\boldsymbol{\sigma}}_h; q_h) - b_h(\mathbf{v}_h, \tilde{\boldsymbol{\tau}}_h; r_h) + \lambda^{-1}(q_h, r_h) , \end{aligned} \quad (5.14)$$

for any $(\mathbf{v}_h, \tilde{\boldsymbol{\tau}}_h, q_h)$ and $(\mathbf{w}_h, \tilde{\boldsymbol{\sigma}}_h, r_h)$ in $V_h \times E_h \times P_h$. The discrete scheme can thus be written as

find $(\mathbf{u}_h, \tilde{\boldsymbol{\varepsilon}}_h, p_h) \in V_h \times E_h \times P_h$ such that

$$\mathcal{A}_h(\mathbf{u}_h, \tilde{\boldsymbol{\varepsilon}}_h, p_h; \mathbf{v}_h, \tilde{\boldsymbol{\tau}}_h, q_h) = (\mathbf{f}, \mathbf{v}_h) \quad \forall (\mathbf{v}_h, \tilde{\boldsymbol{\tau}}_h, q_h) \in V_h \times E_h \times P_h . \quad (5.15)$$

We have the following stability result.

Proposition 5.1.3. Provided that (5.10) and (5.11) hold, for each $(\mathbf{v}_h, \tilde{\boldsymbol{\tau}}_h, q_h) \in V_h \times E_h \times P_h$ there exists $(\mathbf{w}_h, \tilde{\boldsymbol{\sigma}}_h, r_h) \in V_h \times E_h \times P_h$ such that

$$\|(\mathbf{w}_h, \tilde{\boldsymbol{\sigma}}_h, r_h)\| \leq c_1 \|(\mathbf{v}_h, \tilde{\boldsymbol{\tau}}_h, q_h)\|, \quad (5.16)$$

$$\mathcal{A}_h(\mathbf{v}_h, \tilde{\boldsymbol{\tau}}_h, q_h; \mathbf{w}_h, \tilde{\boldsymbol{\sigma}}_h, r_h) \geq c_2 \|(\mathbf{v}_h, \tilde{\boldsymbol{\tau}}_h, q_h)\|^2, \quad (5.17)$$

with c_1 and c_2 constants independent of h and λ .

The proof for this Proposition is reported in Appendix B.

We remark that in the stability result of Proposition 5.1.3, implying in particular existence and uniqueness of problem (5.5), the consistency condition (5.13) does not appear. It however comes into play in the following error estimate.

Theorem 5.1.4. Assume that conditions (5.10)–(5.13) hold true. Let $(\mathbf{u}, p) \in V \times P$ be the solution of problem (5.2) and suppose that

$$\|\mathbf{u}\|_{k+1} + \|p\|_k \leq C, \quad (5.18)$$

with C constant independent of λ . Let $(\mathbf{u}_h, \tilde{\boldsymbol{\varepsilon}}_h, p_h) \in V_h \times E_h \times P_h$ be the solution of the discrete problem (5.5). Then it holds

$$\|\mathbf{u} - \mathbf{u}_h\|_1 + |\tilde{\boldsymbol{\varepsilon}}_h|_0 + |p - p_h|_0 \leq Ch^k, \quad (5.19)$$

with C constant independent of λ .

The proof for this Theorem is reported in Appendix B.

Remark 5.1.5. We notice that the last two terms in equation (B.9) of the proof (see Appendix B) arise from the inconsistency of the enhanced strain Technique (cf. (5.6)). These extra terms are however under control by assumption (5.13), as highlighted by (B.10) and (B.11).

5.1.2.1 L^2 -error estimates.

We now prove an L^2 -error estimate for the displacement field. We recall that Theorem 5.1.4 gives

$$\|\mathbf{u} - \mathbf{u}_h\|_1 + |\tilde{\boldsymbol{\varepsilon}}_h|_0 + |p - p_h|_0 \leq Ch^k. \quad (5.20)$$

In this situation we show that the displacement error in L^2 -norm is $O(h^{k+1})$, provided the problem is regular. More precisely, we assume that for the solution of the problem

find $(\varphi, s) \in V \times P$ such that

$$\begin{cases} 2\mu \left(\varepsilon(\mathbf{v}), \varepsilon(\varphi) \right) + (s, \operatorname{div} \mathbf{v}) = (\gamma, \mathbf{v}) & \forall \mathbf{v} \in V \\ (q, \operatorname{div} \varphi) - \lambda^{-1}(q, s) = 0 & \forall q \in P, \end{cases} \quad (5.21)$$

the regularity result

$$\|\varphi\|_2 + \|s\|_1 \leq C|\gamma|_0 \quad (5.22)$$

holds true for every $\gamma \in L^2(\Omega)^2$.

Remark 5.1.6. The regularity estimate (5.22) holds whenever Ω is a smooth domain, as proved by Vogelius [1983]. In the case of zero boundary conditions for the displacements on the whole boundary $\partial\Omega$, this result still holds when Ω is a convex polygon (cf. Brenner and Sung [1992]).

Proposition 5.1.7. Assume that conditions (5.10)–(5.13) are fulfilled. Moreover, assume (5.12) and the regularity estimate (5.22) for problem (5.21). Then we have the error bound

$$\|\mathbf{u} - \mathbf{u}_h\|_0 \leq Ch^{k+1}, \quad (5.23)$$

with C constant independent of λ .

The proof for this Proposition is reported in Appendix B.

5.1.3 Examples of triangular elements

In this Section we introduce two sets of (first order) enhanced strains to be used in connection with *triangular* elements, already presented and briefly analyzed by Lovadina and Auricchio [2003]. We thus suppose to have a regular triangular mesh \mathcal{T}_h of Ω . The schemes we are going to present are both based on the following choice of spaces

- for the displacement discretization we take

$$V_h = \{v_h \in V : v_h|_T \in \mathcal{P}_1(T) \quad \forall T \in \mathcal{T}_h\}, \quad (5.24)$$

where $\mathcal{P}_1(T)$ is the space of linear functions defined on T ;

- for the pressure interpolation, we set

$$P_h = \{q_h \in H^1(\Omega) : q_h|_T \in \mathcal{P}_1(T) \quad \forall T \in \mathcal{T}_h\} . \quad (5.25)$$

We notice that, as for the element by Pantuso and Bathe [1995], the discrete pressure field is *continuous* across adjacent elements. Before introducing the two sets of enhanced strains, we first define a global Cartesian system of coordinates (x, y) in Ω . Furthermore, for each triangle $T \in \mathcal{T}_h$, let (x_T, y_T) be the coordinates of its barycenter, and define on T a *local* Cartesian system of coordinates by simply setting

$$\bar{x} = x - x_T , \quad \bar{y} = y - y_T . \quad (5.26)$$

We are now ready to present our strain enhancements.

- **First set.** We take

$$E_h^1 = \{\tilde{\boldsymbol{\tau}}_h \in (L^2(\Omega))_s^4 : \tilde{\boldsymbol{\tau}}_h|_T \in E_4^1(T) \quad \forall T \in \mathcal{T}_h\} , \quad (5.27)$$

where $E_4^1(T)$ is the space of tensor-valued functions defined on T , spanned by the following shape functions (cf. (5.26))

$$\begin{bmatrix} \alpha_1 \bar{x} + \alpha_2 \bar{y} & ; & (\alpha_2 - \alpha_4) \bar{x} + (\alpha_3 - \alpha_1) \bar{y} \\ \text{symm.} & ; & \alpha_3 \bar{x} + \alpha_4 \bar{y} \end{bmatrix} \quad \text{with } \alpha_i \in \mathbf{R} . \quad (5.28)$$

We remark that the enhanced strain modes described in (5.28) have already been used by Piltner and Taylor [2000].

- **Second set.** We take

$$E_h^2 = \{\tilde{\boldsymbol{\tau}}_h \in (L^2(\Omega))_s^4 : \tilde{\boldsymbol{\tau}}_h|_T \in E_4^2(T) \quad \forall T \in \mathcal{T}_h\} , \quad (5.29)$$

where $E_4^2(T)$ is the space of tensor-valued functions defined on T , spanned by the following shape functions (cf. (5.26))

$$\begin{bmatrix} \alpha_1 \bar{x} & ; & \alpha_2 \bar{x} + \alpha_3 \bar{y} \\ \text{symm.} & ; & \alpha_4 \bar{y} \end{bmatrix} \quad \text{with } \alpha_i \in \mathbf{R} . \quad (5.30)$$

We remark that this choice is not frame invariant. However, a strategy to make the results at least independent of the user's input data is detailed in Piltner and Taylor [2000].

We now want our discretization spaces to fulfill the basic conditions (5.10)–(5.13). We consider only the first set of enhanced strains (5.28), since the other case can be treated using analogous techniques.

Proposition 5.1.8. The choice (5.24)–(5.25), (5.27)–(5.28) satisfies conditions (5.10)–(5.13) with $k = 1$.

The proof for this Proposition is reported in Appendix B.

Finally Theorem 5.1.4 and Proposition 5.1.7 lead to the following result.

Proposition 5.1.9. For the method detailed by (5.24)–(5.28) and provided that the solution of the continuous problem is sufficiently regular, we have the error estimate

$$\|\mathbf{u} - \mathbf{u}_h\|_1 + |p - p_h|_0 \leq Ch . \quad (5.31)$$

Moreover, under assumptions (5.22) it holds

$$|\mathbf{u} - \mathbf{u}_h|_0 \leq Ch^2 . \quad (5.32)$$

5.1.4 Numerical tests

In this Section we investigate the computational performance of the *mixed-enhanced* elements introduced in Section 5.1.3 and based on Formulation (5.5). We denote our *triangular* schemes with

- $T3E4(I)/T3$ – Element with piecewise linear and continuous approximation for both the displacements and the pressure, enriched by means of the *first set* of enhanced strains (cf. (5.27) and (5.28)).
- $T3E4(II)/T3$ – Element with piecewise linear and continuous approximation for both the displacements and the pressure, enriched by means of the *second set* of enhanced strains (cf. (5.76) and (5.30)).

For comparison purposes, in the sequel we also consider the following methods.

Non-mixed elements.

- $T3$ – Standard displacement-based triangular element with piecewise linear and continuous approximation.

- Q4 – Standard displacement-based quadrilateral element with piecewise bilinear and continuous approximation.
- Q4E6 – Quadrilateral element with piecewise bilinear and continuous approximation for the displacements, enriched by the enhanced strains proposed by Pantuso and Bathe [1995].

Mixed elements.

- T3/T3 – Triangular element with piecewise linear and continuous approximation for both the displacements and the pressure.
- Q4/Q4 – Quadrilateral element with piecewise bilinear and continuous approximation for both the displacements and the pressure.
- Q4E6/Q4 – Quadrilateral element with piecewise bilinear and continuous approximation for both the displacements and the pressure, enriched by means of the enhanced strains proposed by Pantuso and Bathe [1995].

Moreover, we express forces and lengths in KN and m , respectively.

5.1.4.1 Fully constrained block.

We propose a couple of tests in order to numerically assess the convergence rates of the triangular $T3E4(I)/T3$ and $T3E4(II)/T3$ elements, comparing the results with the quadrilateral $Q4E6/Q4$ element.

We consider a fully constrained square block of incompressible material ($\lambda/\mu = +\infty$), occupying the region $\Omega = (-L, L) \times (-L, L)$. Each test consists in choosing a particular body load \mathbf{f} for which the corresponding analytical solution (\mathbf{u}, p) is available.

Figure 5.1 shows the generic adopted mesh for undistorted quadrilaterals, distorted quadrilaterals and triangles, respectively. It is clearly seen that:

- the undistorted quadrilateral mesh simply consists in $n \times n$ equal sub-squares (see Figure 5.1(left));
- the distorted quadrilateral mesh is obtained from the undistorted one, essentially by moving the point of coordinates $(0, 0)$ to the point of coordinates $(L/2, L/2)$ (see Figure 5.1(middle));

- the triangular mesh is obtained from the undistorted quadrilateral mesh, splitting each sub-square into two triangles by means of a diagonal (see Figure 5.1(right)).

In all the numerical experiments, we choose $n = 8, 16, 32, 64, 128$; we also point out that n (i.e. the number of subdivisions per direction) behaves as h^{-1} .

Moreover, since the body is fully constrained, the pressure is defined up to a constant, which is fixed in our computations by imposing $\int_{\Omega} p_h = 0$.

Finally, the results obtained using the $Q4E6/Q4$ element with distorted meshes are here below labelled with “ $Q4E6/Q4(\text{dist})$ ”.

◦ Polynomial load test.

For this problem we set

$$\begin{aligned} L &= 1, \mu = 40 \\ f_1 &= \mu y \left(-\frac{3}{2}x^4 + 6x^2 - 3x^2y^2 + y^2 - \frac{5}{2} \right) - 15x^2(y-1) \\ f_2 &= \mu x \left(\frac{3}{2}y^4 - 6y^2 + 3y^2x^2 - x^2 + \frac{5}{2} \right) - 3y^2 - 5x^3, \end{aligned}$$

where f_1 and f_2 are the components of the body load \mathbf{f} . Accordingly, the analytical solution is

$$\begin{aligned} u_1 &= \frac{(x^2-1)^2(y^2-1)y}{4} \\ u_2 &= \frac{(y^2-1)^2(1-x^2)x}{4} \\ p &= 5x^3(y-1) + y^3. \end{aligned}$$

For all the considered schemes, Figures 5.2–5.4 report the computed relative errors versus n , in log-log scale. More precisely, Figures 5.2 and 5.3 show the L^2 -norm convergence rates for \mathbf{u} and p , respectively.

Furthermore, Figure 5.4 gives the energy-norm convergence rate for \mathbf{u} . The energy-norm is here defined as

$$\|\mathbf{u}\|_{en} := \left(2\mu \int_{\Omega} \boldsymbol{\varepsilon}(\mathbf{u}) : \boldsymbol{\varepsilon}(\mathbf{u}) \right)^{1/2}, \quad (5.33)$$

which is clearly equivalent to the H^1 -norm, due to Korn’s inequality.

For all the elements under investigation, we observe that

- The displacement L^2 -norm convergence rate is $O(h^2)$, as predicted by the theory.
- The pressure L^2 -norm convergence rate is $O(h^{3/2})$, while the theoretical estimate gives only $O(h)$. However, we conjecture this is a super-convergence effect, probably due to the adopted meshes, and it does not show up in general situations.
- The displacement energy-norm convergence rate is $O(h)$, again as predicted by the theory.

Even if all the schemes share *the same convergence rates*, we point out that the undistorted $Q4E6/Q4$ element delivers the best performance. Moreover, the $T3E4(I)/T3$ element essentially behaves as the distorted $Q4E6/Q4(\text{dist})$ element, while the $T3E4(II)/T3$ element returns higher relative errors for the pressure fields.

◦ Trigonometric load test.

For this second problem we set

$$\begin{aligned} L &= \pi/2, \mu = 40 \\ f_1 &= \mu \cos y \sin y (1 - 4 \cos^2 x) - 2xy \cos(x^2 y) \\ f_2 &= -\mu \cos x \sin x (1 - 4 \cos^2 y) - x^2 \cos(x^2 y), \end{aligned}$$

such that the analytical solution is

$$\begin{aligned} u_1 &= -\frac{\cos^2 x \cos y \sin y}{2} \\ u_2 &= \frac{\cos^2 y \cos x \sin x}{2} \\ p &= \sin(x^2 y). \end{aligned}$$

In Figures 5.5–5.7 we report the corresponding computed relative errors versus n , in log-log scale. We remark that all the considerations concerning the first test apply also to this case.

5.1.4.2 Bending test.

The problem consists in the analysis of a beam of length $L = 10$ and height $H = 2$ under pure bending (Figure 5.8). We point out that, as in Hughes [2000] (see the Example on pages 248–249), our goal is to assess the *volumetric* locking behaviour of the elements under investigation in bending dominated problems and not their locking properties in *shear* (see Armero [2000] for a detailed discussion of volumetric versus shear locking).

The beam is first divided into two subdomains Ω_1 and Ω_2 . According to Figure 5.8, we obtain a quadrilateral grid, labelled as “ $n \times n$ mesh”, by meshing *each subdomain* with $n \times n$ quadrilaterals; a corresponding triangular grid, still labelled as “ $n \times n$ mesh” for simplicity, is obtained splitting each quadrilateral element into two triangles by means of a diagonal. Moreover, it is possible to introduce a distortion in the shape of the two subdomains by means of a parameter $a \neq 0$, as shown in Figure 5.8. In the following we will consider

- the undistorted case (i.e. $a = 0$);
- a distorted case with $a = .5$.

We perform the test using the elements presented at the beginning of this Section and we study their behaviours for compressible ($\lambda/\mu = 1$), nearly incompressible ($\lambda/\mu = 10^7$) or incompressible ($\lambda/\mu = +\infty$) materials, reporting the following quantities

- the full elastic energy E associated with the problem, computed as the inner product between the internal force and the solution vector;
- the displacements $u_1(A)$ and $u_2(A)$ of the specific node indicated by letter A in Figure 5.8;
- the pressure $p(A)$ at node A (for mixed formulations).

◦ Compressible case.

We consider a compressible material with $\lambda = 40$ and $\mu = 40$, reporting the results of the analyses in Tables 5.1 and 5.2.

As the analytical solution is not available, we consider as reference solutions the following values, obtained using the $Q4E6/Q4$ element with the fine 128×128 mesh and $a = .5$

$$\begin{aligned} E &= 5.6250 \times 10^{-3} \\ u_1(A) &= -2.8125 \times 10^{-1} \\ u_2(A) &= 1.4062 \\ p(A) &= -7.5000 \times 10^{-1} . \end{aligned}$$

According to Simo and Rifai [1990], we notice that the enhanced $Q4E6$ and $Q4E6/Q4$ elements exactly reproduce the reference solutions using a mesh of just two *undistorted*

quadrilaterals (1×1 mesh). Instead, this property is not fulfilled by the mixed-enhanced triangular elements.

◦ Nearly incompressible and incompressible cases.

We consider nearly incompressible and incompressible materials, choosing $\lambda = 40 \times 10^7$ and $\lambda = +\infty$, respectively; in addition, we set $\mu = 40$ for both cases. In these situations, only the mixed-enhanced schemes are efficient (among the ones presented in this Section). Therefore, we focus only on the $Q4E6/Q4$, $T3E4(I)/T3$ and $T3E4(II)/T3$ elements, as shown in Tables 5.3 and 5.4. Moreover, we point out that the numerical results delivered in the nearly incompressible and incompressible cases are exactly the same.

As before, we consider as reference solutions the following values, obtained using the $Q4E6/Q4$ element with the 128×128 mesh and $a = .5$

$$\begin{aligned} E &= 3.7500 \times 10^{-3} \\ u_1(A) &= -1.8750 \times 10^{-1} \\ u_2(A) &= 9.3750 \times 10^{-1} \\ p(A) &= -1.5000 . \end{aligned}$$

Also here, we notice that the *undistorted* quadrilateral 1×1 mesh exactly reproduces the reference solutions.

As a final remark, we observe that for this bending test the $Q4E6/Q4$ element gives the best results.

5.1.4.3 Cook's membrane.

The last problem under investigation is the so-called Cook's membrane (Figure 5.9), which is another classical bending dominated test introduced here to assess element performances with respect to volumetric locking. Following Piltner and Taylor [2000], we set $L = 48$, $H_1 = 44$, $H_2 = 16$ and $F = 1$, where F is the resultant of the uniformly distributed shear load f .

We perform the test for compressible ($\lambda/\mu = 2$), nearly incompressible ($\lambda/\mu = 2 \times 10^7$) and incompressible ($\lambda/\mu = +\infty$) materials and we report the same quantities described in the previous Subsection.

◦ Compressible case.

We consider a compressible material with $\lambda = .75$ and $\mu = .375$, reporting the results of

the analyses in Table 5.5.

Similarly to the bending test previously described, the analytical solution is not available. Therefore, we consider as reference solutions the following values, obtained using the $Q4E6/Q4$ element with the 128×128 mesh

$$\begin{aligned} E &= 2.1585 \times 10^{-1} \\ u_1(A) &= -9.5775 \\ u_2(A) &= 2.1520 \times 10^1 \\ p(A) &= 4.7192 \times 10^{-2} . \end{aligned}$$

◦ Nearly incompressible and incompressible cases.

We consider nearly incompressible and incompressible materials, choosing $\lambda = .75 \times 10^7$ and $\lambda = +\infty$, respectively; moreover, we set $\mu = .375$ for both cases. As for the corresponding bending tests in nearly incompressible and incompressible regimes, only the mixed-enhanced elements have been examined, as reported in Tables 5.6 and 5.7. Again, the numerical results for the nearly incompressible and the incompressible cases are exactly the same.

Furthermore, the reference solutions obtained using the $Q4E6/Q4$ element with the 128×128 mesh are

$$\begin{aligned} E &= 1.6491 \times 10^{-1} \\ u_1(A) &= -7.2480 \\ u_2(A) &= 1.6442 \times 10^1 \\ p(A) &= 7.0788 \times 10^{-2} . \end{aligned}$$

The numerical results show that for the Cook's membrane the $Q4E6/Q4$, $T3E4(I)/T3$ and $T3E4(II)/T3$ elements provide robust schemes.

5.1.5 Conclusive considerations for Section 5.1

We have investigated the Mixed-Enhanced Strain technique within the context of the u/p formulation for linear elasticity problems. We have developed a general theoretical analysis, extending the results presented by Lovadina [1997]; in particular, we have proved optimal uniform error bounds for the L^2 -norm of the displacements. Moreover, we have presented several numerical tests on triangular and quadrilateral elements to assess their computational performance, and, in particular, numerical results confirm the convergence rates predicted by the theory.

Table 5.1. Bending test. Quadrilateral elements with $\lambda/\mu = 1$. Undistorted ($a = 0$) and distorted ($a = .5$) 1×1 meshes, distorted ($a = .5$) 4×4 , 16×16 and 64×64 meshes.

element	output	1×1		4×4	16×16	64×64
		$a = 0$	$a = .5$	$a = .5$		
$Q4$	E $[\times 10^3]$	1.6216	1.2030	4.6722	5.5538	5.6205
	$u_1(A)$ $[\times 10]$	-.81081	-.60150	-2.3227	-2.7736	-2.8098
	$u_2(A)$.40541	.30075	1.1667	1.3882	1.4051
$Q4/Q4$	E $[\times 10^3]$	1.6216	1.2766	4.7325	5.5594	5.6209
	$u_1(A)$ $[\times 10]$	-.81081	-.63828	-2.3527	-2.7764	-2.8100
	$u_2(A)$.40541	.31914	1.1817	1.3896	1.4052
	$p(A)$ $[\times 10]$	-3.2432	-2.6462	-6.5581	-7.2862	-7.4454
$Q4E6$	E $[\times 10^3]$	5.6250	4.5541	5.6235	5.6250	5.6250
	$u_1(A)$ $[\times 10]$	-2.8125	-2.2770	-2.8117	-2.8125	-2.8125
	$u_2(A)$	1.4062	1.1385	1.4059	1.4062	1.4062
$Q4E6/Q4$	E $[\times 10^3]$	5.6250	4.7738	5.6238	5.6250	5.6250
	$u_1(A)$ $[\times 10]$	-2.8125	-2.3869	-2.8119	-2.8125	-2.8125
	$u_2(A)$	1.4062	1.1934	1.4060	1.4062	1.4062
	$p(A)$ $[\times 10]$	-7.5000	-6.3648	-7.5107	-7.5000	-7.5000

Table 5.2. Bending test. Triangular elements with $\lambda/\mu = 1$. Undistorted ($a = 0$) and distorted ($a = .5$) 1×1 meshes, distorted ($a = .5$) 4×4 , 16×16 and 64×64 meshes.

element	output	1×1		4×4	16×16	64×64
		$a = 0$	$a = .5$	$a = .5$		
$T3$	E $[\times 10^3]$.58387	.71578	3.6527	5.4399	5.6130
	$u_1(A)$ $[\times 10]$	-.29194	-.35789	-1.8076	-2.7125	-2.8055
	$u_2(A)$.14597	.17894	.90983	1.3595	1.4032
$T3/T3$	E $[\times 10^3]$.60856	.71779	3.6899	5.4455	5.6134
	$u_1(A)$ $[\times 10]$	-.30428	-.35889	-1.8257	-2.7153	-2.8057
	$u_2(A)$.15214	.17945	.91912	1.3609	1.4033
	$p(A)$ $[\times 10]$	-1.1150	-.21334	-3.7991	-6.5394	-7.2605
$T3E4(I)/T3$	E $[\times 10^3]$.61437	.71833	3.7051	5.4478	5.6134
	$u_1(A)$ $[\times 10]$	-.30718	-.35916	-1.8331	-2.7164	-2.8057
	$u_2(A)$.15359	.17958	.92288	1.3614	1.4033
	$p(A)$ $[\times 10]$	-.65391	-.09082	-3.9324	-6.6128	-7.2780
$T3E4(II)/T3$	E $[\times 10^3]$.61213	.71805	3.6986	5.4469	5.6135
	$u_1(A)$ $[\times 10]$	-.30606	-.35903	-1.8299	-2.7160	-2.8057
	$u_2(A)$.15303	.17951	.92127	1.3612	1.4033
	$p(A)$ $[\times 10]$	-.81357	-.13990	-3.7377	-6.5448	-7.2618

Table 5.3. Bending test. Quadrilateral and triangular elements with $\lambda/\mu = 10^7$. Undistorted ($a = 0$) 1×1 mesh and distorted ($a = .5$) 4×4 , 16×16 and 64×64 meshes.

element geometry	element	output	1×1	4×4	16×16	64×64
			$a = 0$	$a = .5$		
quadrilateral	$Q4E6/Q4$	E $[\times 10^3]$	3.7500	3.7495	3.7500	3.7500
		$u_1(A)$ $[\times 10]$	-1.8750	-1.8748	-1.8750	-1.8750
		$u_2(A)$ $[\times 10]$	9.3750	9.3737	9.3750	9.3750
		$p(A)$	-1.5000	-1.5016	-1.5000	-1.5000
triangular	$T3E4(I)/T3$	E $[\times 10^3]$.60097	2.8583	3.6788	3.7455
		$u_1(A)$ $[\times 10]$	-.30048	-1.4158	-1.8356	-1.8723
		$u_2(A)$ $[\times 10]$	1.5024	7.1279	9.1951	9.3634
		$p(A)$	-.15465	-.89369	-1.3483	-1.4620
	$T3E4(II)/T3$	E $[\times 10^3]$.57811	2.8220	3.6753	3.7453
		$u_1(A)$ $[\times 10]$	-.28905	-1.3979	-1.8338	-1.8721
		$u_2(A)$ $[\times 10]$	1.4453	7.0376	9.1863	9.3629
		$p(A)$	-.32372	-.72864	-1.2964	-1.4495

Table 5.4. Bending test. Quadrilateral and triangular elements with $\lambda/\mu = +\infty$. Undistorted ($a = 0$) 1×1 mesh and distorted ($a = .5$) 4×4 , 16×16 and 64×64 meshes.

element geometry	element	output	1×1	4×4	16×16	64×64
			$a = 0$	$a = .5$		
quadrilateral	$Q4E6/Q4$	E $[\times 10^3]$	3.7500	3.7495	3.7500	3.7500
		$u_1(A)$ $[\times 10]$	-1.8750	-1.8748	-1.8750	-1.8750
		$u_2(A)$ $[\times 10]$	9.3750	9.3737	9.3750	9.3750
		$p(A)$	-1.5000	-1.5016	-1.5000	-1.5000
triangular	$T3E4(I)/T3$	E $[\times 10^3]$.60097	2.8583	3.6788	3.7455
		$u_1(A)$ $[\times 10]$	-.30048	-1.4158	-1.8356	-1.8723
		$u_2(A)$ $[\times 10]$	1.5024	7.1279	9.1951	9.3634
		$p(A)$	-.15465	-.89369	-1.3483	-1.4620
	$T3E4(II)/T3$	E $[\times 10^3]$.57811	2.8220	3.6753	3.7453
		$u_1(A)$ $[\times 10]$	-.28905	-1.3979	-1.8338	-1.8721
		$u_2(A)$ $[\times 10]$	1.4453	7.0376	9.1863	9.3629
		$p(A)$	-.32372	-.72864	-1.2964	-1.4495

Table 5.5. Cook's membrane. Quadrilateral and triangular elements with $\lambda/\mu = 2$. Meshes: 4×4 , 16×16 and 64×64 .

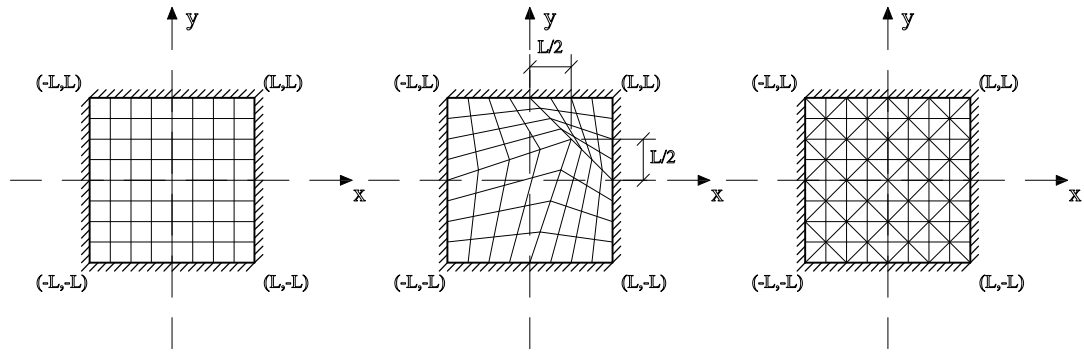
element geometry	element	output	4×4	16×16	64×64
quadrilateral	$Q4E6$	E $[\times 10]$	2.0606	2.1465	2.1573
		$u_1(A)$	-9.0798	-9.5273	-9.5718
		$u_2(A)$ $[\times 10^{-1}]$	2.0591	2.1424	2.1510
	$Q4E6/Q4$	E $[\times 10]$	2.0741	2.1487	2.1576
		$u_1(A)$	-9.1495	-9.5387	-9.5737
		$u_2(A)$ $[\times 10^{-1}]$	2.0724	2.1444	2.1513
		$p(A)$ $[\times 10^2]$	3.3763	4.4639	4.7070
	triangular	$T3E4(I)/T3$	E $[\times 10]$	1.5634	2.0911
$u_1(A)$			-6.3466	-9.2612	-9.5513
$u_2(A)$ $[\times 10^{-1}]$			1.5631	2.0901	2.1470
$p(A)$ $[\times 10^2]$			1.3276	3.0945	4.2997
$T3E4(II)/T3$		E $[\times 10]$	1.5533	2.0895	2.1525
		$u_1(A)$	-6.2907	-9.2544	-9.5506
		$u_2(A)$ $[\times 10^{-1}]$	1.5526	2.0887	2.1469
		$p(A)$ $[\times 10^2]$.89457	2.5825	4.0269

Table 5.6. Cook's membrane. Quadrilateral and triangular elements with $\lambda/\mu = 2 \times 10^7$. Meshes: 4×4 , 16×16 and 64×64 .

element geometry	element	output	4×4	16×16	64×64
quadrilateral	$Q4E6/Q4$	E $[\times 10]$	1.5705	1.6359	1.6476
		$u_1(A)$	-6.7483	-7.1747	-7.2393
		$u_2(A)$ $[\times 10^{-1}]$	1.5658	1.6324	1.6428
		$p(A)$ $[\times 10^2]$	5.3185	6.6875	7.0606
triangular	$T3E4(I)/T3$	E $[\times 10]$	1.2693	1.5995	1.6435
		$u_1(A)$	-5.0490	-6.9812	-7.2170
		$u_2(A)$ $[\times 10^{-1}]$	1.2662	1.5980	1.6391
		$p(A)$ $[\times 10^2]$	2.4461	4.8216	6.4739
	$T3E4(II)/T3$	E $[\times 10]$	1.2263	1.5917	1.6424
		$u_1(A)$	-4.7921	-6.9412	-7.2105
		$u_2(A)$ $[\times 10^{-1}]$	1.2218	1.5909	1.6381
		$p(A)$ $[\times 10^2]$.74186	2.0316	4.6121

Table 5.7. Cook's membrane. Quadrilateral and triangular elements with $\lambda/\mu = +\infty$. Meshes: 4×4 , 16×16 and 64×64 .

element geometry	element	output	4×4	16×16	64×64
quadrilateral	$Q4E6/Q4$	E $[\times 10]$	1.5705	1.6359	1.6476
		$u_1(A)$	-6.7483	-7.1747	-7.2393
		$u_2(A)$ $[\times 10^{-1}]$	1.5658	1.6324	1.6428
		$p(A)$ $[\times 10^2]$	5.3185	6.6875	7.0606
triangular	$T3E4(I)/T3$	E $[\times 10]$	1.2693	1.5995	1.6435
		$u_1(A)$	-5.0490	-6.9812	-7.2170
		$u_2(A)$ $[\times 10^{-1}]$	1.2662	1.5980	1.6391
		$p(A)$ $[\times 10^2]$	2.4461	4.8216	6.4739
	$T3E4(II)/T3$	E $[\times 10]$	1.2263	1.5917	1.6424
		$u_1(A)$	-4.7921	-6.9412	-7.2105
		$u_2(A)$ $[\times 10^{-1}]$	1.2218	1.5909	1.6381
		$p(A)$ $[\times 10^2]$.74186	2.0316	4.6121

**Figure 5.1. Fully constrained block. Problem geometry and boundary conditions. Undistorted quadrilateral, distorted quadrilateral and triangular meshes.**

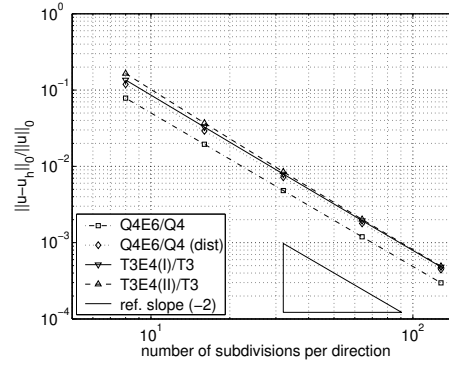


Figure 5.2. Fully constrained block. Polynomial load test. L^2 -norm convergence rate for u .

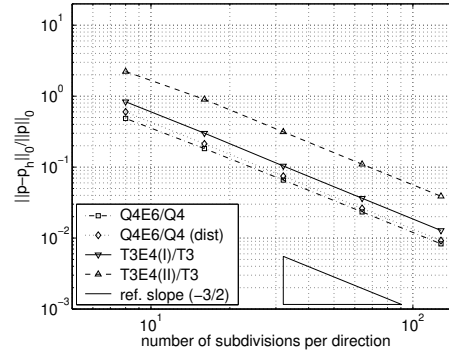


Figure 5.3. Fully constrained block. Polynomial load test. L^2 -norm convergence rate for p .

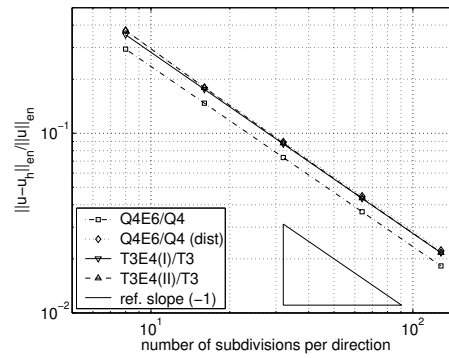


Figure 5.4. Fully constrained block. Polynomial load test. Energy-norm convergence rate for u .

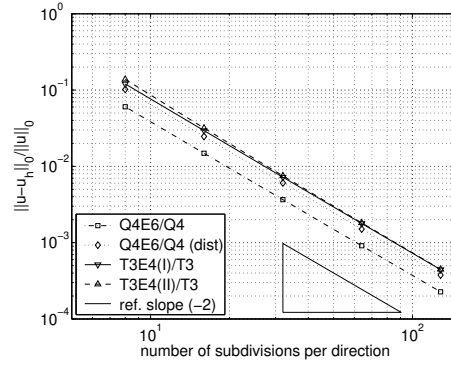


Figure 5.5. Fully constrained block. Trigonometric load test. L^2 -norm convergence rate for u .

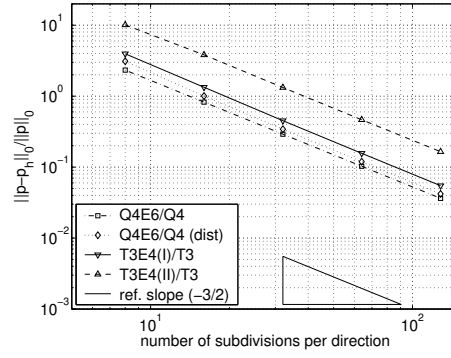


Figure 5.6. Fully constrained block. Trigonometric load test. L^2 -norm convergence rate for p .

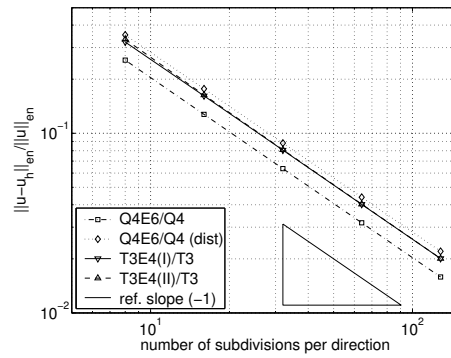


Figure 5.7. Fully constrained block. Trigonometric load test. Energy-norm convergence rate for u .

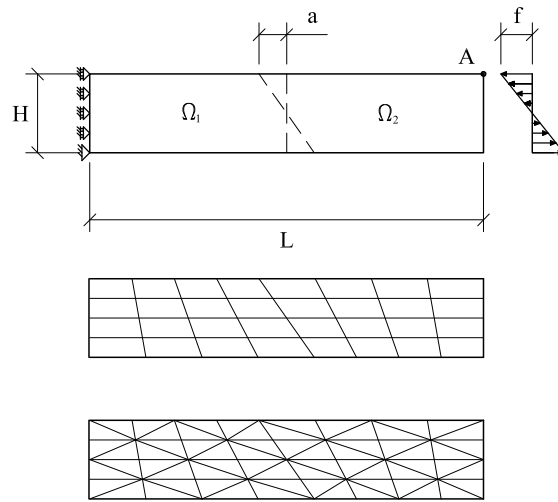


Figure 5.8. Bending test. Problem geometry, boundary and loading conditions. Distorted 4×4 meshes.

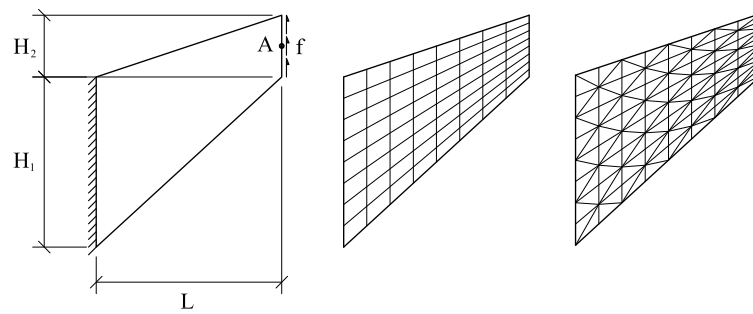


Figure 5.9. Cook's membrane. Problem geometry, boundary and loading conditions. 8×8 meshes.

5.2 A stability study of some mixed finite elements for large deformation elasticity problems

Nowadays there are several finite element interpolation schemes which perform very well (in terms of accuracy and stability) for the case of small deformation problems, also in the presence of highly constrained situations (i.e. incompressible materials). Examples with excellent performance range from standard mixed elements (see, for instance, Brezzi and Fortin [1991]; Bathe [1996]; Hughes [2000] and the references therein) to, as seen in Section 5.1, enhanced strain elements (see Simo and Rifai [1990]; Reddy and Simo [1995]; Pantuso and Bathe [1995]; Braess [1998]; Auricchio *et al.* [2005a]).

However, it is also well established that the extension of such schemes to the case of finite strain problems is by no way trivial; in particular, even elements which seem to be ideal from a theoretical and a numerical perspective may fail in the large strain range, for example due to the rising of non-physical instabilities for high compression/tension states (see for more details Wriggers and Reese [1996]; Pantuso and Bathe [1997]; Armero [2000]; Lovadina and Auricchio [2003]). It is worth recalling that many interesting strategies have been developed in order to stabilize the methods at hand (cf., for instance, Simo and Armero [1992]; Nagtegaal and Fox [1996]; Klaas *et al.* [1999]; Reese *et al.* [1999]; Reese and Wriggers [2000]; Maniatty *et al.* [2002]). However, a satisfactory analysis of finite element methods for finite strain problems is still missing.

According to the cited problematics, the present Section focuses on a simple finite-strain elastic bidimensional problem for which it is possible not only computing the solution in closed form but also drawing some indications on the solution stability.

After recalling the general finite strain elasticity framework (Section 5.2.1), we discuss the proposed 2D continuum problem (Section 5.2.2). We then present some possible finite element discretizations of the problem under investigation. In particular, we consider the extension to large deformation of the MINI mixed finite element (see Arnold *et al.* [1984]) and of the QME mixed-enhanced finite element (see Pantuso and Bathe [1995]), which have been proved to be stable and well performing in linear elasticity. For both finite elements we are able to present some theoretical considerations on the stability limits of the discrete problems, showing that both formulations fail to reproduce the continuum stability features (Section 5.2.4). Finally, we perform extensive numerical simulations to investigate the whole stability range of both finite element discretizations (Section 5.2.5).

5.2.1 The finite strain incompressible elasticity problem

In the following, we adopt the so-called *material description* to study the finite strain elasticity problem. Accordingly, we suppose that we are given a *reference configuration* $\Omega \subset \mathcal{R}^d$ for a d -dimensional bounded material body \mathcal{B} . Therefore, the deformation of \mathcal{B} can be described by means of the map $\hat{\varphi} : \Omega \rightarrow \mathcal{R}^d$ defined by

$$\hat{\varphi}(\mathbf{X}) = \mathbf{X} + \hat{\mathbf{u}}(\mathbf{X}) , \quad (5.34)$$

where $\mathbf{X} = (X_1, \dots, X_d)$ denotes the coordinates of a material point in the reference configuration and $\hat{\mathbf{u}}(\mathbf{X})$ represents the corresponding displacement vector. Following standard notations, we introduce the deformation gradient $\hat{\mathbf{F}} = \mathbf{F}(\hat{\mathbf{u}})$ and the right Cauchy-Green deformation tensor $\hat{\mathbf{C}} = \mathbf{C}(\hat{\mathbf{u}})$ by setting

$$\hat{\mathbf{F}} = \mathbf{I} + \nabla \hat{\mathbf{u}} \quad , \quad \hat{\mathbf{C}} = \hat{\mathbf{F}}^T \hat{\mathbf{F}} , \quad (5.35)$$

where \mathbf{I} is the second-order identity tensor and ∇ is the gradient operator with respect to the coordinates \mathbf{X} .

For a homogeneous neo-Hookean material we define (see for example Bonet and Wood [1997] and Ciarlet [1978]) the potential energy function as

$$\Psi(\hat{\mathbf{u}}) = \frac{1}{2}\mu \left[\mathbf{I} : \hat{\mathbf{C}} - d \right] - \mu \ln \hat{J} + \frac{\lambda}{2} \Theta(\hat{J})^2 , \quad (5.36)$$

where λ and μ are positive constants, “ $:$ ” represents the usual inner product for second-order tensors and $\hat{J} = \det \hat{\mathbf{F}}$. Moreover, Θ is a real function usually chosen as

$$\Theta(J) = \ln J \quad \text{or} \quad \Theta(J) = J - 1 . \quad (5.37)$$

Introducing the pressure-like variable (or simply pressure) $\hat{p} = \lambda \Theta(\hat{J})$, the potential energy (5.36) can be equivalently written as the following function of $\hat{\mathbf{u}}$ and \hat{p} (still denoted with Ψ , with a little abuse of notations)

$$\Psi(\hat{\mathbf{u}}, \hat{p}) = \frac{1}{2}\mu \left[\mathbf{I} : \hat{\mathbf{C}} - d \right] - \mu \ln \hat{J} + \hat{p} \Theta(\hat{J}) - \frac{1}{2\lambda} \hat{p}^2 . \quad (5.38)$$

When the body \mathcal{B} is subjected to a given load $\mathbf{b} = \mathbf{b}(\mathbf{X})$ per unit volume in the reference configuration, the total elastic energy functional reads as follows

$$\Pi(\hat{\mathbf{u}}, \hat{p}) = \int_{\Omega} \Psi(\hat{\mathbf{u}}, \hat{p}) - \int_{\Omega} \mathbf{b} \cdot \hat{\mathbf{u}} . \quad (5.39)$$

Therefore, following the Hellinger-Reissner variational principle, equilibrium is derived by searching for critical points of (5.39) in suitable admissible displacement and pressure

spaces \hat{U} and \hat{P} . The corresponding Euler-Lagrange equations emanating from (5.39) lead to solve

$$\left\{ \begin{array}{l} \text{find } (\hat{\mathbf{u}}, \hat{p}) \in \hat{U} \times \hat{P} \text{ such that} \\ \mu \int_{\Omega} [\hat{\mathbf{F}} - \hat{\mathbf{F}}^{-T}] : \nabla \mathbf{v} + \int_{\Omega} \hat{p} \Theta'(\hat{J}) \hat{J} \hat{\mathbf{F}}^{-T} : \nabla \mathbf{v} = \int_{\Omega} \mathbf{b} \cdot \mathbf{v} \quad \forall \mathbf{v} \in U \\ \int_{\Omega} \left(\Theta(\hat{J}) - \frac{\hat{p}}{\lambda} \right) q = 0 \quad \forall q \in P, \end{array} \right. \quad (5.40)$$

where U and P are the admissible variation spaces for the displacements and the pressures, respectively. We note that in (5.40) we used that the linearization of the deformation gradient jacobian is

$$DJ(\hat{\mathbf{u}})[\mathbf{v}] = J(\hat{\mathbf{u}}) \mathbf{F}(\hat{\mathbf{u}})^{-T} : \nabla \mathbf{v} = \hat{J} \hat{\mathbf{F}}^{-T} : \nabla \mathbf{v} \quad \forall \mathbf{v} \in U. \quad (5.41)$$

Without loss of generality, from now on we select $\Theta(J) = \ln J$ (see (5.37)). Moreover, we focus on the case of an *incompressible* material, which corresponds to take the limit $\lambda \rightarrow +\infty$ in (5.40). Therefore, our problem becomes

$$\left\{ \begin{array}{l} \text{find } (\hat{\mathbf{u}}, \hat{p}) \in \hat{U} \times \hat{P} \text{ such that} \\ \mu \int_{\Omega} \hat{\mathbf{F}} : \nabla \mathbf{v} + \int_{\Omega} (\hat{p} - \mu) \hat{\mathbf{F}}^{-T} : \nabla \mathbf{v} - \int_{\Omega} \mathbf{b} \cdot \mathbf{v} = 0 \quad \forall \mathbf{v} \in U \\ \int_{\Omega} q \ln \hat{J} = 0 \quad \forall q \in P, \end{array} \right. \quad (5.42)$$

or, in residual form,

$$\left\{ \begin{array}{l} \text{find } (\hat{\mathbf{u}}, \hat{p}) \in \hat{U} \times \hat{P} \text{ such that} \\ \mathcal{R}_u((\hat{\mathbf{u}}, \hat{p}), \mathbf{v}) = 0 \quad \forall \mathbf{v} \in U \\ \mathcal{R}_p((\hat{\mathbf{u}}, \hat{p}), q) = 0 \quad \forall q \in P, \end{array} \right. \quad (5.43)$$

where

$$\left\{ \begin{array}{l} \mathcal{R}_u((\hat{\mathbf{u}}, \hat{p}), \mathbf{v}) := \mu \int_{\Omega} \hat{\mathbf{F}} : \nabla \mathbf{v} + \int_{\Omega} (\hat{p} - \mu) \hat{\mathbf{F}}^{-T} : \nabla \mathbf{v} - \int_{\Omega} \mathbf{b} \cdot \mathbf{v} \\ \mathcal{R}_p((\hat{\mathbf{u}}, \hat{p}), q) := \int_{\Omega} q \ln \hat{J}. \end{array} \right. \quad (5.44)$$

We now derive the linearization of problem (5.42) around a generic point $(\hat{\mathbf{u}}, \hat{p})$. Observing that

$$D\hat{\mathbf{F}}^{-T}(\hat{\mathbf{u}})[\mathbf{u}] = -\hat{\mathbf{F}}^{-T}(\nabla \mathbf{u})^T \hat{\mathbf{F}}^{-T} \quad \forall \mathbf{u} \in U, \quad (5.45)$$

we easily get the problem for the *infinitesimal* increment (\mathbf{u}, p)

$$\left\{ \begin{array}{l} \text{find } (\mathbf{u}, p) \in U \times P \text{ such that} \\ \mu \int_{\Omega} \nabla \mathbf{u} : \nabla \mathbf{v} + \int_{\Omega} (\mu - \hat{p})(\hat{\mathbf{F}}^{-1} \nabla \mathbf{u})^T : \hat{\mathbf{F}}^{-1} \nabla \mathbf{v} \\ + \int_{\Omega} p \hat{\mathbf{F}}^{-T} : \nabla \mathbf{v} = -\mathcal{R}_u((\hat{\mathbf{u}}, \hat{p}), \mathbf{v}) \quad \forall \mathbf{v} \in U \\ \int_{\Omega} q \hat{\mathbf{F}}^{-T} : \nabla \mathbf{u} = -\mathcal{R}_p((\hat{\mathbf{u}}, \hat{p}), q) \quad \forall q \in P . \end{array} \right. \quad (5.46)$$

Remark 5.2.1. Since problem (5.46) is the linearization of problem (5.42) (or equivalently (5.43)), it can be interpreted as the generic step of a Newton-like iteration procedure for the solution of the non-linear problem (5.42).

Remark 5.2.2. Taking $(\hat{\mathbf{u}}, \hat{p}) = (\mathbf{0}, 0)$ in (5.46), we immediately recover the classical linear incompressible elasticity problem for small deformations, i.e.

$$\left\{ \begin{array}{l} \text{Find } (\mathbf{u}, p) \in U \times P \text{ such that} \\ 2\mu \int_{\Omega} \boldsymbol{\varepsilon}(\mathbf{u}) : \boldsymbol{\varepsilon}(\mathbf{v}) + \int_{\Omega} p \operatorname{div} \mathbf{v} = \int_{\Omega} \mathbf{b} \cdot \mathbf{v} \quad \forall \mathbf{v} \in U \\ \int_{\Omega} q \operatorname{div} \mathbf{u} = 0 \quad \forall q \in P , \end{array} \right. \quad (5.47)$$

where $\boldsymbol{\varepsilon}(\cdot)$ denotes the symmetric gradient operator.

5.2.2 A model problem for finite strain incompressible elasticity

In this Section we present a *simple* bidimensional problem which nonetheless shows some of the difficulties arising in general nonlinear elastic problems for incompressible materials.

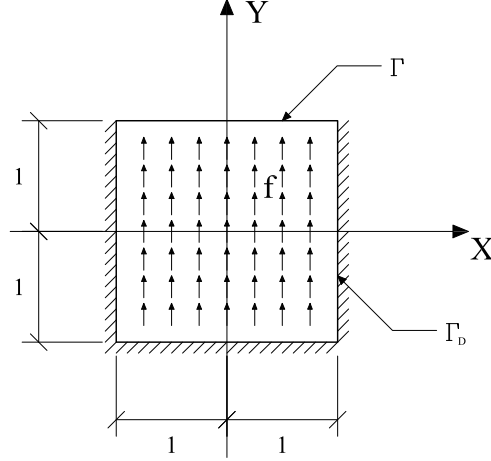


Figure 5.10. Problem domain Ω .

Using the usual Cartesian coordinates (X, Y) , we consider a square material body whose reference configuration is $\Omega = (-1, 1) \times (-1, 1)$; we denote with $\Gamma = [-1, 1] \times \{1\}$ the upper part of its boundary, while the remaining part of $\partial\Omega$ is denoted with Γ_D (cf. Figure 5.2.2). The body Ω is clamped along Γ_D and subjected to the volume force $\mathbf{b} = \gamma \mathbf{f}$, where $\mathbf{f} = (0, 1)^T$ and γ is a real parameter.

Therefore, the equilibrium problem leads to solve the following variational system (see (5.42))

$$\left\{ \begin{array}{l} \text{find } (\hat{\mathbf{u}}, \hat{p}) \in \hat{U} \times \hat{P} \text{ such that} \\ \mu \int_{\Omega} \hat{\mathbf{F}} : \nabla \mathbf{v} + \int_{\Omega} (\hat{p} - \mu) \hat{\mathbf{F}}^{-T} : \nabla \mathbf{v} = \gamma \int_{\Omega} \mathbf{f} \cdot \mathbf{v} \quad \forall \mathbf{v} \in U \\ \int_{\Omega} q \ln \hat{J} = 0 \quad \forall q \in P. \end{array} \right. \quad (5.48)$$

It is not our intention to rigorously specify the regularity needed for the space involved in the variational formulation (5.48), and we refer to Le Tallec [1982, 1994] for details on such a point. Instead, we wish to notice that system (5.48) constitutes a set of *nonlinear* equations for which a trivial solution can be easily found *for every* $\gamma \in \mathbf{R}$, i.e. $(\hat{\mathbf{u}}, \hat{p}) = (\mathbf{0}, \gamma r)$, where $r = r(X, Y) = 1 - Y$.

Remark 5.2.3. We are not claiming that, for each $\gamma \in \mathbf{R}$, $(\hat{\mathbf{u}}, \hat{p}) = (\mathbf{0}, \gamma r)$ is the only solution of the system.

Whenever an incremental loading procedure is considered, the passage from γ to $\gamma + \Delta\gamma$ in (5.48) is typically solved by a Newton's technique. Supposing that at γ convergence has been reached, the first iteration step of Newton's method with initial guess $(\hat{\mathbf{u}}, \hat{p}) = (\mathbf{0}, \gamma r)$ consists (recalling the linearized problem (5.46)) in solving

$$\left\{ \begin{array}{l} \text{find } (\mathbf{u}, p) \in U \times P \text{ such that} \\ 2\mu \int_{\Omega} \boldsymbol{\varepsilon}(\mathbf{u}) : \boldsymbol{\varepsilon}(\mathbf{v}) - \gamma \int_{\Omega} r(\nabla \mathbf{u})^T : \nabla \mathbf{v} + \int_{\Omega} p \operatorname{div} \mathbf{v} = \Delta\gamma \int_{\Omega} \mathbf{f} \cdot \mathbf{v} \\ \int_{\Omega} q \operatorname{div} \mathbf{u} = 0 , \end{array} \right. \quad (5.49)$$

for every $(\mathbf{v}, q) \in U \times P$. Letting

$$U = \{ \mathbf{v} \in H^1(\Omega)^2 : \mathbf{v}|_{\Gamma_D} = 0 \} ; \quad P = L^2(\Omega) , \quad (5.50)$$

we consider system (5.49) as a *model problem* for our subsequent considerations. Denoting with \mathbf{A}^S the symmetric part of a generic second-order tensor \mathbf{A} , introducing the bilinear forms

$$a_{\gamma}(\mathbf{F}, \mathbf{G}) =: 2\mu \int_{\Omega} \mathbf{F}^S : \mathbf{G}^S - \gamma \int_{\Omega} r \mathbf{F}^T : \mathbf{G} \quad (5.51)$$

and

$$b(\mathbf{v}, q) =: \int_{\Omega} q \operatorname{div} \mathbf{v} , \quad (5.52)$$

problem (5.49) can be written as

$$\left\{ \begin{array}{l} \text{find } (\mathbf{u}, p) \in U \times P \text{ such that} \\ a_{\gamma}(\nabla \mathbf{u}, \nabla \mathbf{v}) + b(\mathbf{v}, p) = \Delta\gamma \int_{\Omega} \mathbf{f} \cdot \mathbf{v} \quad \forall \mathbf{v} \in U \\ b(\mathbf{u}, q) = 0 \quad \forall q \in P . \end{array} \right. \quad (5.53)$$

Therefore, we are clearly facing a typical (parameter-depending) saddle-point problem. As it is well-established (cf. Brezzi and Fortin [1991]), the crucial properties for the well-posedness are, together with continuity,

- *the inf-sup condition*, i.e. the existence of a positive constant β such that

$$\inf_{q \in P} \sup_{\mathbf{v} \in U} \frac{b(\mathbf{v}, q)}{\|\mathbf{v}\|_U \|q\|_P} \geq \beta ; \quad (5.54)$$

- *the invertibility on the kernel condition*, i.e. the existence of a positive constant $\alpha(\gamma, \mu)$ such that

$$\inf_{\mathbf{v} \in Ker B} \sup_{\mathbf{u} \in Ker B} \frac{a_\gamma(\nabla \mathbf{u}, \nabla \mathbf{v})}{\|\mathbf{u}\|_U \|\mathbf{v}\|_U} \geq \alpha(\gamma, \mu) , \quad (5.55)$$

where

$$Ker B = \{\mathbf{v} \in U : b(\mathbf{v}, q) = 0 \quad \forall q \in P\} . \quad (5.56)$$

As far as the inf-sup condition is concerned, it is a classical result that it holds for the divergence operator. We therefore focus our attention on condition (5.55). In particular, we will show that the form $a_\gamma(\cdot, \cdot)$ is *coercive* on $Ker B$ whenever γ stays in a suitable range of values. We thus expect that within such choices of the parameters, for the *continuous* problem the trivial solution $(\hat{\mathbf{u}}, \hat{p}) = (\mathbf{0}, \gamma r)$ is unique and stable.

5.2.3 The stability range

We now investigate on the coercivity on $Ker B$ of $a_\gamma(\cdot, \cdot)$. More precisely, recalling the well-known Korn's inequality, we search for conditions on γ implying the existence of a constant $c(\gamma, \mu) > 0$ such that

$$2\mu \int_{\Omega} |\boldsymbol{\epsilon}(\mathbf{v})|^2 - \gamma \int_{\Omega} r (\nabla \mathbf{v})^T : \nabla \mathbf{v} \geq c(\gamma, \mu) \int_{\Omega} |\boldsymbol{\epsilon}(\mathbf{v})|^2 \quad \forall \mathbf{v} \in Ker B . \quad (5.57)$$

Since $\text{div}(\nabla \mathbf{v})^T = \mathbf{0}$ for every divergence-free function \mathbf{v} (i.e. for every $\mathbf{v} \in Ker B$), an integration by parts gives

$$2\mu \int_{\Omega} |\boldsymbol{\epsilon}(\mathbf{v})|^2 - \gamma \int_{\Omega} r (\nabla \mathbf{v})^T : \nabla \mathbf{v} = 2\mu \int_{\Omega} |\boldsymbol{\epsilon}(\mathbf{v})|^2 + \gamma \int_{\Omega} \nabla r \cdot [\nabla \mathbf{v}] \mathbf{v} . \quad (5.58)$$

Above, the boundary integral arising from integration by parts disappears because of the boundary conditions on \mathbf{v} , and because on Γ the function $r = 1 - Y$ vanishes.

Now, a further integration by parts leads to

$$\gamma \int_{\Omega} \nabla r \cdot [\nabla \mathbf{v}] \mathbf{v} = \gamma \left(- \int_{\Omega} H(r) \mathbf{v} \cdot \mathbf{v} + \int_{\Gamma} (\mathbf{v} \cdot \nabla r) (\mathbf{v} \cdot \mathbf{n}) \right) , \quad (5.59)$$

where \mathbf{n} is the outward normal vector and $H(r)$ is the Hessian matrix of the function r . But $r = 1 - Y$ is linear, hence $H(r) = 0$. On the other hand, on the boundary Γ we have $\nabla r = -\mathbf{n}$, so that we deduce that

$$\gamma \int_{\Omega} \nabla r \cdot [\nabla \mathbf{v}] \mathbf{v} = -\gamma \int_{\Gamma} (\mathbf{v} \cdot \mathbf{n})^2 . \quad (5.60)$$

From (5.57), (5.58) and (5.60) we conclude that our form $a_{\gamma}(\cdot, \cdot)$ will be coercive on $\text{Ker } B$ if there exists a constant $c(\gamma, \mu) > 0$ such that

$$2\mu \int_{\Omega} |\boldsymbol{\epsilon}(\mathbf{v})|^2 - \gamma \int_{\Gamma} (\mathbf{v} \cdot \mathbf{n})^2 \geq c(\gamma, \mu) \int_{\Omega} |\boldsymbol{\epsilon}(\mathbf{v})|^2 \quad \forall \mathbf{v} \in \text{Ker } B . \quad (5.61)$$

By (5.61) we first infer that for $\gamma \leq 0$ we can simply take $c(\gamma, \mu) = 2\mu$. Furthermore, setting

$$\alpha_M = \sup_{\mathbf{v} \in \text{Ker } B} \frac{\int_{\Gamma} (\mathbf{v} \cdot \mathbf{n})^2}{\int_{\Omega} |\boldsymbol{\epsilon}(\mathbf{v})|^2} > 0 , \quad (5.62)$$

we see that condition (5.61) still holds whenever

$$\gamma < \frac{2\mu}{\alpha_M} . \quad (5.63)$$

Remark 5.2.4. We remark that condition (5.61) cannot hold for arbitrarily large values of γ . Indeed, let \mathbf{w} be a function in $\text{Ker } B$ which does not vanish on Γ . Hence

$$\int_{\Gamma} (\mathbf{w} \cdot \mathbf{n})^2 > 0 .$$

Choosing γ^* as

$$\gamma^* := \frac{2\mu \int_{\Omega} |\boldsymbol{\epsilon}(\mathbf{w})|^2}{\int_{\Gamma} (\mathbf{w} \cdot \mathbf{n})^2} , \quad (5.64)$$

it follows that

$$2\mu \int_{\Omega} |\boldsymbol{\epsilon}(\mathbf{w})|^2 - \gamma \int_{\Gamma} (\mathbf{w} \cdot \mathbf{n})^2 \leq 0 \quad (5.65)$$

for all $\gamma \geq \gamma^*$. As a consequence, coercivity on the kernel surely fails for sufficiently large values of γ .

We now give an estimate of α_M by establishing the following Proposition.

Proposition 5.2.5. Suppose that $\Omega = (-1, 1) \times (-1, 1)$. Then $\alpha_M \leq 2/3$.

The proof for this Proposition is reported in Appendix B.

Remark 5.2.6. We remark that the above estimate of α_M is not guaranteed to be sharp. However, it is sufficient for our subsequent considerations.

To summarize, our analysis shows that the linearized *continuous* problem (5.49) is well-posed and *positive-definite* on the relevant kernel $\text{Ker } B$ if

$$\gamma \in \left(-\infty, \frac{2\mu}{\alpha_M} \right) \supseteq (-\infty, 3\mu) . \quad (5.66)$$

5.2.4 Discrete stability range: some theoretical results

For a finite analysis of the problem presented in Section 5.2.2, one should obviously focus on schemes which are reliable at least in the infinitesimal strain regime, otherwise even the first iteration step will fail. This can be accomplished by considering finite element methods satisfying the discrete *inf-sup* condition, as the ones studied in this Section.

As proved in Section 5.2.3, the continuous linearized problems (5.49) are surely stable, in the sense that both the *inf-sup* and the *coercivity on the kernel* conditions hold true, whenever the parameter γ satisfies

$$\gamma \in (-\infty, 3\mu) . \quad (5.67)$$

On the other hand, the linearized problems (5.49) become unstable for suitable large values of γ (cf. Remark 5.2.4). We point out that this lack of stability is only addressed to a failure of the *coercivity on the kernel* condition. Indeed, for the proposed problem the *inf-sup* condition is *independent* of γ , and therefore it is the same one required for the small deformation framework.

Since a reliable numerical approximation should be able to correctly reproduce the stability properties of the continuous problem, the discussion above highlights the importance of studying whether or not a given finite element method satisfies a discrete *coercivity on the kernel* condition, at least for γ in the range shown by (5.67). With this respect, we consider the extension to large deformation of the MINI element (cf. Arnold *et al.* [1984]) and of the QME element (cf. Pantuso and Bathe [1995, 1997]), rigorously proving that their stability range are somehow quite different from the continuous problem one. However, we point out that our theoretical analysis is far from being *complete*, although

in accordance with the numerical tests presented in Section 5.2.5.

5.2.4.1 The MINI element.

We now consider the discretized counterpart of problem (5.49), using the MINI element (cf. Arnold *et al.* [1984]).

Let \mathcal{T}_h be a triangular mesh of Ω , h being the mesh size. For the discretization of the displacement field, we take

$$U_h = \{ \mathbf{v}_h \in U : \mathbf{v}_h|_T \in \mathcal{P}_1(T)^2 + \mathcal{B}(T)^2 \quad \forall T \in \mathcal{T}_h \} , \quad (5.68)$$

where $\mathcal{P}_1(T)$ is the space of linear functions on T , and $\mathcal{B}(T)$ is the linear space generated by b_T , the standard cubic bubble function on T . For the pressure discretization, we take

$$P_h = \{ q_h \in H^1(\Omega) : q_h|_T \in \mathcal{P}_1(T) \quad \forall T \in \mathcal{T}_h \} . \quad (5.69)$$

Therefore, the discretization of problem (5.49) reads as follows.

Find $(\mathbf{u}_h; p_h) \in U_h \times P_h$ such that:

$$\left\{ \begin{array}{ll} 2\mu \int_{\Omega} \boldsymbol{\varepsilon}(\mathbf{u}_h) : \boldsymbol{\varepsilon}(\mathbf{v}_h) - \gamma \int_{\Omega} r (\nabla \mathbf{u}_h)^T : \nabla \mathbf{v}_h \\ \quad \quad \quad + \int_{\Omega} p_h \operatorname{div} \mathbf{v}_h = \Delta \gamma \int_{\Omega} \mathbf{f} \cdot \mathbf{v}_h & \forall \mathbf{v}_h \in U_h \\ \int_{\Omega} q_h \operatorname{div} \mathbf{u}_h = 0 & \forall q_h \in P_h . \end{array} \right. \quad (5.70)$$

Introducing the discrete kernel as

$$K_h = \left\{ \mathbf{v}_h \in U_h : \int_{\Omega} q_h \operatorname{div} \mathbf{u}_h = 0 \quad \forall q_h \in P_h \right\} , \quad (5.71)$$

we are interested in analyzing for which γ there exists a constant $c_M(\gamma, \mu) > 0$ such that

$$a_{\gamma}(\nabla \mathbf{v}_h, \nabla \mathbf{v}_h) \geq c_M(\gamma, \mu) \int_{\Omega} | \boldsymbol{\varepsilon}(\mathbf{v}_h) |^2 \quad \forall \mathbf{v}_h \in K_h , \quad (5.72)$$

where

$$a_{\gamma}(\nabla \mathbf{v}_h, \nabla \mathbf{v}_h) := 2\mu \int_{\Omega} \boldsymbol{\varepsilon}(\mathbf{v}_h) : \boldsymbol{\varepsilon}(\mathbf{v}_h) - \gamma \int_{\Omega} r (\nabla \mathbf{v}_h)^T : \nabla \mathbf{v}_h . \quad (5.73)$$

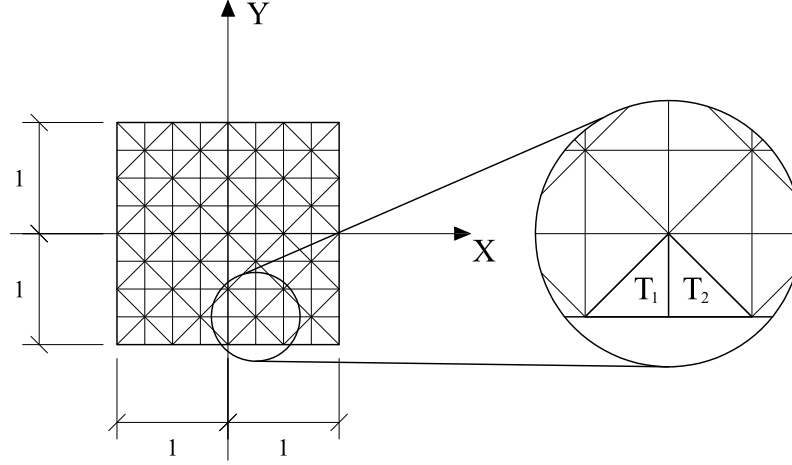


Figure 5.11. Triangular mesh for the MINI element.

We develop our analysis considering the meshes used for the numerical tests presented in Section 5.2.5. Therefore \mathcal{T}_h is built by squares of side $2h$, each divided into eight triangles according with the pattern shown in figure 5.11.

We have the following results.

Proposition 5.2.7. For problem (5.70), the discrete coercivity on the kernel condition (5.72) does not hold, whenever $\gamma > 3\mu/2$.

Proposition 5.2.8. For problem (5.70), the discrete coercivity on the kernel condition (5.72) is satisfied, independently of the mesh size, whenever $\gamma < \mu$.

The proofs for these Propositions are reported in Appendix B.

5.2.4.2 The QME element.

We now consider the discretized counterpart of problem (5.49), using the QME quadrilateral method proposed by Pantuso and Bathe [1997] and based on the *Enhanced Strain Technique*. We have already pointed out that this scheme optimally performs in small deformation regimes, as theoretically proved in Lovadina [1997].

For our analysis we consider uniform meshes \mathcal{T}_h formed by equal square elements K with side length h , as the ones used in the numerical tests of Section 5.2.5.

The Pantuso-Bathe element is described by the following choice of spaces. For the discretization of the displacement field, we take

$$U_h = \{ \mathbf{v}_h \in U : \mathbf{v}_h|_K \in \mathcal{Q}_1(K)^2 \quad \forall K \in \mathcal{T}_h \} , \quad (5.74)$$

where $\mathcal{Q}_1(K)$ is the standard space of bilinear functions. For the pressure discretization, we take

$$P_h = \{ q_h \in H^1(\Omega) : q_h|_K \in \mathcal{Q}_1(K) \quad \forall K \in \mathcal{T}_h \} . \quad (5.75)$$

Furthermore, the *Enhanced Strain* space is described by

$$S_h = \{ \mathbf{E}_h \in (L^2(\Omega))^4 : \mathbf{E}_h|_K \in E_6(K) \quad \forall K \in \mathcal{T}_h \} . \quad (5.76)$$

Above, $E_6(K)$ is the space of tensor-valued functions defined on K , spanned by the following shape functions

$$\begin{bmatrix} \alpha_1\xi + \alpha_2\xi\eta & ; & \alpha_3\xi \\ \alpha_4\eta & ; & \alpha_5\eta + \alpha_6\xi\eta \end{bmatrix} \quad \text{with } \alpha_i \in \mathbf{R} , \quad (5.77)$$

where (ξ, η) denotes the standard local coordinates on K .

Therefore, the discretization of problem (5.49) reads as follows.

Find $(\mathbf{u}_h, \mathbf{H}_h; p_h) \in (U_h \times S_h) \times P_h$ such that

$$\left\{ \begin{array}{l} 2\mu \int_{\Omega} (\nabla \mathbf{u}_h + \mathbf{H}_h)^S : (\nabla \mathbf{v}_h + \mathbf{E}_h)^S - \gamma \int_{\Omega} r (\nabla \mathbf{u}_h + \mathbf{H}_h)^T : (\nabla \mathbf{v}_h + \mathbf{E}_h) \\ + \int_{\Omega} p_h (\operatorname{div} \mathbf{v}_h + \operatorname{tr} \mathbf{E}_h) = \Delta \gamma \int_{\Omega} \mathbf{f} \cdot \mathbf{v}_h \quad \forall (\mathbf{v}_h, \mathbf{E}_h) \in U_h \times S_h \\ \int_{\Omega} q_h (\operatorname{div} \mathbf{u}_h + \operatorname{tr} \mathbf{H}_h) = 0 \quad \forall q_h \in P_h . \end{array} \right. \quad (5.78)$$

Introducing the discrete kernel as

$$K_h = \left\{ (\mathbf{v}_h, \mathbf{E}_h) \in U_h \times S_h : \int_{\Omega} q_h (\operatorname{div} \mathbf{v}_h + \operatorname{tr} \mathbf{E}_h) = 0 \quad \forall q_h \in P_h \right\} . \quad (5.79)$$

we are interested in analyzing for which γ there exists a constant $c_E(\gamma, \mu)$ such that (cf. (5.51))

$$a_\gamma(\nabla \mathbf{v}_h + \mathbf{E}_h, \nabla \mathbf{v}_h + \mathbf{E}_h) \geq c_E(\gamma, \mu) \int_{\Omega} (|\boldsymbol{\epsilon}(\mathbf{v}_h)|^2 + |\mathbf{E}_h|^2) \quad (5.80)$$

for every $(\mathbf{v}_h, \mathbf{E}_h) \in K_h$.

We have the following result.

Proposition 5.2.9. For the choice (5.74)–(5.77), the discrete coercivity on the kernel condition does not hold, whenever $\gamma > \mu$.

The proof for this Proposition is reported in Appendix B.

5.2.5 Numerical tests

We now study the computational performance of specific finite element interpolations on the model problem presented in Section 5.2.2. In particular, we wish to numerically detect the stability range of the elements under investigation and compare such numerical results with the theoretical ones obtained for the *discrete* problems in Sections 5.2.4.1–5.2.4.2 and for the *continuous* problem in Section 5.2.2.

Besides the interpolations discussed in Sections 5.2.4.1 and 5.2.4.2, for the numerical investigation we also consider the so-called Q2P1 (see, for instance, Hughes [2000]), since this is commonly considered as a very stable element. Accordingly, we deal with the following interpolation schemes:

- MINI – Triangular element with piecewise linear continuous approximation for both the displacements and the pressure, with the displacements enriched by a cubic bubble as proposed in Arnold *et al.* [1984].
- QME – Quadrilateral element with piecewise bilinear continuous approximation for both the displacements and the pressure, enriched by the enhanced strains as proposed in Pantuso and Bathe [1997].
- Q2P1 – Quadrilateral element with piecewise biquadratic continuous approximation for the displacements and piecewise linear approximation for the pressure.

All the schemes have been implemented in FEAP (see Taylor [2001]). The model problem is sketched in Figure 5.2.2, and, assuming to express respectively forces and lengths

in KN and m , we set $\mu = 40$ and $\mathbf{f} = (0, \gamma)^T$, where γ plays the role of load multiplier. In particular, we find convenient to express the numerical results in terms of the nondimensional quantity $\tilde{\gamma}$ defined as $\tilde{\gamma} = \gamma L / \mu$ with L some problem characteristic length, in the following set equal to 1 for simplicity and consistent with the model problem.

For a given interpolation scheme and for a given mesh, to detect numerically the element stability range we progressively increase the load multiplier γ , adopting an iterative Newton-Raphson scheme to obtain the solution corresponding to the single load value from the solution corresponding to the previous load value. In particular, we increase the load multiplier until some form of numerical instabilities appears; we indicate the load multiplier corresponding to the appearance of numerical instabilities with γ_{cr} and its corresponding nondimensional multiplier with $\tilde{\gamma}_{cr}$. To investigate very large load multiplier intervals, we adopt different increments $\Delta\gamma$ depending on the load level (Table 5.8).

Clearly, the analyses are performed starting from $\tilde{\gamma} = 0$ for both positive and negative loading conditions, i.e. for $\tilde{\gamma} < 0$ and $\tilde{\gamma} > 0$. Finally, if we do not detect numerical instabilities even for extremely large values of the load multiplier ($\tilde{\gamma} > 10^6$) we set $\tilde{\gamma}_{cr} = \infty$.

Tables 5.9, 5.10 and 5.11 report the stability limits for the different interpolation schemes considered. From the tables we may make the following observations.

- The theoretical predictions for the MINI interpolation scheme are that the *discrete* problem is stable for $-\infty < \tilde{\gamma} < 1$ and unstable for $\tilde{\gamma} > 3/2$ (cf. Propositions 5.2.7 and 5.2.8). The results presented in Table 5.9 show that the corresponding *numerical* problem is stable for $-\infty < \tilde{\gamma} < 1$, unstable for $\tilde{\gamma} > 3/2$. In particular, the stability upper limit approaches monotonically 1 from above during the mesh refinement (i.e. for $h \rightarrow 0$). Accordingly, for the MINI interpolation scheme the numerical results of Table 5.9 confirm the theoretical predictions.
- The theoretical predictions for the QME interpolation scheme are that for sufficiently small h the *discrete* problem is unstable for $\tilde{\gamma} > 1$ (cf. Proposition 5.2.9). The results presented in Table 5.10 seem to indicate that for sufficiently small h the corresponding *numerical* problem is stable for $-\infty < \tilde{\gamma} < 1$ and unstable for $\tilde{\gamma} > 1$. In particular, the stability lower limit is decreasing almost linearly with h , approaching $-\infty$ for $h \rightarrow 0$, while the stability upper limit is about 1 but it does not seem to have a smooth convergence. Accordingly, also for the QME interpolation scheme the numerical results presented in Table 5.10 confirm the theoretical predictions.

- We do not have theoretical prediction for the Q2P1 *discrete* problem, except the trivial one telling that the problem is stable in the range $-1 < \tilde{\gamma} < 1$ (cf. the proof of Proposition 5.2.8, at the beginning). However, the results presented in Table 5.11 and relative to the Q2P1 interpolation scheme seem to indicate that independently of h the *numerical* problem is stable for $-\infty < \tilde{\gamma} < \infty$. However, we note that during the analyses the finite element code FEAP gives a warning about a change in the stiffness matrix properties for $\tilde{\gamma}$ approximatively in the range $[1, 3/2]$. We believe that this point could be of interest, however it requires further investigations.

Finally, we recall that the *continuous* problem is stable at least for $-\infty < \tilde{\gamma} < 3$ (see (5.66)), and that for a sufficiently large value of $\tilde{\gamma}$ the problem gets unstable (see Remark 5.2.4). Therefore, we may conclude that all the interpolation schemes fail in properly detecting the stability range of the continuous problem. In particular, the MINI interpolation scheme seems to be the most effective in the sense that it is the element able to reproduce more closely (but still in a deficient form) the continuum problem; the QME interpolation scheme seems to be too “flexible” while the Q2P1 seems to be too “stiff”.

5.2.6 Conclusive considerations for Section 5.2

We have proposed in this Section a simple 2D finite strain problem depending on a loading parameter, for which a trivial solution can be easily computed. We have proved the stability of such a solution whenever the loading parameter stays in a suitable range of values. Furthermore, we have considered and analyzed the problem discretization by means of some mixed finite elements, which are known to optimally behave in the framework of small deformation problems. In particular, we have proved that the elements fail to properly detect the problem stability range. We have also presented several numerical experiments, in accordance with our theoretical predictions.

Table 5.8. Load increments $\Delta\gamma$ (depending on the load level γ) for the Newton-Raphson scheme.

$\Delta\gamma = 10^{-1}$	up to	$\gamma = 10^2$
$\Delta\gamma = 1$	up to	$\gamma = 10^3$
$\Delta\gamma = 10$	up to	$\gamma = 10^4$
$\Delta\gamma = 10^2$	up to	$\gamma = 10^5$
$\Delta\gamma = 10^3$	up to	$\gamma = 10^6$

Table 5.9. MINI element: numerical stability limits for the model problem.

mesh	$\tilde{\gamma}_{cr}^-$	$\tilde{\gamma}_{cr}^+$
4×4	$-\infty$	1.28
8×8	$-\infty$	1.22
16×16	$-\infty$	1.19
32×32	$-\infty$	1.18
64×64	$-\infty$	1.17
128×128	$-\infty$	1.12

Table 5.10. QME element: numerical stability limits for the model problem.

mesh	$\tilde{\gamma}_{cr}^-$	$\tilde{\gamma}_{cr}^+$
4×4	-52.8	1.21
8×8	-150	1.07
16×16	-335	0.998
32×32	-723	0.978
64×64	-1480	0.980
128×128	-2980	0.983

Table 5.11. Q2P1 element: numerical stability limits for the model problem.

mesh	$\tilde{\gamma}_{cr}^-$	$\tilde{\gamma}_{cr}^+$
4×4	$-\infty$	$+\infty$
8×8	$-\infty$	$+\infty$
16×16	$-\infty$	$+\infty$
32×32	$-\infty$	$+\infty$
64×64	$-\infty$	$+\infty$
128×128	$-\infty$	$+\infty$

6. CONCLUSIONS

Since numerical tools more and more find wide applications in engineering providing powerful modeling bases for design and diagnosis, in this work we have investigated different issues related to computational methods which can be useful in the continuously developing field of earthquake engineering.

Accordingly, in Chapter 2 we have presented a brief overview of significative problems dealing with reliable seismic device modeling as well as with new seismic design frontiers, and we have identified some interesting topics to be deeper studied within this context as *geometric nonlinearities, inelasticity, incompressibility, mesh and geometry complexity*. We have then presented some methods able to overcome part of these difficulties; in particular, the treated issues (each discussed in one of the subsequent Chapters) have been:

- isogeometric analysis for structural dynamics;
- shape memory alloys for earthquake engineering: applications and modeling;
- mixed-enhanced strain techniques for the study of incompressibility and geometric nonlinearities.

In Chapter 3, we have treated the application to structural dynamics of isogeometric analysis, a new technique based on Non-Uniform Rational B-Splines (NURBS), recently proposed by Hughes *et al.* [2005] and able to give good results in many fields as well as to work with *exact geometry* (i.e., no approximation through a mesh is required). When applied to the study of structural vibration, taking advantage of its basis function high continuity and point-wise positivity (implying mass matrix element-wise positivity), this method has shown very good and promising results in a variety of problems. First case studies have been truss and frame elements, membranes and plates. As compared with analogous classical finite element results, the method has exhibited a superior behaviour. Another investigated issue has been the possibility of developing, in a natural way, one- and two-dimensional rotation-free thin bending elements. The problem of the imposition

of boundary conditions on rotations both weakly and with Lagrange multipliers has been discussed and proved to be effective for rotation-free beam elements. Moreover, the exact geometry property of the method has been investigated on a three-dimensional circular problem. In this example, the capability of this technique of studying thin bending structures (a plate in this case) by means of 3D solid elements has been tested, obtaining again good results. Finally, isogeometric analysis has been employed to study a geometrically complicated real problem, the NASA Aluminium Testbed Cylinder, for which extensive experimental modal results were available for single members as well as for the whole structure. The good agreement between numerical and experimental results has highlighted once more the great potential of the method.

Since all of these preliminary results have shown that this technique could be an important tool in the framework of structural vibration study, more research in this context is needed for the future. Required interesting issues are deeper studies on different parametrizations (in particular to avoid the appearance of so-called “outlier frequencies”, i.e. discrete spectrum “optical” branches) and on lumped mass formulations.

Further details on this piece of research may be found in Reali [2004, 2005] and Cottrell *et al.* [2005a,b].

In Chapter 4 the issue of shape memory alloys (SMAs) in earthquake engineering has been considered. After an introduction to SMAs and their general applications, the state-of-the-art of studies and use of such smart material in the field of earthquake engineering has been discussed. The potential of SMA properties has been shown to be promising and intriguing for different seismic applications and the need for an exhaustive modeling has been highlighted as well. Accordingly, a new 3D constitutive model for describing the macroscopic behaviour of SMAs has been proposed. With respect to the existing models considered as a starting point (i.e. Souza *et al.* [1998] and Auricchio and Petrini [2004a]), the new one is able to describe SMA macroscopic behaviours taking into account also permanent inelasticity effects. Such effects can be introduced both with saturating or non-saturating evolution and also degradation can be included. Many numerical experiments have been presented in order to show and assess the model performances both in uniaxial and non-proportional multi-axial problems, all of them giving good results.

A required future development is the implementation of such a model in a finite element framework in order to be able to model and simulate the behaviour of an entire SMA seismic device.

More details on the model and on its simplified one-dimensional formulation may be found in Auricchio and Reali [2005a,b] (1D) and in Auricchio *et al.* [2005d] (3D).

Finally, in the last Chapter we have studied solutions for incompressibility and large strain elasticity problems in the framework of mixed-enhanced strain techniques. The Chapter has been divided into two parts.

In the first one, the mixed-enhanced strain technique has been investigated within the context of the u/p formulation for compressible, nearly incompressible and incompressible linear elasticity problems. A general theoretical analysis has been developed, extending the results presented by Lovadina [1997]; in particular, optimal uniform error bounds for the L^2 -norm of the displacements are proved. Moreover, several numerical tests on triangular and quadrilateral elements have been presented in order to assess the computational performances of the finite elements under investigation. In particular, numerical results have confirmed the convergence rates predicted by the theory.

In the second part, a simple 2D finite strain problem depending on a loading parameter, for which a trivial solution can be easily computed, has been considered. The stability of such a solution has been proved whenever the loading parameter stays in a suitable range of values. Furthermore, the problem discretization has been considered and analyzed by means of some mixed finite elements (including the best performing mixed-enhanced element of the previous part), which are known to optimally behave in the framework of small deformation problems. In particular, the elements have been proved to fail in properly detecting the problem stability range. Several numerical experiments have also been presented, all of them showing results in accordance with the theoretical predictions. Future developments can be the extension from two to three dimensions and deeper studies on the large strain problem in order to find “cures” for the investigated finite elements, to make their stability range closer to the one for the continuous problem. A promising approach in this direction is the stabilization of the mixed-enhanced strain technique in the fashion of Maniatty *et al.* [2002]. Furthermore, the identification of other model problems as the one presented herein could constitute an important tool for the study of finite element stability in the large strain regime.

Further information on these topic can be found in Auricchio *et al.* [2004, 2005a,b].

REFERENCES

- Armero, F. [2000] “On the locking and stability of finite elements in finite deformation plane strain problems,” *Computers & Structures*, Vol. 75, pp. 261–290.
- Arnold, D. N., Brezzi, F., and Fortin, M. [1984] “A stable finite element for the stokes equation,” *Calcolo*, Vol. 21, pp. 337–344.
- ARPACK [1999] <http://www.caam.rice.edu/software/ARPACK/>.
- Arrigoni, M., Auricchio, F., Cacciafesta, V., Petrini, L., and Pietrabissa, R. [2001] “Cyclic effects in shape-memory alloys: a one-dimensional continuum model,” *Journal de Physique IV France*, Vol. 11, pp. 577–582.
- Auricchio, F. [1995] “Shape memory alloys: micromechanics, macromodeling and numerical simulations,” Ph.D. thesis, Department of Civil and Environmental Engineering, University of California at Berkeley.
- Auricchio, F., Beirao da Veiga, L., Lovadina, C., and Reali, A. [2004] “Enhanced strain methods for elasticity problems,” *Proceedings of the Fourth European Congress on Computational Methods in Applied Sciences and Engineering (Jyvaskyla)*.
- Auricchio, F., Beirao da Veiga, L., Lovadina, C., and Reali, A. [2005a] “An analysis of some mixed-enhanced finite element for plane linear elasticity,” *Computer Methods in Applied Mechanics and Engineering*, Vol. 194, pp. 2947–2968.
- Auricchio, F., Beirao da Veiga, L., Lovadina, C., and Reali, A. [2005b] “A stability study of some mixed finite elements for large deformation elasticity problems,” *Computer Methods in Applied Mechanics and Engineering*, Vol. 194, pp. 1075–1092.
- Auricchio, F., Mielke, A., and Stefanelli, U. [2005c] “A rate-independent model for the evolution of shape memory materials,” *in preparation*.
- Auricchio, F. and Petrini, L. [2004a] “A three-dimensional model describing stress-temperature induced solid phase transformations. part i: solution algorithm and boundary value problems,” *International Journal for Numerical Methods in Engineering*, Vol. 61, pp. 807–836.
- Auricchio, F. and Petrini, L. [2004b] “A three-dimensional model describing stress-temperature induced solid phase transformations. part ii: thermomechanical coupling

- and hybrid composite applications,” *International Journal for Numerical Methods in Engineering*, Vol. 61, pp. 716–737.
- Auricchio, F. and Reali, A. [2005a] “A one-dimensional model describing stress-induced solid phase transformation with residual plasticity,” *Proceedings of the II ECCOMAS Thematic Conference on Smart Structures and Materials (Lisbon)*.
- Auricchio, F. and Reali, A. [2005b] “A phenomenological one-dimensional model describing stress-induced solid phase transformation with permanent inelasticity,” *submitted to Computers & Structures*.
- Auricchio, F., Reali, A., and Stefanelli, U. [2005d] “A three-dimensional model describing stress-induced solid phase transformation with permanent inelasticity,” *submitted to International Journal of Plasticity*.
- Baratta, A. and Corbi, O. [2002] “On the dynamic behaviour of elastic-plastic structures equipped with pseudoelastic SMA reinforcements,” *Computational Materials Science*, Vol. 25, pp. 1–13.
- Barns, C. [2003] “Shape Memory and Superelastic Alloys,” <http://www.copper.org>.
- Bathe, K. J. [1996] *Finite Element Procedures*, Prentice Hall, Englewood Cliffs, NJ.
- Benninghof, J. and Lehoucq, R. [2004] “An automated multilevel substructuring method for eigenspace computations in linear elastodynamics,” *SIAM Journal of Scientific Computing*, Vol. 25, pp. 2084–2106.
- Bernardini, D. and Brancaleoni, F. [1999] “Shape memory alloys modelling for seismic applications,” *Atti del MANSIDE Project - Final Workshop - Memory Alloys for Seismic Isolation and Energy Dissipation Devices*, pp. 73–84, part II.
- Blacker, T. D. [1994] “CUBIT mesh generation environment users manual vol. 1,” Tech. rep., Sandia National Laboratories, Albuquerque, NM.
- Bonet, J. and Wood, R. D. [1997] *Nonlinear Continuum Mechanics for Finite Element Analysis*, Cambridge University Press.
- Bouvet, C., Calloch, S., and Lexcellent, C. [2004] “A phenomenological model for pseudoelasticity of shape memory alloys under multiaxial proportional and nonproportional loadings,” *European Journal of Mechanics A/Solids*, Vol. 23, pp. 37–61.
- Braess, D. [1998] “Enhanced assumed strain elements and locking in membrane problems,” *Computer Methods in Applied Mechanics and Engineering*, Vol. 165, pp. 155–174.

- Braess, D., Carstensen, C., and Reddy, B. D. [2004] “Uniform convergence and a posteriori estimators for the enhanced strain finite element method,” *Numerische Mathematik*, Vol. 96, pp. 461–479.
- Brenner, S. C. and Sung, L. Y. [1992] “Linear finite element methods for planar linear elasticity,” *Mathematics of Computation*, Vol. 59, pp. 321–338.
- Brezzi, F. and Fortin, M. [1991] *Mixed and Hybrid Finite Element Methods*, Springer-Verlag, New York.
- Brillouin, L. [1953] *Wave Propagation in Periodic Structures*, Dover Publications, Inc.
- Bruno, S. and Valente, C. [2002] “Comparative response analysis of conventional and innovative seismic protection strategies,” *Earthquake Engineering and Structural Dynamics*, Vol. 31, pp. 1067–1092.
- Buehrle, R., Fleming, G., Pappa, R., and Grosveld, F. [2000] “Finite element model development for aircraft fuselage structures,” *Proceedings of XVIII the International Modal Analysis Conference*, San Antonio, TX.
- Cardone, D., Dolce, M., Bixio, A., and Nigro, D. [1999] “Experimental tests on SMA elements,” *Atti del MANSIDE Project - Final Workshop - Memory Alloys for Seismic Isolation and Energy Dissipation Devices*, pp. 85–104, part II.
- Chopra, A. K. [2001] *Dynamics of Structures. Theory and Applications to Earthquake Engineering, Second Edition*, Prentice-Hall, Upper Saddle River, New Jersey.
- Chung, J. and Hulbert, G. M. [1993] “A time integration algorithm for structural dynamics with improved numerical dissipation: The generalized- α method,” *Journal of Applied Mechanics*, Vol. 60, pp. 371–75.
- Ciarlet, P. G. [1978] *The Finite Element Methods for Elliptic Problems*, North-Holland, Amsterdam.
- Cirak, F. and Ortiz, M. [2001] “Fully C^1 -conforming subdivision elements for finite deformation thin shell analysis,” *International Journal of Numerical Methods in Engineering*, Vol. 51, pp. 813–833.
- Cirak, F., Ortiz, M., and Schröder, P. [2000] “Subdivision Surfaces: a New Paradigm for Thin Shell Analysis,” *International Journal for Numerical Methods in Engineering*, Vol. 47, pp. 2039–2072.

- Cirak, F., Scott, M. J., Antonsson, E. K., Ortiz, M., and Schröder, P. [2002] “Integrated Modeling, Finite-Element Analysis and Engineering Design for Thin Shell Structures using Subdivision,” *Computer-Aided Design*, Vol. 34, pp. 137–148.
- Clarke, F. H. [1990] *Optimization and nonsmooth analysis. Second edition*, Classics in Applied Mathematics, 5, Society for Industrial and Applied Mathematics (SIAM), Philadelphia, PA.
- Clément, P. [1975] “Approximation by finite element functions using local regularization,” *RAIRO Analyse Numerique*, Vol. 9, pp. 77–84.
- Clough, R. W. and Penzien, J. [1993] *Dynamics of Structures*, McGraw-Hill, New York.
- Corbi, O. [2003a] “Influence of SMAs on the attenuation of effects of P-Delta type in shear frames,” *Steel & Composite Structures*.
- Corbi, O. [2003b] “Shape memory alloys and their application in structural oscillations attenuation,” *Simulation Modelling Practice and Theory*.
- Cottrell, J. A., Hughes, T. J. R., Bazilevs, Y., and Reali, A. [2005a] “Isogeometric analysis: Exact geometry and accurate analysis of real structures,” *Proceedings of the 8th US National Congress on Computational Mechanics (Austin)*.
- Cottrell, J. A., Reali, A., Bazilevs, Y., and Hughes, T. J. R. [2005b] “Isogeometric Analysis of structural vibrations,” *submitted to Computer Methods in Applied Mechanics and Engineering*.
- Couchman, L., Dey, S., and Barzow, T. [2003] *ATC Eigen-Analysis, STARS / ARPACK / NRL Solver*, Naval Research Laboratory, Englewood Cliffs, NJ.
- DesRoches, R. and Delemont, M. [2002] “Seismic retrofit of simply supported bridges using shape memory alloys,” *Engineering Structures*, Vol. 24, pp. 325–332.
- DesRoches, R., McCormick, J., and Delemont, M. [2004] “Cyclic properties of shape memory alloy wires and bars,” *Journal of Structural Engineering - ASCE*, Vol. 130, pp. 38–46.
- DesRoches, R. and Smith, B. [2004] “Shape memory alloys in seismic resistant design and retrofit: a critical review of the state of the art, potential and limitations,” *Journal of Earthquake Engineering*, Vol. 8, pp. 415–429.
- Dolce, M. and Cardone, D. [2001a] “Mechanical behaviour of shape memory alloys for seismic applications 1. Martensite and austenite bars subjected to torsion,” *International Journal of Mechanical Sciences*, Vol. 43, pp. 2631–2656.

- Dolce, M. and Cardone, D. [2001b] "Mechanical behaviour of shape memory alloys for seismic applications 2. Austenite NiTi wires subjected to tension," *International Journal of Mechanical Sciences*, Vol. 43, pp. 2657–2677.
- Dolce, M., Cardone, D., and Marnetto, R. [2000] "Implementation and testing of passive control devices based on shape memory alloys," *Earthquake Engineering and Structural Dynamics*, Vol. 29, pp. 945–968.
- Dolce, M., Nicoletti, M., and Ponzo, F. C. [2001] "Protezione sismica con dispositivi basate sulle leghe a memoria di forma: il progetto MANSIDE e gli ulteriori sviluppi," *Ingegneria Sismica*, Vol. 1, pp. 66–78.
- Duerig, T. and Pelton, A., eds. [2003] *SMST-2003 Proceedings of the International Conference on Shape Memory and Superelastic Technology Conference*, ASM International.
- Duerig, T. W., Melton, K. N., Stoekel, D., and Wayman, C. M. [1990] *Engineering aspects of shape memory alloys*, Butterworth-Heinemann, London.
- Engel, G., Garikipati, K., Hughes, T. J. R., Larson, M. G., Mazzei, L., and Taylor, R. L. [2002] "Continuous/Discontinuous Finite Element Approximations of Fourth-Order Elliptic Problems in Structural and Continuum Mechanics with Applications to Thin Beams and Plates, and Strain Gradient Elasticity," *Computer Methods in Applied Mechanics and Engineering*, Vol. 191, pp. 669–3750.
- Farin, G. [1995] *NURBS curves and surfaces: from projective geometry to practical use*, A. K. Peters, Ltd., Natick, MA.
- FEMA 440 [2005] *Improvement of Nonlinear Static Analysis Procedures*, Prepared by Applied Technology Council - 55 Project, Washington D.C.
- FIP Industriale SpA [2005] http://www.fip-group.it/fip_ind/.
- Fried, I. and Malkus, D. S. [1976] "Finite Element Mass Lumping by Numerical Integration Without Convergence Rate Loss," *International Journal of Solids and Structures*, Vol. 11, pp. 461–466.
- Fugazza, D. [2003] "Shape-memory alloy devices in earthquake engineering: mechanical properties, constitutive modelling and numerical simulations," Master's thesis, European School for Advanced Studies in Reduction of Seismic Risk - Università degli Studi di Pavia.

- Govindjee, S. and Miehe, C. [2001] "A multi-variant martensitic phase transformation model: formulation and numerical implementation," *Computer Methods in Applied Mechanics and Engineering*, Vol. 191, pp. 215–238.
- Grant, D. N., Fenves, G. L., and Auricchio, F. [2005] *Modelling and Analysis of High-damping Rubber Bearings for the Seismic Protection of Bridges*, IUSS Press, Pavia.
- Grosveld, F., Pritchard, J., Buehrle, R., and Pappa, R. [2002] "Finite element modeling of the NASA Langley Aluminum Testbed Cylinder," .
- Han, Y.-L., Li, Q. S., Li, A.-Q., Leung, A. Y. Y., and Lin, P.-H. [2003] "Structural vibration control by shape memory alloy damper," *Earthquake Engineering and Structural Dynamics*, Vol. 32, pp. 483–494.
- Helm, D. and Haupt, P. [2003] "Shape memory behaviour: modelling within continuum thermomechanics," *International Journal of Solids and Structures*, Vol. 40, pp. 827–849.
- Hilber, H. and Hughes, T. J. R. [1978] "Collocation, dissipation, and overshoot for time integration schemes in structural dynamics," *Earthquake Engineering and Structural Dynamics*, Vol. 6, pp. 99–117.
- Hughes, T. J. R. [2000] *The Finite Element Method: Linear Static and Dynamic Finite Element Analysis*, Dover Publications, Mineola, New York.
- Hughes, T. J. R., Cottrell, J. A., and Bazilevs, Y. [2005] "Isogeometric Analysis: CAD, Finite Elements, NURBS, Exact Geometry and Mesh Refinement," *Computer Methods in Applied Mechanics and Engineering*, Vol. 194, pp. 4135–4195.
- Hughes, T. J. R., Hilber, H. M., and Taylor, R. L. [1976] "A Reduction Scheme for Problems of Structural Dynamics," *International Journal of Solids and Structures*, Vol. 12, pp. 749–767.
- Johnson Matthey [2005] <http://www.jmmedical.com>.
- Klaas, O., Maniatty, A. M., and Shephard, M. S. [1999] "A stabilized mixed petrov-galerkin finite element method for finite elasticity. formulation for linear displacement and pressure interpolation," *Computer Methods in Applied Mechanics and Engineering*, Vol. 180, pp. 65–79.
- Lagoudas, D. C. and Entchev, P. [2004] "Modeling of transformation-induced plasticity and its effect on the behavior of porous shape memory alloys. part i: constitutive model for fully dense smas," *Mechanics of Materials*, Vol. 36, pp. 865–892.

- Le Tallec, P. [1982] "Existence and approximation results for nonlinear mixed problems: application to incompressible finite elasticity," *Numerische Mathematik*, Vol. 38, pp. 365–382.
- Le Tallec, P. [1994] "Numerical methods for nonlinear three-dimensional elasticity," *Handbook of Numerical Analysis*, eds. P. G. Ciarlet and J. L. Lions, Vol. III, pp. 465–622, Elsevier Science, North Holland.
- Leclercq, S. and Lexcellent, C. [1996] "A general macroscopic description of the thermo-mechanical behavior of shape memory alloys," *Journal of Mechanics and Physics of Solids*, Vol. 44, pp. 953–980.
- Levitas, V. I. [1998] "Thermomechanical theory of martensitic phase transformations in inelastic materials," *International Journal of Solids and Structures*, Vol. 35, pp. 889–940.
- Lim, T. J. and McDowell, D. L. [1995] "Path dependence of shape memory alloys during cyclic loading," *Journal of Intelligent Material Systems and Structures*, Vol. 6, pp. 817–830.
- Lovadina, C. [1997] "Analysis of strain-pressure finite element methods for the stokes problem," *Numerical Methods for PDE's*, Vol. 13, pp. 717–730.
- Lovadina, C. and Auricchio, F. [2003] "On the enhanced strain technique for elasticity problems," *Computers & Structures*, Vol. 81, pp. 777–787.
- Maniatty, A. M., Liu, Y., Klaas, O., and Shephard, M. S. [2002] "Higher order stabilized finite element method for hyperelastic finite deformation," *Computer Methods in Applied Mechanics and Engineering*, Vol. 191, pp. 1491–1503.
- Mazzolani, F. M. and Mandara, A. [2002] "Modern trends in the use of special metals for the improvement of historical and monumental structures," *Engineering Structures*, Vol. 24, pp. 843–856.
- Meirovitch, L. [1967] *Analytical Methods in Vibrations*, The MacMillan Company, New York.
- Memory-Metalle GmbH [2005] <http://www.memory-metalle.de>.
- Memry Corporation [2005] <http://www.memry.com>.
- Mielke, A. [2005] "Evolution of rate-independent systems," *Handbook of Differential Equations*, eds. C. Dafermos and E. Feireisl, Elsevier (to appear).

- Miranda, I., Ferencz, R. M., and Hughes, T. J. R. [1989] “An improved implicit-explicit time integration method for structural dynamics,” *Earthquake Engineering and Structural Dynamics*, Vol. 18, pp. 643–653.
- Montgomery, D. C., Runger, C., and Hubele, N. F. [2003] *Engineering Statistics*, 3rd ed., Wiley, New York.
- Moroni, M. O., Saldivia, R., Sarrazin, M., and Sepulveda, A. [2002] “Damping characteristics of a CuZnAlNi shape memory alloy,” *Materials Science and Engineering*, pp. 313–319, A335.
- Nagtegaal, J. C. and Fox, D. D. [1996] “Using assumed enhanced strain elements for large compressive deformation,” *International Journal of Solids and Structures*, Vol. 33, pp. 3151–3159.
- Nitinol Devices & Components (NDC) [2005] <http://www.nitinol.com>.
- NZS 1170.5 [2004] *Structural Design Actions*, New Zealand Standard Association, Wellington.
- Ocel, J., DesRoches, R., Leon, R. T., Hess, W. G., Krumme, R., Hayes, J. R., and Sweeney, S. [2004] “Steel beam-column connections using shape memory alloys,” *Journal of Structural Engineering - ASCE*, Vol. 130, pp. 732–740.
- Oñate, E. and Cervera, M. [1993] “Derivation of Thin Plate Bending Elements with One Degree of Freedom per Node: a Simple Three Node Triangle,” *Engineering Computations*, Vol. 10, pp. 543–561.
- Oñate, E. and Zarate, F. [2000] “Triangular Plate and Shell Elements,” *International Journal for Numerical Methods in Engineering*, Vol. 47, pp. 557–603.
- OPCM 3274 [2003] *Primi elementi in materia di criteri generali per la classificazione sismica del territorio nazionale e di normative tecniche per le costruzioni in zona sismica*, Gazzetta Ufficiale 72, Roma.
- Paiva, A., Savi, M. A., Braga, A. M. B., and Pacheco, P. M. C. L. [2005] “A for shape memory alloys considering tensile-compressive asymmetry and plasticity,” *International Journal of Solids and Structures*, Vol. 42, pp. 3439–3457.
- Pantuso, D. and Bathe, K. J. [1995] “A four-node quadrilateral mixed-interpolated element for solids and fluids,” *Mathematical Models & Methods in Applied Sciences*, Vol. 5, pp. 1113–1128.

- Pantuso, D. and Bathe, K. J. [1997] "On the stability of mixed finite elements in large strain analysis of incompressible solids," *Finite Elements in Analysis and Design*, Vol. 28, pp. 83–104.
- Paulay, T. and Priestley, M. J. N. [1992] *Seismic Design of Reinforced Concrete and Masonry Buildings*, Wiley, New York.
- Pence, T. J. [1999] "Mathematical modelling of shape memory alloys," *Atti del MAN-SIDE Project - Final Workshop - Memory Alloys for Seismic Isolation and Energy Dissipation Devices*, pp. 45–58, part II.
- Penelis, G. G. and Kappos, A. J. [1997] *Earthquake-resistant Concrete Structures*, E & FN Spon, London.
- Peultier, B., Benzineb, T., and Patoor, E. [2004] "Modelling of the martensitic phase transformation for finite element computation," *Journal de Physique IV France*, Vol. 115, pp. 351–359.
- Phaal, R. and Calladine, C. R. [1992a] "A Simple Class of Finite-Elements for Plate and Shell Problems. 1. Elements for Beams and Thin Flat Plates," *International Journal for Numerical Methods in Engineering*, Vol. 35, pp. 955–977.
- Phaal, R. and Calladine, C. R. [1992b] "A Simple Class of Finite-Elements for Plate and Shell Problems. 2. An Element for Thin Shells with Only Translational Degrees of Freedom," *International Journal for Numerical Methods in Engineering*, Vol. 35, pp. 979–996.
- Piedboeuf, M. C. and Gauvin, R. [1998] "Damping behaviour of shape memory alloys: strain amplitude, frequency and temperature effects," *Journal of Sound and Vibration*, Vol. 214, pp. 885–901.
- Piegl, L. and Tiller, W. [1997] *The NURBS Book, 2nd Edition*, Springer-Verlag, New York.
- Piltner, R. and Taylor, R. L. [2000] "Triangular finite elements with rotational degrees of freedom and enhanced strain modes," *Computers & Structures*, Vol. 75, pp. 361–368.
- Prudhomme, S., Pascal, F., Oden, J. T., and Romkes, A. [2001] "A Priori Error Estimate for the Baumann-Oden Version of the Discontinuous Galerkin Method," *Comptes Rendus de l'Academie des Sciences I, Numerical Analysis*, Vol. 332, pp. 851–856.

- Raniecki, B. and Lexcellent, C. [1994] “ r_l models of pseudoelasticity and their specification for some shape-memory solids,” *European Journal of Mechanics, A: Solids*, Vol. 13, pp. 21–50.
- Reali, A. [2004] “An isogeometric analysis approach for the study of structural vibrations,” Master’s thesis, European School for Advanced Studies in Reduction of Seismic Risk - Università degli Studi di Pavia.
- Reali, A. [2005] “An isogeometric analysis approach for the study of structural vibrations,” *submitted to Journal of Earthquake Engineering*.
- Reddy, B. D. and Simo, J. C. [1995] “Stability and convergence of a class of enhanced strain methods,” *SIAM Journal on Numerical Analysis*, Vol. 32, pp. 705–1728.
- Reese, S., Küssner, M., and Reddy, B. D. [1999] “A new stabilization technique for finite elements in non-linear elasticity,” *International Journal of Numerical Methods in Engineering*, Vol. 44, pp. 1617–1652.
- Reese, S. and Wriggers, P. [2000] “A stabilization technique to avoid hourglassing in finite elasticity,” *International Journal of Numerical Methods in Engineering*, Vol. 48, pp. 79–109.
- Rogers, D. F. [2001] *An Introduction to NURBS With Historical Perspective*, Academic Press, San Diego, CA.
- Shape Memory Applications Inc. [2005] <http://www.sma-inc.com>.
- Simo, J. C. and Armero, F. [1992] “Geometrically nonlinear enhanced strain mixed methods and the method of incompatible modes,” *International Journal of Numerical Methods in Engineering*, Vol. 33, pp. 1413–1449.
- Simo, J. C. and Hughes, T. J. R. [1998] *Computational Inelasticity*, Springer-Verlag, New York.
- Simo, J. C. and Rifai, M. S. [1990] “A class of mixed assumed strain methods and the method of incompatible modes,” *International Journal of Numerical Methods in Engineering*, Vol. 29, pp. 1595–1638.
- Souza, A. C., Mamiya, E. N., and Zouain, N. [1998] “Three-dimensional model for solids undergoing stress-induced phase transformations,” *European Journal of Mechanics, A: Solids*, Vol. 17, pp. 789–806.
- Special Metals Corporation [2005] <http://www.specialmetals.com>.

- Strang, G. and Fix, G. [1973] *An Analysis of the Finite Element Method*, Prentice-Hall, Englewood Cliffs, NJ.
- Strnadel, B., Ohashi, S., Ohtsuka, H., Ishihara, T., and Miyazaki, S. [1995] "Cyclic stress-strain characteristics of Ti-Ni and Ti-Ni-Cu shape memory alloys," *Materials Science and Engineering*, Vol. 202, pp. 148–156.
- Tamai, H. and Kitagawa, Y. [2002] "Pseudoelastic behavior of shape memory alloy wire and its application to seismic resistance member for building," *Computational Materials Science*, Vol. 25, pp. 218–227.
- Taylor, R. L. [2001] "FEAP: A Finite Element Analysis Program, programmer manual," <http://www.ce.berkeley.edu/~rlt/feap/>.
- The A to Z of Materials (AZoM) [2005] <http://www.azom.com>.
- Tobushi, H., Shimeno, Y., Hachisuka, T., and Tanaka, K. [1998] "Influence of strain rate on superelastic properties of TiNi shape memory alloy," *Mechanics of Materials*, Vol. 30, pp. 141–150.
- Valente, C., Cardone, D., Lamonaca, B. G., and Ponzo, F. M. [1999] "Shaking table tests of structures with conventional and sma based protection devices," *Atti del MANSIDE Project - Final Workshop - Memory Alloys for Seismic Isolation and Energy Dissipation Devices*, pp. 177–194, part II.
- Van Humbeeck, J. [1999a] "General aspects of shape memory alloys," *Atti del MANSIDE Project - Final Workshop - Memory Alloys for Seismic Isolation and Energy Dissipation Devices*, pp. 9–44, part II.
- Van Humbeeck, J. [1999b] "Non-medical applications of shape memory alloys," *Materials Science and Engineering*, pp. 134–148, A273–275.
- Vogelius, M. [1983] "An analysis of the p -version of the finite element method for nearly incompressible materials. uniformly valid, optimal error estimates," *Numerische Mathematik*, Vol. 41, pp. 39–53.
- Wilde, K., Gardoni, P., and Fujino, Y. [2000] "Base isolation system with shape memory alloy device for elevated highway bridges," *Engineering Structures*, Vol. 22, pp. 222–229.
- Wilson, J. C. and Wesolowsky, M. J. [2005] "Shape memory alloys for seismic response modification: a state-of-the-art review," *Earthquake Spectra*, Vol. 21, pp. 569–601.

- Wolons, D., Gandhi, F., and Malovrh, B. [1998] “Experimental investigation of the pseudoelastic hysteresis damping characteristics of shape memory alloy wires,” *Journal of Intelligent Material Systems and Structures*, Vol. 9, pp. 116–126.
- Wriggers, P. and Reese, S. [1996] “A note on enhanced strain methods for large deformations,” *Computer Methods in Applied Mechanics and Engineering*, Vol. 135, pp. 201–209.

A. COMPUTATION OF THE ISOGEOMETRIC ANALYSIS ORDER OF ACCURACY FOR THE ROD PROBLEM

Starting from the analytical expressions for the normalized discrete spectra obtained previously, it is possible to compute their order of accuracy by means of Taylor's expansions. In the following we show the computation of the order of accuracy for the rod problem using both consistent and lumped mass formulations and employing quadratic and cubic NURBS.

A.1 Order of accuracy employing quadratic NURBS and consistent mass

The analytical expression for the normalized discrete spectrum in this case is:

$$\frac{\omega^h}{\omega} = \frac{1}{\omega h} \sqrt{\frac{20(2 - \cos(\omega h) - \cos^2(\omega h))}{16 + 13 \cos(\omega h) + \cos^2(\omega h)}}. \quad (\text{A.1})$$

First, we make use of the expansion $\cos(x) \sim 1 - x^2/2 + x^4/4! - x^6/6!$, obtaining after simple computations:

$$\frac{\omega^h}{\omega} \sim \frac{1}{\omega h} \sqrt{\frac{30(\omega h)^2 - \frac{15}{2}(\omega h)^4 + \frac{11}{12}(\omega h)^6}{30 - \frac{15}{2}(\omega h)^2 + \frac{7}{8}(\omega h)^4}}, \quad (\text{A.2})$$

which can be rewritten as:

$$\frac{\omega^h}{\omega} \sim \sqrt{\frac{N}{D}}, \quad (\text{A.3})$$

with N and D defined as follows:

$$\begin{aligned} N &= 30 - \frac{15}{2}(\omega h)^2 + \frac{11}{12}(\omega h)^4, \\ D &= 30 - \frac{15}{2}(\omega h)^2 + \frac{7}{8}(\omega h)^4. \end{aligned} \quad (\text{A.4})$$

Expression (A.3) can be written as:

$$\frac{\omega^h}{\omega} \sim \sqrt{\frac{1}{1 + \frac{D - N}{N}}} \quad (\text{A.5})$$

and, using the expansions $\frac{1}{1+x} \sim 1-x$ and $\sqrt{1-x} \sim 1-x/2$, it gives rise to:

$$\frac{\omega^h}{\omega} \sim 1 + \frac{N - D}{2N}. \quad (\text{A.6})$$

Finally, substituting the expressions (A.4) for N and D , we get that:

$$\frac{\omega^h}{\omega} \sim 1 + \frac{(\omega h)^4}{1440}, \quad (\text{A.7})$$

which reveals that the order of accuracy is equal to 4.

Figure A.1 shows that, for low frequencies, the normalized discrete spectrum has the same behaviour of the function $1 + (\omega h)^4/1440$ (recall: $\omega h = \pi n/n_{el}$).

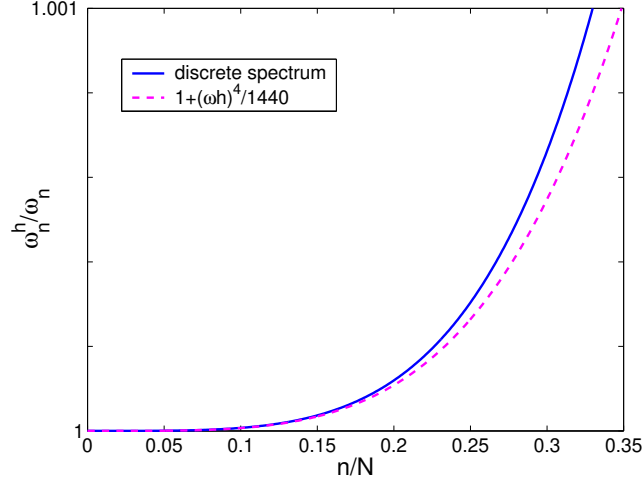


Figure A.1. Rod problem: normalized discrete spectrum using quadratic NURBS versus $1 + (\omega h)^4/1440$ for low frequencies.

A.2 Order of accuracy employing cubic NURBS and consistent mass

Using cubic NURBS, the normalized discrete spectrum is represented by:

$$\frac{\omega^h}{\omega} = \frac{1}{\omega h} \sqrt{\frac{42(16 - 3 \cos(\omega h) - 12 \cos^2(\omega h) - \cos^3(\omega h))}{272 + 297 \cos(\omega h) + 60 \cos^2(\omega h) + \cos^3(\omega h)}}. \quad (\text{A.8})$$

Expanding $\cos(\omega h)$ and repeating the same computations as before, we obtain that:

$$\frac{\omega^h}{\omega} \sim 1 + \frac{(\omega h)^6}{60480}, \quad (\text{A.9})$$

so the order of accuracy in this case is 6 and Figure A.2 confirms this result.

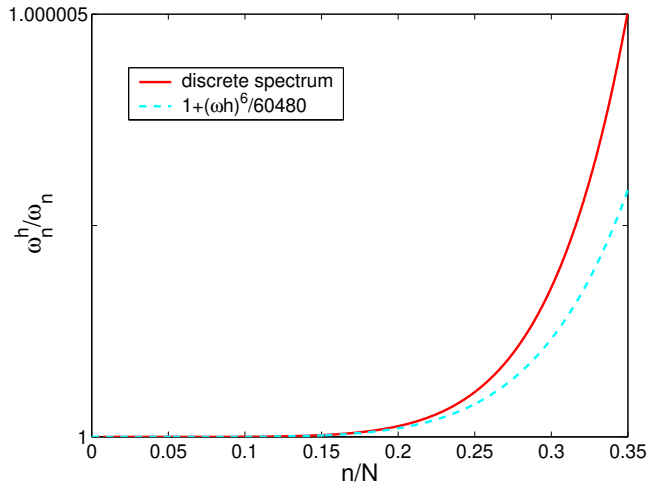


Figure A.2. Rod problem: normalized discrete spectrum using cubic NURBS versus $1 + (\omega h)^6 / 60480$ for low frequencies.

A.3 Order of accuracy employing lumped mass

Similarly to what have been done in the case of consistent mass, also using a lumped mass formulation it is possible to compute the analytical expression for the discrete spectrum arising from the generic interior element equations. In this way, employing quadratic NURBS, we obtain:

$$\frac{\omega^h}{\omega} = \frac{1}{\omega h} \sqrt{\frac{2}{3}(2 - \cos(\omega h) - \cos^2(\omega h))}, \quad (\text{A.10})$$

while with cubic NURBS we get:

$$\frac{\omega^h}{\omega} = \frac{1}{\omega h} \sqrt{\frac{1}{15}(16 - 3 \cos(\omega h) - 12 \cos^2(\omega h) - \cos^3(\omega h))}. \quad (\text{A.11})$$

In this case, these analytical expressions do not reproduce the behaviour of (almost) the whole numerical spectra, but only of their part before the discontinuous derivative point, as shown in Figure A.3.

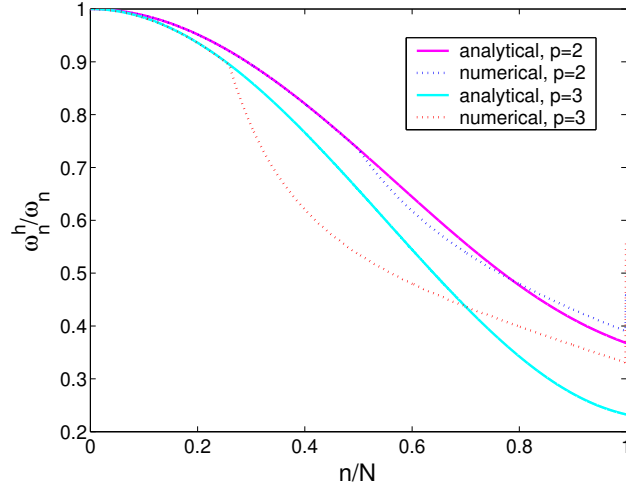


Figure A.3. Rod problem: analytical versus numerical discrete spectrum computed using quadratic and cubic NURBS; lumped mass formulation.

But when we compute the order of accuracy we are interested only in the very low frequency part of the spectrum, so we can carry out the same computation as before.

Hence, by means of Taylor expansions, we obtain, using quadratic NURBS:

$$\frac{\omega^h}{\omega} \sim 1 - \frac{(\omega h)^2}{8} \quad (\text{A.12})$$

and using cubic NURBS:

$$\frac{\omega^h}{\omega} \sim 1 - \frac{(\omega h)^2}{6}. \quad (\text{A.13})$$

We remark that increasing the order p we do not achieve a better order of accuracy (it is always equal to 2).

Finally Figures A.4 and A.5 confirm the validity of expressions (A.12) and (A.13), respectively.

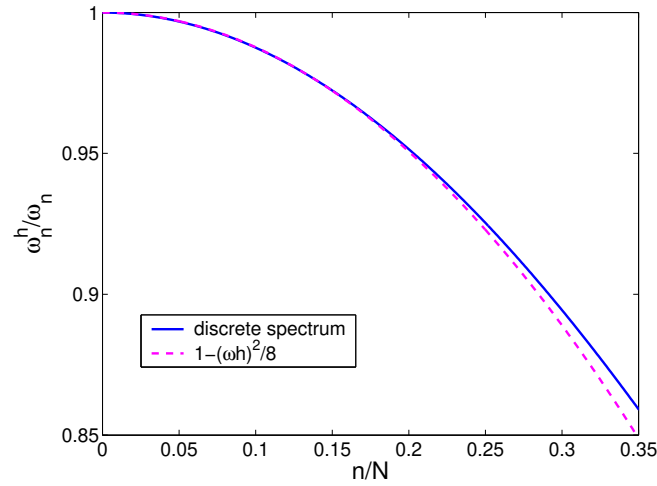


Figure A.4. Rod problem: normalized discrete spectrum using cubic NURBS versus $1 - (\omega h)^2/8$ for low frequencies; lumped mass formulation.

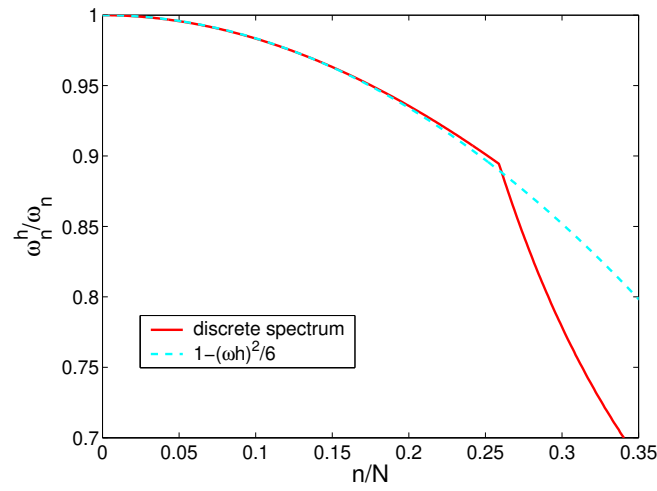


Figure A.5. Rod problem: normalized discrete spectrum using cubic NURBS versus $1 - (\omega h)^2/6$ for low frequencies; lumped mass formulation.

B. PROOFS FOR PROPOSITIONS AND THEOREMS OF CHAPTER 5

B.1 Proof for Proposition 5.1.3

Fix $(\mathbf{v}_h, \tilde{\boldsymbol{\tau}}_h, q_h) \in V_h \times E_h \times P_h$. We first notice that the *inf-sup* condition (5.10) implies the existence of $(\mathbf{z}_h, \tilde{\boldsymbol{\rho}}_h) \in V_h \times E_h$ such that

$$\|(\mathbf{z}_h, \tilde{\boldsymbol{\rho}}_h)\| \leq \beta^{-1} |q_h|_0, \quad b_h(\mathbf{z}_h, \tilde{\boldsymbol{\rho}}_h; q_h) = |q_h|_0^2. \quad (\text{B.1})$$

We will choose

$$(\mathbf{w}_h, \tilde{\boldsymbol{\sigma}}_h, r_h) = (\mathbf{v}_h, \tilde{\boldsymbol{\tau}}_h, q_h) + \delta(\mathbf{z}_h, \tilde{\boldsymbol{\rho}}_h, 0)$$

where δ is a positive parameter still at our disposal. We have

$$\begin{aligned} \mathcal{A}_h(\mathbf{v}_h, \tilde{\boldsymbol{\tau}}_h, q_h; \mathbf{w}_h, \tilde{\boldsymbol{\sigma}}_h, r_h) &= \mathcal{A}_h(\mathbf{v}_h, \tilde{\boldsymbol{\tau}}_h, q_h; \mathbf{v}_h, \tilde{\boldsymbol{\tau}}_h, q_h) \\ &\quad + \delta \mathcal{A}_h(\mathbf{v}_h, \tilde{\boldsymbol{\tau}}_h, q_h; \mathbf{z}_h, \tilde{\boldsymbol{\rho}}_h, 0) \end{aligned} \quad (\text{B.2})$$

Using (5.11) and (5.14) it follows

$$\begin{aligned} \mathcal{A}_h(\mathbf{v}_h, \tilde{\boldsymbol{\tau}}_h, q_h; \mathbf{w}_h, \tilde{\boldsymbol{\sigma}}_h, r_h) &\geq C_1 \|(\mathbf{v}_h, \tilde{\boldsymbol{\tau}}_h)\|^2 \\ &\quad + \delta \mathcal{A}_h(\mathbf{v}_h, \tilde{\boldsymbol{\tau}}_h, q_h; \mathbf{z}_h, \tilde{\boldsymbol{\rho}}_h, 0). \end{aligned} \quad (\text{B.3})$$

Furthermore, using (B.1) and Young's inequality, we obtain for every $\delta_1 > 0$

$$\begin{aligned} \mathcal{A}_h(\mathbf{v}_h, \tilde{\boldsymbol{\tau}}_h, q_h; \mathbf{z}_h, \tilde{\boldsymbol{\rho}}_h, 0) &= 2\mu \left(\boldsymbol{\varepsilon}(\mathbf{v}_h) + \tilde{\boldsymbol{\tau}}_h, \boldsymbol{\varepsilon}(\mathbf{z}_h) + \tilde{\boldsymbol{\rho}}_h \right) + |q_h|_0^2 \\ &\geq -\frac{C_2 \delta_1}{2} \|(\mathbf{v}_h, \tilde{\boldsymbol{\tau}}_h)\|^2 + \left(1 - \frac{C_2 \beta^{-2}}{2\delta_1} \right) |q_h|_0^2. \end{aligned} \quad (\text{B.4})$$

Taking $\delta_1 = C_2\beta^{-2}$ we have

$$\mathcal{A}_h(\mathbf{v}_h, \tilde{\boldsymbol{\tau}}_h, q_h; \mathbf{z}_h, \tilde{\boldsymbol{\rho}}_h, 0) \geq -\frac{C_2^2\beta^{-2}}{2} \|(\mathbf{v}_h, \tilde{\boldsymbol{\tau}}_h)\|^2 + \frac{1}{2}|q_h|_0^2. \quad (\text{B.5})$$

From (B.3) and (B.5) we obtain

$$\mathcal{A}_h(\mathbf{v}_h, \tilde{\boldsymbol{\tau}}_h, q_h; \mathbf{w}_h, \tilde{\boldsymbol{\sigma}}_h, r_h) \geq \left(C_1 - \delta \frac{C_2^2\beta^{-2}}{2}\right) \|(\mathbf{v}_h, \tilde{\boldsymbol{\tau}}_h)\|^2 + \frac{\delta}{2}|q_h|_0^2. \quad (\text{B.6})$$

Therefore, choosing $\delta > 0$ sufficiently small we get (5.17). The continuity condition (5.16) is straightforward.

B.2 Proof for Theorem 5.1.4

Take $(\mathbf{v}_h, q_h) \in V_h \times P_h$ and consider $(\mathbf{u}_h - \mathbf{v}_h, \tilde{\boldsymbol{\varepsilon}}_h, p_h - q_h)$. From Proposition 5.1.3, there exists $(\mathbf{w}_h, \tilde{\boldsymbol{\sigma}}_h, r_h) \in V_h \times E_h \times P_h$ such that

$$\|(\mathbf{w}_h, \tilde{\boldsymbol{\sigma}}_h, r_h)\| \leq c_1 \|(\mathbf{u}_h - \mathbf{v}_h, \tilde{\boldsymbol{\varepsilon}}_h, p_h - q_h)\|, \quad (\text{B.7})$$

$$\mathcal{A}_h(\mathbf{u}_h - \mathbf{v}_h, \tilde{\boldsymbol{\varepsilon}}_h, p_h - q_h; \mathbf{w}_h, \tilde{\boldsymbol{\sigma}}_h, r_h) \geq c_2 \|(\mathbf{u}_h - \mathbf{v}_h, \tilde{\boldsymbol{\varepsilon}}_h, p_h - q_h)\|^2. \quad (\text{B.8})$$

Moreover, it is easily seen that

$$\begin{aligned} \mathcal{A}_h(\mathbf{u}_h - \mathbf{v}_h, \tilde{\boldsymbol{\varepsilon}}_h, p_h - q_h; \mathbf{w}_h, \tilde{\boldsymbol{\sigma}}_h, r_h) &= 2\mu \left(\boldsymbol{\varepsilon}(\mathbf{u} - \mathbf{v}_h), \boldsymbol{\varepsilon}(\mathbf{w}_h) + \tilde{\boldsymbol{\sigma}}_h \right) \\ &+ (p - q_h, \operatorname{div} \mathbf{w}_h + \operatorname{tr} \tilde{\boldsymbol{\sigma}}_h) - (r_h, \operatorname{div}(\mathbf{u} - \mathbf{v}_h)) + \lambda^{-1}(p - q_h, r_h) \\ &- 2\mu \left(\boldsymbol{\varepsilon}(\mathbf{u}), \tilde{\boldsymbol{\sigma}}_h \right) - (p, \operatorname{tr} \tilde{\boldsymbol{\sigma}}_h). \end{aligned} \quad (\text{B.9})$$

We only treat the last two terms, since the others can be handled in a standard way. Let us denote with $\Pi\boldsymbol{\varepsilon}(\mathbf{u})$ (resp. Πp) the L^2 -projection of $\boldsymbol{\varepsilon}(\mathbf{u})$ (resp. p) over the piecewise polynomial functions of order up to $k-1$. Using (5.13), (5.18) and usual approximation results, we have

$$\left(\boldsymbol{\varepsilon}(\mathbf{u}), \tilde{\boldsymbol{\sigma}}_h \right) = \left(\boldsymbol{\varepsilon}(\mathbf{u}) - \Pi\boldsymbol{\varepsilon}(\mathbf{u}), \tilde{\boldsymbol{\sigma}}_h \right) \leq Ch^k |\mathbf{u}|_{k+1} |\tilde{\boldsymbol{\sigma}}_h|_0 \leq Ch^k |\tilde{\boldsymbol{\sigma}}_h|_0 \quad (\text{B.10})$$

and

$$(p, \operatorname{tr} \tilde{\boldsymbol{\sigma}}_h) = (p - \Pi p, \operatorname{tr} \tilde{\boldsymbol{\sigma}}_h) \leq Ch^k |p|_k |\tilde{\boldsymbol{\sigma}}_h|_0 \leq Ch^k |\tilde{\boldsymbol{\sigma}}_h|_0. \quad (\text{B.11})$$

From (B.7)–(B.9) we thus obtain

$$|||(\mathbf{u}_h - \mathbf{v}_h, \tilde{\boldsymbol{\varepsilon}}_h, p_h - q_h)||| \leq C_1 \left(\inf_{\mathbf{v}_h \in V_h} |||\mathbf{u} - \mathbf{v}_h|||_1 + \inf_{q_h \in P_h} |p - q_h|_0 \right) + C_2 h^k . \quad (\text{B.12})$$

Error estimate (5.19) now follows from (5.7)–(5.8), Korn's inequality, assumption (5.12), (5.18) and the triangle inequality.

B.3 Proof for Proposition 5.1.7

Take $\boldsymbol{\gamma} = \mathbf{u} - \mathbf{u}_h$ and $\mathbf{v} = \mathbf{u} - \mathbf{u}_h$ in the first equation of (5.21). We obtain

$$||\boldsymbol{\varphi}||_2 + ||s||_1 \leq C ||\mathbf{u} - \mathbf{u}_h||_0 \quad (\text{cf. (5.22)}) \quad (\text{B.13})$$

and

$$||\mathbf{u} - \mathbf{u}_h||_0^2 = 2\mu \left(\boldsymbol{\varepsilon}(\mathbf{u} - \mathbf{u}_h), \boldsymbol{\varepsilon}(\boldsymbol{\varphi}) \right) + (s, \operatorname{div}(\mathbf{u} - \mathbf{u}_h)) . \quad (\text{B.14})$$

Let $\boldsymbol{\varphi}_I \in V_h$ (resp. $s_I \in P_h$) be an interpolant of $\boldsymbol{\varphi}$ (resp. s) satisfying (see Ciarlet [1978])

$$\begin{cases} ||\boldsymbol{\varphi} - \boldsymbol{\varphi}_I||_1 \leq Ch ||\boldsymbol{\varphi}||_2 , \\ |s - s_I|_0 \leq Ch |s|_1 . \end{cases} \quad (\text{B.15})$$

Taking into account that (\mathbf{u}, p) solve (5.2) and $(\mathbf{u}_h, \tilde{\boldsymbol{\varepsilon}}_h, p_h)$ solve (5.5), we get

$$-2\mu \left(\boldsymbol{\varepsilon}(\mathbf{u} - \mathbf{u}_h), \boldsymbol{\varepsilon}(\boldsymbol{\varphi}_I) \right) - (p - p_h, \operatorname{div} \boldsymbol{\varphi}_I) + 2\mu \left(\tilde{\boldsymbol{\varepsilon}}_h, \boldsymbol{\varepsilon}(\boldsymbol{\varphi}_I) \right) = 0 . \quad (\text{B.16})$$

Similarly, we have

$$-(s_I, \operatorname{div}(\mathbf{u} - \mathbf{u}_h)) + \lambda^{-1}(p - p_h, s_I) + (s_I, \operatorname{tr} \tilde{\boldsymbol{\varepsilon}}_h) = 0 . \quad (\text{B.17})$$

From (B.14)–(B.17) we obtain

$$\begin{aligned} ||\mathbf{u} - \mathbf{u}_h||_0^2 &= 2\mu \left(\boldsymbol{\varepsilon}(\mathbf{u} - \mathbf{u}_h), \boldsymbol{\varepsilon}(\boldsymbol{\varphi} - \boldsymbol{\varphi}_I) \right) + (s - s_I, \operatorname{div}(\mathbf{u} - \mathbf{u}_h)) \\ &\quad - (p - p_h, \operatorname{div} \boldsymbol{\varphi}_I) + \lambda^{-1}(p - p_h, s_I) \\ &\quad + 2\mu \left(\tilde{\boldsymbol{\varepsilon}}_h, \boldsymbol{\varepsilon}(\boldsymbol{\varphi}_I) \right) + (s_I, \operatorname{tr} \tilde{\boldsymbol{\varepsilon}}_h) . \end{aligned} \quad (\text{B.18})$$

Moreover, since $\operatorname{div} \boldsymbol{\varphi} - \lambda^{-1} s = 0$ we have

$$\begin{aligned}
|\mathbf{u} - \mathbf{u}_h|_0^2 &= 2\mu \left(\boldsymbol{\varepsilon}(\mathbf{u} - \mathbf{u}_h), \boldsymbol{\varepsilon}(\boldsymbol{\varphi} - \boldsymbol{\varphi}_I) \right) + (s - s_I, \operatorname{div}(\mathbf{u} - \mathbf{u}_h)) \\
&\quad - (p - p_h, \operatorname{div}(\boldsymbol{\varphi}_I - \boldsymbol{\varphi})) + \lambda^{-1}(p - p_h, s_I - s) \\
&\quad + 2\mu \left(\tilde{\boldsymbol{\varepsilon}}_h, \boldsymbol{\varepsilon}(\boldsymbol{\varphi}_I) \right) + (s_I, \operatorname{tr} \tilde{\boldsymbol{\varepsilon}}_h) \\
&= T_1 + T_2 + T_3 + T_4 + T_5 + T_6 .
\end{aligned} \tag{B.19}$$

Estimates (5.20), (B.15), Cauchy-Schwarz inequality, and (B.13) lead to

$$T_1 \leq 2\mu |\boldsymbol{\varepsilon}(\mathbf{u} - \mathbf{u}_h)|_0 |\boldsymbol{\varepsilon}(\boldsymbol{\varphi} - \boldsymbol{\varphi}_I)|_0 \leq Ch^{k+1} |\boldsymbol{\varphi}|_2 \leq Ch^{k+1} |\mathbf{u} - \mathbf{u}_h|_0 . \tag{B.20}$$

The terms T_2 – T_4 can be handled in the same way to obtain

$$T_i \leq Ch^{k+1} |\mathbf{u} - \mathbf{u}_h|_0 \quad i = 1, \dots, 4 . \tag{B.21}$$

To treat T_5 and T_6 we notice that, due to (5.13), we have

$$\begin{aligned}
T_5 + T_6 &= 2\mu \left(\tilde{\boldsymbol{\varepsilon}}_h, \boldsymbol{\varepsilon}(\boldsymbol{\varphi}_I) - \boldsymbol{\varepsilon}(\boldsymbol{\varphi}) \right) + 2\mu \left(\tilde{\boldsymbol{\varepsilon}}_h, \boldsymbol{\varepsilon}(\boldsymbol{\varphi}) - \overline{\boldsymbol{\varepsilon}(\boldsymbol{\varphi})} \right) \\
&\quad + (s_I - s, \operatorname{tr} \tilde{\boldsymbol{\varepsilon}}_h) + (s - \bar{s}, \operatorname{tr} \tilde{\boldsymbol{\varepsilon}}_h) ,
\end{aligned} \tag{B.22}$$

where $\overline{\boldsymbol{\varepsilon}(\boldsymbol{\varphi})}$ (resp. \bar{s}) is the L^2 -projection of $\boldsymbol{\varepsilon}(\boldsymbol{\varphi})$ (resp. s) over the piecewise constant functions. Recalling that $|\tilde{\boldsymbol{\varepsilon}}_h|_0 \leq Ch^k$ (cf. (5.20)), Cauchy-Schwarz inequality, bounds (B.15) and (B.13) lead to

$$T_5 + T_6 \leq Ch^{k+1} |\mathbf{u} - \mathbf{u}_h|_0 . \tag{B.23}$$

Estimate (5.23) is now a consequence of (B.19), (B.21) and (B.23).

B.4 Proof for Proposition 5.1.7

First of all, notice that by construction conditions (5.12) and (5.13) are satisfied with $k = 1$. Moreover, take $\mathbf{v}_h \in V_h$ and $\tilde{\boldsymbol{\tau}}_h \in E_h^1$. The symmetric gradient $\boldsymbol{\varepsilon}(\mathbf{v}_h)$ is constant on each $T \in \mathcal{T}_h$, so that

$$\int_{\Omega} \boldsymbol{\varepsilon}(\mathbf{v}_h) : \tilde{\boldsymbol{\tau}}_h = 0 . \tag{B.24}$$

It turns out that condition (5.11) holds, with $\theta = 0$. It remains to verify the inf-sup condition (5.10). To this end, we will use Fortin's criterion (cf. Brezzi and Fortin [1991]). In our framework, we thus want to build a linear operator $\Pi_h : V \rightarrow V_h \times E_h^1$ such that

$$\|\Pi_h \mathbf{v}\| \leq C \|\mathbf{v}\|_1 \quad \forall \mathbf{v} \in V \quad (\text{B.25})$$

and

$$b_h(\Pi_h \mathbf{v}; q_h) = \int_{\Omega} q_h \operatorname{div} \mathbf{v} \quad \forall \mathbf{v} \in V, \forall q_h \in P_h. \quad (\text{B.26})$$

We first define $\Pi_1 : V \rightarrow V_h$ as the standard Clément's operator (cf. Clément [1975]). Next, we search for a linear operator $\Pi_2 : V \rightarrow V_h \times E_h^1$ such that

$$b_h(\Pi_2 \mathbf{v}; q_h) = \int_{\Omega} q_h \operatorname{div} \mathbf{v} \quad \forall \mathbf{v} \in V, \forall q_h \in P_h. \quad (\text{B.27})$$

Given $\mathbf{v} \in V$, we will set $\Pi_2 \mathbf{v} = (0, \tilde{\boldsymbol{\sigma}}_h) \in V_h \times E_h^1$, for a suitable $\tilde{\boldsymbol{\sigma}}_h$ dependent on \mathbf{v} . Therefore, the operator Π_2 will be valued only on E_h^1 and condition (B.27) specializes as

$$\int_{\Omega} q_h \operatorname{tr} \tilde{\boldsymbol{\sigma}}_h = \int_{\Omega} q_h \operatorname{div} \mathbf{v} \quad \forall \mathbf{v} \in V, \forall q_h \in P_h. \quad (\text{B.28})$$

Since the pressure interpolation is continuous, from (B.28) we see that we need to solve:

Given $\mathbf{v} \in V$, find $\tilde{\boldsymbol{\sigma}}_h \in E_h^1$ such that

$$\int_{\Omega} q_h \operatorname{tr} \tilde{\boldsymbol{\sigma}}_h = - \int_{\Omega} \nabla q_h \cdot \mathbf{v} \quad \forall q_h \in P_h. \quad (\text{B.29})$$

On each $T \in \mathcal{T}_h$, we locally define $\tilde{\boldsymbol{\sigma}}_h$ by taking $\tilde{\boldsymbol{\sigma}}_T$ as the *unique* solution in $E_4^1(T)$ (cf. (5.28)) of

$$\begin{cases} \tilde{\boldsymbol{\sigma}}_T^D := \tilde{\boldsymbol{\sigma}}_T - \frac{\operatorname{tr} \tilde{\boldsymbol{\sigma}}_T}{2} \boldsymbol{\delta} = 0 \\ \int_T q_1 \operatorname{tr} \tilde{\boldsymbol{\sigma}}_T = - \int_T \nabla q_1 \cdot \mathbf{v} \quad \forall q_1 \in \mathcal{P}_1(T)/\mathbf{R}. \end{cases} \quad (\text{B.30})$$

Setting \bar{q}_h as the L^2 -projection of q_h over the piecewise constant functions, by property (5.13) and (B.30) we have

$$\begin{aligned} \int_{\Omega} q_h \operatorname{tr} \tilde{\boldsymbol{\sigma}}_h &= \int_{\Omega} (q_h - \bar{q}_h) \operatorname{tr} \tilde{\boldsymbol{\sigma}}_h = \sum_{T \in \mathcal{T}_h} \int_T (q_h - \bar{q}_h) \operatorname{tr} \tilde{\boldsymbol{\sigma}}_T \\ &= - \sum_{T \in \mathcal{T}_h} \int_T \nabla (q_h - \bar{q}_h) \cdot \mathbf{v} = - \sum_{T \in \mathcal{T}_h} \int_T \nabla q_h \cdot \mathbf{v} \\ &= - \int_{\Omega} \nabla q_h \cdot \mathbf{v} \quad \forall q_h \in P_h, \end{aligned} \quad (\text{B.31})$$

i.e. $\tilde{\boldsymbol{\sigma}}_h \in E_h^1$ is a solution of system (B.29). Hence, the operator $\Pi_2 : V \rightarrow V_h \times E_h^1$ defined by $\Pi_2 \mathbf{v} = (0, \tilde{\boldsymbol{\sigma}}_h)$ satisfies (B.27).

Moreover, taking $q_1 = \text{tr } \tilde{\boldsymbol{\sigma}}_T$ in (B.30) (notice that this is always possible since $\text{tr } E_4^1(T) = \mathcal{P}_1(T)/\mathbf{R}$), by Cauchy-Schwarz inequality and a scaling argument we get

$$\begin{aligned} |\text{tr } \tilde{\boldsymbol{\sigma}}_T|_{0,T}^2 &= - \int_T \nabla(\text{tr } \tilde{\boldsymbol{\sigma}}_T) \cdot \mathbf{v} \leq |\mathbf{v}|_{0,T} |\nabla(\text{tr } \tilde{\boldsymbol{\sigma}}_T)|_{0,T} \\ &\leq Ch_T^{-1} |\mathbf{v}|_{0,T} |\text{tr } \tilde{\boldsymbol{\sigma}}_T|_{0,T} . \end{aligned} \quad (\text{B.32})$$

Since $\tilde{\boldsymbol{\sigma}}_T^D = 0$, it follows $|\text{tr } \tilde{\boldsymbol{\sigma}}_T|_{0,T} = \sqrt{2} |\tilde{\boldsymbol{\sigma}}_T|_{0,T}$. Therefore, from (B.32) we obtain

$$|\tilde{\boldsymbol{\sigma}}_T|_{0,T} \leq Ch_T^{-1} |\mathbf{v}|_{0,T} . \quad (\text{B.33})$$

If we set

$$\Pi_h \mathbf{v} = \Pi_2(\mathbf{v} - \Pi_1 \mathbf{v}) + \Pi_1 \mathbf{v} \quad \forall \mathbf{v} \in V ,$$

from (B.27), (B.33) and the features of Clément's operator Π_1 , it is easily seen that Π_h verifies (B.25) and (B.26). The proof is complete.

B.5 Proof for Proposition 5.2.5

Take $\mathbf{v} = (v_1, v_2) \in (\text{Ker } B) \cap C^1(\bar{\Omega})$ and observe that on Γ we have $\mathbf{v} \cdot \mathbf{n} = v_2$. Therefore

$$\int_{\Gamma} (\mathbf{v} \cdot \mathbf{n})^2 = \int_{\Gamma} |v_2|^2 . \quad (\text{B.34})$$

Since for every $X \in [-1, 1]$ it holds $v_2(X, -1) = 0$, we get

$$v_2(X, 1) = \int_{-1}^1 v_{2,Y}(X, Y) dY .$$

Hence, the Cauchy-Schwarz inequality gives

$$\int_{\Gamma} |v_2|^2 \leq 2 \int_{\Omega} |v_{2,Y}|^2 . \quad (\text{B.35})$$

Using $\text{div } \mathbf{v} = 0$, we obtain

$$\int_{\Gamma} |v_2|^2 \leq \int_{\Omega} |v_{1,X}|^2 + \int_{\Omega} |v_{2,Y}|^2 \leq \int_{\Omega} |\varepsilon_{11}(\mathbf{v})|^2 + \int_{\Omega} |\varepsilon_{22}(\mathbf{v})|^2 \quad (\text{B.36})$$

for all $\mathbf{v} \in (\text{Ker } B) \cap C^1(\bar{\Omega})$.

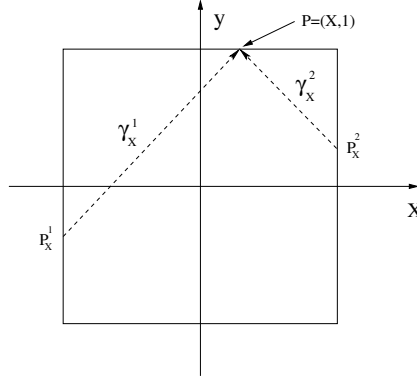


Figure B.1. Oriented paths γ_X^1 and γ_X^2 on Ω .

Before proceeding, we need to introduce some notation. For every point $P = (X, 1)$ with $X \in [-1, 1]$, we define the oriented rectilinear path from point P_X^1 to point P (see Fig. B.1), parametrized by

$$\gamma_X^1(s) = (-1 + s/\sqrt{2}, -X + s/\sqrt{2}) \quad s \in [0, \sqrt{2}(X + 1)] , \quad (\text{B.37})$$

and with unit tangent vector

$$\tau_1 = (1/\sqrt{2}, 1/\sqrt{2}) . \quad (\text{B.38})$$

Similarly, for every $X \in [-1, 1]$, we define the oriented rectilinear path from point P_X^2 to point P (see Fig. B.1), parametrized by

$$\gamma_X^2(s) = (1 - s/\sqrt{2}, X + s/\sqrt{2}) \quad s \in [0, \sqrt{2}(1 - X)] , \quad (\text{B.39})$$

and with unit tangent vector

$$\tau_2 = (-1/\sqrt{2}, 1/\sqrt{2}) . \quad (\text{B.40})$$

Moreover, we introduce the union path $\gamma_X = \gamma_X^1 \cup \{-\gamma_X^2\}$ going from point P_X^1 to point P_X^2 .

For all $X \in [-1, 1]$, it clearly holds

$$v_2(X, 1) = \frac{1}{\sqrt{2}} \mathbf{v}(X, 1) \cdot \tau_1 + \frac{1}{\sqrt{2}} \mathbf{v}(X, 1) \cdot \tau_2 . \quad (\text{B.41})$$

Observing that \mathbf{v} vanishes on $\{-1\} \times [-1, 1]$ and integrating along γ_X^1 , the first term in

the right-hand side of (B.41) can be written as

$$\mathbf{v}(X, 1) \cdot \boldsymbol{\tau}_1 = \int_0^{\sqrt{2}(X+1)} \nabla(\mathbf{v} \cdot \boldsymbol{\tau}_1)(\gamma_X^1(s)) \cdot \boldsymbol{\tau}_1 \, ds, \quad (\text{B.42})$$

which, after some simple algebra, gives

$$\mathbf{v}(X, 1) \cdot \boldsymbol{\tau}_1 = \int_0^{\sqrt{2}(X+1)} \boldsymbol{\varepsilon}(\mathbf{v}(\gamma_X^1(s))) \boldsymbol{\tau}_1 \cdot \boldsymbol{\tau}_1 \, ds. \quad (\text{B.43})$$

Recalling that $\operatorname{div} \mathbf{v} = 0$, it is easy to see that in Ω we have

$$\boldsymbol{\varepsilon}(\mathbf{v}) \boldsymbol{\tau}_1 \cdot \boldsymbol{\tau}_1 = \varepsilon_{12}(\mathbf{v}). \quad (\text{B.44})$$

Using (B.44) and (B.43), we obtain

$$\mathbf{v}(X, 1) \cdot \boldsymbol{\tau}_1 = \int_0^{\sqrt{2}(X+1)} \varepsilon_{12}(\gamma_X^1(s)) \, ds, \quad (\text{B.45})$$

or, in more compact form,

$$\mathbf{v}(X, 1) \cdot \boldsymbol{\tau}_1 = \int_{\gamma_X^1} \varepsilon_{12}(\mathbf{v}). \quad (\text{B.46})$$

Treating similarly the second term in the right-hand side of (B.41), but using the path γ_X^2 , it can be shown that

$$\mathbf{v}(X, 1) \cdot \boldsymbol{\tau}_2 = - \int_{\gamma_X^2} \varepsilon_{12}(\mathbf{v}). \quad (\text{B.47})$$

Recalling (B.41), from (B.46) (B.47) we get

$$v_2(X, 1) = \frac{1}{\sqrt{2}} \left(\int_{\gamma_X^1} \varepsilon_{12}(\mathbf{v}) - \int_{\gamma_X^2} \varepsilon_{12}(\mathbf{v}) \right) = \frac{1}{\sqrt{2}} \int_{\gamma_X} \varepsilon_{12}(\mathbf{v}), \quad (\text{B.48})$$

so that we obtain

$$\int_{\Gamma} |v_2|^2 = \int_{-1}^1 |v_2(X, 1)|^2 \, dX = \frac{1}{2} \int_{-1}^1 \left| \int_{\gamma_X} \varepsilon_{12}(\mathbf{v}) \right|^2 \, dX. \quad (\text{B.49})$$

From (B.49) and observing that $|\gamma_X^1| + |\gamma_X^2| = 2\sqrt{2}$ for all $X \in [-1, 1]$, the Cauchy-Schwarz inequality yields

$$\int_{\Gamma} |v_2|^2 \leq \sqrt{2} \int_{-1}^1 \left(\int_{\gamma_X} |\varepsilon_{12}(\mathbf{v})|^2 \right) \, dX. \quad (\text{B.50})$$

Setting

$$\Omega_1 = \{(X, Y) \in \Omega : Y \geq X\} \quad \Omega_2 = \{(X, Y) \in \Omega : Y \geq -X\} , \quad (\text{B.51})$$

we easily get, using a simple change of variables,

$$\int_{-1}^1 \int_{\gamma_X^1} |\varepsilon_{12}(\mathbf{v})|^2 = \sqrt{2} \int_{\Omega_1} |\varepsilon_{12}(\mathbf{v})|^2 \leq \sqrt{2} \int_{\Omega} |\varepsilon_{12}(\mathbf{v})|^2 , \quad (\text{B.52})$$

and

$$\int_{-1}^1 \int_{\gamma_X^2} |\varepsilon_{12}(\mathbf{v})|^2 = \sqrt{2} \int_{\Omega_2} |\varepsilon_{12}(\mathbf{v})|^2 \leq \sqrt{2} \int_{\Omega} |\varepsilon_{12}(\mathbf{v})|^2 . \quad (\text{B.53})$$

From (B.50), splitting the integral on γ_X into the contributions on γ_X^1 and γ_X^2 , using bounds (B.52)-(B.53) we obtain

$$\int_{\Gamma} |v_2|^2 \leq 4 \int_{\Omega} |\varepsilon_{12}(\mathbf{v})|^2 . \quad (\text{B.54})$$

Recalling (B.34), from (B.36) and (B.54) it follows

$$\int_{\Gamma} |\mathbf{v} \cdot \mathbf{n}|^2 \leq \frac{2}{3} \int_{\Omega} |\boldsymbol{\varepsilon}(\mathbf{v})|^2 \quad (\text{B.55})$$

for all $\mathbf{v} \in (\text{Ker } B) \cap C^1(\bar{\Omega})$.

By density the same estimate holds in $\text{Ker } B$, so that

$$\alpha_M = \sup_{\mathbf{v} \in \text{Ker } B} \frac{\int_{\Gamma} (\mathbf{v} \cdot \mathbf{n})^2}{\int_{\Omega} |\boldsymbol{\varepsilon}(\mathbf{v})|^2} \leq \frac{2}{3} , \quad (\text{B.56})$$

which concludes the proof.

B.6 Proof for Proposition 5.2.7

Take any two adjacent triangles T_1 and T_2 , both with a side contained in $[-1, 1] \times \{-1\}$ (see Fig. 5.11). Consider the function $\mathbf{w}_h = (w_1, w_2) \in U_h$ defined as

$$w_1 = 0 \quad ; \quad w_2 = \begin{cases} b_{T_1} & \text{on } T_1 \\ -b_{T_2} & \text{on } T_2 \\ 0 & \text{otherwise .} \end{cases} \quad (\text{B.57})$$

It is easy to see that

$$\int_{\Omega} q_h \operatorname{div} \mathbf{w}_h = \int_{T_1 \cup T_2} q_h \operatorname{div} \mathbf{w}_h = - \int_{T_1 \cup T_2} \nabla q_h \cdot \mathbf{w}_h = 0 \quad \forall q_h \in P_h, \quad (\text{B.58})$$

so that $\mathbf{w}_h \in K_h$. From (5.73) and (B.57), we get

$$a_{\gamma}(\mathbf{w}_h, \mathbf{w}_h) = 2\mu \int_{T_1 \cup T_2} \left[(w_{2,Y})^2 + \frac{1}{2} (w_{2,X})^2 \right] - \gamma \int_{T_1 \cup T_2} (1 - Y) (w_{2,Y})^2. \quad (\text{B.59})$$

Using that for our particular mesh it holds

$$\int_T (b_{T,Y})^2 = \int_T (b_{T,X})^2 \quad \forall T \in \mathcal{T}_h, \quad (\text{B.60})$$

and noting that on $T_1 \cup T_2$ we obviously have $Y < h - 1$, from (B.57) and (B.59) it follows

$$a_{\gamma}(\mathbf{w}, \mathbf{w}) \leq (3\mu - (2 - h)\gamma) \int_{T_1 \cup T_2} (w_{2,Y})^2. \quad (\text{B.61})$$

Therefore the form $a_{\gamma}(\cdot, \cdot)$ fails to be coercive on K_h whenever γ and h are such that

$$3\mu - (2 - h)\gamma \leq 0. \quad (\text{B.62})$$

It follows that, for $\gamma > 3\mu/2$, the coercivity on the kernel breaks down, provided h is sufficiently small.

B.7 Proof for Proposition 5.2.8

It is easy to check that, for $-\mu < \gamma < \mu$ and $-1 < Y < 1$, there exists a constant $c > 0$ such that

$$2\mu \mathbf{A}^S : \mathbf{A}^S - \gamma r \mathbf{A}^T : \mathbf{A} \geq c |\mathbf{A}^S|^2 \quad (\text{B.63})$$

for every second order tensors \mathbf{A} . From the pointwise positivity property (B.63) it easily follows that, for $-\mu < \gamma < \mu$, the bilinear form (see (5.73))

$$a_{\gamma}(\nabla \mathbf{u}, \nabla \mathbf{v}) = 2\mu \int_{\Omega} \boldsymbol{\varepsilon}(\mathbf{u}) : \boldsymbol{\varepsilon}(\mathbf{v}) - \gamma \int_{\Omega} r (\nabla \mathbf{u})^T : \nabla \mathbf{v} \quad (\text{B.64})$$

is coercive on the whole space U (and therefore in particular for $K_h \subseteq U_h \subseteq U$).

We will now prove that for $\mathbf{v}_h \in K_h$ it holds

$$\int_{\Omega} r (\nabla \mathbf{v}_h)^T : \nabla \mathbf{v}_h \geq 0. \quad (\text{B.65})$$

Once estimate (B.65) has been established, also for $\gamma < 0$ the coercivity property (5.72) immediately follows, and the proof is complete.

We first observe that

$$(\nabla \mathbf{v}_h)^T = (\operatorname{div} \mathbf{v}_h) \mathbf{I} - \operatorname{cof}[\nabla \mathbf{v}_h] . \quad (\text{B.66})$$

Using (B.66) and integrating by parts we have

$$\begin{aligned} \int_{\Omega} r (\nabla \mathbf{v}_h)^T : \nabla \mathbf{v}_h &= \int_{\Omega} r (\operatorname{div} \mathbf{v}_h)^2 - \int_{\Omega} r \operatorname{cof}[\nabla \mathbf{v}_h] : \nabla \mathbf{v}_h \\ &= \int_{\Omega} r (\operatorname{div} \mathbf{v}_h)^2 + \int_{\Omega} \operatorname{div}(r \operatorname{cof}[\nabla \mathbf{v}_h]) \cdot \mathbf{v}_h , \end{aligned} \quad (\text{B.67})$$

where all the boundary integrals vanish because the function $r \mathbf{v}_h$ vanishes on the whole boundary $\partial\Omega$.

Due to Piola's identity and using (B.66) we have

$$\begin{aligned} \int_{\Omega} \operatorname{div}(r \operatorname{cof}[\nabla \mathbf{v}_h]) \cdot \mathbf{v}_h &= \int_{\Omega} \operatorname{cof}[\nabla \mathbf{v}_h] \nabla r \cdot \mathbf{v}_h \\ &= - \int_{\Omega} (\nabla \mathbf{v}_h)^T \nabla r \cdot \mathbf{v}_h + \int_{\Omega} (\operatorname{div} \mathbf{v}_h) \nabla r \cdot \mathbf{v}_h . \end{aligned} \quad (\text{B.68})$$

Recalling that on Γ we have $\nabla r = -\mathbf{n}$, simple algebra and an integration by parts give

$$\begin{aligned} - \int_{\Omega} (\nabla \mathbf{v}_h)^T \nabla r \cdot \mathbf{v}_h &= - \int_{\Omega} \nabla r \cdot [\nabla \mathbf{v}_h] \mathbf{v}_h \\ &= \int_{\Omega} (\operatorname{div} \mathbf{v}_h) \nabla r \cdot \mathbf{v}_h - \int_{\Gamma} (\mathbf{v}_h \cdot \mathbf{n})(\mathbf{v}_h \cdot \nabla r) \\ &= \int_{\Omega} (\operatorname{div} \mathbf{v}_h) \nabla r \cdot \mathbf{v}_h + \int_{\Gamma} |\mathbf{v}_h \cdot \mathbf{n}|^2 . \end{aligned} \quad (\text{B.69})$$

Using (B.67), (B.68) and (B.69) it follows

$$\int_{\Omega} r (\nabla \mathbf{v}_h)^T : \nabla \mathbf{v}_h = \int_{\Omega} r (\operatorname{div} \mathbf{v}_h)^2 + 2 \int_{\Omega} (\operatorname{div} \mathbf{v}_h) (\nabla r \cdot \mathbf{v}_h) + \int_{\Gamma} |\mathbf{v}_h \cdot \mathbf{n}|^2 . \quad (\text{B.70})$$

We now split each component of \mathbf{v}_h in its linear and bubble parts, i.e.

$$\mathbf{v}_h = \mathbf{v}_h^L + \mathbf{v}_h^B = (v_1^L + v_1^B, v_2^L + v_2^B) . \quad (\text{B.71})$$

Accordingly, noting also that

$$\nabla r \cdot \mathbf{v}_h = -(v_2^L + v_2^B) , \quad (\text{B.72})$$

equation (B.70) can be written as

$$\begin{aligned} \int_{\Omega} r (\nabla \mathbf{v}_h)^T : \nabla \mathbf{v}_h &= \int_{\Omega} r (\operatorname{div}(\mathbf{v}_h^L + \mathbf{v}_h^B))^2 \\ &\quad - 2 \int_{\Omega} (\operatorname{div}(\mathbf{v}_h^L + \mathbf{v}_h^B))(v_2^L + v_2^B) + \int_{\Gamma} |(\mathbf{v}_h^L + \mathbf{v}_h^B) \cdot \mathbf{n}|^2 \\ &= A_1 + A_2 + A_3 . \end{aligned} \quad (\text{B.73})$$

We now estimate the three terms above. We obviously have

$$A_1 := \int_{\Omega} r (\operatorname{div}(\mathbf{v}_h^L + \mathbf{v}_h^B))^2 \geq 2 \int_{\Omega} r (\operatorname{div} \mathbf{v}_h^L)(\operatorname{div} \mathbf{v}_h^B) . \quad (\text{B.74})$$

Integrating by parts and using that $\nabla r \cdot \mathbf{v}_h^B = -v_2^B$, from (B.74) we obtain

$$A_1 \geq -2 \int_{\Omega} (\operatorname{div} \mathbf{v}_h^L) \nabla r \cdot \mathbf{v}_h^B = 2 \int_{\Omega} (\operatorname{div} \mathbf{v}_h^L) v_2^B . \quad (\text{B.75})$$

Recalling that $\mathbf{v}_h = \mathbf{v}_h^L + \mathbf{v}_h^B \in K_h$ and observing that \mathbf{v}_2^L is a continuous piecewise linear function, it follows that

$$A_2 := -2 \int_{\Omega} (\operatorname{div}(\mathbf{v}_h^L + \mathbf{v}_h^B))(v_2^L + v_2^B) = -2 \int_{\Omega} (\operatorname{div}(\mathbf{v}_h^L + \mathbf{v}_h^B)) v_2^B . \quad (\text{B.76})$$

Since it holds

$$\int_{\Omega} (\operatorname{div} \mathbf{v}_h^B) v_2^B = 0 , \quad (\text{B.77})$$

from (B.76) we get

$$A_2 = -2 \int_{\Omega} (\operatorname{div} \mathbf{v}_h^L) v_2^B . \quad (\text{B.78})$$

Furthermore, for A_3 we obviously have

$$A_3 := \int_{\Gamma} |(\mathbf{v}_h^L + \mathbf{v}_h^B) \cdot \mathbf{n}|^2 \geq 0 .$$

Collecting (B.75), (B.78) and (B.79), we finally get (cf. (B.73))

$$\int_{\Omega} r (\nabla \mathbf{v}_h)^T : \nabla \mathbf{v}_h \geq 2 \int_{\Omega} (\operatorname{div} \mathbf{v}_h^L) v_2^B - 2 \int_{\Omega} (\operatorname{div} \mathbf{v}_h^L) v_2^B = 0 . \quad (\text{B.79})$$

The Proposition is proved.

B.8 Proof for Proposition 5.2.9

Let us define the set $F(\gamma) \subset \Omega$ by

$$F(\gamma) = \{(X, Y) \in \Omega : 2\mu - \gamma r(X, Y) \leq 0\} . \quad (\text{B.80})$$

Recalling that $r(X, Y) = 1 - Y$, the set $F(\gamma)$ has positive area for $\gamma > \mu$. It follows that, for sufficiently small h , there exists $\tilde{K} \in \mathcal{T}_h$ completely contained in $F(\gamma)$. Now take $(\mathbf{v}_h, \mathbf{E}_h) \in U_h \times S_h$ by choosing $\mathbf{v}_h = 0$ and \mathbf{E}_h vanishing outside \tilde{K} . Moreover, in \tilde{K} choose (cf. (5.77))

$$\mathbf{E}_h|_{\tilde{K}} = \begin{bmatrix} \alpha \xi \eta & ; & 0 \\ 0 & ; & -\alpha \xi \eta \end{bmatrix} \quad \text{with } \alpha \neq 0 . \quad (\text{B.81})$$

Notice that $\operatorname{tr} \mathbf{E}_h = 0$; hence $(0, 0) \neq (0, \mathbf{E}_h) \in K_h$ (cf. (5.79)). On the other hand, a direct computation shows that

$$a_{\gamma}(\mathbf{E}_h, \mathbf{E}_h) = \int_{\tilde{K}} (2\mu - \gamma r) |\mathbf{E}_h|^2 . \quad (\text{B.82})$$

Since $\tilde{K} \subseteq F(\gamma)$, we have $(2\mu - \gamma r) \leq 0$, so that (B.82) implies

$$a_{\gamma}(\mathbf{E}_h, \mathbf{E}_h) \leq 0 . \quad (\text{B.83})$$

As a consequence the form $a_{\gamma}(\cdot, \cdot)$ cannot be coercive on K_h for $\gamma > \mu$, uniformly in h .